Modelling Terrestrial Clear-Air Microwave Radio Fading

by

Stephen John Salamon

B. Sc.(Physics, Comp. Sci.), B. E.(Elec),
University of Adelaide, 1976, 1981

Thesis submitted for the degree of

Doctor of Philosophy

in

Electrical and Electronic Engineering
University of Adelaide

2022

Supervisors:
Prof Derek Abbott, School of Electrical & Electronic Engineering
Dr Hedley J. Hansen, School of Electrical & Electronic Engineering

THE UNIVERSITY of ADELAIDE

Contents

Abstract

The technology of communication systems between population centres has undergone much change over the last century an a half, but radio links continue to be an important part of communication networks. A challenging part of their design is allowing for variations in received signal level, known as radio fading and enhancement, due to the atmosphere between transmitter and receiver.

At high frequencies rain fading is the limiting factor, but below about 10 GHz, temperature and humidity gradients, in the absence of precipitation, may produce clear-air fading that becomes the limiting factor. As the refractive index of the air at radio frequencies depends on temperature and humidity, vertical gradients of these parameters cause bending of ray-paths. Multiple signals may arrive at the receiver over different paths, resulting in multipath fading. Sometimes almost no signal at all is able to find its way from transmitter to receiver, resulting in an impairment known as median depression; this may last for an hour or more, with median signal level up to 50 dB below normal.

Recent long-term observations show this fading to be particularly severe in some parts of Australia, but not well predicted by pre-existing models. This thesis develops a new international model for clear-air fading.

Weather forecasting has made significant progress in recent years due to numerical weather prediction (NWP) models, so radio propagation researchers have aimed to use these models to predict the state of the atmosphere, and Fourier split-step parabolic equation modelling (PEM) to predict radio propagation.

Considering this, we begin this thesis by investigating Fourier split-step PEM, developing new techniques for dealing with finite conductivity lower boundaries, estimating the absorbing upper boundary height, and for dealing with irregular terrain, in both two and three dimensions. A brief description of the internationally adopted empirical model for diffraction over terrain (*Rec. ITU-R P526-15*, 2019), completes this chapter.

We then examine radio refractivity gradient cumulative distributions derived from NWP data, comparing them with measurements from radiosondes, and data from sensors mounted on towers. We find the NWP prediction of anomalous gradients in the surface atmospheric layer to be poor, and develop a new parameter, *surface refractivity anomaly*,

derived from surface weather station time-series data. We find this parameter useful in predicting vertical radio refractivity gradients in the atmospheric surface layer.

Due to NWP surface gradient accuracy problems, we adopt the empirical regression model approach to fading severity prediction. This is not new, but we now have the benefit of more fading data from more regions of the world, and we have our new prediction parameters, generated from several years of data from thousands of world-wide weather stations.

We make novel refinements to the modelling of clear-air fading, by first replacing ordinary least squares (OLS) regression with generalised least squares (GLS) regression, to take spatial correlation into account. We then employ the geostatistical technique of universal kriging, to further improve prediction accuracy.

Our new fading model, as described in this thesis, is now the internationally approved terrestrial line-of-sight model for fading due to multipath and related mechanisms (*Rec. ITU-R P.530-18*, 2021).

Statement of Originality

I certify that this work contains no material which has been accepted for the award of any other degree or diploma in my name, in any university or other tertiary institution and, to the best of my knowledge and belief, contains no material previously published or written by another person, except where due reference has been made in the text. In addition, I certify that no part of this work will, in the future, be used in a submission in my name, for any other degree or diploma in any university or other tertiary institution without the prior approval of the University of Adelaide and where applicable, any partner institution responsible for the joint award of this degree.

I give permission for the digital version of my thesis to be made available on the web, via the University's digital research repository, the Library Search and also through web search engines, unless permission has been granted by the University to restrict access for a period of time.

I acknowledge the support I have received for my research through the provision of an Australian Government Research Training Program Scholarship.

	15th March 2022
Signed	Date

Acknowledgments

Firstly I would like to thank my PhD supervisors at the University of Adelaide, Derek Abbott and Hedley Hansen. Professional researchers in the field of terrestrial radio propagation are rare, so I am truly grateful to Hedley for enthusiastically taking me on as a PhD student to do this reseach, and to Derek, with his wide-ranging knowledge and experience, in accepting me as a student. The time both of them have spent in keeping me on the correct path is greatly appreciated.

Much of the credit for me being able undertake this research must go to colleagues and supervisors going back many years. It started in late 1981, when I had the good fortune to join Telecom Australia's radio link design group in Adelaide, possibly the most scientifically based radio design group in the country.

Towards the end of that career came the opportunity to generate, for the first time in Australia, a significant amount of radio link fading data, and submit it to the international ITU-R databank, with the enthusiatic support of my managers, Martin Turner, followed by Kym Chilton. Robert Testen also was of great assistance in obtaining this fading data, and without that data to add to data already collected in other countries, this research would have been vastly inferior, and of questionable value to design engineers in Australia.

My thanks also go to Terje Tjelta, who provided the radio path profiles for the many links already in the ITU-R databank, and to Frederico Fernandes Neves and Agência Nacional de Telecomunicações, for providing accurate coordinates of the historical Brazilian radio link sites in the ITU-R data. I am grateful to Paul Hettrick and the Bureau of Meteorology for providing detailed Australian radiosonde data, allowing comparison with lower resolution NOAA data for the same ascents.

Particular credit must go to Carol Wilson (CSIRO), who as then Chairman of Australian Radio Study Group 3 (Radiowave Propagation), invited me to join the group in 1998. I am grateful to her and the other members of the group for their support and encouragement, which helped set me on the path to radio propagation research. My special thanks go to one of these members, Andy Kulessa (DSTO), who has been a mentor and collaborator for the last 20 years or so, including assisting me as co-author on the first conference paper I wrote in 2004. Little did we realise at the time, that this frequency

coordination paper would be instrumental in achieving efficient rollout of the first 6000 3G mobile base stations in Australia in 2006.

I would like to thank the administrative staff of the School of Electrical and Electronic Engineering, and those who have kept the department running smoothly of the period of my candidacy, and provided vital support, including Rose-Marie Descalzi, David Bowler, Franca Guest, Stephen Guest, Laura McNamara, Deb Koch, Mark Innes, Jodie Schluter, and Pavel Simcik. I also thank my postgraduate coordinator Withawat Withayachumnankul, and the members of my major review committee.

I would like to dedicate this thesis to the memory of my late beloved wife Sandra, who enthusiastically supported me and our son John in all we did, including that first conference paper I presented in 2004. Only the next year she passed away, but although she is sadly missed, we have both continued on, following her fine example in many ways. As I write this, my son too, has just submitted his PhD thesis. I thank him too, for assistance with things such as implementing automated weather data download for me on his web server, and showing me how to work GitHub.

Conventions

This thesis it typeset using LaTeXsoftware: TeXstudio editor with MiKTeX 2.9 compiler. Harvard style is used for referencing and citation in this thesis. Australian English spelling is adopted, as defined by the Macquarie English Dictionary (Delbridge 2001).

Analysis has been coded, without the use of special toolboxes, generally to run in Matlab or Octave, but the worldwide digital map of terrain elevation area standard deviation, from 30 second Globe v1.0 terrain data, was coded for execution by Python 3.7.4. Bitmap graphics are generated by Matlab or Octave, and vector graphics produced by OpenOffice 3.2.

Two different conventions are frequently used for relative complex permittivity η, in Chapter 2 of this thesis. We follow the convention of Levy (2000, equ.(9.6)), so we use $\eta = \epsilon_r + i\frac{\sigma}{kc\epsilon_0} = \epsilon_r + i\ 59.9585\ \lambda\sigma$, where ϵ_0, λ and k are respectively the absolute permittivity, wavelength and wavenumber, in a vacuum. The alternative convention, seen in some texts, has a negative imaginary component.

For consistency with our parabolic equation references in Chapter 2, we use i to represent $\sqrt{-1}$ rather than the electrical engineering convention of j.

Publications

Journal papers relevant to this thesis:

Salamon-S. J., Hansen-H. J., and Abbott-D.(2015). Modelling radio refractive index in the atmospheric surface layer, *Electronics Letters*, 51(14), pp. 1119–1121.
doi: 10.1049/el.2015.0195

Salamon-S. J., Hansen-H. J., and Abbott-D.(2019). How real are observed trends in small correlated datasets?, *Royal Society Open Science*, 6(3), art. no. 181089.
doi: 10.1098/rsos.181089

Salamon-S. J., Hansen-H. J., and Abbott-D.(2020). Universal kriging prediction of line-of-sight microwave fading, *IEEE Access*, 8, pp. 74743–74758.
doi: 10.1109/ACCESS.2020.2987618

Other journal papers:

Dorraki-M., Fouladzadeh-A., Salamon-S. J., Allison-A., Coventry-B. J., and Abbott-D. (2018). On detection of periodicity in C-reactive protein (CRP) levels, *Scientific Reports*, 8, art. no. 11979. doi:10.1038/s41598-018-30469-8

Dorraki-M., Fouladzadeh-A., Salamon-S. J., Allison-A., Coventry-B. J., and Abbott-D. (2019). Can C-reactive protein (CRP) time series forecasting be achieved via deep learning?, *IEEE Access*, 7, pp. 59311-59320. doi: 10.1109/ACCESS.2019.2914473

Conference papers:

Salamon-S. J., Hansen-H. J., and Abbott-D.(2013). A transform space filtered, wide frequency-range implementation of the parabolic equation method, *Proc. RADAR 2013*, Adelaide, Australia. doi: 10.1109/radar.2013.6652010

Salamon-S. J., Hansen-H. J., and Abbott-D.(2014). Prediction of surface refractivity gradient distributions,from weather station surface data, *Proc. EuCAP 2014*, The Hague, Netherlands, pp. 507–511.

Salamon-S. J., Hansen-H. J., and Abbott-D.(2014). Surface refractivity gradient data for radio system design, *Proc. URSI GASS 2014*, Beijing, China.
doi: 10.1109/ACCESS.2020.2987618

Salamon-S. J., Hansen-H. J., and Abbott-D.(2016). Radio link clear-air fading prediction from surface weather station data, *Proc. ISAP 2016*, Okinawa, Japan, pp. 72–73.

Hansen-H. J., Vanderklugt-A., Kulessa-A. S., Hacker-J.M. , Salamon-S. J., and Veasey-M.(2020). Observations and modelling of propagation loss in the turbulent sea surface environment, *Proc. 14th European Conference on Antennas and Propagation* (*EuCAP*). doi: 10.23919/EuCAP48036.2020.9135963

There were two conference papers published as prime author prior to this candidacy: (Salamon and Kulessa 2004, Salamon and Wilson 2008).

List of Figures

List of Tables

Chapter 1

Introduction

RADIO technology has advanced significantly since fixed line-of-sight radio links started to replace open wire carrier systems to provide broadband communications between poulation centres, over half a century ago. Despite the changes from analog to digital modulation, and increases in the data rate carried by the radio channel bandwidth, one problem is the same now as it was with the first radio transmission routes of the 1960's: the unguided medium between transmitter and receiver suffers signal fading due either to rain attenuation, or resulting from ray bending due to atmospheric refractivity gradients. The link designer needs to predict the severity of this fading, choosing antennas with enough gain, i.e. physically large enough, so the radio link receivers will have sufficient signal in excess of the minimum to operate satisfactorily (known as fade margin), for reliable link performance. At frequencies above 10 GHz, rain attenuation fading dominates link design, limiting path length, but the focus of this thesis is instead prediction of the severity of clear air fading, due to anomalous refractivity gradients. This signal fading defines the performance of line-of-sight links at the lower frequencies, generally required when the distance between transmitter and receiver exceeds 20 kilometres.

1.1 Introduction

Terrestrial microwave radio links have been a significant component of communication networks for over half a century. Empirical models aiming to predict the clear-air fading events (not associated with rain) that they occasionally suffer, have been of interest to radio link designers for most of that time. Optical fibre has largely replaced digital radio on most major long routes in the transmission network, but digital radio is still important on routes where optical fibre is un-economical, such as off-shore islands, or niche applications such as low-latency networks. Unguided radio signals travel at the speed of light, but light signals in optical fibres are slower, due to both the refractive index of the glass fibre, and the group velocity of the guided mode.

Radio link design depends on accurate estimation of the severity of fading events, as this determines the required design fade margin. This is the attenuation of received signal, compared to median conditions, which may be tolerated before serious transmission errors occur. Increasing the system fade margin is expensive as it involves costs such as increased antenna size and stronger support structures, but insufficient fade margin leads to poor link error performance. Above 10 GHz rain attenuation tends to dominate terrestrial radio link fading, but below 10 GHz clear-air fading, the subject of this thesis, tends to dominate, allowing longer radio path lengths than at the higher frequencies.

The following papers cited in this chapter were all produced as part of the work for this thesis: (Salamon *et al.* 2013, Salamon *et al.* 2014a, Salamon *et al.* 2014b, Salamon *et al.* 2015, Salamon *et al.* 2016, Salamon *et al.* 2019, Salamon *et al.* 2020).

1.2 Outline of thesis

The fading model developed in this thesis is a revised version of a previously published model (Salamon *et al.* 2020), so the thesis outline is largely an expansion on the logical sequence of that paper, but with some revisions in the source data. We begin in this chapter, describing the history of line-of-sight radio link clear air fading prediction, and our motivation for development of a new fading model.

Propagation along a terrestrial radio path is affected by refractive index variations in the atmosphere, and diffraction and reflection effects of the intervening terrain, so in Chapter 2 we describe the practical full-wave analysis of these effects, using Fourier split-step parabolic equation modelling (PEM). We develop practical implementations

of this analysis, both in two and three dimensions. We conclude this chapter by describing the internationally agreed empirical general method for estimating terrain diffraction loss, as this description is not available in the open literature.

In Chapter 3 we describe modelling of atmospheric refractive index variations, by numerical weather prediction (NWP) models, and by empirical models that use only meteorological data from surface weather stations.

In Chapter 4 we describe linear regression modelling, and the development of new models for the line-of-sight fading problem, including taking spatial correlation into account.

One traditional approach to solving the problem of predicting radio link clear-air fading severity, has been to implement separate multipath and sub-refraction models. In Chapter 5 we explore this approach, comparing it with the unified regression modelling approach of Chapter 4.

Chapter 6 extends the regression model, combining it with interpolation, by means of universal kriging, to provide local adaptation of the world-wide regression model.

1.3 Radio link design and technology

This research relates to the design of fixed terrestrial radio links, and the prediction of clear-air fading, not due to precipitation, that affects their performance. In order to clarify the scope of this research, we provide a brief overview of the process of designing radio links, and discussion of various radio link technologies.

1.3.1 Fixed radio link design

The process of designing a radio system may be summarised as meeting the need to provide communication of required data capacity, between specified locations. The design engineer will aim to design the system that can be installed for minimum cost, while satisfying a number of constraints.

Constraints include digital error performance objectives, system availability (how much of the time the system is working acceptably), and considerations of equipment types and frequency bands available.

The designer may have to consider whether repeater sites need to be established, at considerable cost, or if the specified end points may be reached satisfactorily with a single radio link, or "radio hop."

As radio is an unguided medium, subject to atmosheric variations, fundamental to the design process is accurate prediction of the severity of level variations in the received signal, known as fading and enhancement.

1.3.2 Technology generations: analog, digital, and IP radio

All early fixed radio links employed analog technology, typically using FM modulation by a baseband signal of up to a few megahertz bandwidth, which might be frequency-division multiplex of many telephone channels, 4 kHz apart (FM-FDM systems), or a single analog TV signal.

The prime consideration then was non-selective fading, uniformly affecting the whole 30 to 40 MHz wide channel, as the signal energy tended to be concentrated near the carrier frequency, and selective fading, varying in fade depth across the channel at any moment in time, was of secondary importance, although not ignored, as it produced "intermodulation noise" in FM-FDM systems.

By the early 1980's, analog broadband radio links were being replaced by digital broadband links, typically with data rates of 140 Mbit/s in 40 MHz channels, employing 16 QAM modulation in Australia. The early systems were quite sensitive to inter-symbol interference, due to the multipath propagation that causes selective fading, so this became the prime consideration in designing high capacity digital radio links.

The emergence of radio equipment since around 2000, where hardware was replaced with software, enabled quite sophisticated correction for inter-symbol interference, such as transversal equalisers, routinely provided in even the cheapest radio equipment. This shifts the focus in performance prediction now back more to predicting non-selective fading. However, the prediction models in *Rec. ITU-R P.530-17,* (2017) estimate both non-selective fading and selective fading performance impairment, as well as signal enhancements, from the single prediction of non-selective fading. Providing an accurate model for non-selective fading is then the prime requirement for predicting all forms of clear-air impairment to fixed links. That therefore is the focus of this research.

Another important type of link fading is due to precipitation, primarily due to rain in Australia, but that tends to dominate only at frequencies above 10 GHz, where the rain

drop size approaches the radio wavelength. We do not deal with that, as it is a separate area of study.

The traditional digital radio links operated at a constant data rate, so the receive level threshold for severe errors was a constant, but internet protocol (IP) digital radios do not have to provide a constant data rate. They may use adaptive code modulation (ACM) to allow operation at a lower data rate during fading conditions, resulting in higher receiver threshold. We do not address this either in this research, as our focus is on the fundamental technology independent problem of accurate fading prediction, which must be addressed before technology dependent problem such as this, can be properly studied.

1.4 Worst month radio fading distributions

Fundamental to understanding this research is understanding the Radio Bureau of the Internation Telecommunications Union (ITU-R) concept of the "worst month." We detail this here, because it relates to the seasonal variability of atmospheric propagation impairment, and that these seasonal variations often vary from year to year. Radio link designers need a measure of the impairment likely to be encountered during the worst month of a typical year in the location of interest, so ITU-R has produced a carefully worded relatively unambiguous definition (*Rec. ITU-R P.581-2*, 1990).

One important definition is "the worst month of a year for a preselected threshold for any performance degrading mechanism, be that month in a period of twelve consecutive calendar months, during which the threshold is exceeded for the longest time. The worst month is not necessarily the same month for all threshold levels." We note that using this definition, the worst month in one year is not necessarily the same calendar month as the worst month for that same threshold in another year. Perhaps this should have been explicitly stated; omitting this may lead to some degree of ambiguity.

Our interpretation is supported by the stated procedure for obtaining the cumulative fading distribution for the average worst month (*Rec. ITU-R P.530-17*, 2017, Attachment 1 to Annex 1): "Obtain the worst calendar month envelope fading distribution for each year of operation, using the long-term median value as a reference. Average these to obtain the cumulative fading distribution for the average worst month and plot this on a semi-logarithmic graph."

We provide this clarification to avoid the assumption that the worst month for a particular threshold is likely to be the same month in all years. This assumption leads to monthly distributions being be averaged over a number of years for each calendar month, and then the worst-month distribution obtained by taking the worst-case of those 12 distributions. An example of this assumption, that we believe is incorrect, is Hewitt (2003, Figure 4.7).

Contrary to this, we assume the worst month distribution is independently determined for each year of data recording, and the average year worst month distribution is the mean of these. This definition avoids under-estimation of propagation impairments that vary from year to year in which month they are most severe.

We define the observed clear-air worst-month fading distribution to be the mean of these individual worst-month distributions from each year of observation, relative to the median receive level, ignoring fading events due to precipitation, such as rain attenuation. At frequencies below 10 GHz, severe rain attenuation only occurs with extreme rain events, so rain gauge data may be inspected to ensure the deep fading tail of the recorded distribution is not being influenced by rain events. Our aim is to model the clear-air fading, as this is the dominant limitation to performance of lower-frequency microwave links.

1.5 Motivation

Electromagnetic wave propagation along the path between a fixed transmitter and a receiver at the other end of the path, is affected by various mechanisms that the radio link designer needs to consider, and methods to predict these effects are provided in *Rec. ITU-R P.530-17,* (2017). The prediction models provided there for clear air effects (non-selective fading, selective fading, diversity improvement, signal enhancement) all depend on the severity of the narrow-band multipath fading distribution. This is represented by multipath occurrence factor, P_0, the proportion of time axis intercept of the extrapolated tail slope of the average year worst month fading distribution. The severity of any of these clear air effects may be predicted from this single parameter, P_0. This is demonstrated for one of the radio links in this research, in Figure 1.1.

This multipath occurrence factor has been found empirically to depend on path length and inclination, local terrain characteristics, and local climatic characteristics. Prior to

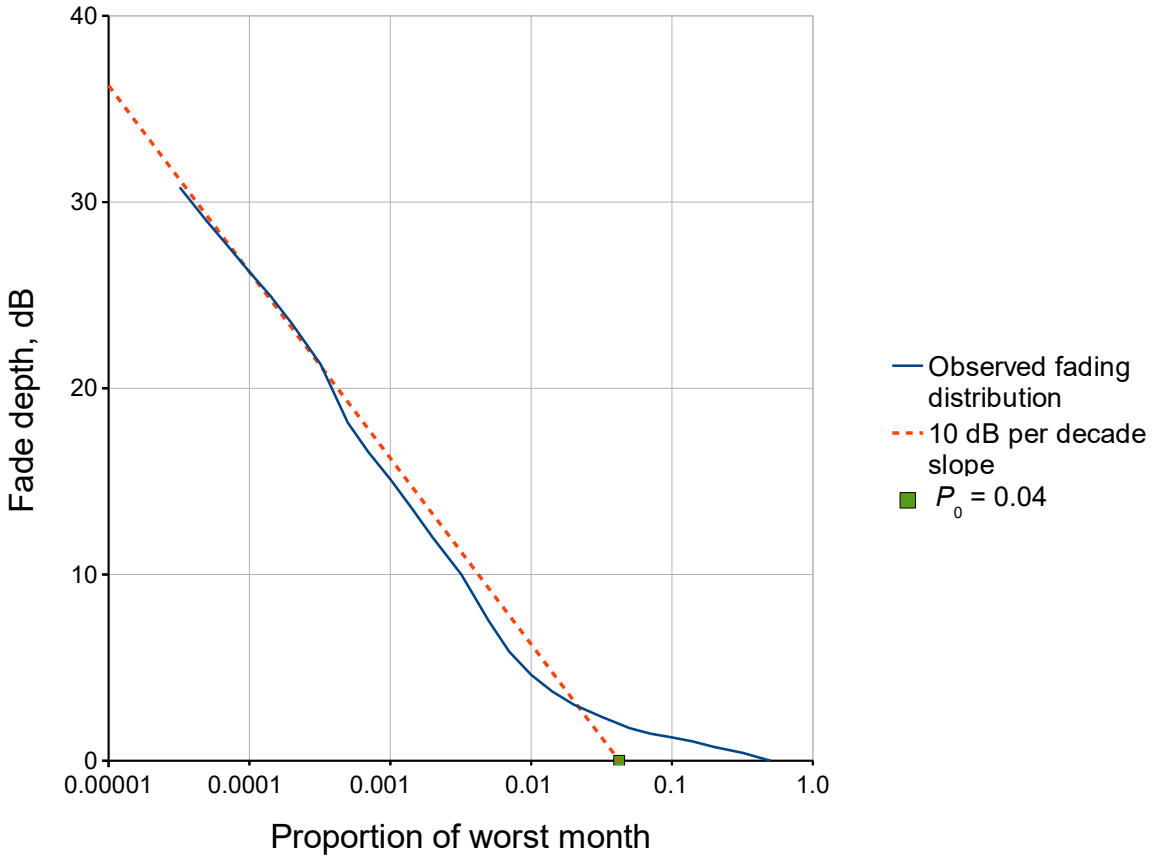

Figure 1.1. Example of multipath occurrence factor, P_0. This is the observed fading distribution for the 50.95 km link from Buckambool to The Cottage at 1.8535 GHz, demonstrating P_0 as the probability axis intercept of the worst month fading distribution tail slope. The observed distribution shown here is the dB attenuation mean of each of the four worst month distributions, from the four years of observation.

our current research, no published line-of-sight link multipath fading models included any long-term measured fading data from the Australian region in their model fitting.

Accurate prediction of P_0 is fundamental to the design of links below 10 GHz, as for a simple non-diversity system (one antenna at each end of the link, and only one frequency channel in each direction of transmission), the amount of time that transmission is lost (outage time) due to the signal fading below receiver threshold, is proportional to P_0. Alternatively, this fading severity may be expressed in terms of the fade depth for 0.01% of the worst month, as $A_{0.01} = 10\log(P_0) + 40$ dB.

Radio links longer than around 30 km typically employ space diversity, with a second receiver antenna at each terminal to provide a second receive signal with fading partially uncorrelated with the main antenna signal. This typical arrangement greatly reduces the amount of outage time, but this time is now roughly proportional to ${P_0}^2$. This is because the short-term variation of the signal in the second receiver is only partially correlated with the short-term variation of the signal in the main receiver. Accurate prediction of P_0 is vital, to allow the designer to reliably estimate if the performance of the radio link is likely to be acceptable.

Accuracy of the pre-existing multipath model (*Rec. ITU-R P.530-17*, 2017) is demonstrated by the Voronoi diagram of residuals in Figure 1.2. This diagram consists of spherical polygons enclosing all points closer to the radio link location, indicated by a small white cross, than to any other. The colour of each tile indicates the difference between observed fade depth and model predicted fade depth for the radio link. Red indicates fading 15 dB more severe than predicted, which for a link with diversity reception, could mean link outage time up to a thousand times worse than predicted!

In Figure 1.2 (a) we see the diagram for links included in generating the current model before our research (*Rec. ITU-R P.530-17*, 2017). In absence of any other information, it would have been difficult to make any assumptions about accuracy in Australia. The closest link to Australia involved in fitting that model, one link in Pakistan, had fading 10 dB more severe than the model, while next closest, three links in Africa, had observed fading within 3 dB of the prediction.

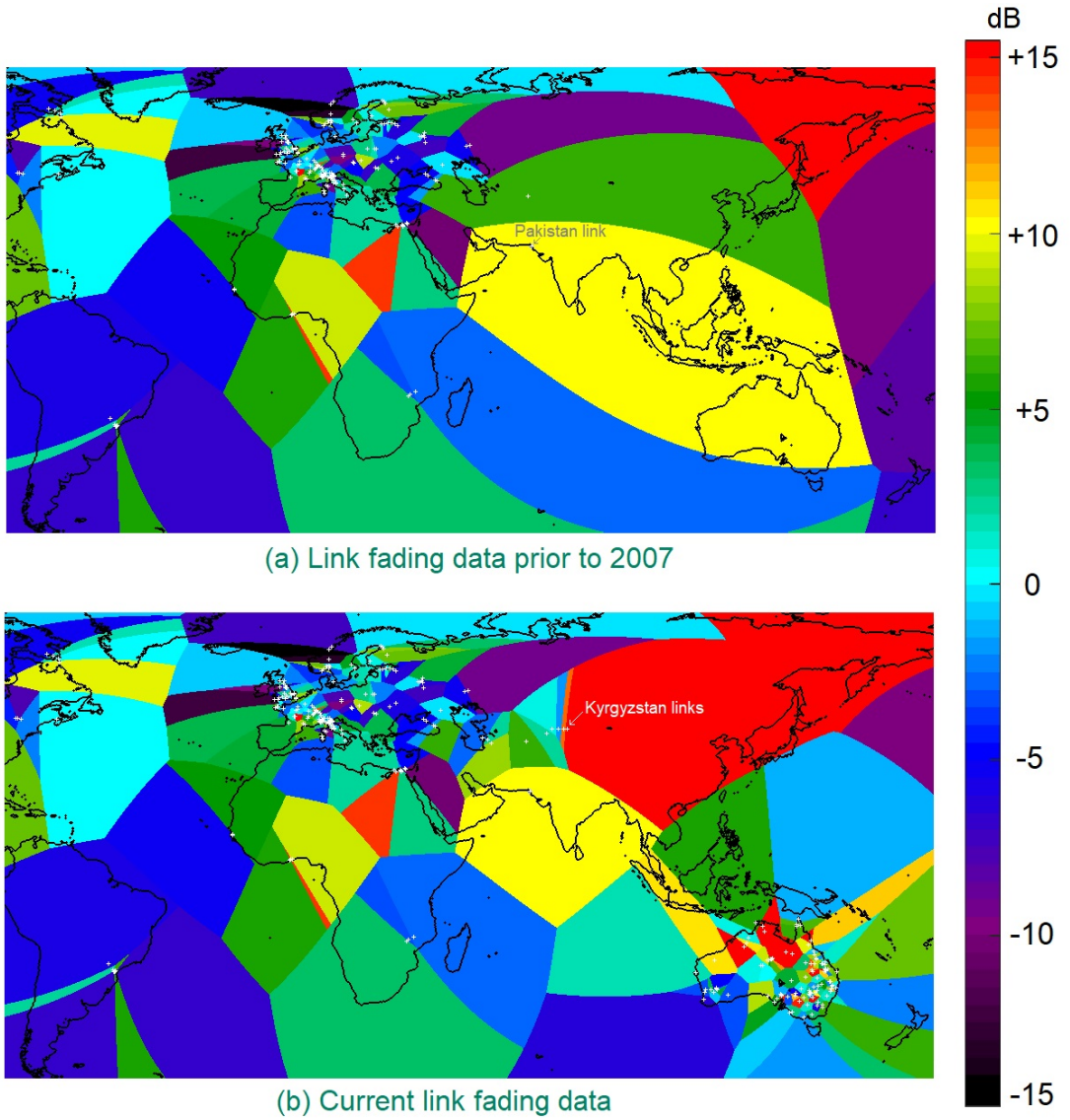

(a) Link fading data prior to 2007

(b) Current link fading data

Figure 1.2. Voronoi diagram of Rec. ITU-R P.530-17 model residuals. The link locations are shown as small white crosses, and the colour of the surrounding spherical polygon indicates observed fading minus predicted, for (a) the data available prior to 2007, and (b) for all current data. The P.530-17 model was fitted to data from the links in (a), none of which were in or near Australia. The closest was one link in Pakistan (+10 dB residual), and next closest are one in Uzbekistan (+6 dB residual), and three links in Zimbabwe, Malawi and Mozambique, with between +3 and –3 dB residuals. With current data we see in (b) that the model under-predicts fade depth by more than 10 dB in eastern Kyrgyzstan and a number of inland areas in Australia. Such an error may lead to radio link designs with insufficient fade-margin, resulting in extremely poor performance, severely affecting communities relying on the links for their communications. Link designers have used local ad-hoc models to avoid these problems, but a new internationally agreed fading model is badly needed.

However, we see in Figure 1.2 (b), if we include new data now available, that fading is severely under-predicted in some parts of Australia, and in eastern Kyrgyzstan. Fortunately most Australian link designers have been aware of some of the areas of severe fading, such as inland Northern New South Wales, through inland Queensland, to Northern Territory (Harvey 1987), or across the Nullabor Plain (Shepherd 1979), and devised ad-hoc local methods to account for these observations, but no worldwide solution to this problem has been available.

The recent availability of fading data from many line-of-sight links in Australia, makes it an opportune time to develop a new prediction model, including the new data.

1.6 Background

1.6.1 Early history of clear-air fading models

It has long been recognised that multipath propagation, due to variations in the refractive index of the air at different heights in the surface layer of the atmosphere, is a significant factor in fading of microwave paths (Pearson 1965). During fading events, signal strength variations may be approximated by a Rayleigh distribution (*Rec. ITU-R P.1057-6*, 2019). This is the distribution of amplitude of the sum of a large number of components with similar amplitude but each having an independent uniform phase distribution. As a result, the tail of the fading distribution for small percentages of time tends to have a slope of 10 dB per decade of probability. The deep-fading distribution may be estimated in terms of a slope of 10 dB per decade of probability relative to the fade depth (dB) for 0.01% of the worst month of an average year, $A_{0.01}$, and this formulation is used throughout this paper.

Based on measurements in the United Kingdom, Pearson (1965) suggested one of the early prediction models, in terms of distance d (km) and path roughness s (m), which may be written as

$$A_{0.01} = 27.8 \log(d) - 12.37 \log(s) + 2.43 \quad \text{dB.} \tag{1.1}$$

Curves predicting fading distributions for path lengths of 150 to 250 km, at 4 GHz and 6 GHz (Battesti and Boithias 1964), were based on observed fading on several French radio links between 1952 and 1963. The 4 GHz curves, with the addition of curves for 75 and 50 km based on United Kingdom observations, led to the first line-of-sight

multipath model provided by the International Radio Consultative Committee (CCIR) (*Report CCIR 338*, 1966). This model is reproduced at Figure 1.3.

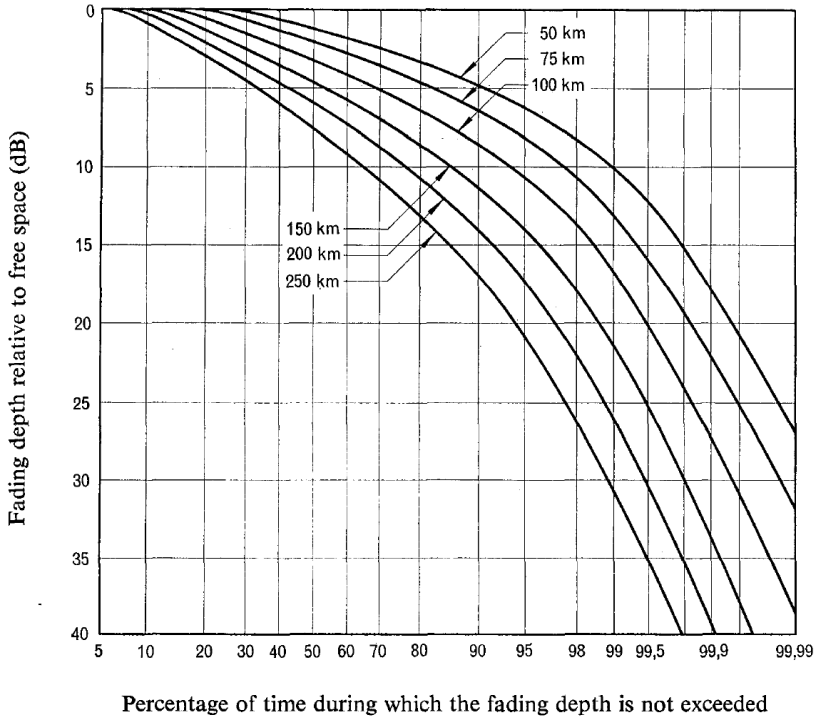

Figure 1.3. The first CCIR line-of-sight multipath model. This fading model, based on observations in France and the United Kingdom, was recommended for line-of-sight microwave fading prediction for the worst month of the year, at 4 GHz, in average rolling terrain, for north-west Europe (after the first version of CCIR Report 338, 1966, Oslo).

Another early example by Morita (1970), had separate models, depending on the terrain or climate type. Expressed in a similar form to (1.1), the version provided in *Report CCIR 338-6*, (1990) is, firstly for inland paths:

$$A_{0.01} = 12\log(f) + 35\log(d) - 30 \quad \text{dB}, \tag{1.2}$$

or mountainous paths:

$$A_{0.01} = 12\log(f) + 35\log(d) - 34.09 \quad \text{dB}, \tag{1.3}$$

or coastal paths, temperate and fairly flat:

$$A_{0.01} = 12\log(f) + 35\log(d) - 5\log(h_1 + h_2) - 10.04 \quad \text{dB}, \tag{1.4}$$

where f is the frequency (GHz), and h_1, h_2 are terminal antenna heights (m) above mean sea level.

Well known is the Barnett-Vigants model (Barnett 1972, Vigants 1975), again consisting of different versions, depending on the terrain or climate. For "average terrain":

$$A_{0.01} = 10\log(f) + 30\log(d) - 22.22 \quad \text{dB}, \tag{1.5}$$

or over-water or Gulf Coast:

$$A_{0.01} = 10\log(f) + 30\log(d) - 16.2 \quad \text{dB}, \tag{1.6}$$

or mountains or dry climate:

$$A_{0.01} = 10\log(f) + 30\log(d) - 28.24 \quad \text{dB}. \tag{1.7}$$

Although expressed above logarithmically in terms of fade depth for 0.01% of the worst month, the above models are often expressed in a power-law form, in terms of percentage p of the worst month that the fade depth exceeds A dB. Thus the Barnett-Vigants model may be written (*Report CCIR 338-6*, 1990) as

$$p = KQfd^3 10^{-A/10} \tag{1.8}$$

where K is a factor representing the effect of terrain and climate, and Q is a factor accounting for the effect of path variables other than d and f. We use the equivalent logarithmic form of the models in this paper, for simplicity in later discussion of multiple linear regression models.

Terrain roughness, or standard deviation of terrain height along the radio path, s, was taken into account in a later version of the US or Barnett-Vigants model, given in *Report CCIR 338-6*, (1990); we note the similarity of the following to (1.1) around 4 GHz. In the case of coastal or over water paths:

$$A_{0.01} = 10\log(f) + 30\log(d) - 13\log(s) - 3.87 \text{ dB}, \tag{1.9}$$

or maritime subtropical:

$$A_{0.01} = 10\log(f) + 30\log(d) - 13\log(s) - 5.09 \text{ dB}, \tag{1.10}$$

or inland:

$$A_{0.01} = 10\log(f) + 30\log(d) - 13\log(s) - 6.78 \text{ dB}, \tag{1.11}$$

or mountainous:

$$A_{0.01} = 10\log(f) + 30\log(d) - 13\log(s) - 10 \text{ dB}. \quad (1.12)$$

A fundamental problem with the above models (1.2) to (1.12), is the need to choose a version of the model, based on the subjective assessment of the terrain or climate type. This problem remained in the ITU-R prediction model until 1999 (*Rec. ITU-R P.530-8,* 1999, Olsen and Tjelta 1999), as the model contained constants to be chosen according to terrain type (plains, hills or mountains). Comparative testing of the above models is provided in Olsen *et al.* (2003).

1.6.2 Line-of-sight radio link fading data

The link fading data used in this research consists of 409 records from the most recently accepted data table the ITU-R line-of-sight link fading databank, DBSG3 Table I-2 (*Rec. ITU-R P.311-17,* 2017), "Line-of-sight average worst-month multipath fading and enhancement in narrow bandwidths." We exclude 48 of the total 457 records because of data inconsistencies, or absence of one or more parameters required for this study. To this we add 126 recently generated Australian records, approved by ITU-R Sub-Working-Group 3M-1 (Terrestrial Systems) for inclusion in the DBSG3 databank, resulting in a total of 535 data records for this study. The complete table, including the new Australian records, is given in *Australia: ITU-R doc. 3M/235,* (2021). This consists of 583 records, but records with station numbers 9, 17, 33, 34, 46, 124, 125, 132, 146 to 160, 175, 180, 183, 189, 192, 205, 243, 259, 264, 266, 273 to 280, 291, 295 and 297 are excluded from our research because essential fields are missing, or there is serious inconsistency between fields in the table data, or between the table data and known path profiles.

We divide these records into 21 regions, each including links within 1500 km of centre coordinates, chosen initially for each region as the link centre coordinates of the first link encountered that falls outside the 1500 km radii of regions already defined, and then updated to the median coordinates as more links are added to each region. The details of these regions are shown in Table 1.1.

The locations of the links in Table 1.1 are shown in Figure 1.4.

In common with previous studies (Tjelta *et al.* 1990, Tjelta *et al.* 1998, *Telenor ASA: ITU-R doc. 3M/175,* 2006), our aim is to predict the Rayleigh fading tail of the multipath fading distribution, assuming a slope of the cumulative distribution of 10 dB per decade of

Table 1.1. Fading data records by region, showing coordinates, number of records, and number of different link locations, for each of the 21 regions. The mid-point coordinates of all links in each region are within 1500 km of the coordinates in the table.

Region Number	Latitude	Longitude	Fading Records	Link Locations	Region
1	+49.06	+1.12	48	42	Western Europe
2	+59.84	+21.11	42	28	Scandinavia
3	+53.01	+37.13	20	16	Russia
4	+39.05	+55.82	3	3	Turkmenistan
5	+45.12	–76.37	13	5	South-East Canada
6	+51.48	–122.1	10	9	South-West Canada
7	+74.78	–98.83	4	4	Arctic Canada
8	–25.27	–49.17	7	6	Brazil
9	+62.53	–65.72	4	4	North-East Canada
10	+24.85	+67.08	1	1	Pakistan
11	+30.84	+31.09	7	7	Egypt
12	+44.40	+10.95	79	55	Southern Europe
13	+5.76	+0.19	3	3	Ghana
14	+12.77	–16.11	3	2	Senegal
15	–16.54	+33.17	3	3	South-East Africa
16	+42.37	+75.20	6	6	Central Asia
17	–20.61	+132.9	50	15	Central-North Australia
18	–32.86	+142.1	91	31	South-East Australia
19	–25.59	+147.7	92	32	Southern Queensland
20	–30.62	+118.7	36	11	South-West Australia
21	–12.48	+142.3	17	7	Far North Queensland

probability, starting at the *first tail point* of the worst-month distribution, $(a_1$ dB, $p_1\%)$. This first tail point is available for all links in the data table, but in most cases additional fade depths and enhancements at several specific percentage points are available. Figure 1.5 illustrates this for one link in Denmark. The 10 dB per decade of probability slope starting from the first tail point and extending to greater fade depths is consistent with the observed tail of the fading distribution.

An inconsistency has been found in in the first tail point of just one record, station number 182. It departs from the observed distribution by about one order of magnitude

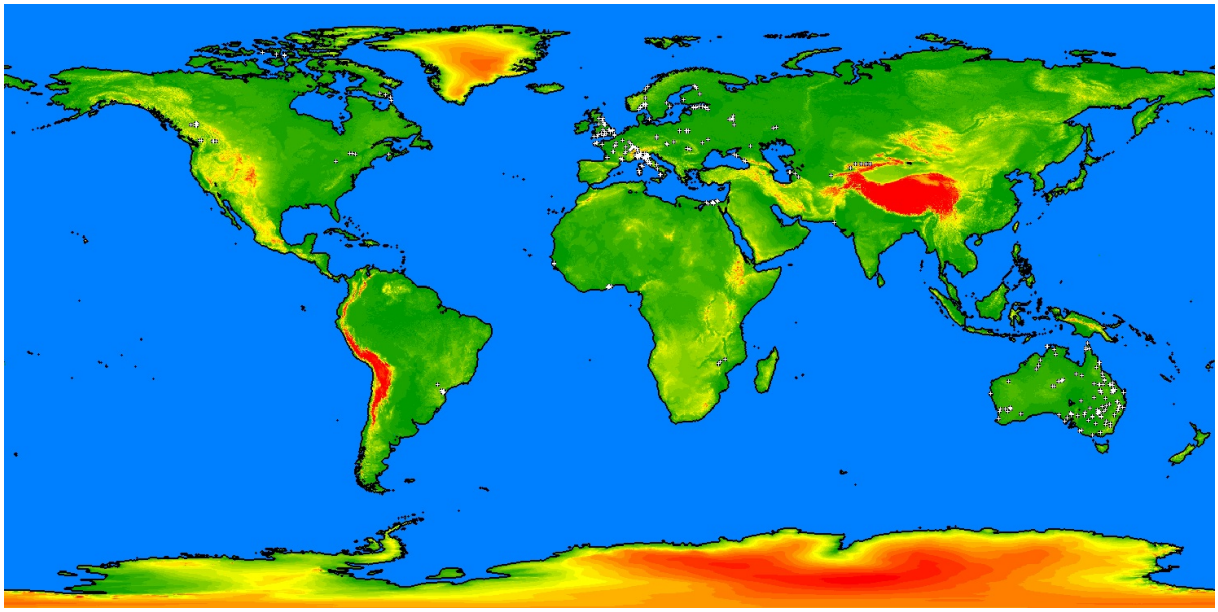

Figure 1.4. Links in the ITU-R line-of-sight multipath data table. The link locations are shown as white crosses. Terrain elevation is indicated by colour, from green at sea level to yellow at 2000 metres, and to red at 4000 metres and above. There is a good density of links in much of Europe and Australia. In the Americas, fading data is only available from Canada and Brazil. There are some data records from various countries in Africa and Asia. Unfortunately there has been no data contributed from Asia from anywhere east of Kyrgyzstan.

in percentage, or about 10 dB in fade depth. This is the only record available in the Pakistan region, so we base the assumed 10 dB per decade tail on the observation of 23.5 dB fade depth at 0.1% of the worst month, as shown by the dashed red line in Figure 1.6.

The complete and corrected link fading data table used in this research is provided in *Australia: ITU-R doc. 3M/235,* (2021).

1.6.3 Median depression fading

During multipath fading events, a depression in the median signal level is often seen. An early description (Pearson 1965) was that "median depression during worst fading hour is approximately $0.3 \times$ fade depth for 0.1% of the worst month." This reference, based on experience in the United Kingdom, even reported "almost complete loss of signal (space-wave fadeout) that can occur on some paths."

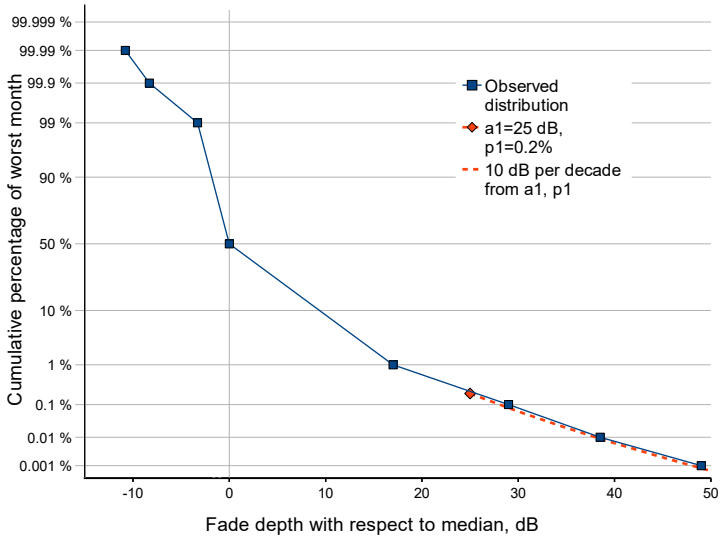

Figure 1.5. Lerbjerg-Borups Alle, Denmark. The the dark blue trace shows the fading distribution at several percentage points. In the data table the first tail point of the distribution, (a_1, p_1) is identified for all records; the start of the approximate 10 dB per decade of probability multipath tail of the fading distribution. The databank first tail point $(a_1, p_1) = (25 \text{ dB}, 0.2\%)$ (red diamond) is consistent with the observed distribution, so assume a 10 dB per decade of probability slope to smaller percentages of the worst month.

One possible cause identified for median depressions was positive vertical gradients of radio refractivity in the atmosphere, known as *sub-refraction*. The upward curvature of ray-paths caused by a linear gradient of this type, if sufficiently severe, may be expected to cause terrain obstruction of a radio link that is normally unobstructed. A ray-path between transmitter and receiver when there is a positive refractivity gradient will travel closer to the ground than the *standard refractivity* case of mildly negative vertical gradient.

While non-linear gradient refractive effects, such as focussing or de-focussing, or even caustics that cause ray-paths from the transmit antenna to miss the receive antenna entirely (Boithias and Battesti 1967), may cause median depression fading, a simple model for the worst sub-refractive gradient likely to be experienced in a temperate climate (Boithias and Battesti 1967) has been employed as part of clearance criteria for line-of-sight path design for many years (*Report CCIR 338-6*, 1990, *Rec. ITU-R P.530-8*, 1999, *Rec. ITU-R P.530-17*, 2017). This model depends on radio path length d (km),

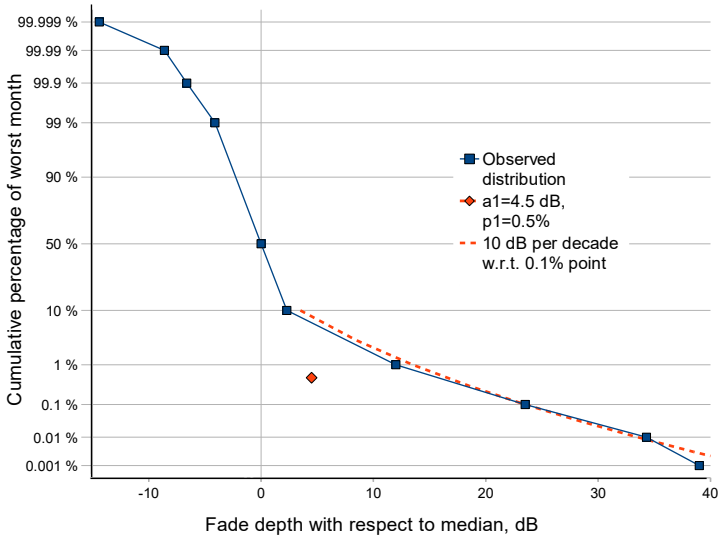

Figure 1.6. Korangi-Marston Road, Pakistan. In this case the databank first tail point $(a_1, p_1) = (4.5 \text{ dB}, 0.5\%)$ (red diamond) is inconsistent with the observed distribution, probably a typographical error, so we assume a 10 dB per decade slope relative to the observed 0.1% point of the distribution.

and may be expressed as a vertical refractivity gradient:

$$\frac{\mathrm{d}N}{\mathrm{d}z} = \frac{2670}{d} - 13 \qquad \text{N-units per km.} \tag{1.13}$$

However, more severe median depression fading has been observed in some regions; for example, the coastal region of the Nullabor Plain in southern Australia (Shepherd 1979), inland Queensland in north-eastern Australia (Harvey 1987), or south-eastern USA (Schiavone 1981, Vigants 1981). A common feature of these studies is the assumption that a linear positive refractivity gradient is the likely worst-case of a sub-refractive atmosphere. Boundary layer similarity theory (Obukhov 1971) indicates that surface refractivity gradients are likely to be stronger near the surface than at greater heights. A sub-refractive profile of this non-linear form has been shown to be capable of greater attenuation on a terrestrial path than a linear gradient with the same increase in refractivity over the lowest 100 m of the atmosphere (Salamon *et al.* 2015).

Nevertheless, the idea of complementing a multipath fading model with a sub-refractive diffraction model (Vigants 1981) has been often adopted as a convenient way to estimate the overall fading of radio paths in regions where the available multipath models alone are insufficient. The necessary data for the Schiavone model (Schiavone 1981) has been produced for the contiguous states of USA, but not for other regions (Kizer 2008). A sub-refractive model, assuming the main cause to be advection of moist air over a

dry nocturnal duct, during the early hours of the morning (Harvey 1987), may in principle be applied world-wide, subject to the availability of suitable (preferably 3-hourly or better) surface weather station data.

1.6.4 Median depression, multipath, and diversity

During the minimum signal conditions in median depression events, received signal fluctuation suggests that multipath is occurring, and this tends to be supported by a fading distribution slope of about 10 dB per decade in the region of 0.1% of the worst month, for the severe median depression fading 7.5 GHz path from Cooks Tank to Rosewood in Queensland, Australia (*Australia: ITU-R doc. 3M/186,* 2011). The worst median depression in this month on that path, with a depth of about 50 dB, cannot be created by multipath cancellation alone, as all four receivers, on two different frequencies for the two directions of transmission, and with receiver antennas at two different heights at each terminal, all experience the deep median depression at the same time. This characteristic is generally seen in other median depression events on other radio paths.

These characteristics suggest that on line-of-sight microwave paths, severe multipath fading and median depression tend to occur together, as parts of a continuum, rather than distinct events. This is inherent in the ITU-R multipath model (*Rec. ITU-R P.530-17,* 2017), since the multipath occurrence factor P_0 (intercept of the extrapolated deep fading distribution with the zero dB or time axis) is generally greater than the multipath activity parameter η, the proportion of the time that multipath is assumed to be occurring. In the model *Rec. ITU-R P.530-17,* (2017), the two are related by the expression

$$\eta = 1 - \exp(-0.2 {P_0}^{0.75}) \, . \tag{1.14}$$

Radio links often employ diversity reception to reduce errors and outage during multipath fading, using two or more receivers with different antenna heights (space diversity) or receiving a second transmission on a different frequency (frequency diversity), taking advantage of their partially correlated multipath fading. Provided the depth of the median depression is less than the system fade margin, there may still be some diversity improvement during median depression fades, albeit quite limited. The median depressions are generally simultaneous between the different receivers, but the superimposed multipath is likely to de-correlated to some extent. A recent revision of the diversity improvement models in *Rec. ITU-R P.530-17,* (2017) has ensured that fading

severity is taken into account in all diversity improvement models, to reflect the degradation in all types diversity improvement seen during severe median depression fading events.

1.7 Original Contributions

This summary cites the relevant papers published, and sections of this thesis:

1. Alerted the terrestrial radio propagation community to accuracy problems in radio refractivity surface gradient data from numerical weather prediction models. This led to the addition of warning text in *Rec. ITU-R P453-14,* (2019): Section 3.5.

2. Empirical prediction models for the distribution of surface gradient, with better accuracy, using only surface weather station data, were presented, firstly in (Salamon *et al.* 2014a), and an improved model (Salamon *et al.* 2014b): Sub-section 3.6.3.

3. Described a new extension of the Paulus evaporation duct model for neutral atmospheres, to cover stable and unstable atmospheres, and described application to sub-refraction as well as ducting, (Salamon *et al.* 2015): Sub-section 3.7.1.

4. Developed a technique to compensate for uncorrelated measurement error, when producing cumulative distributions from periodic measurements. (Salamon *et al.* 2014a): Sub-section 3.4.3.

5. Derived an expression providing guidance on the height of the upper boundary absorber, and hence transform size, to avoid spurious reflections in parabolic equation modelling. This avoids trial-and-error or excessive transform size (unpublished): Sub-section 2.3.8

6. Developed a new approach to parabolic equation modelling of radio propagation over terrain, not using terrain flattening or the staircase approximation (unpublished): Sub-section: 2.3.11. This method has been extended to 3D modelling (un-published): Sub-section: 2.3.12

7. Presented a new OLS worldwide multipath model, including Australian fading data for the first time, successfully modelling severe median depression fading by including parameters generated from the time series of surface weather station data. (Salamon *et al.* 2016): Sub-section 4.2.2.

8. Developed an extension of the Durbin-Watson statistic for testing correlation in one-dimensional (e.g. time series) data, to multiple dimensions, by describing the new concept of the *nearest new neighbour path*, (Salamon *et al.* 2019): Subsection 4.4.2.

9. Presented a new worldwide multipath fading model, using, for the first time in such a model, the technique of universal kriging, to combine the benefits of a worldwide regression model with interpolation of local fading data, where available, (Salamon *et al.* 2020). This new model is the basis of an Australian input to ITU-R Study-Group 3 (Radiowave Propagation) (*Australia: ITU-R doc. 3M/236,* 2021), which has been adopted by Radio Study-Group 3 of the International Telecommunication Union, as its model for predicting fixed-link multipath fading (*Rec. ITU-R P.530-18,* 2021): Chapter 6.

Chapter 2

Radio Propagation Modelling

RADIO propagation between fixed radio stations is affected by atmospheric refraction and by diffraction and reflection from the underlying terrain or water surface. A complete solution to this problem requires a full wave method based on a solution of Maxwell's equations. Fixed radio links have known transmitter and receiver locations, so the paraxial approximation of the parabolic equation, is useful, particularly in the form of the Fourier split-step solution. We describe this, with particular emphasis on the practical requirements to make it work reliably, including some new approaches. For completeness, a simple general terrain diffraction model for linear refractivity gradients, in widespread use in recent years, is described.

2.1 Introduction

The fading prediction models used by radio link designers have been empirical, rather than scientific. A reasonable atmospheric physics approach may be to predict the state of the atmosphere with a numerical weather prediction (NWP) model, and then use a terrain parabolic equation model (PEM)(Barrios 1994, Donohue and Kuttler 2000) to predict the radio propagation. This idea has been pursued for some time, both for radio link propagation (Ewenz *et al.* 2001), and in radar propagation research, but sub-meter resolution may be required in generating the refractivity profile (Claverie 2019).

A reliable very high resolution NWP reanalysis product, to accurately model the boundary layer atmosphere would be required, to practically implement fading prediction for path design, using this approach. Even then, the link designer would have to run a few years equivalent of simulations, to accurately determine the average year worst month performance of the link. Despite advances in computing capability, this may be impractical in the short term.

Nevertheless, this approach deserves to be investigated, with a view to pursuing it, either now or in future research. This is because an empirical model is not necessarily valid beyond the range of conditions represented in the empirical data, while model based on physics can more confidently be expected to have an extended range of validity. In any case, a suitable full wave propagation model is an essential tool if we are to gain an understanding of the impact on radio propagation of physical processes occurring in the atmosphere.

There are numerous ways to model radiowave propagation. Fixed radio links involve scattering, diffraction and reflection from objects in the transmit-receive path, as well as being affected by detailed and complicated refractivity gradients in the propagating medium. Methods using Geometrical Theory of Diffraction (GTD) or Uniform Theory of Diffraction (UTD) rely on idealised diffracting objects such as knife edges or wedges, which do not directly relate to the deep fading process in wave propagation on paths over real terrain that is the topic of this thesis. Numerical techniques associated with integral equation methods are able to cope with arbitrary terrain, but cannot cope readily with refractive index variations in the propagating medium (Levy 1990).

In this chapter we provide a description of the Fourier split-step parabolic equation algorithm. It has the advantage of readily accommodating refractive index variations in the propagating medium, the atmosphere, in its formal derivation, and therefore

it is a most suitable modelling tool for investigating the complex atmospheric effects responsible for the deep fading events reported in this thesis.

Although many papers have been published on Fourier split-step parabolic equation modelling, it is difficult to find complete guidance on the practical criteria to be met for a successful implementation, in order to avoid spurious effects, so this will be a particular focus of this chapter.

In addition, we describe a new method using convolution, derived from the Fourier split-step algorithm, which provides greater flexibility in the treatment of the lower boundary. We describe how these methods relate to finite element methods, and show how they may be applied to three dimensional terrain.

We conclude the chapter with a description of the general terrain diffraction model adopted in 2011 by the International Telecommunication Union. Although the model is completely defined (*Rec. ITU-R P526-15,* 2019), the theoretical and empirical background leading to this model is not available in the literature, so we provide it here, as development of our fading model depends in part on it.

The following paper cited in this chapter was produced as part of the work for this thesis: (Salamon *et al.* 2013).

2.2 Maxwell's equations and the 2D problem

If the medium between transmitter and receiver is known, including relevant boundary conditions, then the radio propagation may be determined by solving Maxwell's equations for the current scenario. As we are investigating clear-air fading of terrestrial fixed radio links, the medium consists of air with refractive index n, and a lower boundary provided by the surface of the ground or water. There is no upper boundary, so a suitable way must be found to address this in the analysis.

We consider the electromagnetic fields in Cartesian coordinates (x, y, z), where the x direction is horizontal in the direction of propagation, the y direction is also horizontal, transverse to the direction of propagation, and the z direction is directed vertically upwards, as is the usual convention for this type of analysis. This is depicted in Figure 2.1.

Initially we assume invariance in the y direction, so we have a two dimensional problem in the $x - z$ plane. Due to the y independence, there is no depolarisation, so we may independently consider horizontally polarised fields in terms of the y component of

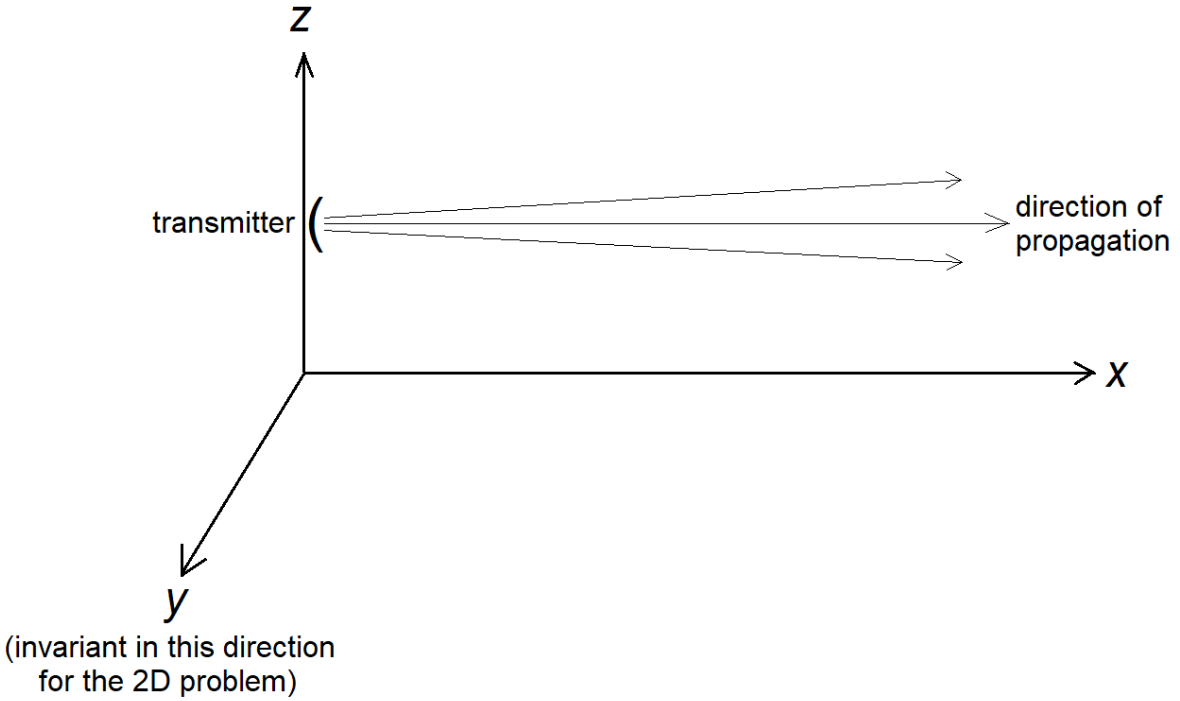

Figure 2.1. Orientation of the coordinate system. We follow the ususal convention for parabolic equation analysis of terrestrial propagation at angles close to the direction of the horizontal x axis, with the z axis being the vertical direction, and the y axis being horizontal but perpendicular to the direction of propagation. The problem may be simplified to two dimensions by assuming invariance in the y direction.

electric field E_y as

$$\psi(x,z) = E_y(x,z)\ , \tag{2.1}$$

or horizontally polarised fields in terms of the y component of magnetic field H_y as

$$\psi(x,z) = H_y(x,z)\ . \tag{2.2}$$

The field $\psi(x,y)$ is then a solution to the two-dimensional scalar wave equation

$$\frac{\partial^2\psi}{\partial x^2} + \frac{\partial^2\psi}{\partial z^2} + k^2n^2\psi = 0 \tag{2.3}$$

where k is the wave number in vacuum (radians per metre), and n is the refractive index of the atmosphere.

As we are dealing with paraxial radiation, propagating close to the x direction, we may replace ψ by $u(x,z)$, which is slowly varying in the x direction:

$$u(x,z) = \mathrm{e}^{-ikx}\psi(x,z)\ . \tag{2.4}$$

In terms of u the scalar wave equation is

$$\frac{\partial^2 u}{\partial x^2} + 2ik\frac{\partial u}{\partial x} + \frac{\partial^2 u}{\partial z^2} + k^2\left(n^2 - 1\right)u = 0\,. \tag{2.5}$$

This may be factorised as

$$\left[\frac{\partial}{\partial x} + ik\left(1 - Q\right)\right]\left[\frac{\partial}{\partial x} + ik\left(1 + Q\right)\right]u = 0 \tag{2.6}$$

where Q is a pseudo-differential operator, such that (Levy 2000)

$$Q\left(Q\left(u\right)\right) = \frac{1}{k^2}\frac{\partial^2 u}{\partial z^2} + n^2 u\,, \quad \text{or} \quad Q = \sqrt{\frac{1}{k^2}\frac{\partial^2}{\partial z^2} + n^2(x,z)}\,. \tag{2.7}$$

From (2.6) we have the forward propagation equation

$$\frac{\partial u}{\partial x} = -ik\left(1 - Q\right)u \tag{2.8}$$

and the backward propagation equation

$$\frac{\partial u}{\partial x} = -ik\left(1 + Q\right)u\,. \tag{2.9}$$

However, the factorisation of (2.6) is only correct if n is invariant with range x, so care is required ensure error is small when this is not the case (Levy 2000).

The forward parabolic wave equation (2.8) has the solution in terms of a marching algorithm, where the field $u(x + \Delta x, .)$ is found from the field $u(x, \cdot)$ as

$$u(x + \Delta x, \cdot) = \mathrm{e}^{ik\Delta x(-1+Q)}u(x, \cdot)\,. \tag{2.10}$$

2.2.1 Standard or narrow angle parabolic equations

Practical implementation of (2.8) requires approximation of the square-root operator Q, and the simplest approximation results from first-order Taylor series expansions of the square-root and exponential functions. This results in the approximation (Thomson and Chapman 1983)

$$Q = \sqrt{\frac{1}{k^2}\frac{\partial^2}{\partial z^2} + n^2} \;\approx\; 1 + \frac{n^2 - 1}{2} + \frac{1}{2k^2}\frac{\partial^2}{\partial z^2} \tag{2.11}$$

and standard parabolic equation (Levy 2000):

$$\left[\frac{\partial^2}{\partial z^2} + 2ik\frac{\partial}{\partial x} + k^2\left(n^2 - 1\right)\right]u(x,z) = 0\,. \tag{2.12}$$

This approximation is accurate for propagation angles within a few degrees of the paraxial direction, so accuracy is good for our terrestrial fixed link application, on long-range paths (Levy 2000). It is often referred to as the Narrow Angle Parabolic Equation (NAPE).

2.2.2 Wide angle parabolic equations

The accuracy of NAPE schemes may not be adequate for short-range paths or strong multipath effects (Ozgun *et al.* 2011), so a Wide Angle Parabolic Equation (WAPE) scheme may be preferred.

We describe here a WAPE scheme having the advantage of efficient numerical evaluation by Fourier split-step techniques. It approximates Q as (Feit and Fleck 1978, Thomson and Chapman 1983, Donohue and Kuttler 2000, Ozgun *et al.* 2011),

$$Q = \sqrt{\frac{1}{k^2}\frac{\partial^2}{\partial z^2} + n^2(x,z)} \quad \approx \quad n(x,z) - 1 + \sqrt{\frac{1}{k^2}\frac{\partial^2}{\partial z^2} + 1}\,. \tag{2.13}$$

In the uniform medium case (constant n), this approximation is an exact representation of the scalar wave equation (2.3) (Thomson and Chapman 1983).

The practical implementation of this WAPE scheme is described in the following section.

2.3 Parabolic equation methods

The parabolic equation solution is efficiently implemented as a marching algorithm by transforming the field $u(x,z)$ in vertical z-space at range x, into far-field vertical angle p-space, where $p = k\sin\theta$, by means of the Fourier transform $F\{\cdot\}$. A phase shift, as a function of p and step spacing Δx, is applied. This shifts the far-field p-space field to that corresponding to the next step. An inverse Fourier transform $F^{-1}\{\cdot\}$ then transforms back to the field $u(x+\Delta x, z)$ in vertical z-space at range $x+\Delta x$. During each step the phase of the z-space field u is corrected to account for refractive index of the atmosphere n, and if required, the curvature of the Earth, and ground elevation in the case of terrain flattening implementations.

The narrow angle (NAPE) scheme, neglecting curvature of the Earth and terrain flattening, is implemented as (Levy 2000, Ozgun *et al.* 2011),

$$u(x+\Delta x, z) = \exp\left[ik(n^2-1)\frac{\Delta x}{2}\right] F^{-1}\left\{\exp\left[-ip^2\frac{\Delta x}{2k}\right] F\{u(x,z)\}\right\}, \tag{2.14}$$

where $p = k\sin\theta$ is the transform variable, as a function of propagation angle θ from the horizontal, k is the wavenumber, and $\exp[-ip^2/(2k)]$ accounts for the phase difference between a ray at angle θ and the paraxial ray.

We note that while most of the literature uses $p = k\sin\theta = 2\pi\sin\theta/\lambda$, where λ is the wavelength, as we do, Levy uses $p = \sin\theta/\lambda$, resulting in a difference by a factor of 2π.

The wide angle (WAPE) scheme (2.13) may be implemented as (Ozgun *et al.* 2011)

$$u(x+\Delta x, z) = \exp\left[ik(n-1)\Delta x\right] \times F^{-1}\left\{\exp\left[\frac{-ip^2\Delta x}{k}\left(\sqrt{1-\frac{p^2}{k^2}}+1\right)^{-1}\right]F\{u(x,z)\}\right\}. \quad (2.15)$$

As $\sin\theta = p/k$, (2.15) is identical to Barrios (1994, eq(8) neglecting terrain term):

$$u(x+\Delta x, z) = \exp\left[ik(n-1)\Delta x\right]F^{-1}\left\{\exp\left[i\Delta x\left(\sqrt{k^2-p^2}-k\right)\right]F\{u(x,z)\}\right\}, \quad (2.16)$$

so our Fourier split-step algorithms in this research are all based on this expression.

The one-way marching algorithm of (2.16) is not a complete solution for the field on a terrestrial path, as it ignores back-scattered field. Including this requires a solution simultaneously solving the coupled system of forward field u_+ satisfying (2.8), backward field u_- satisfying (2.9), and overall $u = u_+ + u_-$ (Levy 2000). This is possible by an iterative process (Ozgun *et al.* 2011), but for our problem of terrestrial fixed radio links, is unlikely to significantly affect the end to end transmitter to receiver propagation path, and would be a potentially significant computational overhead.

2.3.1 The lower boundary

The terrestrial path through the atmosphere is bounded below, either by land or water. The lower boundary condition for the Fourier split-step solution must be set up in a way that represents this. It may be modelled as an interface with an effective complex reflection coefficient R_e. For plane waves reflected by a smooth flat surface, we have $R_e = R_0$, the Fresnel refection coefficient, a function of elevation angle θ, effective relative permittivity ϵ_r, and effective conductivity σ (S/m) (Levy 2000, equ.(10.15)):

$$R_0 = \frac{\sin\theta - \delta}{\sin\theta + \delta} \quad (2.17)$$

where surface impedance δ is (Levy 2000, subst.equ.(9.17) into (9.14),(9.15))

$$\delta = \sqrt{\eta - \cos^2\theta} \quad \text{for horizontal polarisation} \quad (2.18)$$

or

$$\delta = \frac{1}{\eta}\sqrt{\eta - \cos^2\theta} \quad \text{for vertical polarisation,} \quad (2.19)$$

and relative complex permittivity η is (Levy 2000, equ.(9.6))

$$\eta = \epsilon_r + i\frac{\sigma}{kc\epsilon_0} = \epsilon_r + i\ 59.9585\ \lambda\sigma\ , \tag{2.20}$$

where ϵ_0, λ and k are respectively the absolute permittivity, wavelength and wavenumber, in a vacuum. Unity atmospheric refractive index is assumed.

Dirichlet boundary condition

At the grazing angles involved in terrestrial radio links, θ is small, so for horizontal polarisation, $R_e = -1$ is generally a good approximation to (2.17) for smooth surfaces, and may be reasonable for vertical polarisation if θ is small enough. This $R_e = -1$ case is known as the Dirichlet boundary condition (Ozgun *et al.* 2011), which may be stated as

$$u(x, z = 0) = 0\ . \tag{2.21}$$

Due to the odd symmetry of the discrete sine transform (DST), a convenient way to implement the Dirichlet boundary condition is to use the DST as the Fourier transform $F\{\}$ in (2.16), the field elements representing field samples above the surface.

Alternatively a fast Fourier transform (FFT) of double size may be used, with the lower half of the elements representing image samples below the surface. They are then reflected up to super-impose on the above surface samples. Both these methods provide identical results.

The Dirichlet boundary condition is unsuitable if R_0 from (2.17) differs significantly from -1, or if the surface is sufficiently rough.

Neumann boundary condition

It can be seen from (2.17) that if surface impedance δ is very small compared to $\sin\theta$, the reflection coefficient may approach $R_0 \approx +1$. This case is known as the Neumann boundary condition (Ozgun *et al.* 2011), which may be stated as

$$\frac{\partial u(x, z)}{\partial z} = 0 \quad \text{at } z = 0\ . \tag{2.22}$$

Due to the even symmetry of the discrete cosine transform (DCT), a convenient way to implement the Neumann boundary condition is to use the DCT as the Fourier transform $F\{\}$ in (2.16). Alternatively a fast Fourier transform (FFT) of double size may be used, together with reflection of the below-surface field, as for the Dirichlet boundary condition.

Over a horizontal surface, the Neumann boundary condition is only relevant to vertically polarised waves at high enough angles for $\sin\theta$ to be much greater than δ, so this boundary condition has little practical relevance to our problem of terrestrial point-to-point radio propagation.

Leontovich boundary condition

In the case of a finite conductivity surface, the boundary condition of zero field at the surface in (2.21) no longer applies. Instead, the approximation of the Leontovich boundary condition may be used, provided the refractive index of the ground is sufficiently large (Levy 2000). This boundary condition may be stated as

$$\frac{\partial u(x,z)}{\partial z} + \alpha u(x,z) = 0 \quad \text{at } z = 0\,, \tag{2.23}$$

where, for a smooth surface (Kuttler and Dockery 1991)

$$\alpha = ik\sin\theta\left(\frac{1-R_0}{1+R_0}\right)\,. \tag{2.24}$$

Substituting for R_0 from (2.17) gives

$$\alpha = ik\delta\,, \tag{2.25}$$

with δ given by (2.18) or (2.19), for horizontal or vertical polarisation respectively. Hence α is essentially independent of θ for smooth surfaces at grazing angles.

This may be implemented in Fourier split-step parabolic equation modelling by use of the mixed Fourier transform (MFT) (Kuttler and Dockery 1991), or the discrete mixed Fourier transform (DMFT) (Dockery and Kuttler 1996). Step by step descriptions of the implementation of DMFT are provided in Dockery and Kuttler (1996) and Levy (2000). A forward and inverse DST may be used, as for the Dirichlet boundary condition, but instead of transforming the field $u(x,z)$, a matched function $v(x,z)$, which is zero at the boundary, is transformed. The matched function is

$$v(x,z) = \frac{\partial u(x,z)}{\partial z} + \alpha u(x,z)\,. \tag{2.26}$$

The computational burden in addition to that for the Dirichlet case, involves calculating the matched function from the field, and then retrieving the field from the propagated matched function, at each step (Levy 2000).

Although the Leontovich boundary condition is approximately independent of grazing angle θ for a smooth surface, this is not the case for a rough surface, such as a rough

sea surface. For such a surface it is important to obtain a good estimate of local grazing angle at each step (Dockery and Kuttler 1996, Levy 2000). A technique such as geometric optics or spectral estimation needs to be employed to estimate the dominant grazing angle at each step (Dockery and Kuttler 1996); problematic at locations with multiple rays incident on the surface, or locations where no traced rays are incident on the surface (Levy 2000).

2.3.2 A new convolutional marching solution, and the lower boundary

The DMFT standard technique for implementing the Leontovich boundary condition in Fourier split-step parabolic equation modelling largely overcame the numerical problems encountered with the inverse transform of the original mixed Fourier transform (MFT) implementation (Kuttler and Dockery 1991) of the Leontovich boundary condition, but still in some cases stability problems may occur (Kuttler and Janaswamy 2002).

We propose an alternate approach to implementation of the Leontovich boundary condition in parabolic equation modelling, that avoids MFT or DMFT numerical stability problems, and provides a marching solution to the problem that does not require an estimate the dominant grazing angle at each step for rough surfaces, as the solution accepts multiple rays incident on the same part of the surface at different angles.

This new approach bears some similarity to the Kirchhoff integral (KI) technique (Coleman 2005), although that original form of KI is not necessarily restricted to paraxial scenarios. The Leontovich boundary condition has not been implemented in that form of KI, but it could be, in the same way that we describe here for our new approach. The later form of KI, implemented with fast Fourier transforms (Coleman 2010), has an execution speed advantage over the earlier form, but is not suitable for implementing a Leontovich boundary condition, except by approximating it by a fixed reflection coefficient for all angles of incidence.

Instead of integrating Kirchhoff relations, we derive our new method directly from the Fourier split step wide angle parabolic equation scheme described above.

Excluding the atmospheric refractive index component of (2.16), we have

$$u(x+\Delta x,z)=F^{-1}\left\{\exp\left[i\Delta x\left(\sqrt{k^2-p^2}-k\right)\right]F\{u(x,z)\}\right\}. \qquad (2.27)$$

In the discrete implementation, the field $u(x,z)$ is a vector of field samples, vertically spaced Δz apart, as $u(x, z = ..., -2\Delta z, -\Delta z, 0, \Delta z, 2\Delta z, ...)$, and (2.27) may be represented by first transforming spatial field vector $u(x,z)$ to angular field vector $v(x,m)$

with the fast Fourier transform FFT$(\cdot)$:

$$v(x,m) = \text{FFT}(u(x,z)), \tag{2.28}$$

then propagate to the angular field vector to $v(x+\Delta x, z)$, noting that $p = k\sin\theta$, and θ is the propagation angle relative to the paraxial for each element m of vector v:

$$v(x+\Delta x, m) = v(x,m)\exp(ik\Delta x(\cos\theta - 1)). \tag{2.29}$$

At this point a window function is normally applied to v to attenuate the highest angle components, rolling off to zero amplitude at the extreme values of θ, to prevent the generation of spurious aliasing components in the following step. The field at the end of the step, $u(x+\Delta x, z)$, is obtained by the inverse fast Fourier transform IFFT$()$:

$$u(x+\Delta x, z) = \text{IFFT}v(x+\Delta x, m). \tag{2.30}$$

Our new alternative method is to replace the marching propagation step of (2.28), (2.29) and (2.30), with a convolution CONV$(\cdot,\cdot)$, of field vector $u(x,z)$ with vector w:

$$u(x+\Delta x, z) = \text{CONV}(u(x,z), w). \tag{2.31}$$

The convolution vector w may be estimated by applying an input field vector with $u(x, z=0) = 1$ and $u(x, z\neq 0) = 0$, to (2.28), (2.29) and (2.30), and then the convolution vector is $w = u(x+\Delta x, z)$. Taking the usual definition of the FFT-IFFT pair, where this input results in $v(x,m)$ being all ones, this is equivalent to transforming the Fourier split step propagator, $\exp(ik\Delta x(\cos\theta - 1))$, including its anti-aliasing window function, with the inverse fast Fourier transform (IFFT).

The elements of the output of the IFFT are then re-arranged into a symmetrical convolution vector w with an odd number of elements, the bottom element of the IFFT output becoming the central element of w. If the IFFT has an even number of elements n, then the $(n/2+1)$-th element is omitted in forming w, as it would be zero due to the anti-aliasiing window function anyway.

We have described above, the version of Fourier split-step parabolic equation modelling that uses a double-height field vector, and FFT Fourier transforms, which may implement the Dirichlet boundary condition by reflecting the below-surface field. The same may be done with this new convolutional approach of (2.31), but there is an important difference. This new approach can model boundary conditions that have angle dependent reflection coefficients.

For boundary conditions other than Dirichlet, there may be non-zero field at the surface. If there is a field sample at the surface, it represents field over the z interval $-\Delta z/2$ to $+\Delta z/2$, but only the upper half, $z \geq 0$, actually propagates. This must be corrected by halving the amplitude of this surface sample. Another solution is to offset the field samples by $\Delta z/2$ relative to the surface. Samples for $z > 0$ then fully propagate, and those for $z < 0$ do not propagate, and are set to zero before starting the next step of the marching solution.

The new convolution method provides no benefit over Fourier split step in modelling an infinitely conducting boundary, but it may be able to model non-Leontovich boundaries such as rough sea, and it avoids numerical instability that may occur with DMFT (Kuttler and Janaswamy 2002).

The disadvantage of this convolution method is that its execution speed is generally slower than the equivalent Fourier split step analysis. Execution speed may be optimised by analysing the direct field for each step with Fourier split-step, as in (2.28), (2.29) and (2.30), and the reflected field with the convolutional technique, in order to satisfy the boundary condition.

2.3.3 The Lentovich boundary condition in the convolution method

The Dirichlet boundary condition in 2.3.1 is readily implemented in the convolution method by reflecting the image field with an effective reflection coefficient $R_e = -1$, so it might be expected that the Leontovich boundary condition in 2.3.1 would be implemented by using an effective reflection coefficient given by (2.17), but this reflection coefficient only satisfies the Leontovich boundary condition for plane waves.

If the direct and reflected fields are plane waves, incident on a plane surface at grazing angle θ, then the variation in resultant field $u(x, z)$ with z, will be purely due to variation in the phases of the direct and reflected fields, giving the partial derivative

$$\frac{\partial u}{\partial z} = ik \sin\theta \left(\frac{R_0 - 1}{R_0 + 1} \right) u(x, 0) \; . \tag{2.32}$$

Substituting R_0 from (2.17), we have

$$\frac{\partial u}{\partial z} = -ik\delta \sin\theta \; u(x, 0) = -\alpha u(x, 0) \; , \tag{2.33}$$

which is the Leontovich boundary condition of (2.23). However, if we have an incident wave from a source above the surface and at finite distance, then there will be slight

amplitude variations, in addition to the phase variations with height z above the surface at distance x. Especially with vertically polarised waves, there may be significant variation in reflection coefficient with height, due to the change in incidence angle with height. In this case, the derivation of (2.32) and (2.33) above will not be valid.

It is therefore not surprising that we find in testing our marching convolutional algorithm, that the Leontovich boundary condition is generally not satisfied by using the reflection coefficient of (2.17), with vertically polarised propagation.

Sommerfeld-Norton flat-Earth theory (Milsom 2003) includes both the space wave (consisting of the direct wave and the (2.17) reflected wave), and the surface wave (Norton 1937), which may be considered as a reflected wave, with reflection coefficient R_s, in addition to the Fresnel plane-wave reflected wave with coefficient R_0 given by (2.17).

Although there is general agreement in the literature on this broad concept of a surface wave in addition to the space wave, there has been controversy over some of the finer detail for many years (Wait 1998, Collin 2004). One of the issues has been whether Sommerfeld did (Barclay 2008), or did not (Collin 2004), make a sign error in his original paper on this subject (Sommerfeld 1909). Contemporary solutions to this problem have been published (Collin 2004, Green 2007).

We resolve the uncertainty over different solutions to the surface wave problem, by choosing a published surface wave model for our convolutional technique that empirically satisfies two simple criteria:

1. When a component of reflection coefficient from the surface wave model, R_s, is included in the convolutional marching analysis, the Leontovich boundary condition (2.23) must be accurately satisfied at the surface at each step of the analysis. This may be checked using $e_{\text{BC}} = 1 + \alpha u(z = 0)/(\partial u/\partial z)$, an estimate of boundary condition error, aiming for $e_{\text{BC}} \approx 0$. The partial derivative may be estimated from $u(z = 0)$, $u(z = \Delta z)$, and $u(z = 2\Delta z)$. The first two provide an estimate of the derivative at $z = \Delta z/2$, and the last two give an estimate at $z = 3\Delta z/2$, and an estimate of the partial derivative at $z = 0$ is obtained by linear extrapolation of these two estimates. For a smooth surface, α is essentially constant for angles close to grazing, so we may readily check for $e_{\text{BC}} \approx 0$ at each step.

2. The results of the analysis must satisfy the parabolic wave equation. This is more difficult to check, but we compare our results with those from Fourier split-step

parabolic equation modelling with DMFT (Dockery and Kuttler 1996). This paper reproduced surface wave effects, by applying the mixed Fourier transform and its inverse, without invoking any specific surface wave model. The results were in accurate agreement with existing models at both 10 MHz and 10 GHz.

By applying these two criteria in selecting a surface wave model for our marching algorithm, we avoid the controversies over different surface-wave models, and instead rely on the track-record of DMFT in modelling surface wave effects, using these two criteria.

We take our expressions for surface wave reflection coefficient R_s directly from a flat-Earth formulation (Norton 1941), which caters for transmitter and receiver both elevated above the surface, and either vertical or horizontal polarisation. The horizontally polarised surface wave case is usually ignored, as it is generally quite insignificant, but has been included in this method.

Although this implementation (Norton 1941), is an early one, we have found it accurately satisfies the Leontovich boundary condition for all the examples we have tested, over a wide range of frequencies.

Like most surface wave methods, this uses the concept of "numerical distance" p, as

$$p = \pi \frac{r_2}{\lambda} \frac{\cos^2 b_2}{x \cos b_1} \qquad \text{(for vertical polarisation)} \tag{2.34}$$

with phase

$$b = 2b_2 - b_1 \ , \tag{2.35}$$

or

$$p = \pi \frac{r_2}{\lambda} \frac{x}{\cos b_1} \qquad \text{(for horizontal polarisation)} \tag{2.36}$$

with phase

$$b = \pi - b_1 \ , \tag{2.37}$$

where r_2 is the total reflected path length, λ the wavelength,

$$b_1 = \arctan((\epsilon_r - \cos^2(\theta))/x) \ , \tag{2.38}$$

$$b_2 = \arctan(\epsilon_r/x) \ , \text{ and} \tag{2.39}$$

$$x = 59.9585\lambda\sigma \ . \tag{2.40}$$

Then p and b are combined, including correction for heights of transmitter and receiver above the surface, in terms of R_0 from (2.17), to give p_1

$$p_1 = \frac{4p \exp(ib)}{(1 - R_0)^2} \ , \tag{2.41}$$

and the surface wave attenuation function $f_s(p_1)$ is (Norton 1941, Appendix II (44)):

$$f_s(p_1) = 1 + i\sqrt{\pi p_1}\,\exp(-p_1)\mathrm{erfc}(-i\sqrt{p_1})\ . \tag{2.42}$$

There is a potential computational problem in (2.42), as the complimentary error function $\mathrm{erfc}(\cdot)$ has to be evaluated for a complex argument. This is not available in some computer languages. Where it is available, there may be an upper limit on $|p_1|$ in (2.42). We have addressed this limit by developing the following approximation, using $p_2 = p_1\exp(-ib)$, which may be used when $\mathrm{erfc}(\cdot)$ fails, detected by (2.42) evaluating as either infinite, or undefined (Not a Number):

$$f_s(p_2, b) \approx \exp[i(\pi - b)]\left(\frac{1}{p_2}\right)\left(0.5 + \frac{0.75\sin(b + \pi/2)}{p_2}\right)\ . \tag{2.43}$$

The surface wave contribution R_s to the reflection coefficient is then simply

$$R_s = f_s(p_1)(1 - R_0)\ , \tag{2.44}$$

and the overall reflection coefficient is

$$R_t = R_0 + R_s\ . \tag{2.45}$$

2.3.4 Validity limits and sources of error

Sample spacing Δz

The upper limit for vertical field sample spacing is that the phase difference between adjacent field samples, Δz apart, must be less than $\pi/2$ radians, in order to meet the Nyquist criterion. In checking this, all factors leading to this phase difference must be considered: the angle to the horizontal of rays that are required to be accurately represented, the phase difference between adjacent samples due to strong refractivity gradients, and phase difference introduced for beam steering in order to analyse varying terrain elevation, which we discuss later in this chapter.

Of those factors, ray angle is the one most commonly considered in determining Δz, and if a problem, may only be addressed by reducing Δz accordingly. The other factors are generally only significant only in the cases of extreme refractivity gradients, or very rough terrain in the case of terrain flattening.

If strong refractivity gradients are the cause of adjacent field samples having phase difference exceeding π radians, a better alternative to reducing Δz, may be to reduce step

length Δx, which we consider next. This is especially the case in analysing evaporation ducts, discussed in the next chapter, which have very strong refractivity gradients near the surface.

Step length Δx

In an environment of uniform refractive index and uniform flat lower boundary, there is no particular requirement for step length Δx for a Dirichlet or Neumann lower boundaries implemented as a Fourier split step solution, or our new convolutional method, and the same applies to a Leontovich lower boundary implemented as a DMFT Fourier split step solution. However, all these methods are derived from the factorisation of the scalar wave equation (2.5) into (2.6), which assumes refractive index n is constant over the step length. Accordingly, some error is expected if n varies over the step length, which is expected to increase as step length Δx increases.

The formulation of the split-step solution in (2.16) has the phase correction to account for refractive index at the end of the step, and in terms of partial derivatives of refractive index n with respect to x and z, this can be shown to result in error proportional to Δx squared (Levy 2000). Ideally it is a Δx cubed dependency if half the phase correction is applied at the beginning of the step, and half at the end (Levy 2000), although in practice, if the vertical refractivity profile remains the same from step to step, it makes negligible difference. Either way, when steps are concatenated, the phase correction occurs every Δx. The important point is that reducing Δx significantly reduces error in the Fourier split step analysis due to non-zero partial derivatives of n with respect to both x and z.

As mentioned above, where there are very strong vertical gradients of refractive index n, it is important to check that the phase difference due to n, over the step, of vertically adjacent field samples, is less than π radians. The step length should be reduced if necessary, to meet this.

The above considerations on Δx and Δz apply equally to the Fourier split step algorithm, and our new convolutional technique, and to the FFT implementation of the KI approach (Coleman 2010).

Reflection coefficient R

This applies to all marching algorithms where the lower boundary is implemented by reflection or image theory, in cases other than $R = -1$ or $R = +1$, although it does not apply to the DMFT implementation of Leontovich boundaries.

Consider propagation between a transmitter and a receiver, both located above a plane boundary with reflection coefficient R. The field at the receiver may be modelled as a direct field from transmitter to receiver, plus a reflected field, which may be considered as field coming from an image source below the surface, but with its amplitude multiplied by R. This is equivalent to modelling this problem as a single step in any of the marching algorithms we are considering.

Consider now that we model the same problem as two steps of one of these algorithms. The result is equivalent to the sum of four paths, each diffracted by a knife edge with its top at the point where the surface intersects the join between the two steps, due to the below-surface field being deleted after it has been reflected up. These four paths are:

1. direct - diffracted - direct
2. direct - diffracted - reflected
3. reflected - diffracted - direct
4. reflected - diffracted - reflected.

The four paths are depicted in Figure 2.2.

Image theory suggests that reflection coefficient R is applied to the single-reflected paths, and that the double reflected path should have its amplitude multiplied by R^2. However, the correct result is only obtained if the double reflected path is left unchanged, not multiplied by R^2.

This type of error applies to marching algorithms with more that two steps as well, and may be thought of as diffraction from spurious knife edges embedded in the surface, produced by discarding the below-surface field at the end of the step, which are only revealed when the surface has finite conductivity.

An alternative explanation may be that the image theory treatment of finite conductivity problems deals with the partially-reflected image, but ignores the influence on

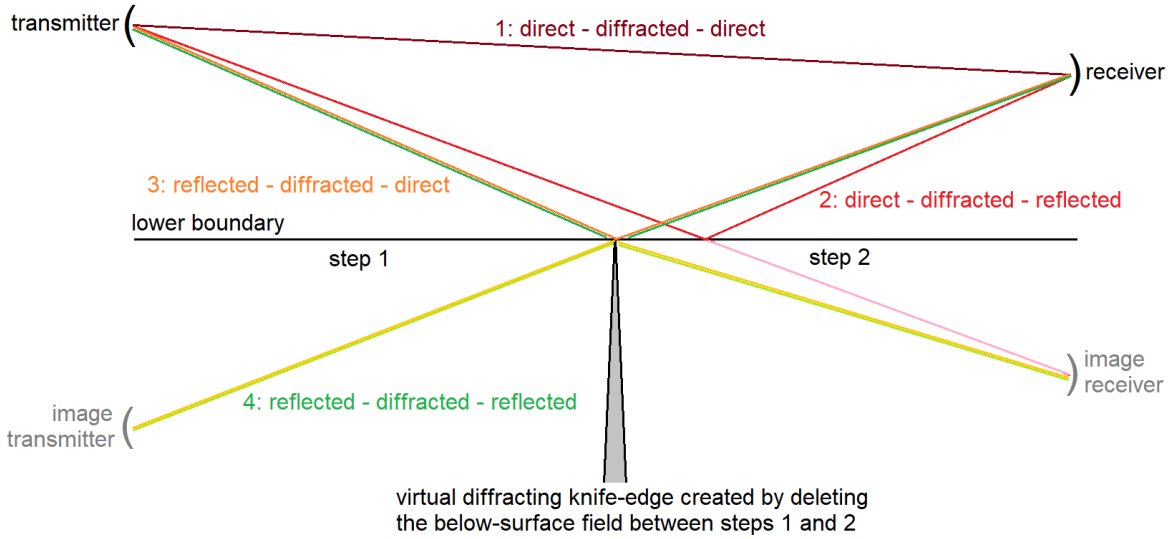

Figure 2.2. A two-step reflecting plane as superposition of 4 paths. Image theory suggests that if a reflecting plane is split into two steps, propagation above the combined plane might be considered as the superposition of four paths. However, this approach is not accurate for a finite conductivity boundary.

the field above the surface, of the refracted field entering the surface. Both of these explanations suggest an error in some sense roughly proportional to the number of steps used to model a particular problem, and that this type of error will not occur in cases of infinite conductivity, where there is no refracted field.

This type of error is not a problem for a Leontovich boundary implemented by the DMFT algorithm, because the original problem is effectively transformed to a Dirichlet boundary problem, which may be validly implemented by the DST.

2.3.5 Propagation testing the convolution method

Testing of the marching convolution method over a range of frequencies, step lengths, and surface electrical characteristics, indicates that including the surface wave component in the reflection coefficient, as described in (2.34) to (2.45), accurately satisfies the Leontovich boundary condition. However, this does not guarantee accurate field strength prediction. We test this by comparing results from our new method with previously published results.

A sensitive test is likely to be vertically polarised propagation over a finite conductivity surface, at a low frequency, where the surface wave is likely to be significant.

Smooth sea, 10 MHz vertical polarisation, linear atmosphere

We take as our example, propagation over a smooth sea, $\epsilon_r = 80$ and $\sigma = 4$, at 10 MHz, with linear refractivity gradient of +118 M-units/km. This was modelled (Dockery and Kuttler 1996, Figure 5) using the Fourier split-step parabolic equation method with DMFT, which was found to agree within 0.1 dB with their reference method.

Figure 2.3 demonstrates, with a step length $\Delta x = 500$ m, and sample spacing $\Delta z = 4$ m, that the convolutional method, with only plane-wave reflection coefficient R_0, severely under-estimates field strength (dashed magenta curve), and in this case the Leontovich boundary condition is not satisfied.

Adding the surface wave component of the reflection coefficient, (2.44) to (2.45), satisfies the boundary condition, and field-strength estimation is in good agreement with the DMFT result; this supports the noted similarity between the $K(x)$ term in the MFT inverse transform, and surface wave propagation (Kuttler and Dockery 1991, Dockery and Kuttler 1996). Repeating our analysis, but with Δx reduced to 250 m, yields a similar result, the greatest difference being 0.15 dB less field strength at 493 km.

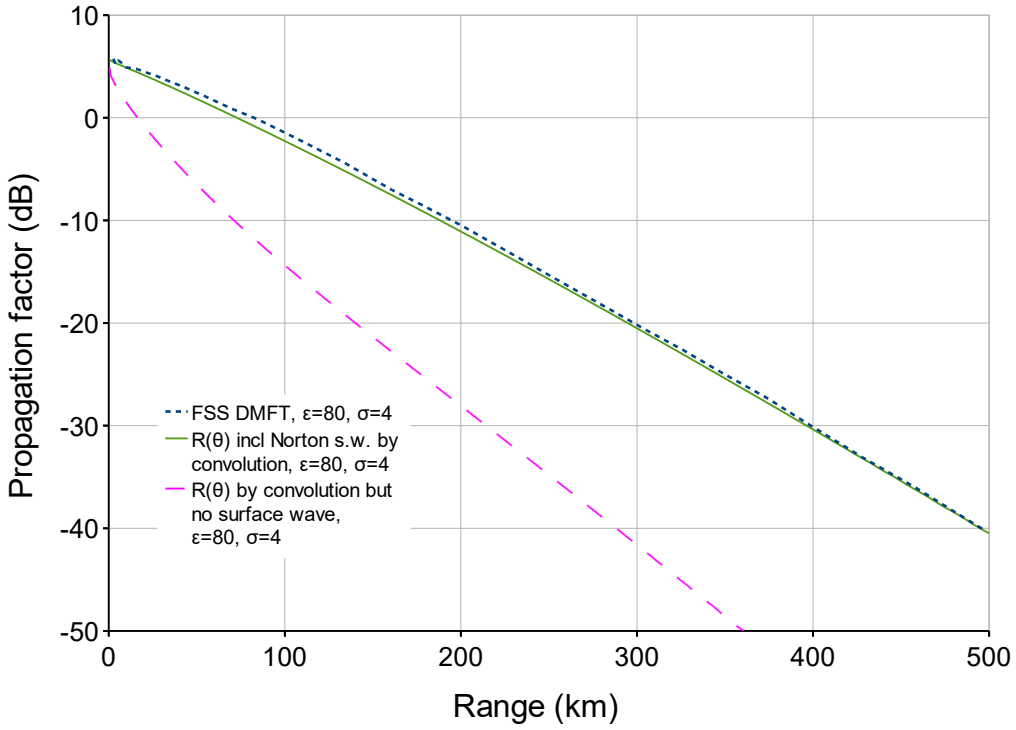

Figure 2.3. Convolutional modelling, 10 MHz over sea. The surface wave is important in low frequency vertically polarised propagation. The fine dashed blue curve is the reference method: Fourier split-step parabolic equation modelling with DMFT (Dockery and Kuttler 1996), at 10 MHz with transmitter 30 m above the surface, and receiver at 4 m. In the convolutional method, the surface wave component of the reflection coefficient, (2.44), must be included to satisfy the boundary condition, providing estimated field-strength in close agreement with the DMFT result (green curve). The dashed magenta curve demonstrates field under-prediction with only plane-wave reflection coefficient. The green and magenta curves use step length $\Delta x = 500$ m, and sample spacing $\Delta z = 4$ m.

Smooth sea, 10 GHz vertical polarisation, with linear surface duct

Our microwave test-case (Dockery and Kuttler 1996, Figure 3) is 10 GHz vertically polarised propagation over sea, again with $\epsilon_r = 80$ and $\sigma = 4$, both for smooth sea, and with 1 m rms wave height. The implementation of the convolutional technique, is as before, including the surface wave, although at 10 GHz its contribution is negligible. The reference method, Fourier split-step parabolic equation method with DMFT (Dockery and Kuttler 1996), used $\Delta z = 0.2$ m, or 6.67 wavelengths, so we use the same Δz for our convolutional method. A step length $\Delta x = 100$ m is used in the reference method, and we use it here in our test for the smooth sea case ($h = 0$ m). Different values of

Δx are found to make negligible difference in the smooth sea case, and in Figure 2.4 we see from the dark blue curve, very close agreement with the reference method for this case.

It is worth noting that the smooth sea predicted vertically polarised field is slightly less than the prediction for a reflection coefficient $R = -1$, the Dirichlet boundary condition, which may often be assumed for grazing angles at 10 GHz.

Rough sea, 10 GHz vertical polarisation, with linear surface duct

In the reference method (Dockery and Kuttler 1996) and in our method, the effect of waves is implemented by the Miller model (Levy 2000), where the smooth surface reflection coefficient R_0 is multiplied by a reduction factor ρ to give an effective reflection coefficient R as

$$R = \rho R_0 \, . \tag{2.46}$$

The reduction factor in the Miller model is

$$\rho = \exp\left(-\frac{1}{2}\gamma^2\right) I_0\left(\frac{1}{2}\gamma^2\right) \, , \tag{2.47}$$

where I_0 is the modified Bessel function of order 0, and γ is Rayleigh roughness parameter for rms wave height h, given by

$$\gamma = 2kh \sin\theta \, . \tag{2.48}$$

The Fourier split-step method with DMFT assumes the same α for all incident rays in any particular step, and so in the rough sea case, requires the dominant angle of incidence to be estimated at each step of the analysis (Dockery and Kuttler 1996, Levy 2000).

Our convolutional method allows Leontovich α to be a function of incidence angle, as is required for the rough sea case if the step of estimating the dominant grazing angle is to be avoided. The disadvantage of our method is that image theory is only strictly valid in a marching analysis method for Dirichlet or Neumann boundaries, and is only a good approximation for reflection coefficients close to $R = -1$ or $R = +1$. In Figure 2.4 it may be seen to be a poor approximation for the rough sea case, referring to the dotted and dashed orange trace ($\Delta x = 100$ m), or the dotted and dashed magenta trace ($\Delta x = 200$ m).

However, extrapolation of the complex field, taking twice the prediction for $\Delta x = 200$ m, minus the prediction for $\Delta x = 100$ m, yields a moderately accurate result. In

some cases, extrapolation of the field strengths in dB, rather than the complex amplitude, may be more effective.

2.3.6 Future work on the convolution method

Shortly before a rigorous implementation of the finite conductivity Leontovich boundary in the Fourier split-step method was first published (Kuttler and Dockery 1991), it was suggested that image theory with plane-wave reflection coefficients might be used as an approximation (Craig and Levy 1991), and this idea was also incorporated in the Kirchhoff integral technique (Coleman 2005).

In this thesis we identify two additional considerations, not identified in this earlier work. Firstly we find that for vertical polarisation above a finite conductivity boundary, in addition to the Fresnel plane-wave reflection coefficient, an additional component derived from the Norton surface wave is required, to correctly analyse problems where the surface wave is significant.

Secondly, we identify that implementing the lower boundary by image theory is not strictly valid for cases where $|1 - R^2| > 0$, even if the surface is smooth, and that it may be a poor approximation for rough surfaces. So far we have only identified an approximate solution to this problem, by extrapolation from different step lengths.

Clearly there is scope for more work to be done on this problem. As this is not essential to the development of our new fixed link fading model, we do not pursue it further in this thesis.

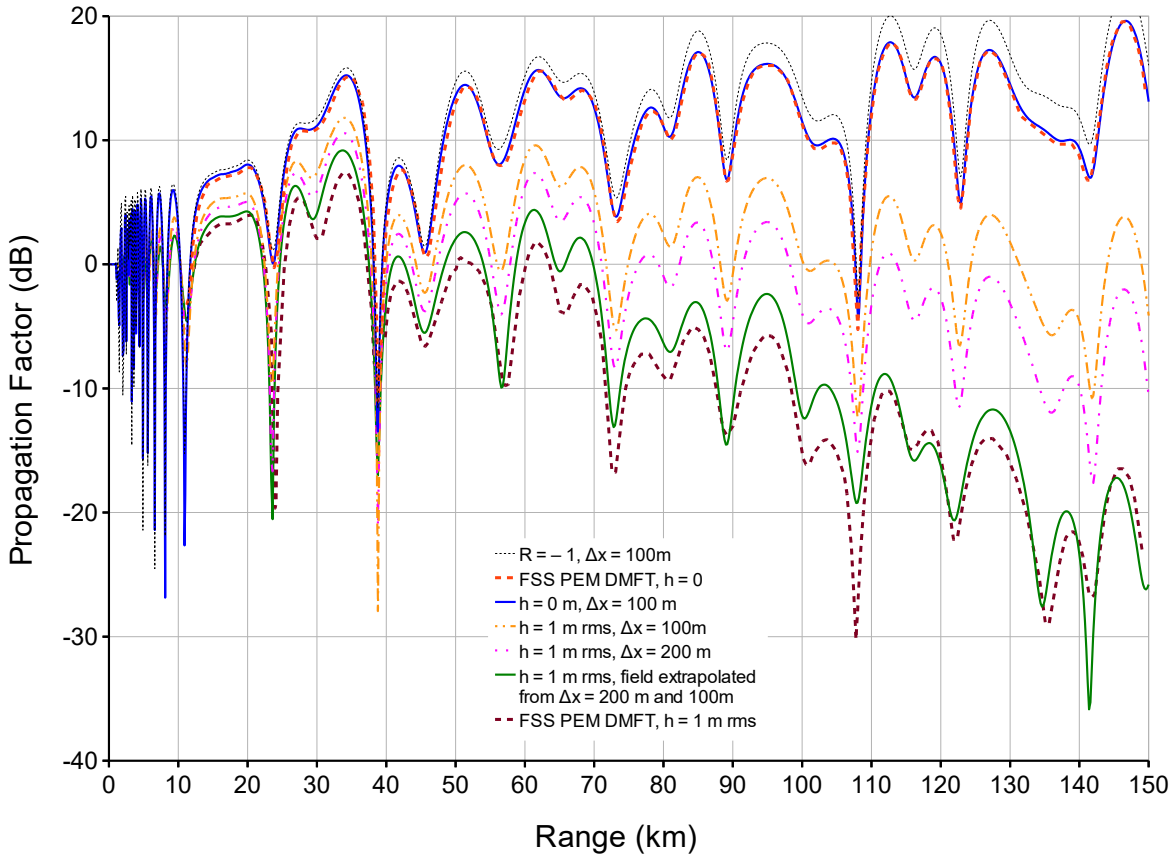

Figure 2.4. Convolutional modelling, 10 GHz over sea. The surface wave is of negligible importance at higher microwave frequencies, although it is included in the convolutional modelling here. The dashed curves are from the reference method: Fourier split-step parabolic equation modelling with DMFT (Dockery and Kuttler 1996), at 10 GHz with transmitter and receiver both 25 m above the surface, with a 50 m surface duct. The refractivity gradient is -243 M-units/km (-400 N-units/km) below 50 m, and +118 M-units/km (-39 N-units/km) above that. Two dashed reference curves are shown, for smooth sea (red dashed), and sea with 1 m rms wave height (brown dashed). At grazing angles and microwave frequencies, a reflection coefficient $R = -1$ is often assumed, shown here as a fine black dotted line, but this appears to over-estimate field, slightly for smooth sea, and significantly with 1 m waves. The convolutional method shows excellent agreement with the reference for smooth sea (blue line), but predicts greater field strength (orange and magenta dashed and dotted lines) than the reference for sea with 1 m rms wave height. These curves have been generated with a 100 m and 200 m step lengths respectively, but much better accuracy for the 1 m wave height is achieved by extrapolating from these step length predictions (green curve).

2.3.7 The upper boundary

The real physical problem has no upper boundary, but the computer model must have an upper boundary, to limit the size of the vector of field values. Truncating the field at a certain height would act as a reflector, reflecting a spurious field back down into the region of interest. This reflection may be prevented by implementing a perfectly matched layer (PML) (Bérenger 1994), or by introducing an artificial absorbing layer above the height of interest; this can be done by adding an imaginary component to the refractive index, to make it lossy (Ryan 1991).

However, for simplicity and practicality for long grazing angle paths (Levy 2000), we apply a window function to the field, to introduce gradually increasing loss above the height of interest. A convenient form of window function is the Tukey window. We define the window function amplitude A as a function of height z, as

$$A(z) = \begin{cases} 1 & \text{if } z \leq h, \\ 0.5 + 0.5\cos\left(\pi \frac{z-h}{h}\right) & \text{if } h < z < 2h, \\ 0 & \text{if } z \geq 2h. \end{cases} \tag{2.49}$$

We choose the vector of field elements to represent the height range $0 \leq z \leq 2h$, so the field is un-attenuated for heights below h.

In the Fourier split-step PEM algorithm (2.16), we apply a similar window function to the p-space field $F\{u(x,z)\}$, to prevent aliasing. This has the effect of attenuating higher angle rays, so this must be taken into account in the choice of vertical field sample spacing, Δz.

The choice of the height h of the start of the upper absorber in (2.49) is not as simple as it might seem. Obviously h must be above the greatest height of interest, but we find that particularly at lower frequencies and grazing angles, substantial spurious reflection may still occur, due to the rate of onset of attenuation with height, relative to Fresnel zone spacing, although we have not seen this effect mentioned in the existing literature.

Our initial solution to this problem (Salamon *et al.* 2013) was to apply filtering to the p-space field to attenuate high angle spurious rays reflected from the upper absorber, but this risks attenuating ground reflected rays that may be significant.

A successful, but somewhat inefficient approach that we have used, is to implement two parallel PEM solutions, each with Tukey window functions (2.49) applied to the field, but with slightly different height h, differing by one Fresnel zone, such that any spurious upper boundary reflection will be anti-phase in the two solutions. The displayed

solution is the mean of the two, but if the difference between the two amplitudes exceeds a threshold, such as 1 dB, the field display is partially greyed to indicate uncertainty. If the areas of uncertainty are excessive, the absorber heights are increased.

2.3.8 Estimation of required absorber height

In much of the published literature, the interest is in propagation at field strengths not far below free-space propagation, or even stronger than free-space field strengths with ducting propagation, so choosing the characteristics of the upper absorber is of minor importance. In this research we aim to model field strengths 50 dB or more below free-space levels, so it may be vital to suppress spurious reflections from the upper absorber to 70 dB or more below free-space levels.

While the solution of dual analysis with different absorber heights described above has been found to be very effective, a more efficient solution may be to derive an approximate expression for the required height to ensure spurious reflection is insignificant, as follows.

We derive this solution for a Tukey window, but it could be adapted to other window functions, or even to the technique of lossy refractive index, provided the imaginary component of the refractive index is introduced gradually as a parabolic function of height above the base of the absorber. Abrupt introduction of the imaginary component would lead to more severe spurious reflections.

The assumption in this method, is that the absorber height is significantly greater than the transmitters and receivers of interest, and that although anomalous refractivity gradients may exist in the atmosphere, their vertical extent is small compared to the absorber height. Accordingly the incidence angle at the absorber is assumed to be similar to the incidence angle under standard refractivity gradient conditions.

Although the surface of the Earth is curved, for convenience PEM analysis replaces the refractivity profiles, or N-profiles, in terms of N-units (ppm exceeding unity refractive index) as a function of height, with M-profiles, where M-units are modified N-units. The modification is $M = N + 0.157z$ where z is the elevation in metres. This modification provides an equivalent problem, where the Earth is flat, which is very convenient for the analysis.

Under this flat-Earth scheme, ray paths generally curve upwards, unless trapped in a duct, so their incidence angle on the lower edge of the upper absorber will generally

be greater than if the rays travelled in straight lines from the transmitter. The spurious reflection problem will be more severe at lower values of the grazing angle θ, so we assume rays travelling in straight lines in the modified refractivity environment, as a likely worst-case for analysing this problem.

Referring to Figure 2.5, for a path of length d and wavelength λ, the mid-path first Fresnel zone radius is $r_1 = 0.5\sqrt{\lambda d}$, or the N-th zone has a radius of $r_N = 0.5\sqrt{N\lambda d}$.

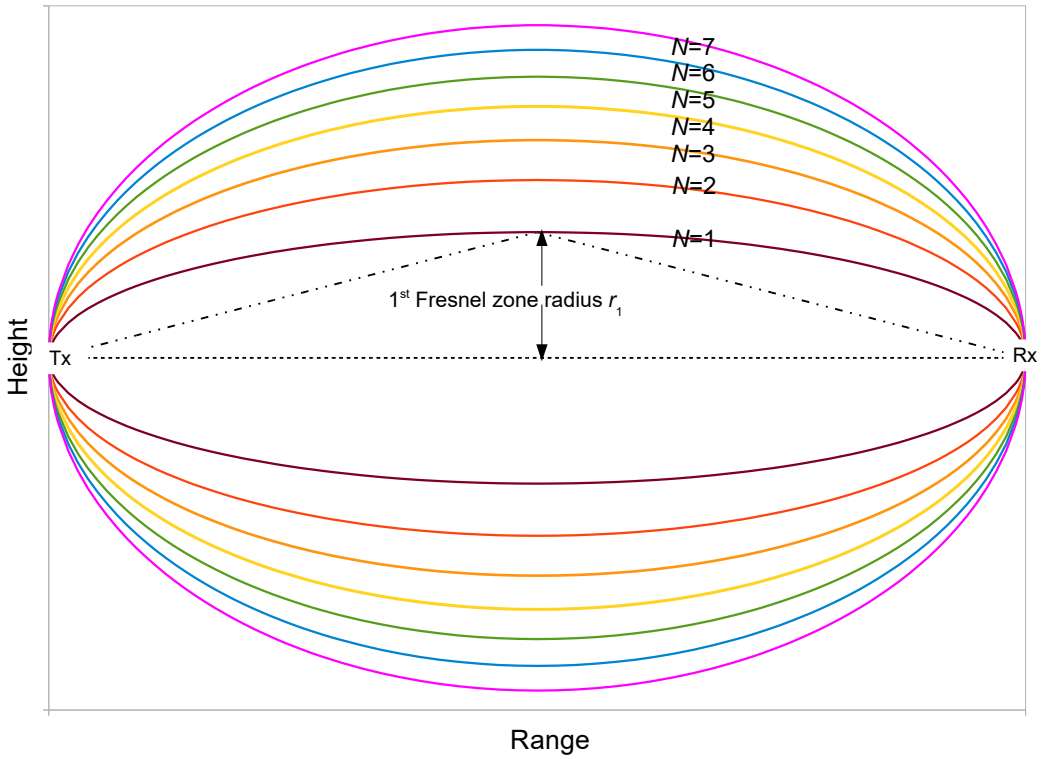

Figure 2.5. Fresnel zones. The N-th Fresnel zone is the locus of points such that the total distance from transmitter (Tx) to that point to receiver (Rx), is N half wavelengths longer than the direct path from Tx to Rx.

If an aperture of height r_1 and infinite width is placed at the mid-path, the field amplitude at the receiver will be approximately the same as free space.

Therefore, for a grazing angle reflection from a flat surface, assumed to be height h above transmitter and receiver, we may consider the effective length of the reflection l, along that surface in the direction of propagation, to be

$$l = \frac{\sqrt{\lambda d}}{2\sin\theta} \approx \frac{\sqrt{\lambda d^3}}{4h}\,, \tag{2.50}$$

so with step length Δx the number of steps N_{sr} involved in the spurious reflection is of the order of

$$N_{\text{sr}} \approx \frac{\sqrt{\lambda d^3}}{4h\Delta x} \,. \tag{2.51}$$

The Fresnel zone spacing s at the reflection point will be

$$s \approx \frac{\lambda d}{8h} \,. \tag{2.52}$$

We find the solution by considering the amount of absorber attenuation ΔA introduced between height h and height $h+s$ over the N_{sr} steps likely to be involved in the spurious reflection. If ΔA is negligible, then the spurious reflection is likely to be insignificant.

For one step, from (2.49), $A(h+s)$ is

$$A(h+s) = 0.5 + 0.5\cos\left(\pi\frac{s}{h}\right) \approx 1 - \frac{1}{4}\left(\frac{\pi s}{h}\right)^2 \,, \tag{2.53}$$

so for N_{sr} steps we have

$$\Delta A \approx \frac{\sqrt{\lambda d^3}}{4h\Delta x}\left(\frac{\pi\lambda d}{16h^2}\right)^2 = \frac{\pi^2\sqrt{\lambda^5 d^7}}{1024h^5\Delta x} \,, \tag{2.54}$$

or in terms of h

$$h = \left(\frac{\pi^2\sqrt{\lambda^5 d^7}}{1024\Delta A\Delta x}\right)^{0.2} \,. \tag{2.55}$$

The expression (2.55) suggests the required absorber height may depend on the weakest field required to be predicted with reasonable accuracy. We find that this is the case, and that the minimum absorber start height h_{min}, to reproduce propagation factors (dB relative to free space) down to dB_{min}, is empirically approximately given by

$$h_{\text{min}} \approx 10^{-\left(\frac{\text{dB}_{\text{min}}+80}{100}\right)}\left(\frac{\pi^2\sqrt{\lambda^5 d^7}}{\Delta x}\right)^{0.2} \,. \tag{2.56}$$

All length parameters in (2.49) to (2.56), z, h, l, d, λ, s, Δx and h_{min}, are in the same units. The effect of differing absorber lower edge heights is shown in Figure 2.6, ranging from 574 m in (a), just above the displayed field, as predicted by (2.56) for validity to 20 dB below free space, to 3623 m, as indicated by (2.56) for predictions to 100 dB below free space field.

These plots are for vertical polarisation, 300 MHz, with linear refractivity gradient of +118 M-units per km, over average ground, $\epsilon_r = 15$, $\sigma = 0.001$ S/m.

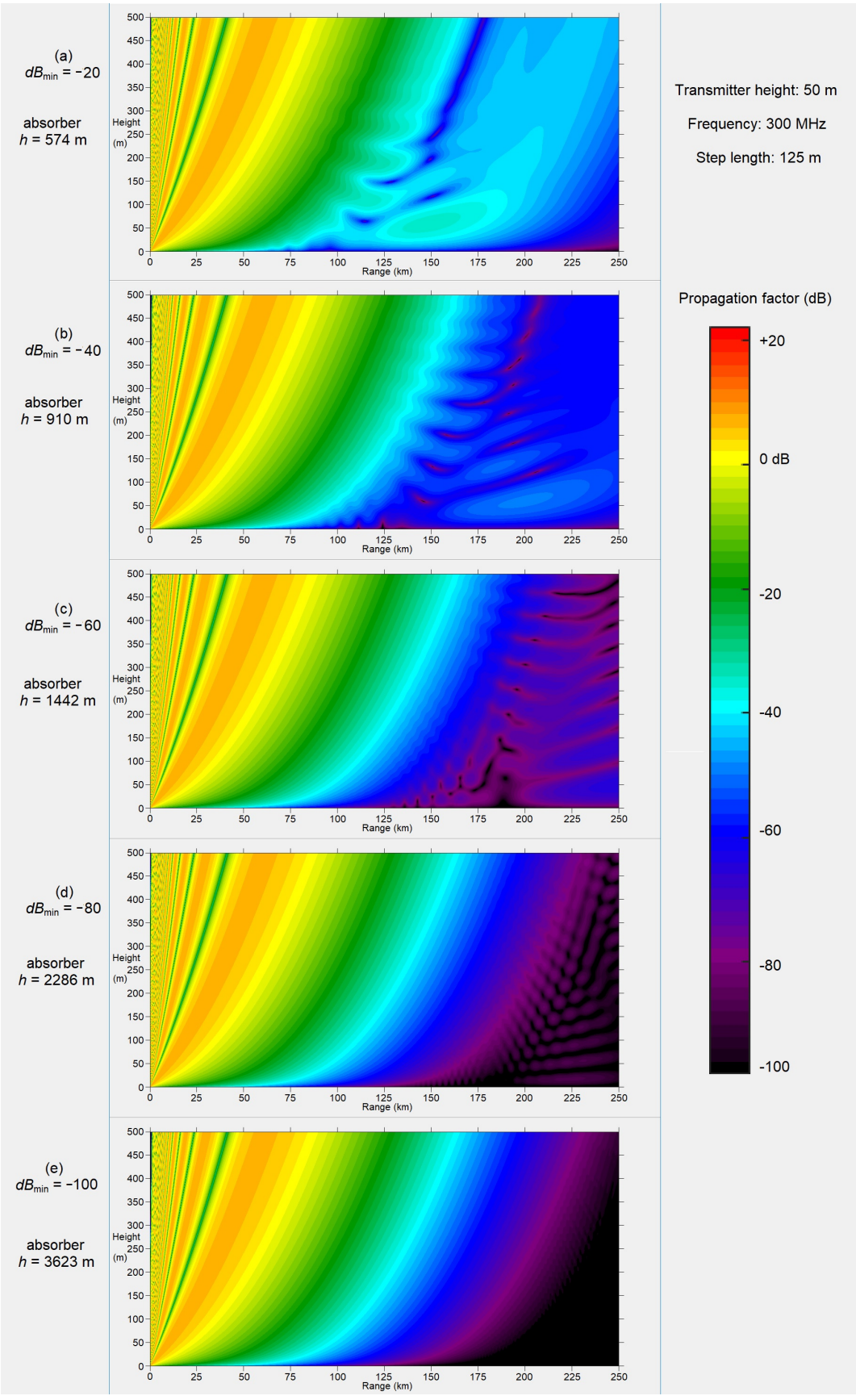

Figure 2.6. The effect of varying upper absorber height. The five examples (a) to (e) are as suggested by (2.56) for $\mathrm{dB_{min}}$ values of -20, -40, -60, -80 and -100 dB respectively.

2.3.9 Terrain flattening

The simplest approach to modelling irregular terrain is to take the Fourier split-step solution for a flat lower boundary (2.16), and add the second derivative of terrain height t'' with respect to range x to the refractive index correction (Barrios 1994):

$$u(x+\Delta x,z) = \exp\left[ik(10^{-6}M(z) - zt'')\Delta x\right] \times F^{-1}\left\{\exp\left[i\Delta x\left(\sqrt{k^2-p^2}-k\right)\right]F\{u(x,z)\}\right\}. \quad (2.57)$$

Here modified refractivity $M(z) = (n-1+z/a)\times 10^6$ replaces refractivity n, with z being elevation above a height datum such as mean sea level, t terrain elevation above that datum, and a the radius of the Earth. The idea of terrain flattening is to replace variations in terrain elevation, by equal and opposite variations in ray paths, by beam steering. This is an extension of the principle of replacing refractivity by modified refractivity, so that with uniform modified refractivity, ray paths follow the curvature of the Earth.

If the terrain variation is approximated by a piece-wise linear model, the idea of terrain flattening is as demonstrated in Figure 2.7.

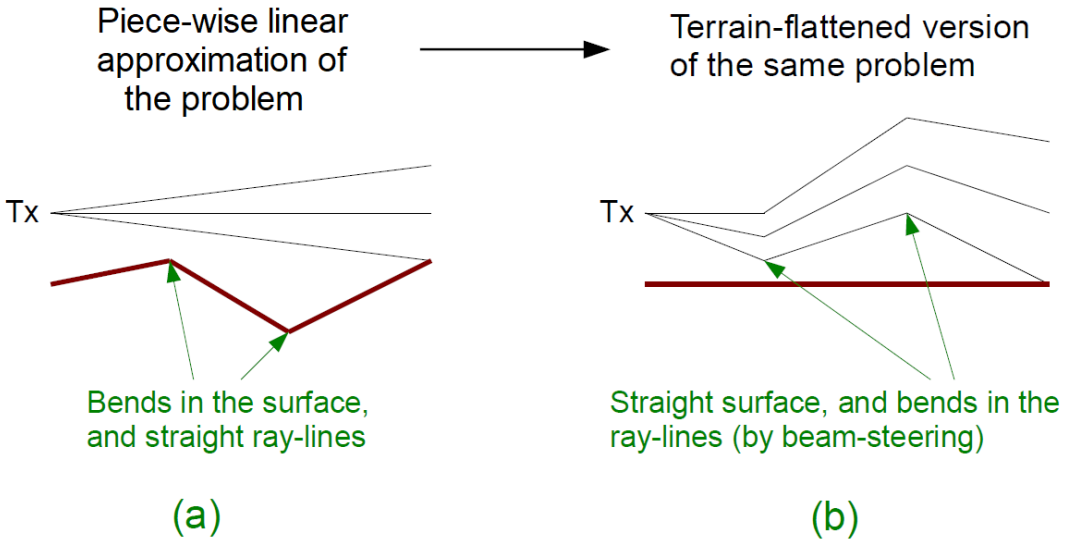

Figure 2.7. Propagation over terrain by terrain flattening. The terrain may be approximated by a piece-wise linear model, the brown heavy line in (a). The PEM analysis may be performed by replacing the bends in the terrain by beam-steering of the PEM analysis, to obtain a flat lower boundary (b). Tx is the transmitter.

The success of terrain flattening depends on the success of the beam steering, especially when an abrupt change in direction occurs within one step of the marching algorithm.

The choice of Δz

The Fourier transforms in (2.16) and (2.57) are implemented in practice as discrete transforms, such as fast Fourier transforms (FFT) or discrete sine transforms (DST). This requires a suitable choice for the vertical field sample spacing Δz. The generally stated requirement is the Nyquist criterion

$$\Delta z \leq \frac{\lambda}{2 \sin \theta_{\text{max}}} , \tag{2.58}$$

where θ_{max} is the maximum ray angle to the horizontal to be modelled.

We note that if a window function is applied to attenuate the upper half of the p-space transformed field to prevent aliasing, accurate representation of all rays present requires an amendment to (2.58):

$$\Delta z \leq \frac{\lambda}{4 \sin \theta_{\text{max}}} . \tag{2.59}$$

This still allows $\Delta z > \lambda$ if $\sin \theta_{\text{max}} < 0.25$, but in the case of piece-wise linear approximation of the terrain, it has been noted (Donohue and Kuttler 2000) that the abrupt beam steering occurring where the terrain slope changes, is equivalent to beam-steering an antenna array. This imposes the additional requirement

$$\Delta z < \frac{\lambda}{1 + \sin \theta_M} , \tag{2.60}$$

where θ_M is the largest angle through which the field is steered. This limitation avoids loss of signal that may occur due to grating lobes.

Piece-wise linear terrain implementation

For a piece-wise linear terrain model, the second derivative of terrain, t'' in (2.57), is replaced by beam steering at the range x where the terrain changes slope. Accurate implementation, to steer rays by the same angle as the change in slope of the terrain, from $u_1(x, z)$ before the change, to $u_2(x, z)$ afterwards, is (Donohue and Kuttler 2000)

$$u_2(x, z) = u_1(x, z) \exp \left[ikz(\sin \beta_1 - \sin \beta_2)\right] , \tag{2.61}$$

where β_1 and β_2 are the angles of the terrain to the horizontal, before and after the terrain slope change respectively.

This modification to the phase of the field samples is applied after the end of one step (after reflecting image samples to obtain the Dirichlet boundary condition if using FFT instead of DST) and before the beginning of the next, assuming the terrain slope changes are coincident with the Fourier split-step marching algorithm steps. However, there is a limit to terrain slope changes that may be handled by this method (Donohue and Kuttler 2000).

2.3.10 Modelling terrain without flattening

Although the Dirichlet boundary condition (reflection coefficient $R = -1$) may be automatically implemented by use of the DST as the Fourier transform in the split-step algorithm, the use of a fast Fourier transform (FFT) with twice as many elements, is an alternative that facilitates techniques to avoid terrain flattening. The lower elements in the field vector, elements 1, 2, 3, ... $N/2$, can be used to represent heights $z = 0$, $z = \Delta z$, $z = 2\Delta z$, ... $z = (N/2-1)\Delta z$ respectively, while the upper elements N, $N-1$, ... $N/2+1$ represent negative heights $z = -\Delta z$, $z = -2\Delta z$, ... $z = (1 - N/2)\Delta z$ respectively. A boundary condition at $z = 0$ may be imposed by taking the field $u_1(x, z)$ and reflecting the $z < 0$ field up and multiplying by R, to give field $u_2(x, z)$ as

$$u_2(x,z) = \begin{cases} u_1(x,z) + Ru_1(x,-z) & \text{if } z \geq 0, \\ 0 & \text{if } z < 0. \end{cases} \tag{2.62}$$

This is valid for $R = -1$, the Dirichlet boundary condition, or $R = +1$, the Neumann boundary condition. It is also valid for $R = 0$, although in this case the marching algorithm models a series of knife edge obstructions, with their tops at $z = 0$, placed at the end of each step. It is not valid for finite conductivity boundaries as it fails to model the surface wave that exists on finite conductivity plane surfaces (Norton 1941).

This idea can be extended to the conventional techniques of the terrain masking approximation, the staircase approximation, and our new technique to model piece-wise linear terrain without terrain flattening.

Terrain masking approximation

Rough terrain may be usefully modelled as a series of knife-edge obstructing screens, with their tops at the terrain height $t(x)$ at the end of each step. This may be achieved

by a modification of (2.62), with $R = 0$:

$$u_2(x,z) = \begin{cases} u_1(x,z) & \text{if } z > t(x), \\ 0.5u_1(x,z) & \text{if } z = t(x), \\ 0 & \text{if } z < t(x). \end{cases} \tag{2.63}$$

For clarity, this expression assumes terrain $t(x)$ is quantised in the same Δz steps as the field samples, but in the case of continuous t, the $z = t(x)$ case is amended to be the $|z - t(x)| < \Delta z/2$ case, with value $[0.5 + (z - t(x))/\Delta z]u_1(x,z)$. The terrain masking approximation avoids any spurious reflections due to steep terrain slopes, as reflections are ignored. However, this approach may over-predict the field in valleys, and should not be used where surface reflections may be important (Donohue and Kuttler 2000).

Staircase approximation

This approximation replaces the terrain by a series of horizontal flat surfaces, to model terrain of varying heights along the path, without needing terrain flattening. Unlike terrain masking, the staircase approximation includes surface reflection, so it has the potential to more accurately model the field in valleys. Reflection from the front faces of steps is ignored, as it would be spurious if included, so at the end of each step in the marching algorithm, surface reflection is implemented at the height of the terrain:

$$u_2(x,z) = \begin{cases} u_1(x,z) + Ru_1(x, 2t(x) - z) & \text{if } z \geq t(x), \\ 0 & \text{if } z < t(x). \end{cases} \tag{2.64}$$

However, this implementation of the surface reflection is only valid if the terrain height difference from one step to the next is a negligible fraction of a wavelength.

2.3.11 Piece-wise linear terrain by reflection steering

Terrain flattening, with the beam steering of (2.61), accurately models propagation over a piecewise linear model of the terrain, provided the changes in terrain slopes are not too severe. We present a new alternative, providing the same results for moderate terrain, but without terrain flattening, by applying a terrain slope correction to (2.64). The reflecting surface is at an angle β to the horizontal, resulting in the image of source points at the beginning of the step rotating by an angle 2β around the surface point at the end of the step. This is accounted for, by applying beam steering by an angle 2β to

the reflected image only. At the end of each step in the marching algorithm, at range x, surface reflection is implemented by including a phase correction factor $\alpha(z)$ as

$$u_2(x,z) = \begin{cases} u_1(x,z) + R\alpha(z)u_1(x,2t(x)-z) & \text{if } z \geq t(x), \\ 0 & \text{if } z < t(x), \end{cases} \tag{2.65}$$

with

$$\alpha(z) = \exp\left[ik\sin(2\beta)(z-t(x))\right], \tag{2.66}$$

and

$$\beta = \arctan\left(\frac{t(x)-t(x-\Delta x)}{\Delta x}\right). \tag{2.67}$$

Unlike the terrain flattening implementation of a piece-wise linear terrain model, here the beam steering is only applied to the reflected field, not the direct field, so if terrain slopes exceed the beam steering limit, the reflected field may be omitted. If that happens, the terrain is modelled as a series of knife-edges, an appropriate model for such rough terrain. Therefore it is useful to attenuate α as the steering angle 2β approaches a limit. We find it sufficient to apply a Tukey window function, such that α falls to zero at the Nyquist limit (2.58), when $s = |\sin(2\beta)|$ reaches $s_{\max} = \lambda/(2\Delta z)$. We then have

$$\alpha(z) = w\exp\left[ik\sin(2\beta)(z-t(x))\right], \tag{2.68}$$

with

$$w = \begin{cases} 1 & \text{if } s \leq 0.5s_{\max}, \\ 0.5 + 0.5\cos\left(\pi\frac{2s-s_{\max}}{s_{\max}}\right) & \text{if } 0.5s_{\max} < s < s_{\max}, \\ 0 & \text{if } s \geq s_{\max}. \end{cases} \tag{2.69}$$

Although this implementation of a piece-wise linear terrain model provides the same results for moderate terrain as the conventional approach (Donohue and Kuttler 2000), this new method is robust in very rough terrain where terrain flattening is not.

Figure 2.8 is an example of terrain with moderate slopes, within the terrain flattening limit of 0.2 radians set by (2.60). Plot (a) uses terrain flattening to accurately implement the piece-wise linear terrain, while (c) uses the slope correction of (2.65) to achive the same result without terrain flattening. Given the simplicity of (2.65), the well-known staircase approximation (b), cannot be recommended, due to missing angled reflections from terrain, and spurious fringing from non-existent horizontal surfaces. The terrain masking approximation is shown at (d); a robust option for rough terrain, but over-predicts field in valley bottoms, and cannot model reflections from terrain facets.

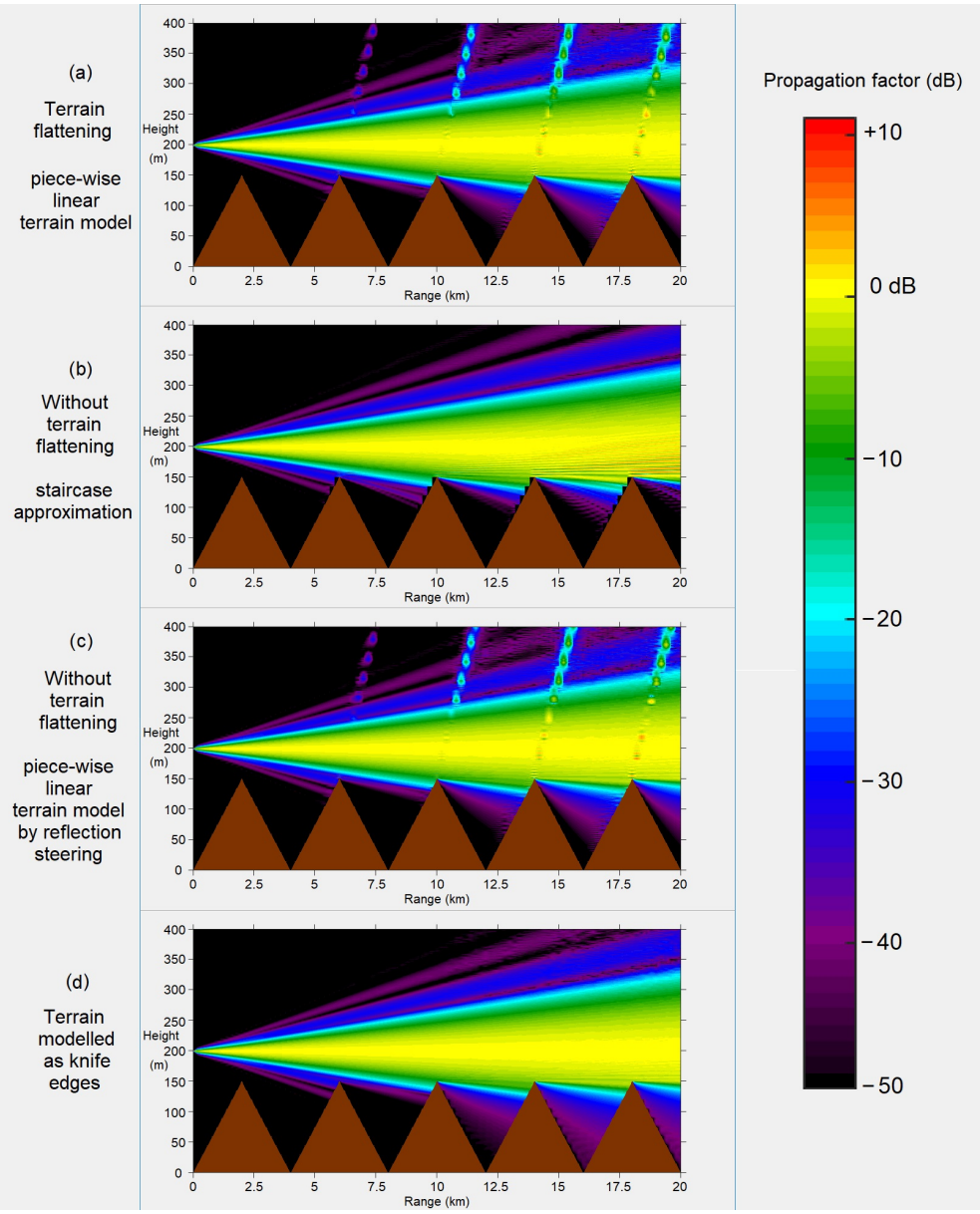

Figure 2.8. Terrain modelling, with and without flattening. The four examples (a) to (d) are for the same terrain consisting of five wedges, shown in brown. All have apex angles of 0.15 radians, within the limit from (2.60) for $\Delta z = 0.025$ m at 10 GHz. Plot (a) uses terrain flattening to implement the piece-wise linear terrain, while (c) achieves the same result without terrain flattening, by beam-steering the reflection, using (2.65). Both (a) and (c) show the high-angle reflection from the front face of the wedge (the dotted appearance is an artifact of the field display interpolating 200 m analysis steps to 8 pixel width). These reflections are missing from the staircase approximation (b) due to its horizontal reflecting surfaces, which result in spurious fringing, seen towards the end of the path. Plot (d) is the terrain masking option, modelling the terrain as knife edges at the end of each step, every 0.2 km. Reflections from the front faces of wedges are missing, and the field-strength in valleys is stronger than in (a) or (c).

Figure 2.9 (a) shows the failure of terrain flattening with extreme terrain slope changes. This becomes catastrophic once they exceed the Nyquist criterion limit of 0.643 radians, set by (2.58). Loss of the line of sight signal is prevented by not using terrain flattening, and implementing the reflection steering of (2.65), in Figure 2.9 (b) and (c). Spurious products appear for the extreme slopes in (b) with α from (2.66), but applying windowing to attenuate reflections from extreme slopes, using (2.68) and (2.69), eliminates the spurious products, as demonstrated in (c). The field plots of Figures 2.8 and 2.9 are with a narrow beamwidth transmit antenna with a raised cosine aperture, for clarity in showing the effect of different analysis options.

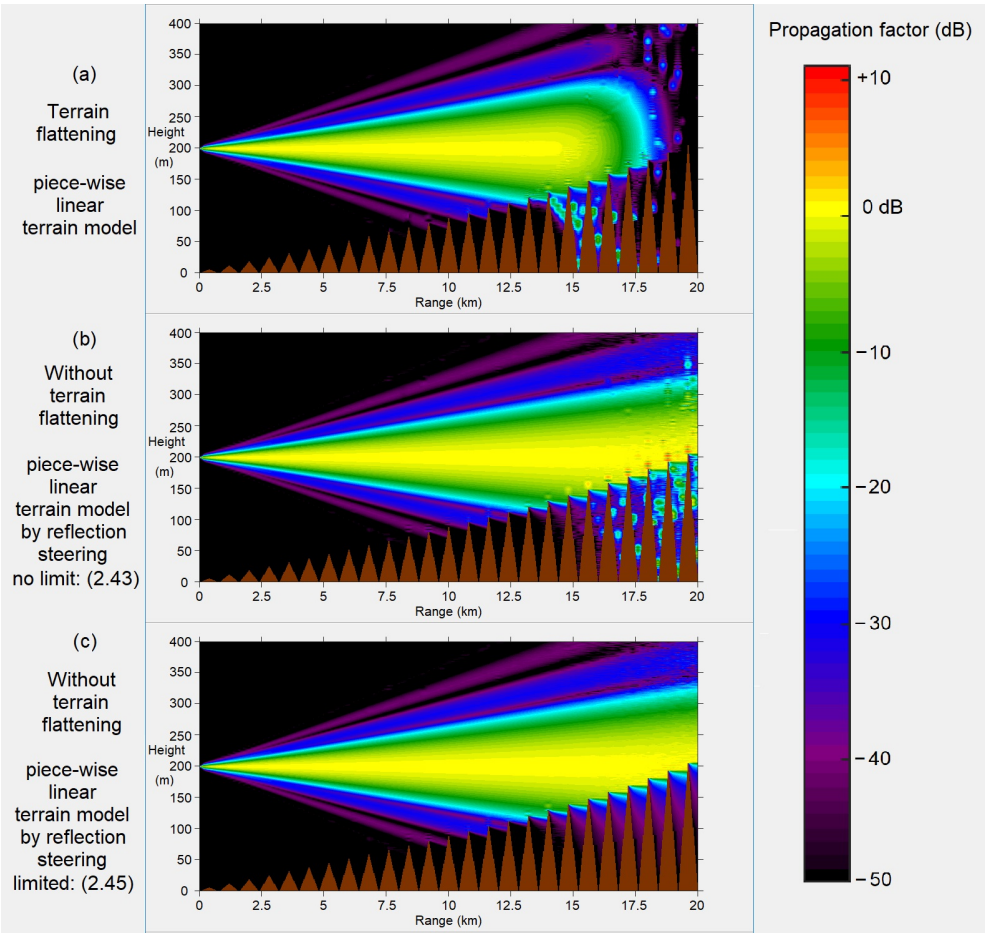

Figure 2.9. Rough terrain, with and without flattening. The three examples (a) to (c) are for the same terrain consisting of 25 wedges, with apex angles increasing in 0.032 radian steps to a maximum of 0.8 radians. Plot (a) uses terrain flattening to implement the piece-wise linear terrain, demonstrating propagation failure with rough terrain. Line-of-sight signal loss is prevented by not using terrain flattening in (b) and (c), but reflection windowing using (2.69), shown in (c), avoids spurious products.

2.3.12 Extension to 3 dimensions

The reflection steering approach for terrain without flattening, may be readily extended to a three-dimensional approach for point to point propagation, by replacing the one-dimensional field vector of samples at range x, $u(x, z)$ in (2.16), by a two-dimensional array of samples at range x, $u(x, y, z)$. The two dimensional analysis of (2.16) or (2.57) assumed complete uniformity in the y-direction of space, or in other words, cylindrical wave-fronts emerging from the transmitter, and parallel cylindrical terrain obstructions. Where there is significant variation in terrain elevation in the y-direction, that simplifying assumption may not be valid, so we present here a method for three dimensional analysis over terrain, with elevation variations in both x and y directions.

For convenience and simplicity in our point-to-point application, we retain Cartesian coordinates (x, y, z) for three dimensions, although in other applications, such as area coverage, polar coordinates may be preferred.

Taking (2.16), and including a vertical modified refractivity profile $M(z)$ as in (2.57), but not including terrain flattening, and replacing p/k with $\sin\theta$ we have

$$u(x+\Delta x, y, z) = \exp\left[ik10^{-6}M(z)\Delta x\right] \times F^{-1}\left\{\exp\left[ik\Delta x\left(\cos\theta - 1\right)\right]F\{u(x, y, z)\}\right\}, \tag{2.70}$$

where θ, as before, is the angle between the ray and the paraxial direction, but this time evaluated in 3 dimensions.

The Fourier transform F is now implemented as a two-dimensional FFT instead of a one-dimensional FFT, with equal sample spacings in y and z directions, so $\Delta y = \Delta z$.

We are now dealing with spherical wave-fronts instead of cylindrical. In order to provide the best insight in field plots Figures 2.6, 2.8 and 2.9, we have shown the field strength in terms of propagation factor, or relative to free-space propagation for the range. This is readily achieved by scaling the field at the end of the step $u(x + \Delta x, z)$ by a factor $\sqrt{(x + \Delta x)/x}$, the square root resulting from the cylindrical wave-fronts. In 3D we have spherical wave-fronts, so the scaling factor is simply $((x + \Delta x)/x)$, as field strength is inversely proportional to range for a spherical wave-front.

Terrain masking approximation in 3D

Considering first terrain masking, or obstruction without reflection, we re-write (2.63), with field quantised vertically in Δz steps, but terrain height $t(x, y)$ not quantised, as

$$u_2(x,y,z) = \begin{cases} u_1(x,y,z) & \text{if } z > t(x,y) + \Delta z/2, \\ \left(0.5 + \frac{z - t(x,y)}{\Delta z}\right) u_1(x,y,z) & \text{if } |z - t(x,y)| < \Delta z/2, \\ 0 & \text{if } z < t(x,y) - \Delta z/2. \end{cases} \tag{2.71}$$

In addition to the upper boundary, artificial aborbing boundaries are required either side of the problem to limit the size of the field arrays. For our point-to-point application, a convenient boundary is a cylindrical one, centred on the line $y = 0, z = z_t$ in the paraxial direction, where z_t is a convenient elevation, such as minimum terrain height along the path. We attenuate extreme off-axis fields as before, with attenuation progressively introduced from radius h_{min} from the $y = 0, z = z_t$ line, with h_{min} set by (2.56). A Tukey window function, in terms of distance from the centre line, results in field falling to zero at radius $2h_{\text{min}}$. The size of the 2D field array $u(x, y, z)$ at range x is then $4h_{\text{min}} \times 4h_{\text{min}}$.

The remaining problem is the terrain $t(x, y)$, as it typically will be interpolated from a digital terrain model at resolution much coarser than Δy. This is not generally a problem for 2D analysis, because the analysis step size may be simply chosen to match the sampling of the terrain in the x-direction. For 3D analysis, interpolation of the terrain data in the y-direction at Δy spacing is required. The simplest alternative for terrain masking would be linear interpolation, but when we later consider surface reflection, a continuous estimate of surface slope in the y-direction may be preferred. As cubic spline interpolation functions are readily available in scientific programming languages, for each step in the analysis we interpolate the transverse (y-direction) terrain profile at field array grid points, or Δy spacing, with cubic splines.

Irregular terrain in 3D by reflection steering

Reflection steering, readily implemented for 2D in (2.65) to (2.69), is more complicated to implement in 3D, because terrain variation in the y-direction, transverse to the direction of propagation, now needs to be considered, so we potentially have terrain slope in both x and y directions.

We retain the coarse Δx terrain resolution in the x-direction, and again in 3D assume piece-wise linear variation in that direction, but in the y-direction we smoothly interpolate to Δy spacing, by cubic splines, to approximate transverse curvature that may be present. This may seem inconsistent, but is consistent with the differing transverse and longitudinal nature of Fresnel zones. Their transverse radius of curvature is equal to the zone radius as they are circles around the line-of-sight, while their longitudinal radius of curvature is much greater than the zone radius for most of the path, as they are elongated ellipses, with transmitter at one focus and receiver at the other.

At range x and transverse coordinate y, the longitudinal angle of the terrain over the previous step, β_L, is then

$$\beta_L = \arctan\left(\frac{t(x,y) - t(x-\Delta x, y)}{\Delta x}\right) . \tag{2.72}$$

For the analysis step ending at range x, there are two transverse terrain angles to consider, β_S at the beginning of the step, and β_E at the end, given by

$$\beta_S = \arctan\left(\frac{t(x-\Delta x, y+\Delta y) - t(x-\Delta x, y-\Delta y)}{2\Delta y}\right) , \text{and} \tag{2.73}$$

$$\beta_E = \arctan\left(\frac{t(x, y+\Delta y) - t(x, y-\Delta y)}{2\Delta y}\right) . \tag{2.74}$$

The overall terrain angle β for use in (2.68) is given by

$$\tan(\beta) = \begin{cases} \tan\beta_L \cos\beta_E & \text{if } \beta_S = \beta_E, \\ \frac{\tan\beta_L \tan(\beta_E - \beta_S)}{(\tan\beta_E - \tan\beta_S)\cos\beta_E} & \text{otherwise,} \end{cases} \tag{2.75}$$

using the simplifying assumption that transverse terrain slope is constant at the beginning and end of the step.

The 3D methods we have described here may be implemented either by Fourier split-step PEM, using 2D Fourier transforms, or our new convolutional method in 2.3.2, by using 2D convolution, but the latter requires field sample spacing Δz of approximately half a wavelength or less, which may be computationally onerous at higher frequencies.

2.3.13 The finite element approach

We have so far described conventional Fourier split-step parabolic equation methods, and our new convolutional approach, which although derived from wide-angle Fourier

split-step, allows the lower boundary to be configured in terms of a complex reflection coefficient as a function of grazing angle. However it is an approximation that loses accuracy if the reflection coefficient departs too far from Dirichlet or Neumann boundary conditions. An accurate solution to this problem with the convolutional approach is yet to be found.

In contrast, the DMFT technique (Dockery and Kuttler 1996) accurately models a Leontovich boundary condition, but only with single value of α at each step of the analysis, and may suffer stability problems at some values of α (Kuttler and Janaswamy 2002).

For completeness, we should mention another parabolic equation method, providing greater flexibility in the treatment of the lower boundary than Fourier split-step with DMFT. It is the finite element approach (Levy 1990, Levy 2000, Holm 2007), which represents the partial differential wave equation in terms of differences between points on a regular grid of field sample points.

The difference scheme for a marching analysis method may be represented as (Holm 2007)

$$\mathbf{A}_m \mathbf{U}_m = \mathbf{B}_m \mathbf{U}_{m-1} \,, \tag{2.76}$$

where $\mathbf{U}_{m-1}$ is the vector of field samples at the end of the previous step, $\mathbf{A}_m$ and $\mathbf{B}_m$ are tri-diagonal matrices derived from the wave equation and boundary condition, and $\mathbf{U}_m$ is the vector of field samples at the end of the current step.

Solution of (2.76) for $\mathbf{U}_m$ requires inversion of $\mathbf{A}_m$, and the inversion propagates the boundary condition through the inverted matrix. Although the matrix inversion may be carried out efficiently, provided it is non-singular (Levy 2000), if step parameters such as step length or boundary condition change from step to step, the matrix inversion must be repeated at each step. This may result in a considerable execution overhead, compared to Fourier split-step, or our new convolutional approach.

2.4 The ITU-R general terrain diffraction model

The current ITU-R general model for terrain diffraction (*Rec. ITU-R P526-15*, 2019), known as the delta-Bullington model, is empirically based on many measurements of obstructed VHF and UHF radio paths in a number of countries. It was adopted in 2011 by ITU-R Study Group 3 (Radiowave Propagation), and internationally approved in *Rec. ITU-R P526-12*, (2012), as the general terrain diffraction model for all P-series

Recommendations of the ITU-R, after intense international discussion in the previous few years. We provide here a brief summary of the development of this model, as a full description is not available in the literature.

The "Bullington" part of the model name refers to an early paper (Bullington 1947), where the "Bullington triangle" construction is described in two contexts. One is described in Fig. 10 of that paper as shadow loss relative to smooth Earth, relevant to low frequencies, but the one used in the delta-Bullington model is that in Fig. 9 of that paper, where line-of-sight is obstructed by two sharp ridges. The suggested approximate solution is to find the intersection point of the horizon rays from the antennas at each end of the path, and model the double knife-edge obstruction as a single knife-edge at that point. It should be noted that this was prior to a formal solution to the double knife-edge problem (Millington *et al.* 1962).

This effective knife-edge construction became known as the Bullington model, estimating diffraction loss of arbitrary terrain obstructing line-of-sight as a single knife-edge obstruction at the intersection of horizon rays from each end of the path. If line-of-sight is un-obstructed, the point on the terrain with greatest Fresnel obstruction is taken as the equivalent knife-edge point.

Later, reasonably accurate but quite simple models for multiple knife-edge diffraction emerged (Epstein and Peterson 1953, Deygout 1966, Giovaneli 1984), and this Bullington model fell out of favour. However, testing of some of these models, including the Bullington model, against datasets of measurements (Liniger *et al.* 2003), suggested that the Bullington model appeared to be more accurate than some of the later multiple knife-edge models, albeit with some degree of under-prediction of diffraction loss.

Another study (da Silva *et al.* 2005) provided further empirical evidence that the simple Bullington construction appeared to have good error standard deviation compared to the many other methods trialled, but tended over-estimate field strength by several dB, to an increasing degree for paths with more obstacles.

A considerable amount of testing work followed by members of the ITU-R 3K-1 Correspondence Group over the next couple of years, with the conclusion that applying a correction the Bullington model knife-edge loss L_{uc} to give a predicted loss L_b as

$$L_b = L_{\text{uc}} + [1 - \exp(-L_{\text{uc}}/6)](10 + 0.2d) \,, \tag{2.77}$$

where d is the path length in km,

is a good practical diffraction model for irregular or even mountainous terrain. As well as demonstrating good empirical accuracy, this model is continuous, with no discontinuities in predicted loss as path parameters are varied.

However, this model may not be accurate for long paths over smooth Earth. An accurate model for this situation is available (*Rec. ITU-R P526-15*, 2019), based on the first term of the residue series for distances beyond line-of-sight, with a smooth transition to an extended plane-Earth model within line-of-sight, so a technique was devised (*United Kingdom: ITU-R doc. 3J/64*, 2009) to effectively make use of the smooth-Earth model for smooth-Earth paths, but use some other irregular terrain model to take account of differences between the terrain and the smooth-Earth case.

Taking the corrected Bullington model (2.77) as the irregular terrain model, this technique became known as the delta-Bullington model. A smooth-Earth path being a least-squares best fit to the actual terrain is found, and the smooth-Earth model loss for this path L_{sph}, is calculated. The Bullington model loss L_{bs} for this same best-fit smooth-Earth path from (2.77), is also calculated.

Then the Bullington model loss L_{ba} for the actual terrain is calculated from (2.77), and the difference $L_{\text{ba}} - L_{\text{bs}}$ is effectively a correction to the smooth-Earth loss L_{sph}, to take account of the roughness of the terrain. There may be cases where $L_{\text{sph}} < L_{\text{bs}}$, so to ensure the overall diffraction loss prediction L cannot be less than L_{ba}, we have

$$L = L_{\text{ba}} + \max[L_{\text{sph}} - L_{\text{bs}}, 0] \, . \tag{2.78}$$

However, for mountainous terrain, the best-fit smooth-Earth path has no significance, so we require $L = L_{\text{ba}}$ in this case. Switching between two different models is undesirable, so a single continuous model for all terrain types was achieved by taking terrain roughness into account (*Australia: ITU-R doc. 3J/112*, 2010), adjusting the notional smooth-Earth surface such that $L_{\text{sph}} = L_{\text{bs}} = 0$ for mountainous paths.

2.5 Conclusion

If the state of the atmosphere, particularly vertical refractivity gradients, can be predicted with sufficient accuracy and resolution, then the appropriate physical approach to clear-air fading prediction of terrestrial fixed paths is to use a full-wave propagation method, such as the parabolic equation approaches discussed above.

We provide some new developments in parabolic equation modelling. These include a new method for deciding the height of the absorbing upper boundary to avoid fringing effects, in 2.3.8, and a new robust method for dealing with irregular terrain, in 2.3.11, and its extension to three dimensions in 2.3.12.

We describe a new alternative to Fourier split-step modelling, in 2.3.2, using convolution instead of Fourier transforms. While this approach offers no advantage for situations where a Dirichlet boundary condition may be assumed, it may provide an alternative to DMFT for analysing finite conductivity Leontovich boundary condition problems, as it avoids the "bad alpha" numerical instability problem in DMFT (Kuttler and Janaswamy 2002).

For rough surface problems, the new method does not require an estimate of dominant grazing angle at each step of the analysis, as it is a general method for all angles of incidence that may occur at each step. The disadvantage of the new method is error in cases of high surface reflection loss, although it appears this may be to some extent addressed by extrapolating from different step lengths.

The new method may provide a computationally efficient alternative to finite element analysis for problems requiring greater flexibility in the boundary condition than can be provided by existing Fourier split-step analysis techniques, but the problem of accurately modelling finite conductivity boundaries by this type of image theory approach, remains to be solved. The aim of this thesis, modelling fixed radio link clear-air fading, does not require a solution to this problem, so we identify it as future work.

We have detailed these parabolic equation methods in this chapter, as they may be required in the future, for researching terrestrial fixed radio link fading, should detailed and accurate data on atmospheric refractivity profiles become available.

However, these full-wave methods are too involved and computationally demanding for day-to-day link engineering design. For this, the simple general terrestrial terrain diffraction model, briefly described in Section 2.4, is recommended for cases where a linear vertical refractivity gradient may be assumed.

This chapter has described research carried out, to develop efficient practical methods for full-wave analysis of propagation on terrestrial fixed radio link paths. This needs to be combined with accurate modelling of the refractive index structure of the atmosphere, to provide a complete physical model of propagation along the radio path, so we explore that possibility in the next chapter.

Chapter 3

Atmospheric Modelling

WEATHER forecasting has made considerable advances in recent years, due to numerical weather prediction (NWP) models running on super computers, simulating the physics of weather events, with these models continually updated by current weather data at good resolution. This computer model of the state of the atmosphere suggests the promise of a physics based solution to the clear-air radio link fading problem, but this requires accurate modelling of radio refractivity gradients in the surface layer of the atmosphere. We investigate the accuracy of this approach by comparing NWP re-analysis data with meteorological observations from weather balloons (radiosondes) as well as tower measurements, and investigate empirical modelling of gradient distributions.

3.1 Introduction

The fading prediction models used by radio link designers have been empirical, rather than scientific (Salamon *et al.* 2020). A potential atmospheric physics approach may be to predict the state of the atmosphere with a numerical weather prediction (NWP) model, and then use a terrain parabolic equation model (PEM) (Barrios 1994, Donohue and Kuttler 2000) to predict the radio propagation. This idea has been pursued for some time, both for radio link propagation (Ewenz *et al.* 2001), and in radar propagation research, but sub-meter resolution may be required in generating the refractivity profile (Claverie 2019). An NWP reanalysis product with at least several years of data at very high resolution would be required, to practically implement fading prediction for path design, using this approach. Even then, the link designer would have to run a few years equivalent of PEM simulations, to accurately determine the average year worst month performance of the link. Despite advances in computing capability, this still seems rather impractical in the short term.

Nevertheless, this approach should be investigated, as an empirical model is not necessarily valid beyond the range of conditions represented in the empirical data, while model based on physics can more confidently be expected to have an extended range of validity.

The following papers cited in this chapter were all produced as part of the work for this thesis: (Salamon *et al.* 2014a, Salamon *et al.* 2014b, Salamon *et al.* 2015, Salamon *et al.* 2020).

3.2 Radio refractivity

Radio refractivity is normally expressed in "N-units," or parts per million by which atmospheric refractive index for radio waves exceeds unity. Thus, vertical refractivity gradients are expressed in N-units per km. Standard refactivity for terrestrial radio links is typically assumed to be a gradient of –39 N-units per km.

The refractivity N is estimated as proportional to the partial pressures of various gas constituents of the atmosphere and inversely proportional to absolute temperature T, except that in the case of water vapour pressure e, there is another term inversely proportional to absolute temperature squared, due to the polar nature of the water molecule.

Expressed simply, with total air pressure P, consisting of dry air pressure $P-e$ and water vapour pressure e, we have, for example, the Bean model (Bean 1962)

$$N = 77.6\left(\frac{P-e}{T}\right) + 72\frac{e}{T} + 375000\frac{e}{T^2}\,, \tag{3.1}$$

or the more recent Rueger "best average" model (Rueger 2002)

$$N = 77.689\left(\frac{P-e}{T}\right) + 71.295\frac{e}{T} + 375463\frac{e}{T^2}\,. \tag{3.2}$$

While *Rec. ITU-R P453-14,* (2019) has retained the early Bean model as its standard model, many alternatives are available, and in fact the Rueger "best average" model was used to generate recent ITU-R gradient maps (Grabner *et al.* 2014). Practically speaking, for the atmospheric surface layer, although there is a small absolute difference between (3.1) and (3.2), as far as gradients are concerned, the difference is negligible, so we use the more recent Rueger "best average" model in this research.

3.3 NWP re-analysis

Weather forecasting uses numerical weather prediction (NWP) models which assimilate meteorological data to build a model of the current atmosphere, which can be run forward in time, in order to produce forecasts. The assimilation system may in principle be used to produce historical records of the estimated state of the whole atmosphere world-wide, even though actual measurements only take place at a limited number of locations, such as radiosonde stations, and perhaps only once or twice a day. This is known as a reanalysis.

As an example of a numerical atmosphere model, the "windflow model" employed in Kulessa *et al.* (2001) solves the conservation equations of

momentum:

$$\frac{\mathrm{d}\mathbf{v}}{\mathrm{d}t} = \frac{-1}{\rho}\nabla p - \mathbf{g} - 2\Omega \times \mathbf{v}\,, \tag{3.3}$$

heat:

$$\frac{\mathrm{d}\theta}{\mathrm{d}t} = Q_\theta\,, \tag{3.4}$$

humidity:

$$\frac{\mathrm{d}q}{\mathrm{d}t} = Q_q\,, \tag{3.5}$$

and mass:

$$\frac{\partial\rho}{\partial t} + \nabla\cdot(\rho\mathbf{v}) = 0\,, \tag{3.6}$$

where the differential operator $\mathrm{d}/\mathrm{d}t$ is defined as

$$\frac{\mathrm{d}}{\mathrm{d}t} = \frac{\partial}{\partial t} + \mathbf{v} \cdot \nabla \tag{3.7}$$

and $\mathbf{v} \cdot \nabla$ is the advection term. The variables are t: time, $\mathbf{v}$: wind velocity, ρ: air density, Ω: spin vector for Earth, p: air pressure, $\mathbf{g}$: acceleration due to gravity directed in the vertical, θ: potential temperature, q: water content, and Q_θ and Q_q are source or sink terms.

One of the current world-wide NWP models used in weather forecasting is that of the European Centre for Medium-range Weather Forecasting (ECMWF), and the ECMWF-Interim reanalysis product (ERA-I) (Dee *et al.* 2011) has been used to generate digital maps of radio refractivity gradient (Grabner *et al.* 2014) for ITU-R, published in *Rec. ITU-R P453-14,* (2019).

3.4 Measured refractivity gradient data

3.4.1 Radiosonde data

There are a very limited number of stations regularly providing data from ascents at 6 hourly intervals (Salamon *et al.* 2014b). Many more stations around the world provide radiosonde data at 12 hourly intervals, but caution is required in using data from stations with 24 hourly data, as gradient distributions can vary considerably depending on the local time of day that the ascents occur. Figure 3.1 illustrates this for a station in India. The data is from *NOAA / ESRL Radiosonde Database,* (2018), with the data now available at *NOAA IGRA Radiosonde Database,* (2022).

The NOAA/ESRL database provides a valuable repository for world-wide regular ascent data from radiosonde stations, but at lower vertical resolution than the full data generally collected as only salient points are saved. An example for the ascent nominally at 23:00 UTC on the 21st of March 2008, for the radiosonde station at Charleville, Queensland, is shown in Figure 3.2. Ascent speed is about 5 metres per second, so with samples taken every 2 seconds, original vertical resolution is about 10 metres.

Radio refractivity gradient distributions for the 65 metre surface layer are shown in Figures 3.3 and 3.4, comparing the high resolution data distributions with the low resolution data distributions, for the same ascents. Charleville, with median first height of 90 m reported in the NOAA data, showed good agreement, as did several other stations with lower median first heights, while Kalgoorlie, with median first height of 117

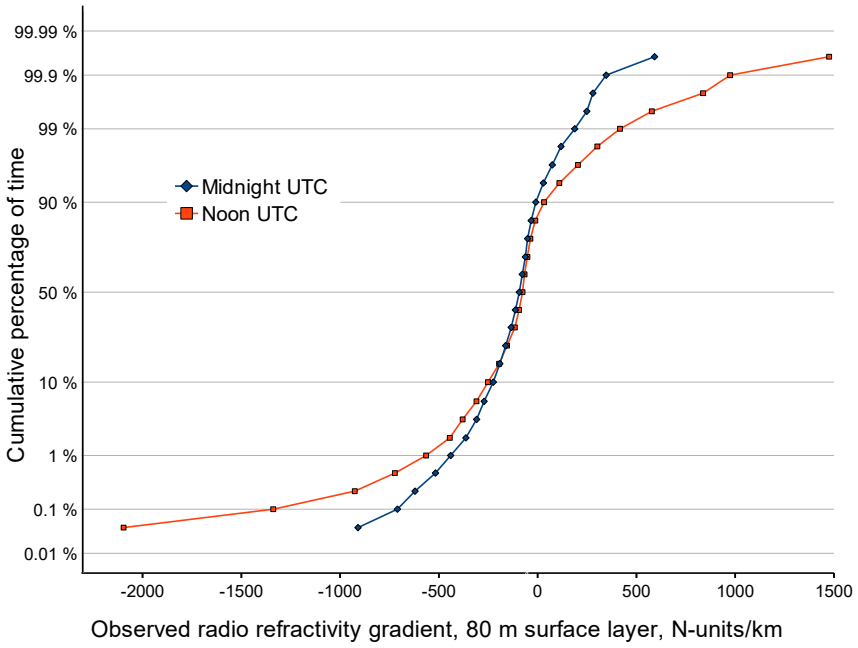

Figure 3.1. Radiosonde observed gradient distributions for Aurangabad, India. Observations from 1994 to 2013 at latitude 19.85 degrees, longitude 75.4 degrees, at around midnight UTC (early morning local time) and noon UTC (late afternoon local time).

m, under-reported the sub-refractive end of the distribution. We conclude that stations with 90 m or less median first height in the NOAA data, will provide reasonably accurate gradient distributions for the 65 m surface layer, while those with median first height well in excess of 100 m may not.

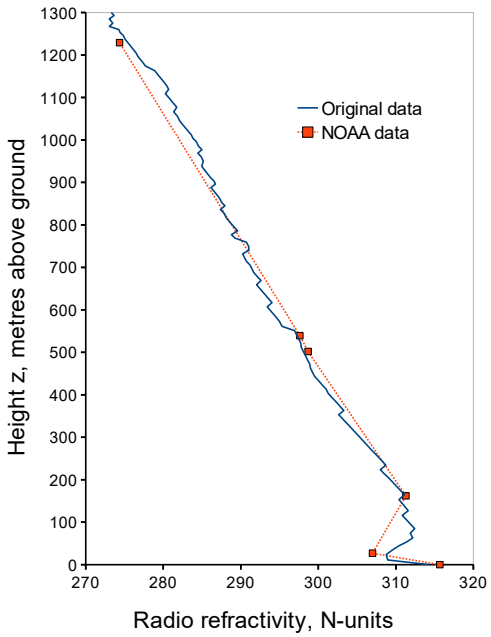

Figure 3.2. Charleville radiosonde ascent at 2100 UTC 21st March 2008. Original data at about 10 metres vertical resolution, and the salient points stored in the NOAA / ESRL database for the same ascent are shown.

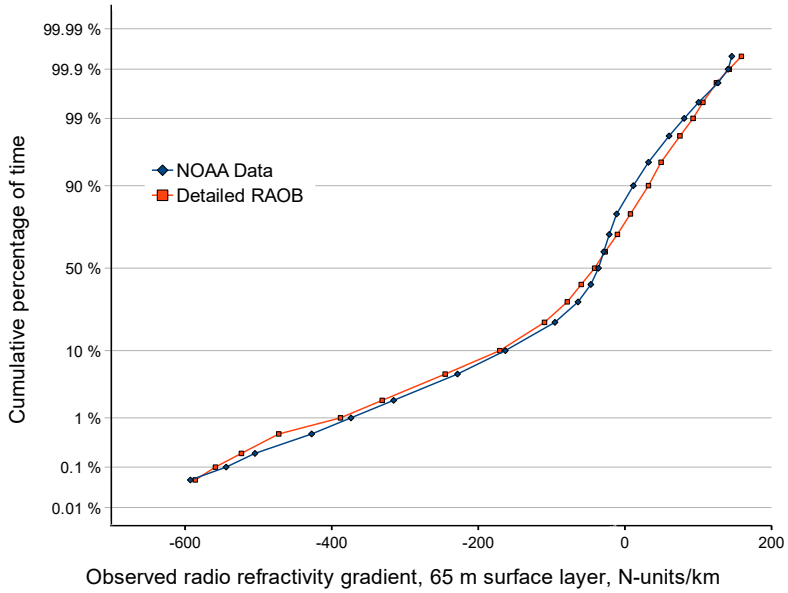

Figure 3.3. Detailed and NOAA Charleville RAOB comparison. Gradient distibution for the 65 m surface layer; original data compared with the salient points in NOAA data, for the same 2437 ascents between 2003 and 2011. Median first height in the NOAA data is 90 m.

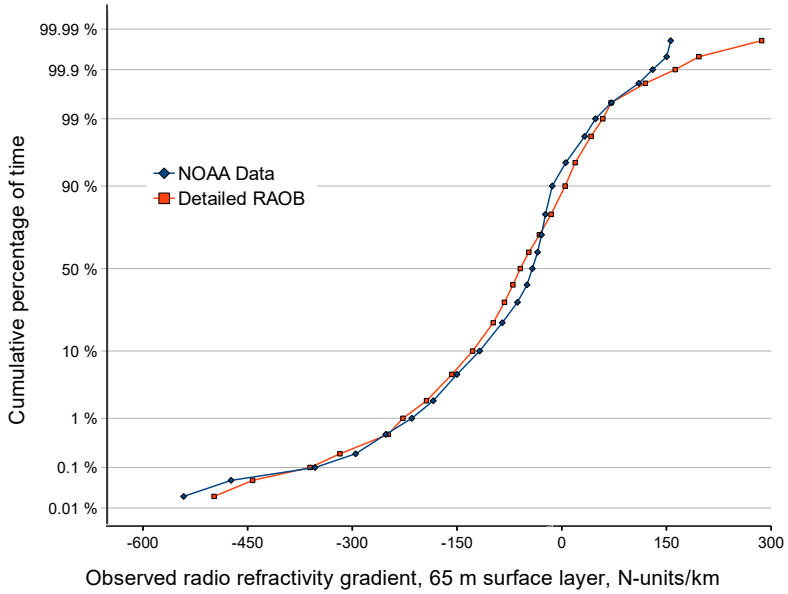

Figure 3.4. Detailed and NOAA Kalgoorlie RAOB comparison. Gradient distibution for the 65 m surface layer; original data compared with the salient points in NOAA data, for the same 2674 ascents between 2003 and 2011. Median first height in the NOAA data is 117 m. Sub-refraction from the 99.9% point and beyond is under-represented in the low resolution data.

3.4.2 Tower measurements

The radio refractivity profile in the lower atmosphere above land areas may be measured with either radio refractometers or temperature and humidity sensors on a mast or tower. A single instrument may be raised or lowered on the mast (Zhamsuyeva 1998), but this may limit the number of measurements conducted each day and the overall duration of measurements. In that measurement campaign, eight measurements a day were conducted over a period of two and a half months. A more convenient arrangement is to mount a number of temperature and humidity sensors, fixed at various heights on the mast (Grabner and Kvicera 2005, *Australia: ITU-R doc. 3J/169*, 2018). This permits un-attended data logging many times a day over an extended period. Pressure may be measured at ground level and estimated for the heights of the temperature and humidity sensors.

The Kopisty measurements in north-western Czech Republic (Grabner and Kvicera 2005) were recorded every 15 minutes for a full year, at heights of 2, 20, 40, 60 and 80 metres above ground. Figure 3.5 demonstrates the gradient variation in the 2 to 20 metre layer being greater than that to greater heights. In these measurements, both sub-refractive and super-refractive gradient variation in the 2 to 20 metre layer was significantly greater than in the next layer from 20 to 40 metres, or the higher layers (Grabner and Kvicera 2005, box plot Fig. 4).

Tower measurements were conducted at a coastal location in the North-West of Australia (*Australia: ITU-R doc. 3J/169*, 2018), with data collected over a period of seven and a half months, at four heights on a 100 metre radio mast. Vaisala HMS-110 temperature and humidity sensors were installed on the radio mast at Hilda Well, latitude -21.123602 degrees, longitude 115.967964 degrees, at heights of 1.5 m, 19 m, 60 m, and 97 m above ground. Readings were logged from these sensors every 5 minutes, from 18:15 local time (10:15 UTC) on 18 March 2016, until 10:00 local time (02:00 UTC) on 6 November 2016. Continuous data every 5 minutes was collected for the complete months of April to October. This provided the temperature and water vapour pressure data for the radio refractivity calculation, and air pressure was derived from measurements every 30 minutes from Mardie automatic weather station, latitude -21.1906 degrees, longitude 115.9797 degrees (WMO 94306). These locations are shown in Figure 3.6.

In this measurement campaign, the super-refractive (negative) part of gradient variation in the three measured layers, 1.5 to 19 m, 19 m to 60 m, and 60 to 97 m, were similar, but much greater sub-refractive (positive) variation was seen in the 1.5 to 19 m

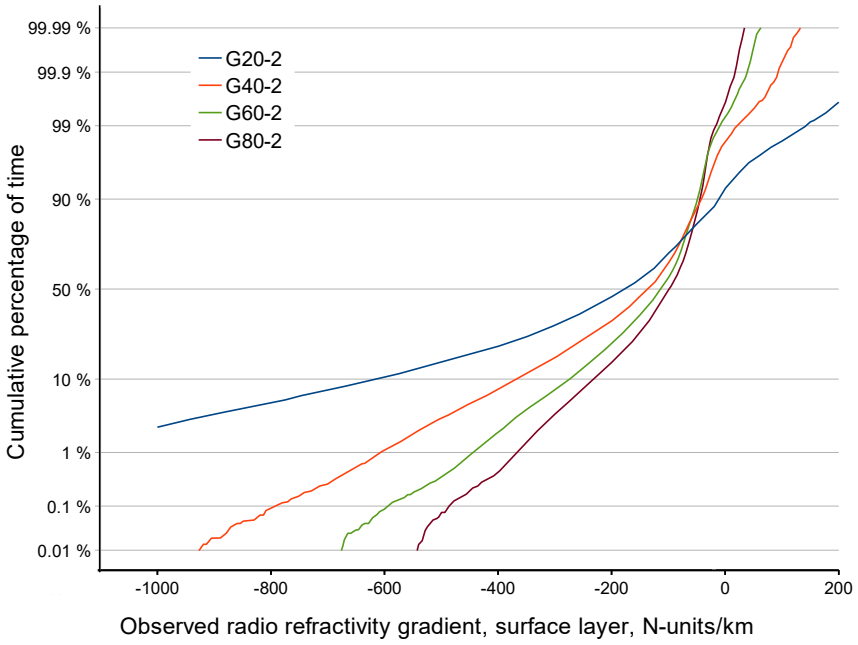

Figure 3.5. Observed surface refractivity gradients at Kopisty in 2004. Five Vaisala HMP45D temperature and humidity sensors were installed on a mast at Kopisty meteorological station, north-west of Prague, Czech Republic, at heights of 2 m, 20 m, 40 m, 60 m, and 80 m above ground, and pressure was derived from ground level measurements with a PTB100A sensor. Gradient distributions are shown for the full year, January to December, for the layer between heights of 2 m, and 20, 40, 60 or 80 m, with measurements every 15 minutes, after Grabner and Kvicera (2005, from Figures 1 and 2). Gradient variations are greatest in the lowest 2 to 20 metre layer.

layer than in the upper layers, as shown in Figure 3.7 for April. Despite the similarity of the super-refractive part of gradient distribution, the gradients in the three layers were quite un-correlated, as demonstrated by the scatter plots for April in Figures 3.8 and 3.9. This indicates that overall, the vertical refractivity gradient profile at this location tends to be non-linear, with both elevated and surface ducts, and strong sub-refraction near the surface at times.

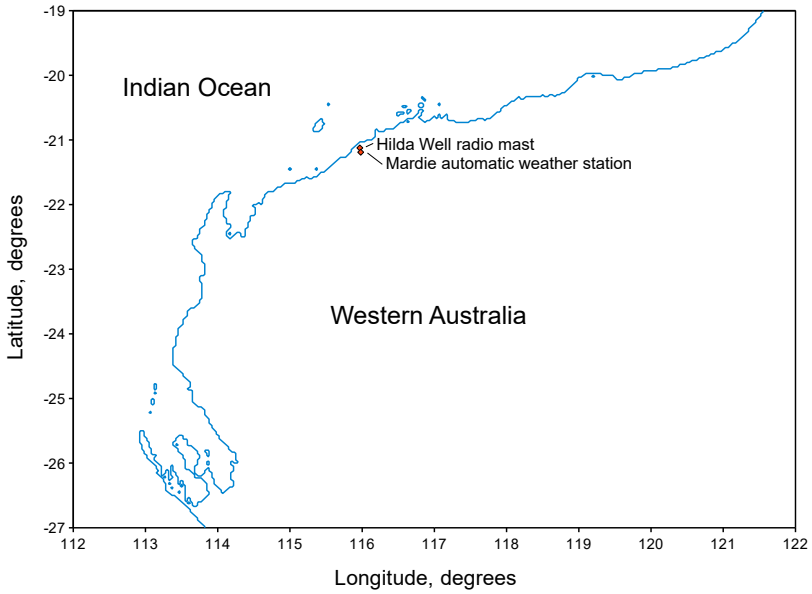

Figure 3.6. Hilda Well radio mast, and Mardie automatic weather station. Four Vaisala HMS-110 temperature and humidity sensors were installed on the radio mast at latitude -21.123602 degrees, longitude 115.967964 degrees, at heights of 1.5 m, 19 m, 60 m, and 97 m above ground, and pressure was derived from Mardie weather station, 7.6 km away at latitude -21.1906 degrees, longitude 115.9797 degrees (WMO 94306).

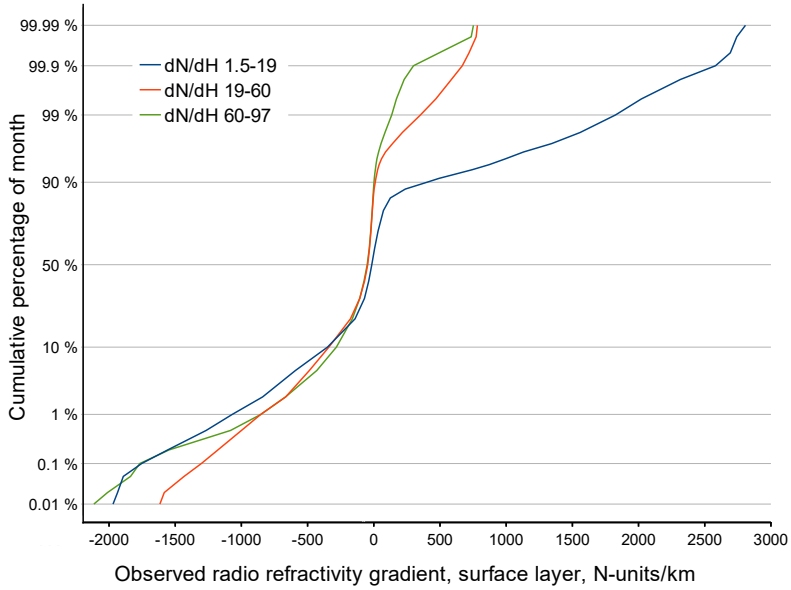

Figure 3.7. Refractivity gradient distributions, 1.5–19 m, 19–60 m, and 60–97 m. The super-refractive (negative) part of the gradient distributions are similar, but the sub-refractive (positive) part of the distribution in the lowest layer is stronger than the upper layers. The observations are every 5 minutes, during April 2016.

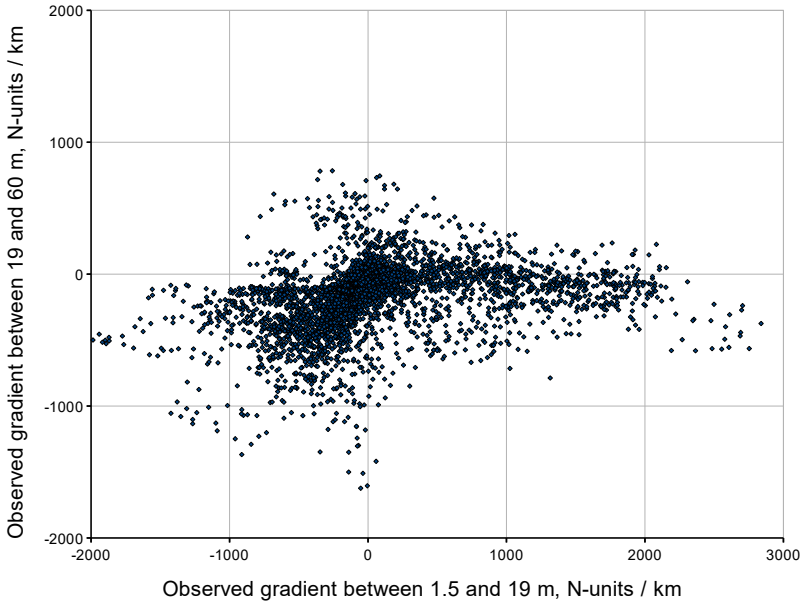

Figure 3.8. Observed refractivity gradients, comparing 1.5 to 19 m with 19 to 60 m. While milder gradients appear to be moderately correlated between the two layers, indicating reasonable linearity in the vertical refractivity profile, extreme gradients in the bottom layer are not reflected in the upper layer, indicating significant non-linearity. Overall correlation coefficient is 0.24.

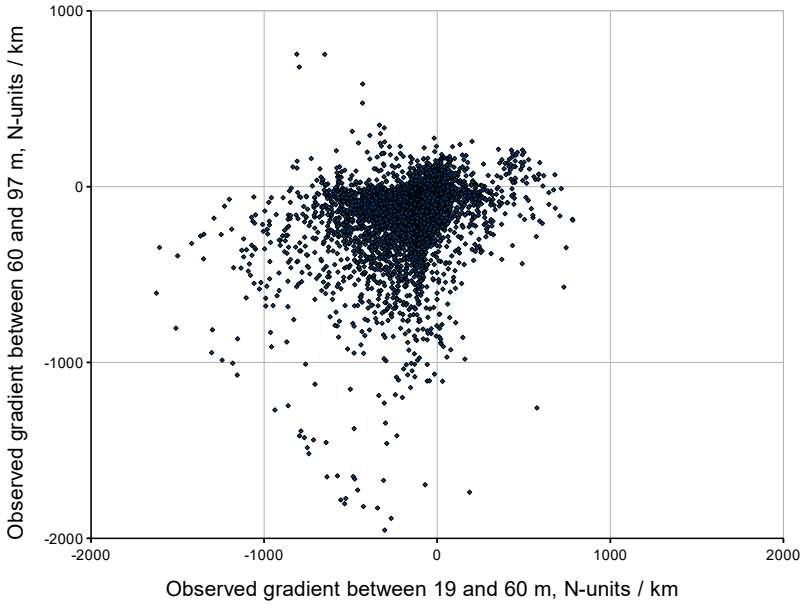

Figure 3.9. Observed refractivity gradients, comparing 19 to 60 m with 60 to 97 m. Despite similar distributions, the gradients in the upper two layers are largely uncorrelated; correlation coefficient = 0.37.

3.4.3 Effect of measurement error on gradient distributions

The tails of an observed cumulative distribution may have statistical variations, due to the small number of data points contributing to the tail region of the distribution (Salamon *et al.* 2014a). However, in the case of refractivity gradient distributions, which have their minimum slope near the median, measurement error can easily mask the true slope of the cumulative distribution in this region.

We consider the distribution in terms of an inverse cumulative normal probability variable X_p:

$$X_p = \text{norminv}(p, 0, 1) \tag{3.8}$$

$$\text{where } p : \text{proportion of data points}$$

$$\text{norminv}(p, 0, 1) : \text{inverse cumulative normal distribution}$$

If the measurement error can be assumed normally distributed and uncorrelated with the gradient $G(X_p)$, then the observed gradient will be (Salamon *et al.* 2014a)

$$G_{\text{obs}}(X_p) = \sqrt{[G(X_p) - G(0)]^2 + [\sigma_n X_p]^2} \tag{3.9}$$

$$\text{where } \sigma_n : \text{gradient measurement error standard deviation.}$$

Inversion of (3.9) to produce a corrected estimate $G_{\text{corr}}(X_p)$ of the true gradient $G(X_p)$, not biassed by the error noise σ_n, involves the square root of a quantity that may sometimes be negative, so the following alternative approximation

$$G_{\text{corr}}(X_p) \approx G_{\text{obs}}(X_p) - \frac{(\sigma_n X_p)^2}{2\Delta G} - \frac{(\sigma_n X_p)^8}{3\Delta G^7} \tag{3.10}$$

$$\text{where } \Delta G = G_{\text{obs}}(X_p) - G_{\text{obs}}(0),$$

is found to be useful, from simulation testing, shown in Figures 3.10 and 3.11.

The difficulty is in determining the the random variation σ_n. In the case of the Hilda Well data we have data frequently sampled, every 5 minutes, so a reasonable estimate is the standard deviation of gradient forward differences divided by $\sqrt{2}$. For the 1.5 to 60 metre gradient distribution, this suggests $\sigma_n = 25$ N-units/km. This is roughly half the minimum slope in the measured gradient distribution, of 52.9 N-units per km per standard deviation. In this case the effect of the correction of (3.10) on the plotted distribution is almost imperceptible, with sub-refractive gradients from the 80% point and above all reduced by around 4.8 N-units/km, and super-refractive gradients from the 20% point and below all reduced by around 3.6 N-units/km.

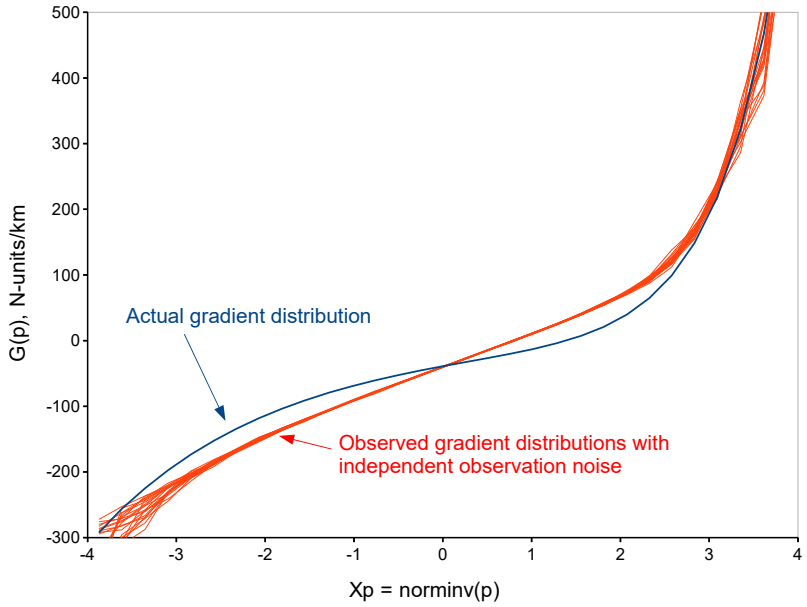

Figure 3.10. Simulated refractivity distribution, with measurement noise. A typical gradient distribution, the true gradient in dark blue, with 20 trials each of 10,000 observations, with added measurement white noise of 40 N-units per km RMS amplitude.

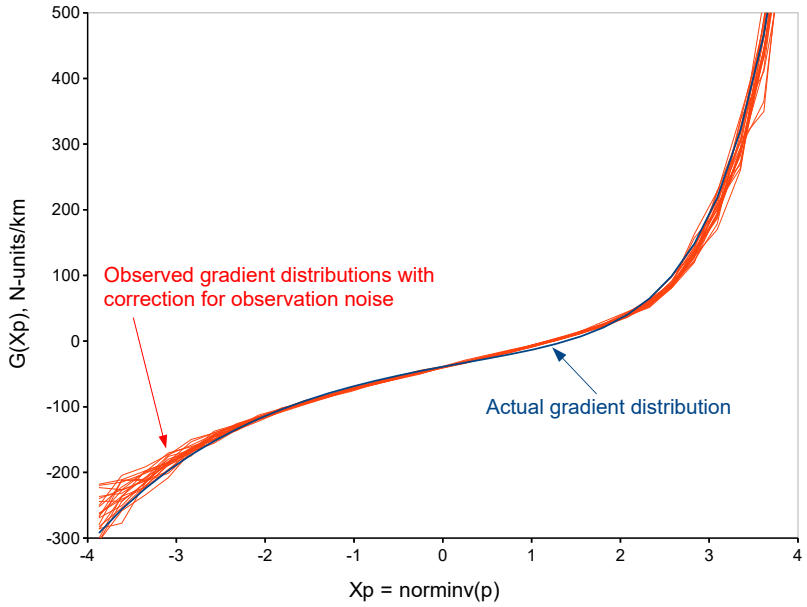

Figure 3.11. Simulated refractivity distribution, with noise correction. The same typical true gradient in dark blue, with the same 20 trials each of 10,000 observations, but with noise correction of the observed gradient distributions, using (3.10).

If we assume the random measurement variation is independent of the true gradient variaton, σ_n must be less than the minimum observed slope of the distribution. For cases where we don't have a direct measurement of σ_n, based on the Hilda well example, we assume σ_n to be half the minimum slope of the observed gradient distribution, reasonable considering the minimal effect of (3.10) on the distribution.

3.5 NWP surface gradient accuracy

3.5.1 Tower measurements

Comparison between the observed refractivity gradient distribution for one year in Kopisty, Czech Republic (Grabner and Kvicera 2005) for the surface layer between heights of 2 and 60 metres above ground, and the ERA-I annual gradient distribution for the 65 metre surface layer, is shown in Figure 3.12. While the NWP reanalysis gradient distribution is reasonably accurate in the sub-refractive region beyond the 90% point, from the median to the whole super-refractive part of the distribution, the negative gradients are under-estimated by ERA-I data.

We note however, that excellent agreement was seen between the ERA-I annual gradient distribution for the 65 metre surface layer, and detailed tower measurements from 2008 to 2012 at another location in the Czech Republic, Poděbrady, east (not west) of Prague, at latitude 50.13, longitude 15.13 degrees (Grabner *et al.* 2014, Fig. 19). This is only 117 km from Kopisty, but the NWP surface gradient modelling appears to be much more successful in the very flat region of Poděbrady than the more undulating country around Kopisty.

In the study (*Australia: ITU-R doc. 3J/169*, 2018) of data collected at Hilda Well in Western Australia in 2016, super-refractive gradients were only slightly under-predicted by ERA-I in the mild month of September, and were reasonably accurate in August and October, but were significantly under-predicted in April to July. The gradients in the below 19 metres are generally more severe than higher up. Severe sub-refractive gradients were under-predicted by ERA-I reanalysis in all seven and a half months that measurements were taken.

The measured monthly gradient distribution for the month of April is compared with the ERA-I 65 m April distribution in Figure 3.13. This study resulted in the warning text "Note that particularly in coastal and maritime locations, or at latitudes between approximately 40° N and 40° S, severe refractivity gradients in the surface layer may

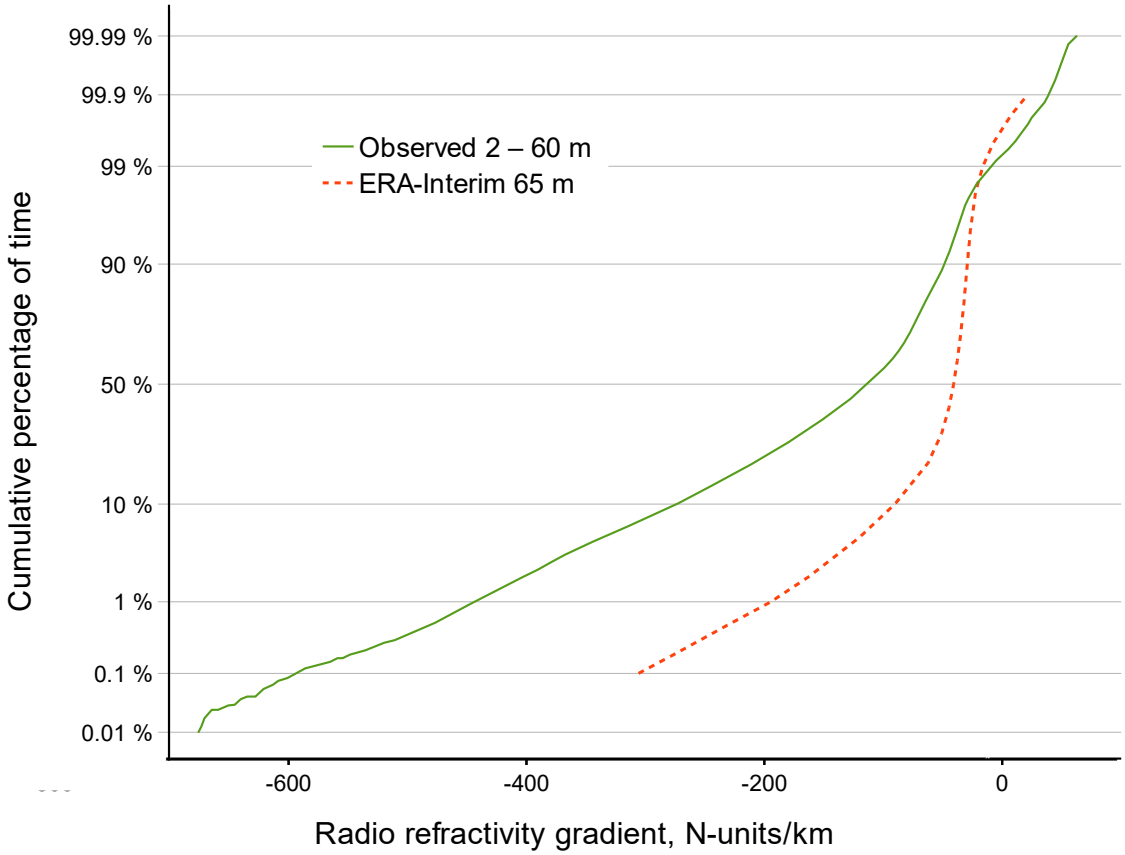

Figure 3.12. Refractivity gradients at Kopisty compared with ERA-I. Agreement between the 2004 observations and ERA-I is reasonable for the sub-refractive part of the distribution beyond the 90% point. Super-refractive gradients, however, are under-estimated by ERA-I NWP reanalysis data.

be underestimated by these digital maps," referring to the ERA-I reanalysis 65 m data, being added to *Rec. ITU-R P453-14,* (2019).

The gradient non-linearity demonstrated by Figures 3.8 and 3.9 may not necessarily be replicated by NWP models, as shown in the example of Figure 3.14.

3.5.2 Radiosondes with 6 hourly data and fixed masts

As a test of the ERA-I NWP digital maps of radio refractivity gradient in the lowest 65 m of the atmosphere (Grabner *et al.* 2014, *Rec. ITU-R P453-14,* 2019), we use data from the NOAA/ESRL Radiosonde Database, now at *NOAA IGRA Radiosonde Database,* (2022), for sixteen radiosonde stations, including only periods of time where regular

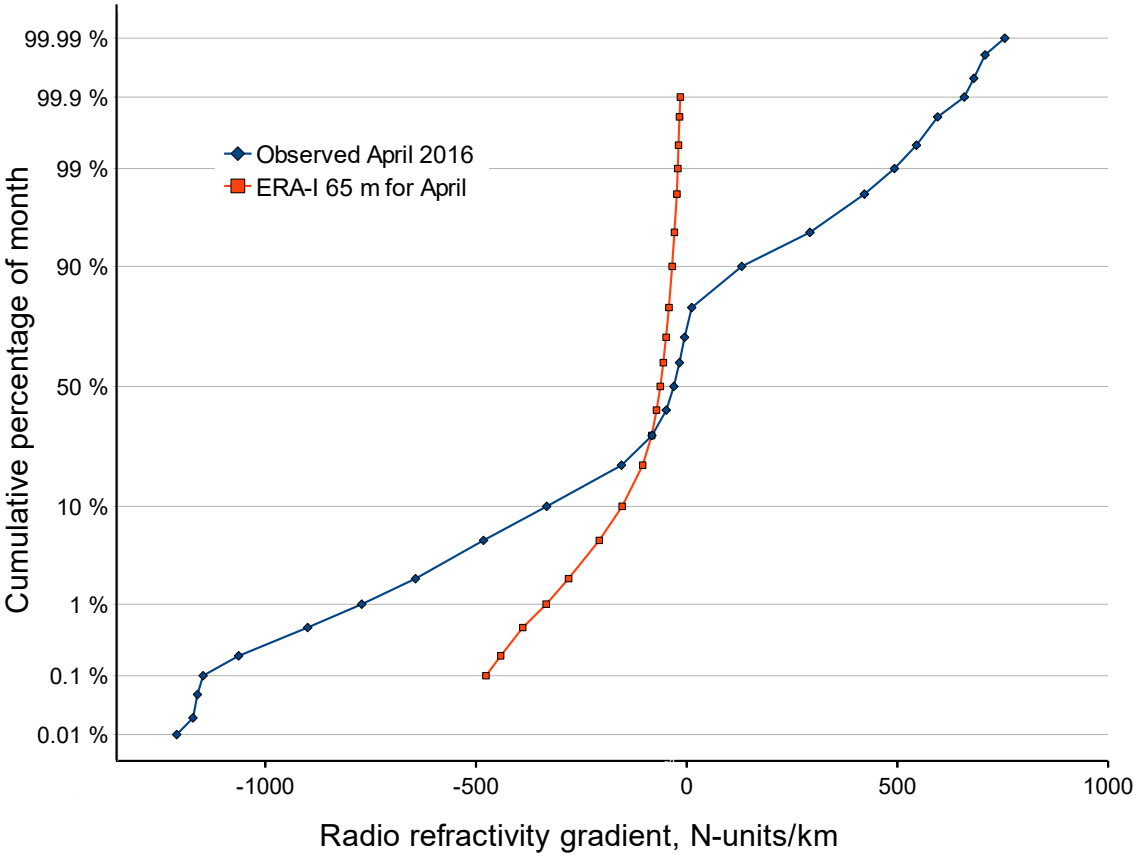

Figure 3.13. April 2016 surface refractivity gradient distribution at Hilda Well. Measured 1.5 to 60 m gradient (blue curve) compared with ERA-I reanalysis 0 to 65 m gradient distribution for April (red).

6-hourly ascents have occurred, listed in Table 3.1. To this dataset we add data from three locations where fixed sensors were installed on guyed masts.

Another radiosonde station with long-term 6-hourly ascents was identified, World Meteorological Organisation (WMO) station number 11520, Libuš, Prague, with 6-hourly ascents from 1994 to 2012, but the median first height in the NOAA/ESRL Database for those years is 337 metres. This is well in excess of our interpolation height of 65 metres, and exceeding median first height in our 65 metre surface layer testing, comparing high and low height resolution data for the same ascents, in Figures 3.3 and 3.4. As there are already two mast measurement locations in the Czech Republic in Table 3.1, the Prague Libuš radiosonde is not included.

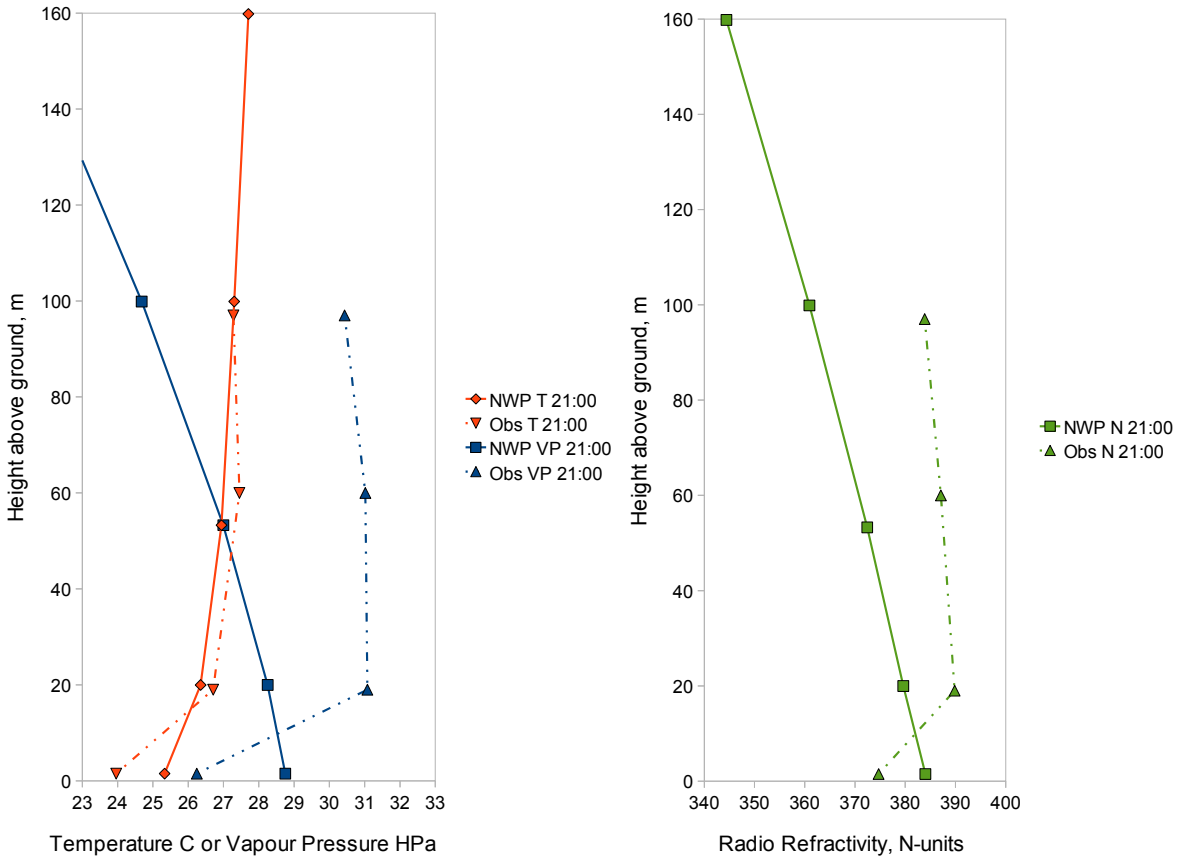

Figure 3.14. Tower measured refractivity profiles compared with ACCESS-R NWP. The NWP profiles (solid lines) are the forecast at 21:00 UTC 3 April 2016, from assimilation at 12:00 UTC, and measured data from the Hilda well radio mast are indicated by dotted lines, after *Australia: ITU-R doc. 3J/169,* (2018, Figure 12).

The Hilda Well measurements in the north-west of Australia are only for 227 days, not a full year. This risks an over-estimate, relative to a full year distribution, of the percentage of time for severe gradients that were observed, by a factor of up to 366/227, or an under-estimate of severe gradients that were not observed, but the Hilda Well measurements are included in this testing, in order to provide at least one test station in the tropics.

While there are a number of regular radiosonde stations in the tropics providing long-term data, many of them with 12 hourly ascents, we have found none with regular 6 hourly ascents.

Table 3.1. Sixteen radiosonde stations with 6-hourly data, and three mast measurement locations, for NWP gradient testing. Radiosondes with median first height z_1 in the 6 hourly data, of less than 170 metres have been included, for reasonable accuracy in estimating the refractivity gradient in the first 65 metres. The fixed mast measurements at Kopisty and Hilda well are for the gradients to 60 metres.

WMO number	Radiosonde or mast location	included years	data days	latitude	longitude	median z_1
3882	Herstomonceux West, UK	1995–2016	1715	+50.90	+0.32	15
3808	Camborne, UK	1998–2002	1648	+50.22	-5.32	17
3496	Hemsby, UK	1994–2001	1768	+52.68	+1.68	17
8507	Graciosa, Azores, Portugal	2009–2011	505	+39.10	–28.03	42
16560	Cagliari, Italy	1995–2010	3434	+39.25	+9.05	50
16044	Udine, Italy	1995–2015	3581	+46.03	+13.18	52
3953	Valentia, Ireland	1999–2020	4672	+51.93	–10.25	58
16080	Linate, Milano, Italy	1995–2010	3362	+45.43	+9.28	59
10393	Lin, Germany	1994–2020	9605	+52.22	+14.12	68
16320	Casale, Brindisi, Italy	1996–2004	2864	+40.65	+17.95	75
10238	Bergen, Niedersachen, Germany	2006–2019	4768	+52.82	+9.93	76
6260	De Bilt, Netherlands	1994–2002	2990	+52.10	+5.18	84
47122	Osan, Korea	1994–2019	9274	+37.10	+127.03	102
74646	Lamont, Oklahoma, US	1997–2020	6608	+36.68	–97.47	131
10771	Kuemmersbruck, Germany	1995–2020	8176	+49.43	+11.90	157
10618	Idar Oberstein, Germany	1995–2020	8086	+49.70	+7.333	166
fixed {	Kopisty, Czech Republic	2004	365	+50.54	+13.62	–
mast {	Poděbrady, Czech Republic	2008–2012	1826	+50.14	+15.14	–
data {	Hilda Well, Western Australia	2016	227	–21.12	+115.97	–

Test results for these 19 locations

The long-term 65 metre surface refractivity gradient distributions for the stations in Table 3.1 are compared with the NWP gradient distributions obtained by bilinear interpolation for the station coordinates, of the ECMWF Reanalysis Interim (ERA-I) data provided in *Rec. ITU-R P453-14,* (2019). Results for the super-refractive 0.1%, 1% and 10% points of the distribution are shown in Tables 3.2 and 3.3, and for the sub-refractive 99.9%, 99% and 90% points of the distribution in Tables 3.4 and 3.5.

The observations in these tables have been corrected for bias due to the effect of measurement varions on the observed gradient distributions, using (3.10).

There is a general tendency of the NWP reanalysis to under-estimate the magnitude of the extreme gradients seen in the radiosonde and mast observations. This cannot be attributed to observational error, as this trend was not only seen at most of these 19 locations; it was seen at around a hundred other radiosonde stations providing high quality 12 hourly data. In all our analysis of radiosonde data, great care was taken to exclude data from the very small number of ascents where faulty data (usually dew-point data) could contribute to error in the tails of the gradient distribution.

For some locations such as Kuemmersbruck, Germany, accuracy of the ERA-I 65 metre surface gradients is good for most of the distribution, from the super-refractive extreme of the 0.1% point, Table 3.2, to the mildly sub-refractive 90% point, but even here, the sub-refractive part of the distribution beyond the 90% point, Table 3.4, is severely under-estimated by the NWP reanalysis.

Super-refractive gradients for the 1% point of the distribution are under-estimated at 17 of the 19 locations, while sub-refractive gradients for the 99% point of the distribution are under-estimated at all 19 locations.

Perhaps the most serious indictment of the NWP reanalysis data for radio surface refractivity gradients is seen in the correlation across the 19 locations between this modelling and the observations, in Tables 3.3 and 3.5.

If r is the Pearson correlation coefficient between the observations and the NWP reanalysis at the $n = 19$ locations, for a particular percentage point, the statistical significance of the correlation may be estimated by assuming that for the null hypothesis of no correlation between the two, that t, given by

$$t = r\sqrt{\frac{n-2}{1-r^2}}\,, \tag{3.11}$$

follows Student's t-distribution with $n-2$ degrees of freedom. This is the same t-value associated with the regression slope for simple linear regression.

We find that correlation between the observations and the NWP reanalysis is only statistically significant at the most super-refractive 0.1% and 1% points of the distribution. Correlation is not significant at the 10% point, in Table 3.3, and not significant at any of the sub-refractive points in Table 3.5. A scatter plot of the 0.1% level data from Table 3.2 and the 99.9% level data from Table 3.4 is provided in Figure 3.15.

Table 3.2. Radiosonde and fixed mast stations observed super-refractive gradients, compared with NWP reanalysis. The NWP gradient distributions are by bilinear interpolation of the ECMWF Reanalysis Interim data provided in *Rec. ITU-R P453-14,* (2019).

Radiosonde or mast location	0.1% OBS,NWP		1% OBS,NWP		10% OBS,NWP	
Herstomonceux West UK, 1995-2016	–306.9	–265.9	–198.4	–158.3	–96.3	–66.6
Camborne, UK, 1998-2002	–269.3	–230.0	–190.3	–121.5	–127.3	–58.1
Hemsby, UK, 1994-2001	–353.4	–314.2	–222.7	–172.3	–130.9	–72.5
Graciosa, Azores, Portugal, 2009-2011	–386.8	–100.7	–278.6	–76.9	–182.7	–62.8
Cagliari, Italy, 1995-2010	–922.0	–664.8	–631.0	–384.4	–371.1	–112.4
Udine, Italy, 1995-2015	–473.8	–349.5	–297.0	–247.8	–152.9	–127.2
Valentia, Ireland, 1999-2020	–434.4	–193.2	–295.2	–92.4	–197.6	–54.3
Linate, Milano, Italy, 1995-2010	–430.4	–296.3	–291.7	–213.3	–151.1	–118.6
Lin, Germany, 1994-2020	–364.1	–244.0	–216.5	–163.6	–114.3	–75.1
Casale, Brindisi, Italy, 1996-2004	–699.5	–805.7	–380.9	–532.1	–136.8	–190.7
Bergen, Niedersachen, Germany, 2006-19	–398.8	–233.4	–243.3	–145.4	–106.9	–68.8
De Bilt, Netherlands, 1994-2002	–407.8	–249.6	–286.2	–146.2	–171.9	–66.2
Osan, Korea, 1994-2019	–493.3	–253.4	–319.4	–181.4	–130.5	–92.1
Lamont, Oklahoma, US, 1997-2020	–515.8	–257.7	–310.2	–170.9	–160.3	–83.9
Kuemmersbruck, Germany, 1995-2020	–346.1	–291.7	–205.5	–193.6	–102.1	–92.7
Idar Oberstein, Germany, 1995-2020	–270.0	–292.4	–172.0	–193.2	–90.8	–87.0
Kopisty, Czech Republic, 2004	–590.7	–305.8	–442.1	–194.6	–272.8	–90.2
Poděbrady, Czech Republic, 2008-2012	–284.2	–287.2	–203.9	–186.2	–104.2	–88.7
Hilda Well, Western Australia, 2016	–854.5	–506.5	–546.3	–327.8	–254.3	–153.3

Table 3.3. Error statistics of NWP reanalysis surface super-refractive gradients, at radiosonde and fixed mast station locations. The ERA-I gradients for the 0.1% and 1% points of the distribution are significantly correlated with observations, but not the 10% points. However, super-refraction is generally under-predicted.

Statistical parameter	0.1% of the time	1% of the time	10% of the time
mean NWP error	+140.0 Nu/km	+96.0 Nu/km	+68.1 Nu/km
NWP error standard dev.	124.7 Nu/km	101.8 Nu/km	71.8 Nu/km
Correlation coefficient r	+0.754	+0.615	+0.234
t-statistic of r	+4.734	+3.216	+0.990
Prob($\|t\|$ exceeded if null)	0.00019	0.0051	0.3359
Statistical signficance of correlation coefficient	Significant positive correlation	Significant positive correlation	Correlation not significant

Table 3.4. Radiosonde and fixed mast stations observed sub-refractive gradients, compared with NWP reanalysis. The NWP gradient distributions are by bilinear interpolation of the ECMWF Reanalysis Interim data provided in *Rec. ITU-R P453-14,* (2019).

Radiosonde or mast location	99.9% OBS,NWP		99% OBS,NWP		90% OBS,NWP	
Herstomonceux West UK, 1995-2016	+151.4	+23.9	+85.1	−14.0	+19.6	−31.3
Camborne, UK, 1998-2002	+78.3	−10.7	+5.5	−23.3	−36.8	−33.9
Hemsby, UK, 1994-2001	+122.8	+3.8	+20.0	−19.8	−32.4	−33.7
Graciosa, Azores, Portugal, 2009-2011	+372.5	−22.2	+161.8	−32.3	+13.2	−39.7
Cagliari, Italy, 1995-2010	+431.4	+5.5	+91.9	−16.9	−35.9	−38.6
Udine, Italy, 1995-2015	+182.9	+43.5	+64.0	−2.4	−15.3	−30.3
Valentia, Ireland, 1999-2020	+22.1	−15.3	−19.4	−24.4	−38.9	−34.0
Linate, Milano, Italy, 1995-2010	+146.8	+39.4	+44.0	−12.5	−20.1	−33.5
Lin, Germany, 1994-2020	+58.2	+1.2	+5.6	−22.5	−29.5	−30.4
Casale, Brindisi, Italy, 1996-2004	+404.3	−13.8	+208.1	−31.0	+27.3	−42.5
Bergen, Niedersachen, Germany, 2006-19	+179.2	+9.6	+62.6	−21.3	−22.9	−30.5
De Bilt, Netherlands, 1994-2002	+111.4	+23.3	+5.5	−15.1	−41.9	−32.3
Osan, Korea, 1994-2019	+194.4	+27.1	+72.5	−16.0	−3.1	−28.0
Lamont, Oklahoma, US, 1997-2020	+288.1	+15.2	+67.9	−14.7	−25.9	−26.5
Kuemmersbruck, Germany, 1995-2020	+133.7	+35.5	+46.5	−12.3	−22.7	−28.1
Idar Oberstein, Germany, 1995-2020	+132.2	+25.9	+51.8	−16.6	−23.0	−29.8
Kopisty, Czech Republic, 2004	+31.4	+21.3	−15.2	−16.3	−51.9	−29.3
Poděbrady, Czech Republic, 2008-2012	+10.9	+17.2	−17.5	−18.6	−30.7	−29.5
Hilda Well, Western Australia, 2016	+551.1	−15.6	+343.3	−21.1	+17.5	−35.0

Table 3.5. Error statistics of NWP reanalysis surface sub-refractive gradients, at radiosonde and fixed mast station locations. The ERA-I gradients for the 99.9%, 99%, and 90% points of the distribution are not significantly correlated with observations across the 19 locations, and gradients are under-predicted at most locations.

Statistical parameter	99.9% of the time	99% of the time	90% of the time
mean NWP error	−178.3 Nu/km	−86.1 Nu/km	−13.8 Nu/km
NWP error standard dev.	160.4 Nu/km	91.2 Nu/km	25.0 Nu/km
Correlation coefficient r	−0.387	−0.297	−0.420
t-statistic of r	−1.730	−1.283	−1.911
Prob($\|t\|$ exceeded if null)	0.1018	0.2165	0.0731
Statistical signficance of correlation coefficient	Correlation not significant	Correlation not significant	Correlation not significant

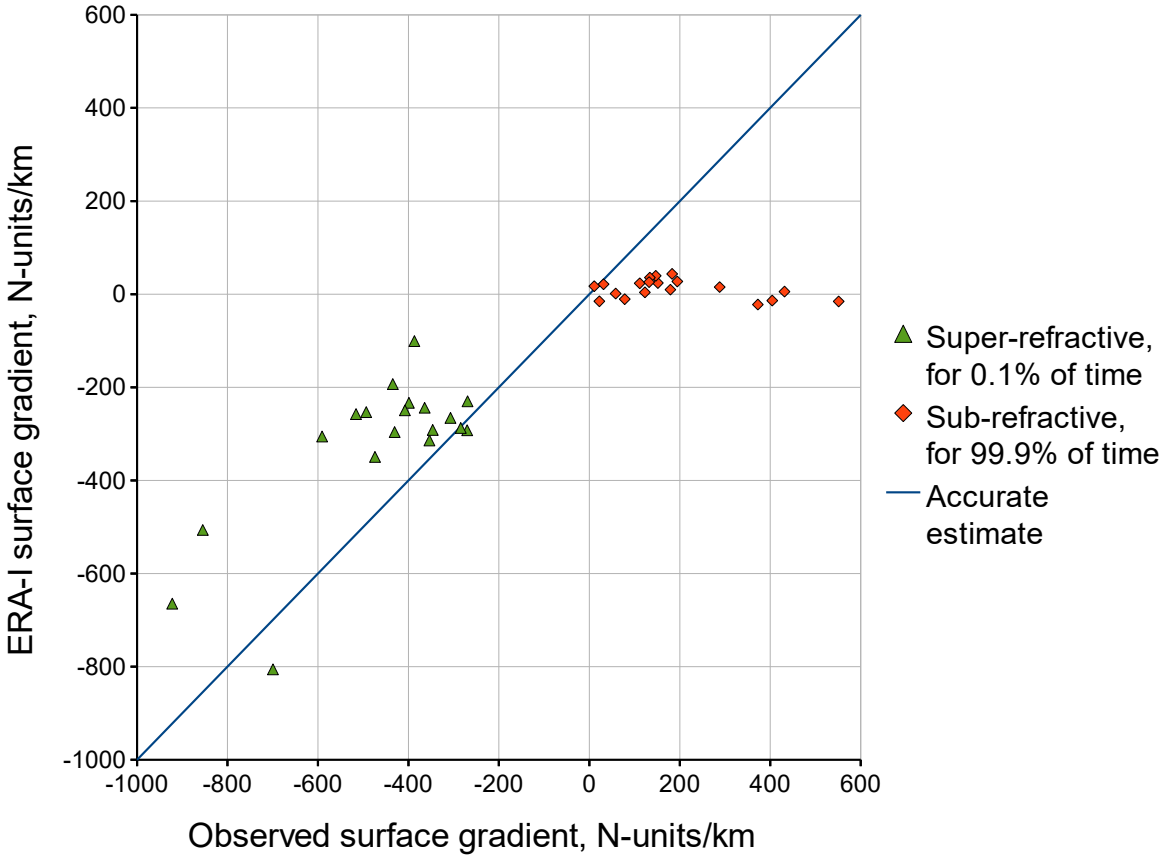

Figure 3.15. Scatter plot of ERA-I gradients compared with observations. Super-refractive gradients for 0.1% of the time (green triangles) and sub-refractive gradients gradients for 99.9% of the time (red diamonds), for the 19 locations in Table 3.1, and the data of Tables 3.2 and 3.4, for the 65 metre surface layer. Although the majority of super-refractive gradients at the 0.1% level are under-predicted, the correlation between the ERA-I NWP reanalysis data and the observations is reasonably good; however the ERA-I NWP reanalysis prediction of sub-refractive gradients at the 99.9% level appears to be poor. Points that lie close to the diagonal dark blue line are accurate estimates.

3.5.3 Conclusions from NWP reanalysis testing

While numerical weather prediction models such as ECMWF have been very successful in the field of weather forecasting, this testing casts doubt on the use of current NWP data in modelling radio refractivity gradients in the surface layer of the atmosphere, especially at the sub-refractive end of the distribution.

At low or mid latitudes, the dominant contributor to radio refractivity surface gradient is often the gradient of water vapour pressure. We note that although surface moisture is assimilated (Dee *et al.* 2011), moisture gradients near the surface are not. Perhaps it is unfair to expect a parameter that is not assimilated to be accurately modelled.

Since the testing described here was completed, reanalysis data from ECMWF that is more detailed than ERA-I, known as ERA5, has become available, which provides greater spatial and temporal resolution than ERA-I (Hersbach *et al.* 2020). If the failure of ERA-I to model sub-refractive surface gradients adequately is due to the lack of suitable surface gradient data for assimilation, as we suspect, then the greater resolution of ERA5 may provide little improvement in modelling sub-refractive surface gradients, though it would be worthwhile to test this as part of future work.

We therefore proceed to investigate empirical modelling of radio refractivity surface gradient distributions.

3.6 Empirical modelling of surface gradients

The numerical weather prediction models discussed in Section 3.3 are physical models, where the refractivity data are the results of solving a reasonable approximation to the atmospheric physics that is understood to govern the way the atmosphere behaves. When physical models are found to be to be impractical, empirical or semi-empirical models may be employed.

Empirical models are developed by finding measurable parameters that are correlated with the parameter to be modelled, in the case of linear regression models, or alternatively a non-linear approach might be employed, such as deep learning.

If the choice of parameters for the prediction is informed by a knowledge of the atmospheric physics involved, then a linear regression model may be used to predict the magnitude of the response. This may be regarded as a semi-empirical model.

3.6.1 Surface weather station data for empirical modelling

Surface weather station data for this research is obtained from the NOAA FTP site(*NOAA Global Hourly Data*, 2022), for the eight years 2010 to 2017 (Salamon *et al.* 2020). In regions with a relatively dense population of stations having temperature, humidity, and air pressure data, we included those with 7.5 or more measurements per day in every month for at least 5 full years; there were 2778 stations in those regions. Elsewhere, we included stations with at least 3 full years of data, and 5 or more measurements per day; this provided a further 2781 stations. There remained extensive regions in three continents with no data, due to an absence of air pressure data, so a further 67 stations with only temperature and humidity data were included. For these stations a nominal sea-level pressure of 1000 hPa is assumed. All station pressures were estimated from sea-level pressures by assuming a lapse rate of -0.12 hPa per m.

Overall, 5626 surface weather stations are included in generating the digital maps used in this study, as depicted in Figure 3.16.

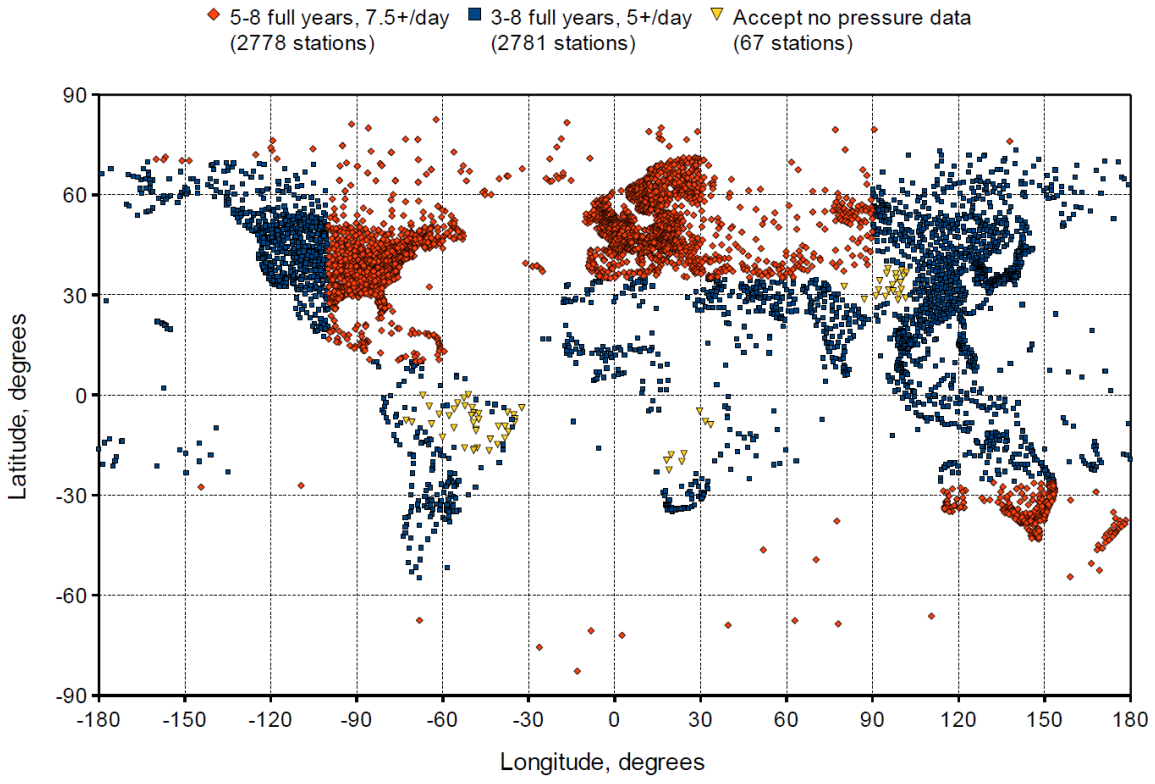

Figure 3.16. Surface weather stations, 5626 worldwide. Stations are indicated in regions with many stations by red diamonds, or less stations by blue squares, and 67 stations with no pressure data (yellow triangles) are included where necessary, after Salamon *et al.* (2020, Figure 1)

3.6.2 Surface dew point and Harvey sub-refractive model

As detailed above, we analyse surface weather station data for the eight years 2010 to 2020. For each night, we define the overnight dewpoint rise as the maximum dewpoint between 6 am or after local time the next morning, minus the minimum dewpoint before or up to midnight local time the previous evening, with local time defined as hours UTC + longitude / 15. The maximum overnight dewpoint rise for the year, ΔT_{DP}, is converted to an estimate of worst sub-refractive event refractivity increase (N-units) over the lowest 75 metres of the atmosphere for the year $\mathrm{dN}_{75\mathrm{y}}$, by the empirical expression (Harvey 1987)

$$\mathrm{dN}_{75\mathrm{y}} = 0.9\Delta T_{\mathrm{DP}} - 4\ . \tag{3.12}$$

We take the mean of the eight annual $\mathrm{dN}_{75\mathrm{y}}$ values, substituting $\mathrm{dN}_{75\mathrm{y}} = 0$ for years with $\mathrm{dN}_{75\mathrm{y}} < 0$, as the estimate of the Harvey sub-refractive parameter dN_{75}.

A world-wide map of dN_{75} is shown in Figure 3.17. This parameter suggests that sub-refraction appears to be a wide-spread problem in much of Australia, and North Africa to the Middle East and west India. It appears to be particularly severe in the Arabian Gulf region. Southern United States appears to be another reasonably severe region. This map shows more severe sub-refraction in the Arabian Gulf, and less severe sub-refraction in Australia and South America, than a previously published version (Salamon *et al.* 2020) due to revised time of day calculations.

We note that unlike the weak negative correlation between observed sub-refractive surface gradients for 99.9% of the time and NWP reanalysis in Table 3.5, the observed sub-refractive surface gradients for 99.9% of the time for those same 19 locations, taken from the digital map of Figure 3.17, are significantly positively correlated with dN_{75}, with correlation coefficient $r = 0.746$.

The t-statistic of this r is +4.618, and for the null hypothesis, Pr($|t|$>4.618) = 0.00025; in other words there is a very significant positive correlation.

In the median case of those 19 locations, the gradient $dN_{75}/0.075$ N-units per km corresponds to the 0.167% point of the observed annual 65 m surface gradient. The ITU-R general model for converting a small annual percentage $p(\%)$ to a worst-month percentage $p_w(\%)$ (*Rec. ITU-R P.841-6*, 2019) is

$$p_w = 2.85p^{0.87}. \tag{3.13}$$

Using (3.13), we conclude that the Harvey model positive refractivity gradient corresponds to approximately the 0.6% point of the worst-month distribution.

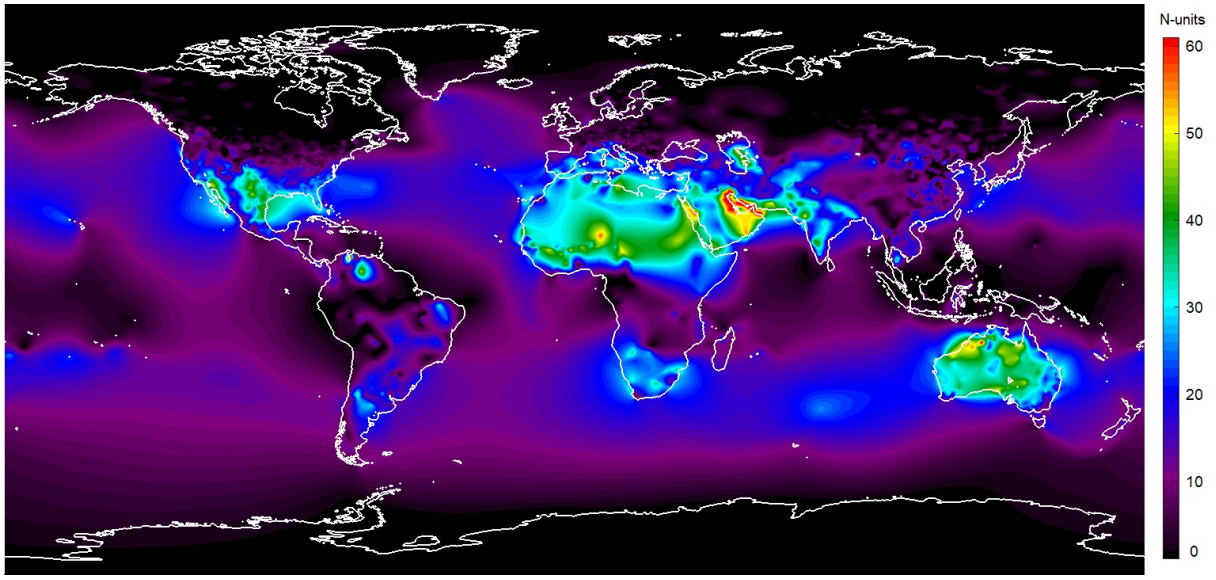

Figure 3.17. Worldwide map of the Harvey model for refractivity increase in the lowest 75 m of the atmosphere, dN_{75}. This is an empirical model, from overnight surface dewpoint increase, assuming advection of moist air over a dry nocturnal surface duct to be the dominant mechanism. The map is produced by spatial interpolation, as described in Appendix A, using data from the weather stations of Figure 3.16.

Alternatively, for radio link design purposes, we may wish to estimate the 65 m surface layer gradient not exceeded for 99.9% of the worst month, $G_{65}(99.9\%\mathrm{wm})$. From (3.13) we estimate that 99.9% of the worst month corresponds to 0.021% of the year, and the following model is a logarithmic linear regression fit to the observed $G_{65}(0.021\%)$ from the stations in Table 3.1:

$$G_{65}(99.9\%\mathrm{wm}) = 48.4\ \mathrm{dN}_{75}{}^{0.71} \quad \text{N-units per km.} \tag{3.14}$$

For this fit we have correlation coefficient $r = 0.66$, giving a t-statistic of 3.622, or a significance of $\Pr(|t|>3.622) = 0.00211$.

3.6.3 Surface refractivity anomaly and gradient distribution

An empirical model was developed (Salamon *et al.* 2014a), to predict the surface gradient distribution from the distribution of a variable N_{sA}, referred to as *surface refractivity anomaly*, which is the difference between surface refractivity N_s and its median value for that season of the year and hour of the day. A simpler model based on this work is obtained by taking only the 0.01% and 99.99% tail-points of the N_{sA} distribution, $N_{sA0.01}$ and $N_{sA99.99}$, to predict the 0.01% and 99.99% tail-points of the 0-80m surface gradient distribution, $G_{80}(0.01\%)$ and $G_{80}(99.99\%)$ (Salamon *et al.* 2014b).

Linear regression analysis of data from 60 radiosonde stations provides the following models, firstly for the super-refractive tail-point, in units of N-units per km,

$$G_{80}(0.01\%) = 216 - 7.86\,(N_{sA99.99} - N_{sA0.01})\,. \tag{3.15}$$

and the sub-refractive tail-point, in the same units,

$$G_{80}(99.99\%) = -25 + 9.8\,\max\,(-N_{sA0.01}, 0.75N_{sA99.99})\,. \tag{3.16}$$

A complete distribution is then interpolated from these two extremes, by considering the distribution in terms of an inverse cumulative normal probability variable X_p given in (3.8). Denoting the values of X_p corresponding to the 0.01% and 99.99% tail points as $X_{0.01}$ and $X_{99.99}$, the complete cumulative distribution of refractivity gradient can be estimated by interpolation, using a modified sinh function (Salamon *et al.* 2014b):

$$\begin{aligned} G_{80}(X_p) = {} & (G_{80}(99.99\%) + 1.7C)\exp\left[A\,(X_p - X_{99.99\%})\right] \\ & + (G_{80}(0.01\%) - 1.47C)\exp\left[B\,(X_{0.01\%} - X_p)\right] - 2C\tanh\left(\frac{X_p}{4}\right) \end{aligned} \tag{3.17}$$

$$\text{with } A = \frac{8000}{5000 + G_{80}(99.99\%)} \text{ and } B = \frac{4000 - G_{80}(0.01\%)}{8000}. \tag{3.18}$$

and C, which reduces the slope of the distribution in the region of the median, is

$$C = -G_{80}(99.99\%)A\exp\left(-AX_{99.99\%}\right) + G_{80}(0.01\%)B\exp\left(BX_{0.01\%}\right). \tag{3.19}$$

Considering this idea now in terms of the 65 metre surface layer for the locations in Table 3.1, we test regression models for the 0.1% and 99.9% points of the 65 metre surface gradient distribution, denoted respectively as $G_{65}(0.1\%)$ and $G_{65}(99.9\%)$, as a linear function of refractivity parameters at the surface. As well as the corresponding points of the surface refractivity anomaly, $N_{sA0.1}$ and $N_{sA99.9}$, we now add median radio refractivity N_{smed}, as it has significant correlation with observed gradients, and find the best ordinary least squares (OLS) regression models.

For the super-refractive tail value we have

$$G_{65}(0.1\%) = 1758.6 - 5.70N_{\text{smed}} - 10.12N_{sA99.9}. \tag{3.20}$$

The $N_{sA0.1}$ parameter is not included in (3.20) as its contribution to the accuracy of the OLS model is negligible; error standard deviation is 103.6 N-units either with it or without it. The real test is with *leave one out* cross-validation, where each observation

Table 3.6. Error statistics of an OLS model for 65 m super-refractive gradients at the 0.1% point, compared with the ERA-I NWP. The correlation between the OLS model leave-one-out cross-validated values and the observations at the 19 locations, is similar to that between the ERA-I values and the observations, but the ERA-I NWP has greater mean error.

Statistical parameter	OLS model leave-one-out test	ERA-I NWP
mean error	–6.8 Nu/km	+140.0 Nu/km
error standard deviation	131.7 Nu/km	124.7 Nu/km
Correlation coefficient r	+0.740	+0.754
t-statistic of r	+4.255	+4.734
Prob($\|t\|$ exceeded if null)	0.00069	0.00019

is compared with an OLS model fitted to the other observed values; the error standard deviation of (3.20) is then 131.7 N-units. This is degraded to 136.6 N-units if $N_{sA0.1}$ is included in the OLS model. The error statistics of the OLS model, using leave-one-out cross-validation are compared with those of the ERA-I NWP in Table 3.6. Both have similar correlation with the observations, and error standard deviation, but the NWP has a substantial positive error, resulting in under-prediction of the negative super-refractive gradients.

In the case of the sub-refractive tail, $N_{sA99.9}$ is found to be not only less significant than $N_{sA0.1}$, but the leave-one-out testing shows that $N_{sA99.9}$ is not useful as a parameter in the OLS model. The OLS model fitted to the 19 observations is

$$G_{65}(99.9\%) = -2004.6 + 6.09N_{\text{smed}} - 6.26N_{sA0.1}. \tag{3.21}$$

The error statistics of the OLS model, again with leave-one-out cross-validation are compared with those of the ERA-I NWP in Table 3.7. In this case, the OLS model appears to have much better accuracy than the ERA-I NWP, and the correlation of the OLS model with observations, $r = +0.867$, is somewhat better than that of the Harvey model, $r = +0.746$. Therefore, (3.21) would appear to be an alternative to the Harvey model, for predicting sub-refractive gradients.

However, these models (3.20) and (3.21), are fitted to data from stations that are all either inland, or at coastal locations of large land masses. While it seems logical that the super-refractive extreme $G_{65}(0.1\%)$ is correlated with unusual increases in surface refractivity indicated by $N_{sA99.9}$ as indicted by (3.20), and the sub-refractive extreme

Table 3.7. Error statistics of an OLS model for 65 m sub-refractive gradients at the 99.9% point, compared with the ERA-I NWP. The correlation between the OLS model leave-one-out cross-validated values and the observations at the 19 locations, is much better than that between the ERA-I values and the observations.

Statistical parameter	OLS model leave-one-out test	ERA-I NWP
mean error	–1.4 Nu/km	–178.3 Nu/km
error standard deviation	76.1 Nu/km	160.4 Nu/km
Correlation coefficient r	+0.867	–0.387
t-statistic of r	+6.727	–1.730
Prob($\|t\|$ exceeded if null)	0.000007	0.10175

$G_{65}(99.9\%)$ is correlated with unusual reductions in surface refractivity indicated by $N_{sA0.1}$ as indicted by (3.21), there is no reason to assume the relationship between these surface observations and the gradient near the surface, will be the same in mid-ocean locations as it is on land.

In fact, water vapour and temperature may be more uniform with height in mid ocean than over land, leading to reduced gradients for the same observations at the surface. In order to identify mid-ocean radiosonde stations to test this, we use the criteria that 12 hourly ascents are available, station elevation is 5 metres or less, and 50 kilometre radius mean terrain or sea elevation is less than 0.25 metres. We have processed long-term data from 226 radiosonde stations during this research, but only seven meet these criteria, listed in Table 3.8.

The empirical model (3.20) over-predicts relative to the 99.9% point of the observed distribution for these stations, with a mean ratio of 3.77. The Harvey model (3.12), based on advection of moist air, over-predicts slightly relative to the 99.8% point of the observed distribution, with a mean ratio of 1.11. Hence we conclude that even though the Harvey model was developed to predict over-land sub-refraction, it appears empirically to provide a reasonable world-wide model for sub-refractive gradients.

The world map of the Harvey model dN_{75} is shown in Figure 3.17. Strong sub-refraction in mid ocean regions appears to be largely supressed.

Table 3.8. Mid-ocean island radiosonde stations with 12-hourly ascents. These stations all have positive observed gradients for at least 0.5% of ascents, but varying over a wide range, so we test the ratio betwween the model predicted gradients and the observed gradients. The empirical model (3.20) over-predicts severely with a mean ratio of 3.77, while the Harvey model (3.12) over-predicts slightly relative to the 99.8% point of the observed distribution, with a mean ratio of 1.11.

WMO	Station	latitude, deg	longitude, deg	elevation, m
91376	Majuro/Marshall Island	+7.08	+171.38	3
61967	Diego Garcia	–7.3	+72.4	3
96996	Cocos Island	–12.18	+96.82	3
43369	Minicoy Island	+8.3	+73.15	2
72201	KeyWest	+24.55	–81.75	1
71600	Sable Island	+43.93	–60.02	4
59981	Xisha Island	+16.83	+112.33	5

3.7 Similarity theory and surface duct models

Knowledge of the refractive index profile at radio frequencies in the surface layer of the atmosphere is required to predict the performance of terrestrial radio systems. Although a constant gradient of refractivity with height is often assumed, both measurements and theory suggest that gradients in the lowest 20 metres of the atmosphere may often be greater than those above this level. For the special case of evaporation ducts over water in a neutral atmosphere, a logarithmic refractivity profile is normally assumed, but we propose (Salamon *et al.* 2015) a general model that includes both this case and the linear profile, as special cases, and may also be used to approximately model stable and unstable surface atmospheres. This new model may be particularly suited to predicting sub-refractive fading.

A logarithmic refractivity profile, for a neutral atmosphere, or for a stable atmosphere at heights below the Obukhov length, is a consequence of the exchange coefficient $K(z)$ increasing linearly with height (Obukhov 1971). However, in an unstable atmosphere, where the heat flux is directed upwards, the increase in $K(z)$ with height is more rapid, asymptotically proportional to $z^{4/3}$ (Obukhov 1971).

Refractivity profiles are often expressed in terms of modified refractivity $M(z)$, given in terms of M-units, by

$$M(z) = N(z) + 0.157z \,, \tag{3.22}$$

where $N(z)$ is the refractive index, as parts-per-million in excess of unity, at height z metres. The modification term $0.157z$ replaces the physical curvature of the Earth by an added refractive index gradient, to allow the convenience of *flat-Earth* analysis.

Evaporation ducts, resulting from wind over a water surface, are typically modelled (Paulus 1990) as

$$M(z) = M(0) + G_{\mathrm{M}} \left[z - (\delta + z_0) \ln \left(\frac{z + z_0}{z_0} \right) \right] , \tag{3.23}$$

where z_0 is the roughness length, usually assumed to be 0.00015 metres in evaporation duct modelling, and δ is the duct height, defined as the height where the modified gradient $M'(z) = 0$. G_{M} is the standard modified refractivity gradient, with approximate value of +0.12 M-units/m. Positive modified gradients greater than this are referred to as sub-refractive, and may result in diffraction loss on terrestrial radio paths, due to the strong curvature of ray-lines away from the Earth.

Positive modified gradients less than the standard gradient are referred to as super-refractive, as line-of-sight distances are greater than under standard conditions. Linear refractivity profiles are often assumed in the case of sub-refaction (Vigants 1981, Harvey 1987) or mild super-refraction, i.e modified refractivity gradient $M'(z)$ is assumed to be constant.

If the modified gradient becomes negative, the downward curvature of ray-lines exceeds the curvature of the Earth. This is referred to as a duct, which may result in strong terrestrial propagation over large distances.

3.7.1 A new general surface layer model

The logarithmic model of (3.23), and the linear model with constant $M'(z)$, may both be expressed as special cases of the one model, by considering that $\ln(x)$ is the limit, as p approaches zero, of $(x^p - 1)/p$. We then introduce a new parameter D_{p}, with units of height, and re-state (3.23) as the special case $p = 0$ of the general model, in the form

$$M(z) = M(0) + G_{\mathrm{M}} \left[z - D_{\mathrm{p}} \ln \left(\frac{z + z_0}{z_0} \right) \right] , \quad \text{if } p = 0, \tag{3.24}$$

and for all other values of p, we have

$$M(z) = M(0) + G_{\mathrm{M}} \left[z - D_{\mathrm{p}} \frac{\left(\frac{z+z_0}{z_0} \right)^p - 1}{p} \right] . \tag{3.25}$$

The modified refractivity gradient $M'(z)$, by differentiating (3) or (4) with respect to z, for all values of p, is

$$M'(z) = G_{\mathrm{M}} \left[1 - D_{\mathrm{p}} \frac{\left(\frac{z+z_0}{z_0} \right)^{p-1}}{z_0} \right] . \tag{3.26}$$

If $D_{\mathrm{p}} > 0$ and $p < 1$, the profile $M(z)$ represents a surface duct, and the duct height δ is determined by setting $M'(z) = 0$, giving

$$\delta = \left(\frac{D_{\mathrm{p}}}{z_0^p} \right)^{\frac{1}{1-p}} - z_0 \, , \tag{3.27}$$

or alternatively

$$D_{\mathrm{p}} = \left[(\delta + z_0)^{1-p} \right] z_0^p \, . \tag{3.28}$$

A surface sub-refractive layer may be represented by this model, by using a negative value of D_{p}. This generalises a previous suggestion (Tang *et al.* 2012), which described sub-refraction as an *anti-duct*, using negative D_{p} in (3.24).

3.7.2 Fitting the model to observations

If refractivity at the surface $M(0)$, and $M(z_1)$ at height z_1 above the surface, are both known, then D_{p} is given by

$$D_{\mathrm{p}} = \frac{z_1 - \left[M(z_1) - M(0) \right] / G_{\mathrm{M}}}{\ln \left[(z_1 + z_0) / z_0 \right]} \, , \text{for } p = 0, \tag{3.29}$$

or otherwise

$$D_{\mathrm{p}} = p \, \frac{z_1 - \left[M(z_1) - M(0) \right] / G_{\mathrm{M}}}{\left[(z_1 + z_0) / z_0 \right]^p - 1} \, . \tag{3.30}$$

Substituting D_{p} in (3.24) or (3.25) then provides a family of possible refractivity curves for the same values of $M(0)$, z_1, $M(z_1)$, and z_0, depending on the value of p.

For the $p = 0$ case of (3.24), z_0 has a specific physical meaning, as the roughness length of the surface, but this physical meaning may not necessarily hold for (3.25), and in fact z_0 becomes irrelevant in (3.25) if $p = 1$.

In practice, model variations that result from varying the value of z_0 can be fairly accurately compensated for, by adjusting the value of p. This is demonstrated in Figure 3.18 for two different ducting refractivity profiles, each produced in three ways, each having significantly different values of z_0. Despite widely different z_0 values, closely replicated profiles are achieved, by varying the value of p.

Figure 3.19 is a similar demonstration for two non-linear sub-refractive profiles, as well as the linear $p = 1$ case, which is independent of z_0.

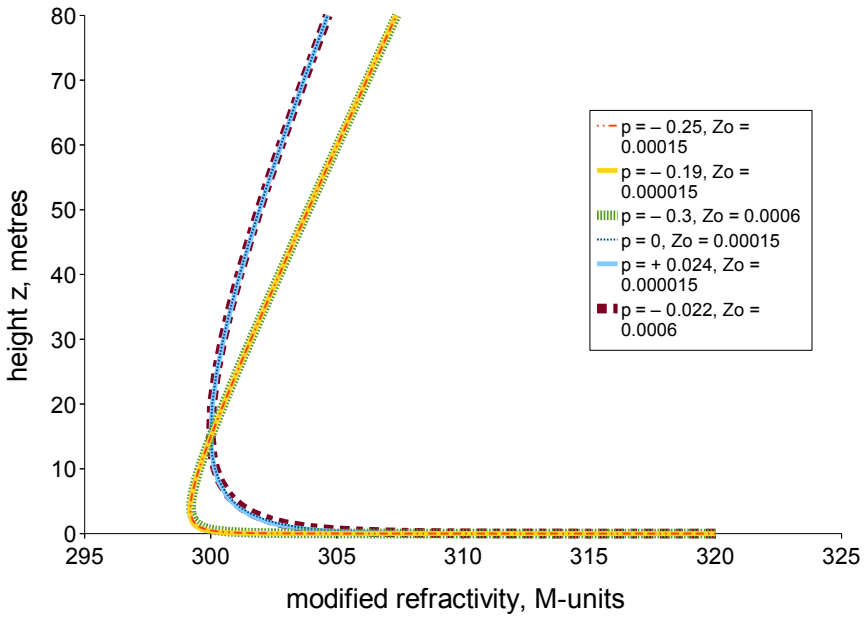

Figure 3.18. Modelling two different ducts, each with three different values of z_0. Refractivity profiles for $M(0) = 320$, $M(15) = 300$, and $G_{\mathrm{M}} = 0.12$ M-units/m, the two duct profiles being generated firstly with the usual z_0 value for evaporation ducts of 0.00015 metres, and then super-imposed profiles with smaller and larger z_0 values, produced by adjusting the value of p in (3.25), after Salamon *et al.* (2015, Fig. 1).

Thus we may, for practical purposes, choose to define z_0 to be the physical parameter roughness length, for all values of p, and then let p and D_p be the parameters that control the shape of the refractivity profile.

3.7.3 Practical significance of different p-values – super-refraction

Considering ducting propagation, different propagation characteristics would be expected due to differences in duct height. In the example of Figure 3.18, with $z_0 = 0.00015$ m, and the same mean gradient in the lowest 15 metres, duct height is 15.8 m with $p = 0$, and 3.8 m with $p = -0.25$.

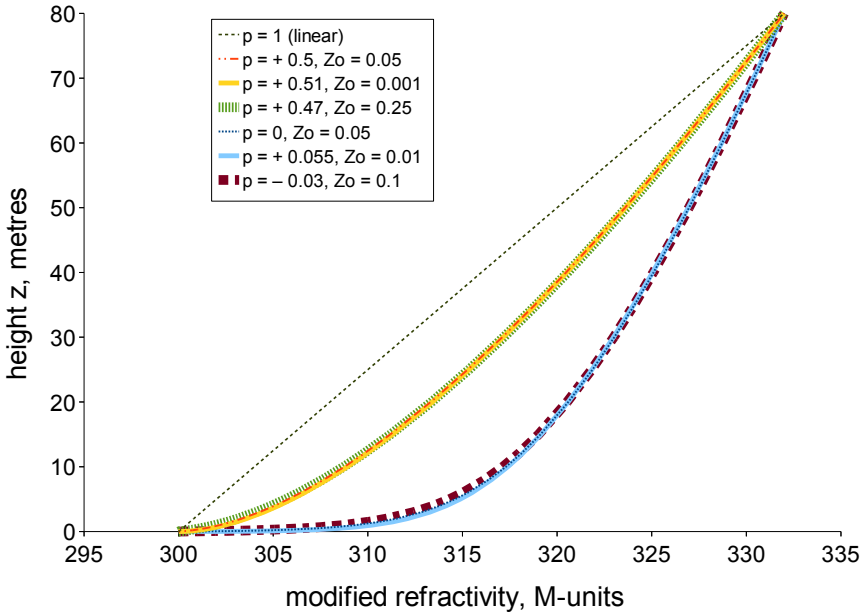

Figure 3.19. Modelling three sub-refractive profiles, using various values of z_0. Refractivity profiles for $M(0) = 300$, $M(80) = 332$, and $G_{\mathrm{M}} = 0.12$ M-units/m, for the usual linear assumption $p = 1$, and two non-linear profiles, each generated firstly with $z_0 = 0.05$ m, and then super-imposed profiles with smaller and larger z_0 values, produced by adjusting the value of p in (3.25), after Salamon *et al.* (2015, Fig. 2).

3.7.4 Practical significance of different p-values – sub-refraction

Modelling of sub-refraction conventionally assumes a linear refractivity profile (Vigants 1981, Harvey 1987), or $p = 1$ in terms of (4), but non-linear profiles, particularly in the region of $p = 0.5$, may result in greater diffraction loss than the linear case. This may be important for predicting sub-refractive fading, as this type of fading predominantly occurs in a stable atmosphere prior to sunrise (Harvey 1987). In a stable atmosphere, the refractivity profile is expected (Obukhov 1971) to be logarithmic at heights below the Obukhov length L; and essentially linear at heights exceeding L. Although something of the order of 20 metres may be considered typical, L is proportional to the cube of wind speed and inversely proportional to heat flux (Obukhov 1971), so the value of L would vary considerably. The model presented here, with $p = 0.5$, may be a useful compromise for predicting sub-refractive fading, as it seems to be close to a worst-case profile, and mid-way between the type of profiles expected above and below the varying Obukhov length.

The impact on radio propagation of different refractivity profiles, for the same mean gradient, may be studied using the parabolic equation method (Barrios 1994, Donohue and Kuttler 2000). Field-strength predictions for the three refractivity profiles of Figure 3.19, at 10 GHz, with a transmitter height of 80 m, are shown in Figures 3.20, 3.21, and 3.22, for p values of 1, 0.5, and 0, respectively. Considering diffraction loss to receivers at low heights, more than 30 km from the transmitter, the linear case $p = 1$ of Figure 3.20 suffers less loss than the logarithmic case $p = 0$ of Figure 3.22, but the greatest loss is encountered by the $p = 0.5$ case of Figure 3.21.

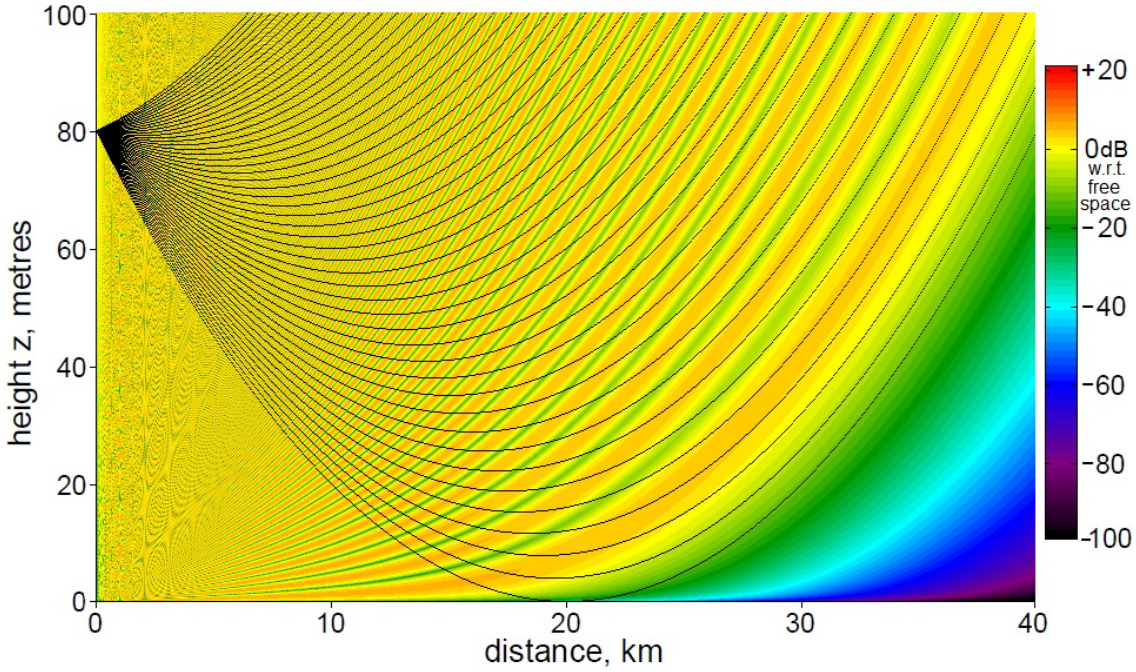

Figure 3.20. Predicted field relative to free-space, and ray tracing, for $p = 1$. Sub-refraction +400 M-units/km: $M(0) = 300$, $M(80) = 332$. Transmitter: 10 GHz at 80 m, with traced rays 0.2 milliradians apart, after Salamon *et al.* (2015, Fig. 3).

3.7.5 Summary - the new log power model

We have shown that the conventional logarithmic evaporation duct refractivity profile model, and the simple linear refractivity profile model, are both special cases of a general readily differentiable *log-power* model. It has parameters p and D_{p}, which may both be varied to produce a range of surface refractivity profiles, while maintaining the same values of the parameters of roughness length z_0 and standard modified refractivity gradient G_{M}.

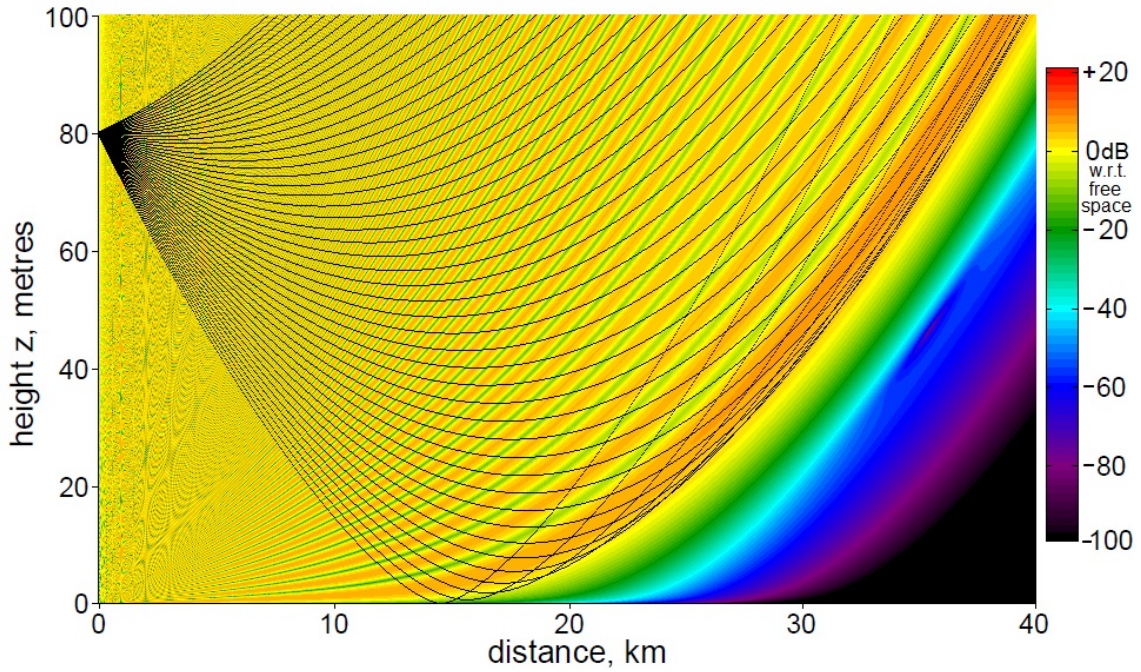

Figure 3.21. Predicted field relative to free-space, and ray tracing, for $p = 0.5$. Sub-refraction +400 M-units/km: $M(0) = 300$, $M(80) = 332$. Transmitter: 10 GHz at 80 m. $G_{\mathrm{M}} = 0.12$ M-units/m and $z_0 = 0.05$ m, after Salamon *et al.* (2015, Fig. 4).

We have demonstrated that for a given mean refractivity gradient in the surface layer of the atmosphere, varying the power parameter p may result in considerable differences in the predicted radio field-strength. Information about a shape parameter such as this may be required for accurate field strength prediction, in addition to the usual parameters of surface refractivity gradient or duct height. This model has been found to be a useful extension of the conventional neutral atmosphere model (Claverie 2019).

3.8 Conclusion

Numerical weather prediction models aim to represent the physics of the atmosphere, to allow forecasting of the future state of the atmosphere, or by assimilation of data about the current state of the atmosphere, provide an estimate of additional parameters that have not been measured, in a process known as re-analysis.

It was hoped that this would be able to provide reliable world-wide radio refractivity surface gradient data, to assist with terrestrial radio propagation modelling. While this has been moderately successful in some locations for the median to super-refractive part of the surface gradient distribution, it has been less successful in some littoral and

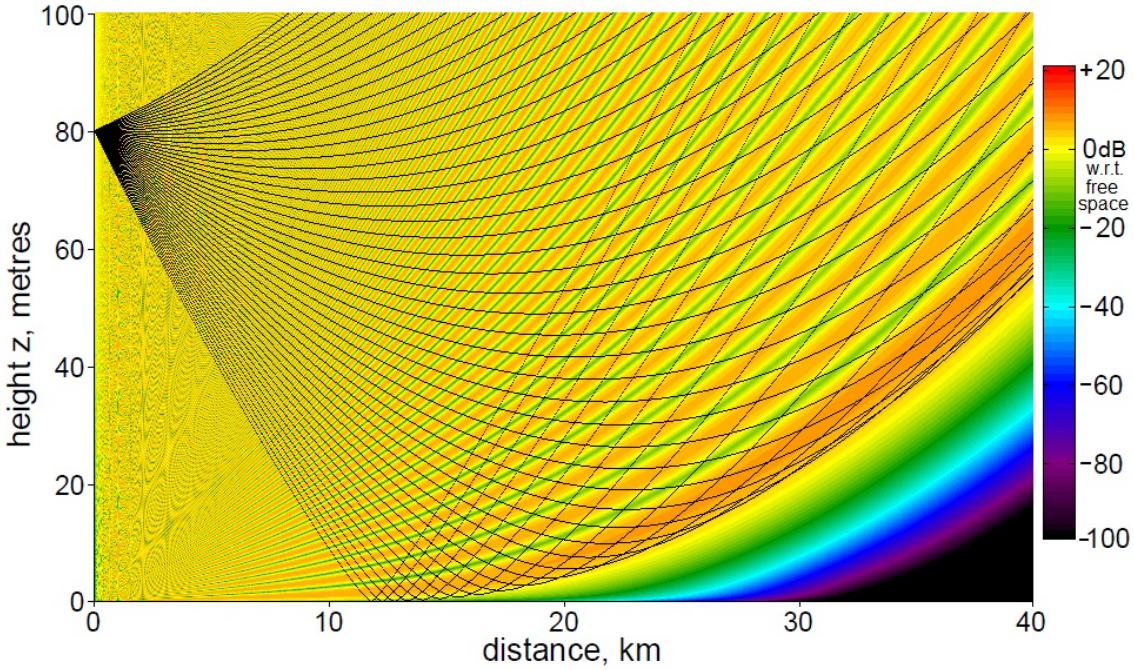

Figure 3.22. Predicted field relative to free-space, and ray tracing, for $p = 0$. Sub-refraction +400 M-units/km: $M(0) = 300$, $M(80) = 332$. Transmitter: 10 GHz at 80 m. $G_{\mathrm{M}} = 0.12$ M-units/m and $z_0 = 0.05$ m, after Salamon *et al.* (2015, Fig. 5).

maritime locations, especially at low latitudes. We have found, by comparison of NWP re-analysis data with measurements, the NWP approach to be un-successful at almost all locations, in modelling the sub-refractive extreme of the surface gradient distribution, with NWP models available until recently. However, as future work, it would be worthwhile to test if this deficiency in NWP modelling remains with the recently available ERA5 reanalysis data (Hersbach *et al.* 2020).

A central aim of this research is to predict the severe median depressions due to clear-air atmospheric effects, seen in many line-of-sight radio links. In the past this has often been attributed to sub-refraction, and while this may not be the main cause, we must conclude that NWP modelling combined with PEM analysis cannot be relied on at this stage to solve the problem. In any case, that approach would have been computationally difficult to implement in practical design work, even with recent developments in computing power.

Instead, we require a more empirical approach to the problem. The success of empirical regression models in predicting surface gradient cumulative distributions in Section 3.6, using only time series data from surface weather stations, suggests these same

surface parameters may be useful for predicting clear-air fading cumulative distributions for line-of-sight microwave radio links. Therefore we explore regression modelling of radio link fading severity in the next chapter.

Chapter 4

Regression modelling of fixed radio link multipath fading

CONVENTIONAL multipath prediction models have been based on ordinary least squares (OLS) regression, which assumes the observations are independent. However, the spatial distribution of fading observations is uneven, with many in Europe, which may be to some extent correlated, but few observations in Africa or Asia. We refine the regression modelling, taking spatial correlation into account with generalised least squares (GLS) regression. In this chapter we describe a cross-validation technique to optimise the selection of regression parameters, and find parameters generated from surface weather station data useful.

4.1 Introduction

As previously described (Salamon *et al.* 2020), significant advance in multipath fading models came with the development of ordinary least squares (OLS) regression models, using as many parameters as were found to be practically useful (Tjelta *et al.* 1998). By the time of that model, 265 records had been accumulated in the ITU-R line-of-sight link fading databank, DBSG3 Table I-2 (*Rec. ITU-R P.311-17*, 2017), "Line-of-sight average worst-month multipath fading and enhancement in narrow bandwidths," and 251 of those were found to be suitable for the regression analysis.

The following papers cited in this chapter were all produced as part of the work for this thesis: (Salamon *et al.* 2016, Salamon *et al.* 2019).

4.2 Ordinary least squares (OLS) regression models

As well as additional observed fading records, several new prediction parameters had been added since an earlier study with only 47 observed records (Tjelta *et al.* 1990). A progressive approach was now used in selecting prediction parameters; the one with most significant correlation with the observed fading selected first, and an OLS regression model generated. The next parameter chosen was that with strongest correlation with the residuals (observed minus predicted) from the previous model, and a new regression model produced. This process was continued until further improvements in the model accuracy became minimal.

4.2.1 The Recommendation ITU-R P.530-9 2001 model

Most early prediction models, such as (1.2) to (1.12), included link frequency in the form $a\log(f)$, or $f^{a/10}$ in the power-law form of (1.8). Despite the 251 databank records then available, $\log(f)$ did not appear to be a significant parameter in the regression analysis; f was statistically more significant, so based on this work, the ITU-R prediction model was amended (*Rec. ITU-R P.530-9*, 2001) to

$$\begin{aligned} A_{0.01} = {} & 32\log(d) - 9.2\log(1+|\epsilon_p|) - 4.2\log(s_a) \\ & + 0.32f - 0.03\mathrm{dN}_1 - 0.0085h_L - 39 \quad \mathrm{dB}, \end{aligned} \tag{4.1}$$

where ϵ_p is the path inclination in mr, h_L is the height above sea level of the lowest antenna, s_a is terrain elevation standard deviation (m, over a 1 degree latitude by 1 degree

longitude square), and dN_1 is the 1% point of the cumulative distribution of refractivity gradient in the 65 m surface layer. This was derived from 2 years of NWP reanalysis data from the European Centre for Medium-range Weather Forecasting (ECMWF).

Although not evident from the OLS regression analysis, there was concern that the model variation between 1 GHz and 10 GHz (3 dB) was insufficient, while the increase in model prediction between 10 GHz and 80 GHz (22 dB) appeared to be excessive. Accordingly, it was decided, and internationally agreed, to amend the frequency term (*Rec. ITU-R P.530-13*, 2009) to $8\log(f)$. Clearly there was a need for more data from links in different frequency bands in the databank, to clarify the choice of frequency coefficient in future models.

4.2.2 Development of the ISAP 2016 model

More data records were added to the DBSG3 table, 3 from Turkmenistan and 8 from Kyrgyzstan in 2007. Then a technique was developed in Australia to produce monthly fading distributions from installed radio links, by estimating the cumulative distribution in each 15 minute period from observed maximum and minimum receive levels, and number of seconds below certain thresholds (*Australia: ITU-R doc. 3M/186*, 2011); data that was being routinely captured by the network management system. This enabled average-year worst-month fading distributions to be produced for many links, without the cost of installing additional monitoring equipment. By 2016, 70 records from Australia had been produced, all in the 7.5 and 8 GHz bands. Additional information on processing this data from small and medium capacity systems to avoid the influence of selective fading is given in (*Australia: ITU-R doc. 3M/45*, 2016), and summarised in Appendix B. A new OLS model was developed, for the first time including a number of records from Australia (Salamon *et al.* 2016).

A similar process to that described above (Tjelta *et al.* 1998) was used to select variables for the OLS regression, but as well as new data records (there were now 327), we added new prediction parameters, obtained from surface weather station data. Two were composite parameters v_1 and v_2, given by

$$v_1 = \frac{N_{\mathrm{sA90-10}}^{0.3}\, d^{0.5}}{h_c^{0.25}} \text{ , and} \tag{4.2}$$

$$v_2 = \frac{\mathrm{dN_{75}}^3}{h_c^2} \text{ ,} \tag{4.3}$$

where h_c is the mean height of the rayline above the terrain (at standard refractivity gradient of -39 N-units per km, ignoring tree cover, if any). The predicted (Harvey 1987) refractivity increase in the lowest 75 m of the atmosphere (we assume for 0.6% of the worst month of the year) is dN_{75}, while $N_{sA90-10}$ and $N_{sA0.1}$ are the interdecile range and 0.1% point respectively of the distribution of surface refractivity anomaly, the difference between surface refractivity and the median value at that location for the same hour of the day and month of the year. In that study (Salamon *et al.* 2016), these parameters dN_{75}, $N_{\mathrm{sA90-10}}$, and $N_{\mathrm{sA0.1}}$, were obtained from surface weather station data for the years 2012 to 2014. The resulting OLS regression model was

$$\begin{aligned} A_{0.01} = {} & 2.04v_1 + 0.0679v_2 + 17.71\log(d) - 0.171N_{\mathrm{sA0.1}} \\ & - 9.06\log(1+|\epsilon_p|) - 0.0278\mathrm{dN}_1 + 0.0374\mathrm{dN}_{\mathrm{1ERAI}} \\ & + 7.41\log(f+6) - 0.003h_L - 19.63 \quad \mathrm{dB}, \end{aligned} \tag{4.4}$$

This OLS model had much better accuracy than the existing ITU-R model (*Rec. ITU-R P.530-17*, 2017) for the post-2007 links that were not included in fitting that model, and similar accuracy as before for the ones that were included in fitting that model. The $\log(f)$ term still appeared insignificant, but $\log(f+6)$ was found to be significant.

It was suspected that the statistical significance attributed to some of the parameters in this new model by the t-statistic may have been inflated, so we investigated taking spatial correlation into account, by using generalised least squares (GLS) regression instead of OLS regression (Salamon *et al.* 2019). This analysis confirmed that parameter $\mathrm{dN}_{\mathrm{1ERAI}}$, nominally the same parameter as dN_1 but from a more recent and much more extensive ECMWF reanalysis (Grabner *et al.* 2014), was not significant after all.

4.3 Potential impact of climate change

Direct observation of a trend in average year worst month fading is not possible because worst month fading data for individual years is not recorded in the data table. Even if it were, year-to-year variability would obscure any trend as the fading data from most links is only generated from one or two years of observations. We can however make long-term observations of weather station data parameters that we find to be significant in predicting fading severity.

The fading measurements used in this study date back to as early as 1953, with many of the measurements outside Australia occurring in the 1970's to 1990's. However, we

use parameters generated from weather station data from 2010 to 2017. This is an appropriate time period for the Australian fading data, all from 2009 to 2019, but is two or more decades later than the fading observed in other countries.

The possibility that there may have been some drift in the prediction parameters from weather stations, over time, must be considered. The 5626 stations for the years 2010 to 2017 includes many that are in regions where there was no fading data prior to 2007, so we exclude stations east of 90 degrees east longitude, or west of 140 degrees west longitude, or stations in the USA south of 42 degrees north latitude. There are no USA fading records in the data table, but a number of records are from Canada, the southernmost with a latitude of 43.12 degrees. Only stations with continuous data for the years 2010 to 2017 as well as 1990 to 1997 are included in this comparison.

These leaves 543 stations where we compare parameters $N_{\mathrm{sA0.1}}$ and dN_{75} from the years 2010 to 2017 with the same parameters from the same stations for years 1990 to 1997. For both these parameters, the number of stations having an increase or a decrease over the 20 years are reasonably similar; 55% of them have an increase in severity of $N_{sA0.1}$, while 46% of them have an increase in severity of dN_{75}.

In the case of the $N_{sA0.1}$ parameter, the mean difference is –0.147 N-units, but an unweighted mean is an OLS estimate, which ignores spatial correlation that may exist between nearby stations. This correlation may be taken into account with a GLS estimate, using the methods described in (Salamon *et al.* 2019), or in the following section, as the mean difference is a regression model with only an intercept and no other parameters. In the case of $N_{sA0.1}$, the GLS estimate of the difference over 20 years is -0.41 N-units, but this is only marginally significant, with a 95% confidence interval from –0.81 to –0.01 N-units. While a time correction for $N_{sA0.1}$ drift does not appear essential, we assume the minor correction of -0.02 N-units per year, based on the GLS difference over 20 years.

The change in dN_{75} is less significant, with an OLS mean difference of –0.014 N-units, or an insignificant GLS estimated increase of +0.052 N-units. The 95% GLS confidence interval is from –0.47 to +0.57 N-units. Hence the 2010 to 2017 dN_{75} data appears appropriate for the earlier fading data.

The above results for $N_{\mathrm{sA0.1}}$ and dN_{75}, parameters significant for predicting clear-air fading, are in marked contrast to mean temperature difference for the same surface weather stations, comparing the same time periods. The overwhelming majority (94%) of these stations have 2010 to 2017 mean temperature greater than 1990 to 1997 mean

temperature, with an OLS mean difference of +0.69 degrees. The GLS difference is +0.767 degrees, with a 95% confidence interval from +0.688 to +0.847 degrees.

4.4 Development of the new model

4.4.1 OLS and GLS

A detailed desciption of OLS and GLS estimation is given in Salamon *et al.* (2019), but briefly, OLS assumes uncorrelated errors, and the regression coefficients $\mathbf{b}_{\text{OLS}}$ are given by

$$\mathbf{b}_{\text{OLS}} = (\mathbf{X}'\,\mathbf{X})^{-1}\mathbf{X}'\mathbf{y}, \tag{4.5}$$

where $\mathbf{y}$ is the column vector of observed responses, corresponding to the rows of matrix $\mathbf{X}$, whose columns are the prediction parameters, the first column being all ones, to estimate the intercept, the first element of $\mathbf{b}_{\text{OLS}}$. The regression model estimate $\hat{\mathbf{y}} = \mathbf{X}\mathbf{b}_{\text{OLS}}$ minimises the sum of squared residuals $\mathbf{e} = \hat{\mathbf{y}} - \mathbf{y}$.

If the errors are known to be correlated, GLS estimation minimises the squared residuals of a transformed problem, the aim being to eliminate error correlation by pre-multiplying $\mathbf{X}$ and $\mathbf{y}$ by symmetrical matrix $\mathbf{P}$:

$$\begin{gathered}\mathbf{b}_{\text{GLS}} = (\mathbf{X}'\mathbf{S}^{-1}\,\mathbf{X})^{-1}\mathbf{X}'\mathbf{S}^{-1}\mathbf{y} \\ \text{where} \\ \mathbf{S}^{-1} = \mathbf{P}'\mathbf{P}.\end{gathered} \tag{4.6}$$

For simplicity, we assume an exponential spatial correlation function (Salamon *et al.* 2019) of the form

$$\phi_{ij} = (1 - k_n)\exp\left(-\frac{r_{ij}}{r_0}\right), \tag{4.7}$$

where r_{ij} is the distance between different locations i and j, and k_n is a small positive real "nugget affect" parameter representing incomplete correlation between co-located data points, to give matrix $\mathbf{S}$ as

$$\mathbf{S} = \begin{pmatrix} 1 & \phi_{12} & \phi_{13} & \dots & \phi_{1n} \\ \phi_{21} & 1 & \phi_{23} & \dots & \phi_{2n} \\ \phi_{31} & \phi_{32} & 1 & \dots & \phi_{3n} \\ \vdots & \vdots & \vdots & \ddots & \vdots \\ \phi_{n1} & \phi_{n2} & \phi_{n3} & \dots & 1 \end{pmatrix}. \tag{4.8}$$

The suitability of the GLS scheme may be judged by a correlation test on the transformed residuals $\mathbf{Pe}$. We do this with a spatial equivalent (Salamon *et al.* 2019) of the Durbin-Watson statistic d_w, the sum of squared residual forward differences divided

by the sum of squared residuals. A value of d_w close to 2 is expected for uncorrelated residuals; $d_w < 2$ for a positive correlation, or $d_w > 2$ for a negative correlation.

The Durbin-Watson statistic d_w (Durbin and Watson 1951, Durbin and Watson 1971) for a uniformly spaced one dimensional series of residuals **e** is defined as

$$d_w = \frac{\text{SSRFD}}{\text{SSR}} = \frac{\sum_{i=2}^{N}(e_i - e_{i-1})^2}{\sum_{i=1}^{N} e_i^2}, \tag{4.9}$$

where SSRFD is the sum of squares of residual forward differences, and SSR as the sum of squares of residuals. A matrix formulation is available for these, by constructing the matrix **A** as (Durbin and Watson 1951)

$$\mathbf{A} = \begin{pmatrix} 1 & -1 & 0 & \dots & 0 & 0 \\ -1 & 2 & -1 & \ddots & 0 & 0 \\ 0 & -1 & 2 & \ddots & 0 & 0 \\ \vdots & \ddots & \ddots & \ddots & \ddots & \vdots \\ 0 & 0 & 0 & \ddots & 2 & -1 \\ 0 & 0 & 0 & \dots & -1 & 1 \end{pmatrix}. \tag{4.10}$$

Using **A**, SSRFD may be evaluated as **e'Ae**, and with SSR = **e'e** we have

$$d_w = \frac{\mathbf{e'Ae}}{\mathbf{e'e}}. \tag{4.11}$$

4.4.2 The nearest new neighbour path

We generalise the concept of the sum of squares of forward differences from a one-dimensional time-line, to space of any number of dimensions, by constructing the *nearest new neighbour path* through space from data point to data point, starting with the point having the greatest sum of distances to all other data points (Salamon *et al.* 2019). Then move from point to point, each time going to the nearest neighbour not already selected, until all data points are included in the path, as demonstrated in Figure 4.1. Where more than one data point share the same location, for the calculation of d_w we take them as a single data point, having value equal to the mean of the individual values.

The parameters in (4.7) are found by producing a semivariogram $\gamma(h)$ of the OLS residuals, using the Cressie-Hawkins robust estimator (Cressie 1993) applied to distance classes numerically equal to the number of residual pairs with zero geographic distance ($h = 0$). The sill value of the semivariogram is assumed to be OLS residual

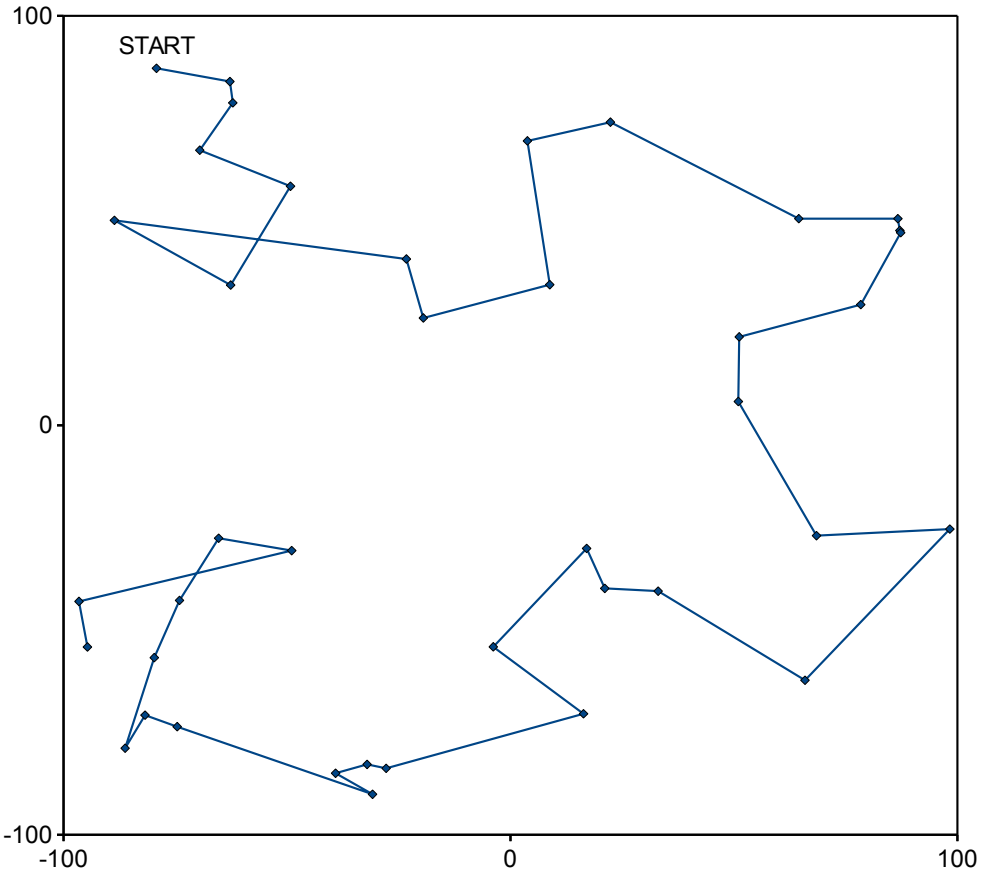

Figure 4.1. Nearest new neighbour path in two dimensions, with 40 randomly located points. The start point is the one with greatest sum of distances to all other points. At each step, the next one is the closest point not already selected. For locations with more than one data point, the nearest neighbour may be co-located, but to calculate the effective Durbin-Watson statistic d_w, they are taken as a single point, with value the mean of the individual values, after Salamon *et al.* (2019, Figure 7).

variance σ_{OLS}, and the nugget parameter k_n is set to the Cressie-Hawkins estimate of $\gamma(h = 0)$ divided by σ_{OLS}. The parameter r_0 is set to the value where equal numbers of the semivariogram estimates for distances less than 2000 km are above and below the exponential curve $\gamma(h) = \sigma_{\mathrm{OLS}}[1 - (1 - k_n)\exp(-h/r_0)]$.

While OLS estimation of the regression parameters minimises the RMS error of the model with respect to observations included in the model fitting, we explore the use of GLS regression models, the aim being to reduce the influence of spatially correlated observations. The effective spatial Durbin-Watson statistic (Salamon *et al.* 2019) of the residuals of the following OLS model, $d_w = 1.06$, indicates very significant positive

spatial correlation. The GLS model, with $k_n = 0.105$ and $r_0 = 219.5$ km, has transformed residual $d_w = 1.95$, indicating substantial elimination of the spatial correlation.

4.4.3 Cross-validation and parameter selection

In previous OLS regression models for multipath fading (Tjelta *et al.* 1998, Salamon *et al.* 2016), model parameters have been selected one at a time, as the one with the strongest correlation, initially with the observations, and then with the residuals of the previous regression model. The risk with this procedure is that an initially significant parameter may become insignificant, as more parameters are added.

Another problem is that if OLS residual RMS is taken as the criterion, without cross-validation (testing with observations not included in the model fitting), the model will appear to always improve as new parameters are added, whether they are really useful or not.

We address these problems by a form of cross-validation that may be described as *leave-one-region-out*. For each of the regions described in Table 1.1, predictions are performed with a regression model fitted to all the data from the other 20 regions. Rather than progressively adding parameters to the model, all possible binary combinations of including or not including parameters in the model are tested, and the combination producing the lowest overall leave-one-region-out RMS error is chosen.

The new parameters

The parameters are similar to those in (4.4), but using more extensive weather station data, and with some improvements, as follows.

A new regression parameter h_c is now included, the mean rayline clearance (m) above terrain (ignoring tree cover, as its height is often unknown) at standard refractivity gradient (effective Earth radius of 8500 km).

The sub-refractive parameter v_2 of (4.3) is now replaced by v_{sr}, now depending on path length d (km) as well as h_c, to avoid excessive values for low clearance very short paths in regions of high dN_{75}:

$$v_{\text{sr}} = \left(\frac{\text{dN}_{75}}{50}\right)^{1.8} \exp\left(-\frac{h_c}{2.5\sqrt{d}}\right) . \tag{4.12}$$

The previous cubic dependency with dN_{75} is now reduced to a power of 1.8, as that is found to provide better accuracy than alternative exponents.

After testing of a number of different options, we find that a new path inclination parameter $|\epsilon_p|^{0.39}$ appears to be an improvement over the conventional $\log(1+|\epsilon_p|)$.

The recent inclusion of a number of relatively low frequency 2 GHz records in the fading data, reduces uncertainty in estimating frequency dependence of the model. A new frequency parameter $\log(f^2+13)$ appears to be more significant than the previous parameters $\log(f+6)$ in (4.4), or $\log(f)$ in the current ITU-R model (*Rec. ITU-R P.530-17*, 2017).

Terrain area standard deviation S_a is used in this new model, similar to that employed in (*Rec. ITU-R P.530-17*, 2017), but with a refined method of evaluation.

The new S_a is a standard deviation from the same world-wide 30 second gridded terrain data, but over a circular area of 100 km radius, with raised cosine weighting tapering to zero at the edge of the area. In order to avoid undue weighting of polar regions due to the longitude grid converging at the poles, random sampling of the terrain data with probability $4\cos(\phi)$, where ϕ is latitude in radians, is used at latitudes with magnitude exceeding 75.522 degrees.

Parameter refinement

Four of the regression parameters are simple ones, involving no arbitrary internal coefficients, namely $\log(d)$, h_L, dN_1, and $N_{\mathrm{sA0.1}}$, and their respective regression coefficients are automatically determined by the OLS or GLS regression.

The other five do include arbitrary coefficients: $\log(f^2+13)$, $|\epsilon_p|^{0.39}$, $\tanh((h_c-147)/125)$, $v_{\mathrm{sr}} = (\mathrm{dN}_{75}/50)^{1.8}\exp[-h_c/(2.5\sqrt{d})]$, and $\tanh((S_a-48)/53)$. These eight coefficients, 13, 0.39, 147, 125, 1.8, 2.5, 48 and 53 respectively, are manually optimised by using only rounded values, optimising each in turn for the lowest overall leave-one-region-out cross-validated RMS error, repeating the process until no further improvement is obtained. The use of rounded rather than exact coefficients makes this a manageable finite procedure.

After this parameter refinement, the above parameter selection procedure, testing in turn all 512 possible combinations of the nine parameters for lowest overall leave-one-region-out cross-validated RMS error, is repeated to ensure all these parameters are still useful. This overall cross-validated RMS error is 5.849 dB for the OLS model, and slightly lower, 5.827 dB, for the GLS model.

Table 4.1. Best leave-one-region-out cross-validated OLS (RMS error 5.85 dB) and GLS (RMS error 5.83 dB) models. Both regression coefficients, and the corresponding t-statistics, indicating statistical significance, are shown. As there are many data points, the t-distribution here is close to a normal distribution with unit variance.

Parameter	OLS coefficient	OLS t-statistic	GLS coefficient	GLS t-statistic
(Intercept)	–41.28	–10.9	–39.17	–8.47
$\log(d)$	+35.56	+22.7	+35.09	+19.0
$\log(f^2 + 13)$	+5.876	+6.56	+4.473	+5.66
$\lvert\epsilon_p\rvert^{0.39}$	–4.024	–8.77	–3.340	–6.63
h_L	–0.00576	–6.03	–0.00273	–1.99
$\tanh((h_c - 147)/125)$	–3.531	–4.69	–3.764	–3.80
v_{sr}	+150.7	+5.09	+178.5	+4.82
$\tanh((S_a - 48)/53)$	–2.707	–4.58	–3.880	–3.35
dN_1	–0.01223	–4.91	–0.00972	–1.80
$N_{\text{sA0.1}}$	–0.1994	–9.98	–0.1970	–4.05

Final parameters

The final regression coefficients for the best OLS and GLS models, found by leave-one-region-out cross validation, and resulting from the parameter reinement process, are shown in Table 4.1. The best OLS model and the best GLS model, use the same nine parameters.

There are some differences in the regression model coefficients between the OLS and GLS models, and their significance indicated by the t-statistic is generally less for the GLS model than the OLS model.

The most extreme example of this coefficient difference is the elevation of the lowest antenna, h_L. It has a coefficient of -0.00576 dB per m in the OLS model, and highly significant with $t = -6.03$. In the GLS model its coefficient is -0.00273 dB per m, and much less significant with $t = -1.99$. However, we retain it in the GLS model as the leave-one-region-out cross-validation suggests that it is a useful model parameter.

The new GLS model

$$\begin{aligned} A_{0.01} = {} & -39.17 + 35.09\log(d) - 3.34|\epsilon_p|^{0.39} - 3.88\tanh((S_a - 48)/53) \\ & + 4.473\log(f^2 + 13) - 0.00972\text{dN}_1 - 0.00273h_L \\ & - 3.764\tanh((h_c - 147)/125) + 178.5v_{\text{sr}} - 0.197N_{\text{sA0.1}} \quad \text{dB}, \end{aligned} \tag{4.13}$$

has parameters $\log(d)$, h_L and dN_1 in common with the current ITU-R model (*Rec. ITU-R P.530-17*, 2017) for detailed design

$$A_{0.01} = -44 + 34\log(d) - 10.3\log(1 + |\epsilon_p|) - 4.6\log(10 + s_a) + 8\log(f) - 0.027\mathrm{dN}_1 - 0.0076h_L \quad \mathrm{dB}, \tag{4.14}$$

while (4.13) has revised forms of the frequency f, path inclination ϵ_p and terrain area standard deviation S_a parameters, as well as a new sub-refractive parameter v_{sr}, path clearance parameter $\tanh((h_c - 250)/75)$, and surface refractivity anomaly parameter $N_{\mathrm{sA0.1}}$.

4.4.4 Accuracy of the new GLS model

The prediction error statistics of the GLS model of Table 4.1 are detailed in Table 4.2, separated into the 21 regions of Table 1.1, as well as overall. The error statistics for predictions with the current ITU-R model (*Rec. ITU-R P.530-17*, 2017) are shown for comparison. The new GLS model demonstrates a significant improvement in accuracy over the ITU-R model in Central Asia, Ghana, Pakistan, and the three northern Australian regions, due to elimination of the large mean underprediction errors of the ITU-R model in these regions.

Overall, the new GLS model has less less mean error and lower error standard deviation than the current ITU-R model. In the next chapter we consider the alternative approach of treating multipath fading and sub-refractive median depression fading as separate mechanisms.

4.4.5 Application of the new model in regions of extreme sub-refraction

The Harvey parameter dN_{75} is used by the new model as an estimate of severity of sub-refraction, but the highest value of this parameter in the links contributing to the model is +53.47 N-units, at latitude 16.19 degrees south, longitude 128.4, in Western Australia, but higher values are found in some locations. In particular, at the northern end of the Arabian Gulf, at latitude 30 degrees north, longitude 48.5 degrees east, we have $\mathrm{dN}_{75} = 84.7$, significantly higher than for any of the links in the dataset.

This may be of concern, as parameter v_{sr} is proportional to $\mathrm{dN}_{75}{}^{1.8}$ in (4.12), and a limitation of empirical regression models is that they may not be valid outside the range

Table 4.2. Mean and standard deviation of prediction error by region, showing number of records, error statistics of the existing Rec. ITU-R P.530 model, and the new GLS model of Table 4.1. Significant mean under-prediction by the P.530 model in Pakistan, Ghana, Central Asia, and Northern Australia, is largely eliminated by the new GLS model, and is substantially reduced in Arctic Canada. Mild over-prediction of fading occurs with the new model in southern Western Australia, South-East Africa, and South-West Canada, compared with the existing ITU-R model, but in all these regions the new model has lower error standard deviation.

Records	P.530 mean	P.530 std dev	GLS mean	GLS std dev	Region
48	–0.96	4.94	–2.22	4.77	Western Europe
42	–0.37	5.48	–2.81	4.99	Scandinavia
20	+2.87	4.82	+0.72	3.80	Russia
3	–2.36	5.45	–1.67	4.03	Turkmenistan
13	+2.95	4.94	+1.93	5.06	South-East Canada
10	+5.75	4.93	+7.37	2.68	South-West Canada
4	–11.2	10.0	–7.42	8.94	Arctic Canada
7	+0.25	6.06	+2.03	4.70	Brazil
4	–1.38	6.27	+0.37	6.12	North-East Canada
1	–9.87	—	–4.20	—	Pakistan
7	–0.55	7.76	–3.45	8.01	Egypt
79	–0.49	6.13	–1.11	5.56	Southern Europe
3	–9.34	4.21	+0.29	3.61	Ghana
3	–1.47	5.87	–4.99	4.68	Senegal
3	+1.08	3.52	+4.35	2.94	South-East Africa
6	–6.45	8.07	–0.80	6.69	Central Asia
50	–9.83	7.27	–0.37	6.85	Cent-North Australia
91	–3.69	5.71	+0.71	4.79	South-East Australia
92	–6.02	6.52	–0.96	5.23	Southern Queensland
36	+0.72	5.42	+4.64	3.78	South-West Australia
17	–6.09	5.18	–0.88	5.20	Far North Queensland
539	–2.86	6.96	–0.26	5.59	All Regions

of observed parameters. We propose to address this by imposing an upper limit on the sub-refractive component of the regression model, $178.5 v_{\text{sr}}$, obtained by an approximate estimate of diffraction loss for the sub-refractive gradient suggested by dN_{75}.

We assume for simplicity that diffraction loss increases 10 dB per first Fresnel zone radius (Vigants 1981) of depression of the ray-path due to positive refractivity gradient at mid-path, as the refractivity gradient increases from zero N-units per km to $\text{dN}_{75}/0.02$ N-units per km (*Australia: ITU-R doc. 3M/236*, 2021), and take this as a notional upper limit on the contribution of v_{sr} to the predicted multipath fading.

This recognises that the bulk of the predicted refractivity increase in the lowest 75 m, dN_{75}, will normally be in the lowest 20 m of the atmosphere.

This simple estimate of subrefractive obstruction loss is $\text{dN}_{75}\ d^{1.5} f^{0.5}/138.516$ dB, but dividing this by the regression coefficient 178.5 for v_{sr} in (4.13), we have an upper limit $v_{\text{sr-limit}}$ for v_{sr} as

$$v_{\text{sr-limit}} = \frac{\text{dN}_{75}\ d^{1.5} f^{0.5}}{24730} \tag{4.15}$$

This upper limit only applies to very low clearance paths, typically with h_c of the order of 10 m or less, and does not come into effect for any of the paths used to generate our new model. This results in a revised expression for v_{sr} as

$$v_{\text{sr}} = \left[\left(\frac{\text{dN}_{75}}{50} \right)^{1.8} \exp\left(-\frac{h_c}{2.5\sqrt{d}} \right), v_{\text{sr-limit}} \right] . \tag{4.16}$$

4.5 Conclusion

The GLS regression model of (4.13) is fitted to more measured fading data than available for earlier models, and takes spatial correlation between observations into account in fitting the regression parameters. We have added new parameters, obtained from analysis of several years of time series data, from a few thousand surface weather stations around the world, and used an exhaustive cross-validation process to decide which parameters are significant for inclusion in the model.

One of the surface weather station parameters is a previously published sub-refractive parameter (Harvey 1987), applied on a world-wide basis for the first time in our research, so in the next chapter we investiate whether the combined fading regression model described in this chapter is appropriate, or whether there is an advantage in separate models for sub-refractive effects and multipath effects.

Chapter 5

Unified or Separate Models?

SEVERE median depression fading has in the past been modelled as sub-refraction, viewed as a separate mechanism from multipath fading. Here we compare that conventional approach with the unified GLS model of the previous chapter.

5.1 Introduction

A conventional approach to clear-air radio link fading prediction (Schiavone 1981, Harvey 1987) assumes a linear refractivity gradient diffraction loss model for sub-refractive median depressions, with a separate multipath model to represent other clear-air fading events. This approach suggests sub-refractive events and other clear-air fading events are separate mechanisms, that should be modelled separately, rather than a single unified model such as our new model (4.13). The aim of this chapter is to compare those two approaches.

The following paper cited in this chapter was produced as part of the work for this thesis: (Salamon *et al.* 2020).

5.2 Separate multipath and sub-refractive models

We simulate the conventional approach by taking the GLS model of Table 4.1 or (4.13), omitting the sub-refractive term $+178.5v_{\text{sr}}$, to estimate the non-sub-refractive multipath model for fade depth $A_{0.01\text{MP}}$ for 0.01% of the worst month of the average year.

A separate sub-refractive model for fade depth for 0.01% of the worst month is estimated from an effective sub-refractive gradient, G_{eff} (N-units/km), applied to the whole end-to-end path, not exceeded for 99.9% of the worst month. The diffraction loss not exceeded for 0.1% of the worst month, $L_{0.1\text{SR}}$ is predicted using the "method for a general terrestrial path" (*Rec. ITU-R P526-15*, 2019), with this gradient.

Rapid fluctuation of level during median depression events, explained as multipath interference between multiple components of differing phase, has been described (Shepherd 1979, Harvey 1987). Hence fading during these sub-refractive median depressions is assumed approximately Rayleigh distributed, indicating a 10 dB fade-depth difference between 0.01% and 0.1% of the worst month. This suggests a sub-refractive model for fade depth for 0.01% of the worst month of $A_{0.01\text{SR}} = L_{0.1\text{SR}} + 10$ dB. Assuming a Rayleigh fading tail slope for the multipath fading as well, and assuming the multipath fading represented by $A_{0.01\text{MP}}$ and the subrefractive fading represented by $A_{0.01\text{SR}}$ to be separate uncorrelated mechanisms, leads to the estimate of overall fade depth $A_{0.01}$ for 0.01% of the worst-month (Salamon *et al.* 2020) as

$$A_{0.01} = 10 \log \left[10^{\frac{A_{0.01\text{MP}}}{10}} + 10^{\frac{A_{0.01\text{SR}}}{10}} \right]. \tag{5.1}$$

However, (5.1) may not be valid in cases where $L_{0.1SR} = 0$ or $A_{0.01SR} = 10$ dB, as in these cases sub-refractive fading should not contribute to the overall fading.

In fact (5.1) assumes a simple fading model where the proportion of the worst month P_w when fade margin M dB is exceeded (the fade depth the radio system can tolerate before severe errors occur), is given in terms of multipath occurrence factor P_0 as

$$P_w = P_0 10^{-M/10} \text{ , with } P_0 = 10^{(A_{0.01}/10\ -\ 4)} \ . \tag{5.2}$$

However, this 10 dB per decade of probability model is for the low probability tail of the distribution, and only applies for $M \geq A_t$, where $A_t = 25 + 1.2 \log(P_0/100)$ dB (*Rec. ITU-R P.530-17*, 2017). For $M < A_t$ a set of equations are used to find P_w as a smooth continuous function of P_0 and M, such that $P_w = 0.632$ for all values of P_0 at $M = 0$. This model is known as the "Method for all percentages of time" (*Rec. ITU-R P.530-17*, 2017), and is demonstrated in Figure 5.1.

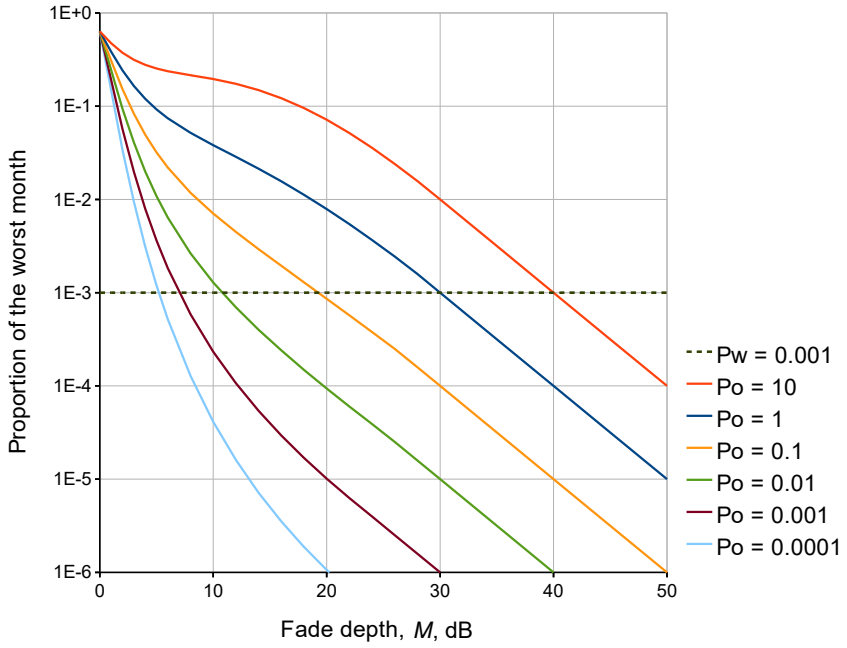

Figure 5.1. Recommendation ITU-R P.530-17 "Method for all percentages of time". This provides a smooth continuous function of P_0 and M, such that $P_w = 0.632$ for all values of P_0 at $M = 0$, while P_w is proportional to P_0 and to $10^{-M/10}$ at large M.

We wish to find a value of P_0 for fade depth $L_{0.1SR}$, the estimated sub-refractive diffraction loss for 0.1% of the worst month, such that the P_0 curve intersects the $P_w = 0.001$ line, as in Figure 5.1.

This "method for all percentages of time" is only invertible by iteration, but we find that a good approximation to A_t, the lower limit on M for (5.2) to be valid, when P_0 is iteratively adjusted for $P_w = 0.001$, is $A_t \approx 23.926 + 0.11629M - 24\exp(-M/2)$.

The resulting expresssion for sub-refractive multipath occurrence factor $P_{0\text{-SR}}$ as a function of fade depth $L_{0.1\text{SR}}$ is

$$P_{0\text{-SR}} = \begin{cases} 10^{(L_{0.1\text{SR}}-30)/10} + 0.011\exp(25.53 - L_{0.1\text{SR}}) & \text{if } L_{0.1\text{SR}} \geq 25.53\ , \\ 10^{(At-25)/1.2-2} - 0.011\exp(L_{0.1\text{SR}} - 25.53) & \text{if } L_{0.1\text{SR}} < 25.53\ , \end{cases} \tag{5.3}$$

with

$$A_t = 23.926 + 0.11629L_{0.1\text{SR}} - 24\exp(-0.5L_{0.1\text{SR}})\ . \tag{5.4}$$

The terms $+0.011\exp(25.53 - L_{0.1\text{SR}})$ and $-0.011\exp(L_{0.1\text{SR}} - 25.53)$ in (5.3) are a correction in the region of $L_{0.1\text{SR}} \approx 25.53$ to provide continuity and improved accuracy.

This gives a revised overall fading model as

$$A_{0.01} = 10\log\left[10^{\frac{A_{0.01\text{MP}}}{10}} + 10^4 \times P_{0\text{-SR}}\right]. \tag{5.5}$$

Path profiles, of terrain elevation with distance along the path, are available for 483 of the 535 data records in this research, so we compare our GLS model with the separate sub-refractive gradient approach of (5.5) for these records. For these the GLS model has a mean error of –0.05 dB, and an error standard deviation of 5.60 dB.

The parameters for the Schiavone sub-refractive model (Schiavone 1981) are not available for the fading data locations (Kizer 2008), so we test a model based on two sub-refractive models: the Harvey model (Harvey 1987) for severe gradient at a location, dN_{75}, shown in Figure 3.17, and the model of (1.13) (Boithias and Battesti 1967).

5.3 Combined Harvey-Boithias-Battesti gradient model

The effective sub-refractive gradient model (1.13), is for a "continental temperate" climate. There is no indication (Boithias and Battesti 1967) of the location of the radio links used to develop this model, but we assume a climate corresponding to $dN_{75} = 4.2$, the median of the 10 inland stations of those in Table 3.1: Udine and Linate (Milano), Italy; Lin, Bergen (Niedersachen), Kuemmersbruck, and Idar Oberstein, Germany; De Bilt, Netherlands; Lamont, Oklahoma; Kopisty and Poděbrady, Czech Republic. From

(3.14) we estimate the 65 m surface gradient not exceeded for 99.9% of the worst month in this climate is $G_{65}(99.9\%\text{wm}) = +134$ N-units/km.

While (1.13) suggests infinite effective gradient for zero path length, it is a function fitting a curve that was only plotted for path lengths around 20 km and above. Generalising this to a model for all path lengths in the "continental temperate" we suggest

$$\frac{\mathrm{d}N}{\mathrm{d}z} = \begin{cases} 134 - 58[(\frac{d}{30})^{1.5}] & \text{if } d < 30, \\ \frac{2670}{d} - 13 & \text{if } d \geq 30 \quad \text{N-units per km.} \end{cases} \tag{5.6}$$

This provides a continuous curve to $G_{65}(99.9\%\text{wm})$ from (3.14), the gradient at a single point, at $d = 0$, and is compared with the Boithias-Battesti model (1.13) in Figure 5.2.

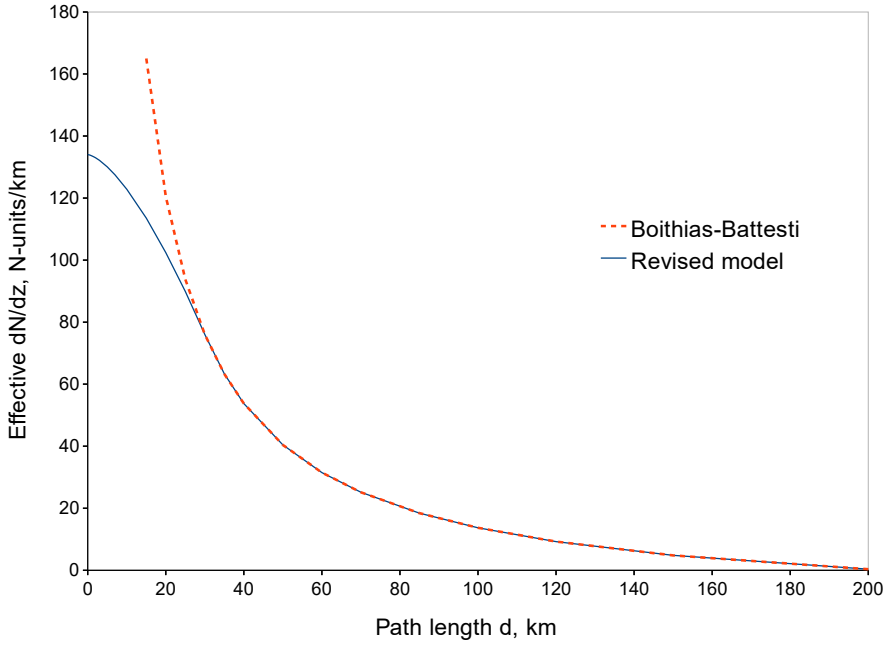

Figure 5.2. Models of effective gradient not exceeded for 99.9% of the worst month. The Boithias-Battesti model of (1.13), compared with the revised model of (5.6), providing continuous extension to the gradient at a point, at $d = 0$. Effective gradient is applied to the whole path to estimate the fading effect of varying gradients along the path.

In order to further generalise this to all climates, we scale (5.6) according to location, using the Harvey parameter dN_{75}, in proportion to $\mathrm{dN}_{75}{}^{0.71}$. This scaling is based on (3.14), leading to the 99.9% worst-month effective gradient model

$$G_{\text{eff}} = \left(\frac{\mathrm{dN}_{75}}{4.2}\right)^{0.71} \begin{cases} 134 - 58[(\frac{d}{30})^{1.5}] & \text{if } d < 30, \\ \frac{2670}{d} - 13 & \text{if } d \geq 30 \quad \text{N-units per km.} \end{cases} \tag{5.7}$$

This model, together with (5.3), (5.4) and (5.5), performs well for the 483 records where path profiles are available: mean error is +0.62 dB, with error standard deviation of 5.93 dB. This is only slightly inferior to the accuracy of the unified GLS model (4.13).

However, the results are very different considering only the 20 cases where $L_{0.1\text{SR}} > 35$ dB. For these the combined GLS model (4.13) has mean error of +0.01 dB and error standard deviation of 6.06 dB, while the separate sub-refractive plus multipath model (5.5) has mean error of +6.94 dB and error standard deviation of 8.89 dB, indicating fairly severe over-prediction of fading.

5.4 Height-gain prediction accuracy

An important issue for radio link designers is accurate prediction of fading reduction with antenna height (height-gain), for systems affected by severe fading. We now test a sub-refractive model such as (5.5), to compare its height-gain predictions with those of our unified GLS model (4.13).

There are a number of records in the fading data with simultaneous observations at two different receive antenna heights, where the data was collected from space-diversity systems. We identify those for testing where the separate sub-refractive plus multipath model (5.5) predicts greater than 2 dB difference between the two $A_{0.01}$ fade depths for the two different heights. This yields 19 pairs of measurements, all from Australia, and all have the same measurement period for the two antenna heights.

In predicting fade depth reduction with height, the GLS model (4.13) has mean error of +0.03 dB, and 2.33 dB standard deviation. The separate sub-refractive plus multipath model (5.5) has mean +2.45 dB over-prediction of height gain, with 1.39 dB standard deviation, and greater correlation between height-gain predictions and observations than the GLS model.

These results are depicted in Figure 5.3. Least-squares regression lines for each are shown, with slope of 0.28 and correlation coefficient of 0.7 for (4.13), and slope of 0.85 and correlation coefficient of 0.89 for (5.5).

The separate sub-refractive plus multipath model (5.5) appears to be the more accurate predictor of height-gain for the few cases where observed height gain is large, but it generally over-predicts height gain, especially where observed height-gain is modest.

It may be suggested that (5.5) is a better height-gain model, but only if 2.5 dB is subtracted from the prediction – don't expect improvement unless (5.5) predicts it to exceed 2.5 dB.

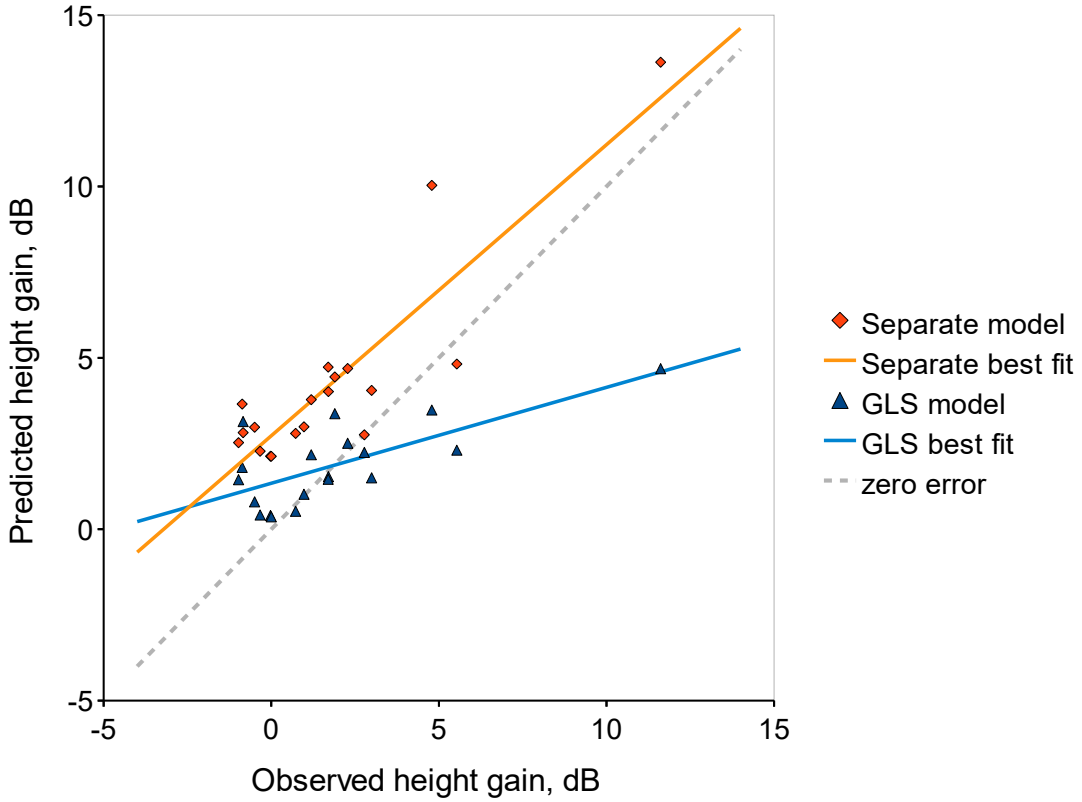

Figure 5.3. Predicted height gain, comparing unified GLS model with separate models. Predicted fading reduction, or improvement, with increased antenna height, plotted against observed improvement, for the GLS model (4.13) (blue triangles), and the separate sub-refractive plus multipath model (5.5), for the 19 pairs of observations where (5.5) predicts an improvement exceeding 2 dB. Least-squares best fit lines for each are shown, with regression slopes of 0.28 for (4.13), and 0.85 for (5.5). However, the separate sub-refractive plus multipath model (5.5) has 2.45 dB mean over-prediction of improvement, unlike the GLS model (4.13).

5.5 Clearance criteria

The conventional approach to line-of-sight radio links (*Rec. ITU-R P.530-17*, 2017) requires grazing line-of-sight clearance at the refractivity gradient given by (1.13) in a temperate climate, or an unobstructed path at this gradient in a tropical climate. An alternative proposal (Vigants 1981) is to design for a limited amount of obstruction

fading, estimated by assuming diffraction loss at a certain positive refractivity gradient. This approach may risk over-design with excessive antenna heights, considering the over-prediction of fading with (5.5) observed above, when $L_{0.1SR}$ exceeds 35 dB.

Often radio links employ diversity reception schemes (Boithias and Battesti 1967, *Rec. ITU-R P.530-17,* 2017) to improve performance, by taking advantage of multiple receivers with partially correlated fading. This breaks down if the depth of median depression fade approaches or exceeds the system fade margin. Recent amendments to diversity improvement prediction models (*Rec. ITU-R P.530-17,* 2017), now ensure that fading severity is now taken into account for all forms of diversity reception. Hence the idea of choosing antenna heights based primarily on performance estimates rather than clearance criteria, seems a valid approach with our new model. This may lead to more economical system designs in some cases.

5.6 Conclusion

An important issue for empirical models is the range of validity, which may not extend significantly beyond the parameter space of the data used to fit the model.

We find no evidence that the accuracy of the GLS model (4.13) is affected by path clearances approaching grazing line-of-sight at median refractivity gradient, despite several dB of path obstruction. We note here that the GLS model is for fading with respect to median signal level, not unobstructed free-space signal level.

However, accuracy cannot be assumed for paths beyond grazing line-of-sight at median refractivity gradient. Such paths should be avoided for fixed links due to the difficulty of predicting and ensuring long-term maintenance of median path loss, due to growth of vegetation or construction of new buildings.

A weakness of our new GLS model is that accuracy is unknown for very short paths, as no links in the data are shorter than 7.5 km. Minimum frequency in the data is 450 MHz, and minimum frequency-path length product is 33.7 GHz-km. A future revision of the model may be required if data from very short links, especially at low frequencies, becomes available. Appendix B provides advice on generating suitable data from long-term measurements on installed links.

In general, a model such as (5.5) that treats sub-refractive fading and multipath as separate mechanisms, appears to have little advantage over the unified GLS model (4.13),

and may even risk over-prediction of fading in regions of severe sub-refractive surface gradients. As a result, we return to considering the unified GLS regression model of Chapter 4, but improve on its accuracy in the next chapter, by employing the geostatistical technique of universal kriging.

Chapter 6

The Universal Kriging Model

UNIVERSAL kriging combines regression analysis of spatially correlated data with interpolation, to take advantage of nearby measurements. We demonstrate further improvement on our GLS fading model in regions well populated by measured data, by employing this technique.

6.1 Introduction

Kriging is a spatial interpolation technique that takes many forms, with simple, ordinary, and universal kriging, described in Section A.3. Universal kriging combines spatial interpolation with GLS regression, so that the estimate tends towards the GLS regression model estimate at locations distant from measured data points, while the estimate is primarily based on the measured data at locations close to measured data. Like GLS regression, kriging is based on an estimated spatial correlation function, usually obtained by semivariogram analysis.

If the nugget effect is employed in the univeral kriging semivariogram function, as in (4.7), the requirement to exactly pass through the known points is relaxed, and in their region the value surface is a best fit rather than an exact interpolation. We use the same exponential model with nugget effect, (4.7), that we use for the GLS estimation. As a semvariogram function, (A.6) then becomes

$$\gamma(r_{ij}) = \sigma^2[1 - (1 - k_n)\exp(-r_{ij}/r_0)] \text{ for } i \neq j,$$

otherwise

$$\gamma(r_{ij}) = \sigma^2. \tag{6.1}$$

At locations distant from known points the estimation becomes predominantly a GLS estimate in terms of the functions $f_1(s)$ to $f_p(s)$; see (A.8) and (A.9).

The universal kriging model described in this chapter is developed in the same way as previously published (Salamon *et al.* 2020), except for differences in the underlying GLS regression model.

The following paper cited in this chapter was produced as part of the work for this thesis: (Salamon *et al.* 2020).

6.2 Application to fading prediction

Geoclimatic factor may be defined for a multipath fading model as the part of the model that is invariant for any link with the same path centre coordinates. For the GLS model of Table 4.1, it may be defined as

$$K_G = -39.17 - 3.88\tanh((S_a - 48)/53) - 0.00972\mathrm{dN}_1 - 0.197N_{\mathrm{sA0.1}} \text{ dB}. \tag{6.2}$$

The predicted fade depth for 0.01% of the worst month $A_{0.01}$ is then

$$\begin{aligned} A_{0.01} = K_G &+ 35.09\log(d) + 4.473\log(f^2 + 13) \\ &- 3.34|\epsilon_p|^{0.39} - 0.00273h_L + 178.5v_{sr} \\ &- 3.764\tanh((h_c - 147)/125) \quad \text{dB.} \end{aligned} \tag{6.3}$$

The sub-refractive parameter v_{sr} is included in (6.3), and not in the geoclimatic factor (6.2), because its value, given by (4.12), depends on mean rayline clearance height H_c and path length d, as well as the Harvey sub-refractive climate parameter dN_{75}.

At locations where link fading data provides an observed value of $A_{0.01}$, an observed value of K_G may be obtained by re-arranging (6.3) as

$$\begin{aligned} K_G = A_{0.01} &- 35.09\log(d) - 4.473\log(f^2 + 13) \\ &+ 3.34|\epsilon_p|^{0.39} + 0.00273h_L - 178.5v_{sr} \\ &+ 3.764\tanh((h_c - 147)/125) \quad \text{dB.} \end{aligned} \tag{6.4}$$

If there is more than one observation at the same location, we take the mean of the K_G values for those observations.

The universal kriging system of (A.8) and (A.9) is set up, using the exponential semi-variogram function (6.1), and the functions f_1 to f_p are the parameters $\tanh((S_a - 48)/53)$, $\log(N_{\text{sA0.1}})$, and dN_1, in (6.2).

A world-wide map of the resulting universal kriging geoclimatic factor K_G is provided in Figure 6.1. This takes into account local variations between observations and the GLS regression model. This difference is shown in Figure 6.2.

6.3 Accuracy of the universal kriging model

As the universal kriging geoclimatic factor prediction error at known locations is minimised, a useful test of prediction accuracy requires the test location to be excluded from the matrix **G** of (A.8). This may be described as "leave-one-location-out" cross validation.

The results of this testing are shown in Table 6.1, comparing prediction error means and standard deviations with those of the model of *Rec. ITU-R P.530-17,* (2017). A notable characteristic of these universal kriging results is the very low mean prediction error in

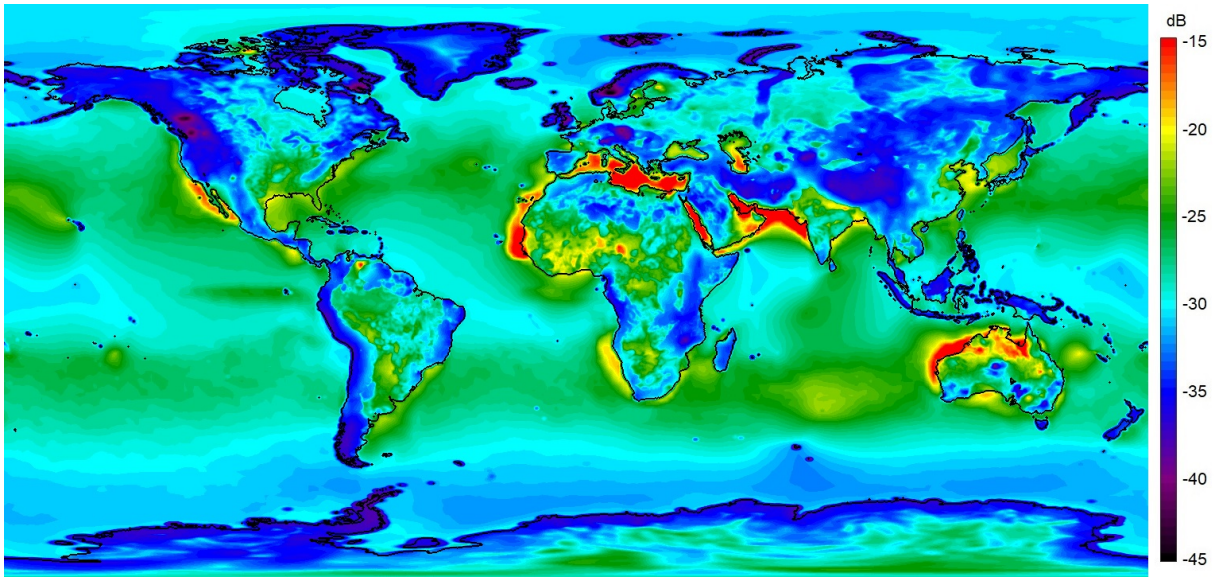

Figure 6.1. Worldwide map of geoclimatic factor K_G, produced by universal kriging. This indicates predicted severity of multipath fading, based on the best information available from the GLS regression model and any nearby link fading measurements.

all regions. Only one has magnitude exceeding 3 dB, and all regions with more than 15 link locations have mean error magnitude less than 0.5 dB.

The regions with more than 15 link locations all have universal kriging "leave-one-location-out" error standard deviation less than 6 dB.

The use of universal kriging fading prediction can provide a significant benefit to regions of the world that are currently under-represented in the fading data, if they provide new fading data records, and the universal kriging model is updated accordingly.

Table 6.1. Mean and standard deviation of prediction error by region, of the new universal kriging model. The number of locations and records, error statistics of the *Rec. ITU-R P.530-17,* (2017) model, and leave-one-location-out testing of the new universal kriging model, are shown.

Locations	P.530-17 mean	P.530-17 std. deviation	Univ. kriging mean	Univ. kriging std. deviation	Region
42	–0.96	4.94	–0.11	4.77	Western Europe
28	–0.37	5.48	+0.48	4.93	Scandinavia
16	+2.87	4.82	+0.14	4.59	Russia
3	–2.36	5.45	+0.90	4.37	Turkmenistan
5	+2.95	4.94	+1.30	4.46	South-East Canada
9	+5.75	4.93	–1.69	3.29	South-West Canada
4	–11.2	10.0	+2.63	11.0	Arctic Canada
6	+0.17	6.25	–0.18	6.75	Brazil
4	–1.38	6.27	–0.20	7.23	North-East Canada
1	–9.87	—	+4.65	—	Pakistan
7	–0.55	7.76	+0.47	7.17	Egypt
55	–0.49	6.13	–0.19	5.79	Southern Europe
3	–9.34	4.21	–0.92	6.00	Ghana
2	–1.47	5.87	+2.96	8.80	Senegal
3	+1.08	3.52	–2.17	3.78	South-East Africa
6	–6.45	8.07	+0.79	5.84	Central Asia
15	–9.83	7.27	+0.92	5.01	Cent-North Australia
31	–3.69	5.71	–0.45	5.47	South-East Australia
32	–6.02	6.52	+0.32	5.57	Southern Queensland
11	+0.72	5.42	–1.92	4.48	South-West Australia
7	–6.09	5.18	–0.47	4.75	Far North Queensland
290	–2.86	6.96	–0.03	5.31	All Regions

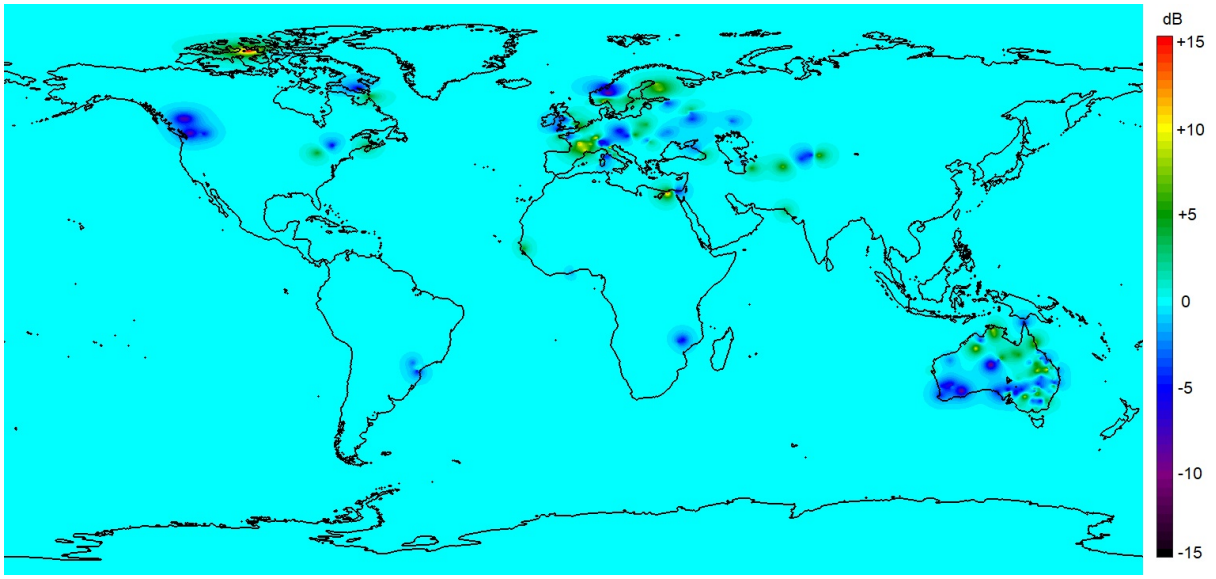

Figure 6.2. World map of geoclimatic factor difference, between universal kriging and GLS. This shows the difference in predicted severity of multipath fading, between the universal kriging and the GLS regression models. Although the differences are generally small, this map demonstates areas of the world where fading observations are available, and highlights vast areas, such as East Asia, without fixed link multipath fading neasurements.

6.4 Conclusion

The new universal kriging model described in this research is based on extensive data from Australia, and some new data from central Asia, in addition to the data from Europe, The Americas, and Africa, that was used to produce the internationally approved model prior to 2021 (*Rec. ITU-R P.530-17*, 2017), and our new model fits the data taking into account spatial correlation, and makes best use of local data, where available, by the technique of universal kriging.

These enhancements provide a general improvement in accuracy over the previous model, so our new model, as described in this chapter, has been adopted by Radio Study-Group 3 of the International Telecommunication Union, as the new model for predicting fixed-link multipath fading (*Rec. ITU-R P.530-18*, 2021).

6.4.1 Scope for expanding geographic coverage

As can be seen in Figure 6.2, there are a number of regions of the world where there is no measured fading data contributing to development of this model. Adding data from these regions may be expected to improve the accuracy of the regression model,

as well as provide local data for predictions predominantly based on measurements, in areas local to those data points.

Information on processing receive level time-series data from network installed small and medium capacity systems is given in *Australia: ITU-R doc. 3M/45,* (2016), and summarised in Appendix B. New data may be incorporated into the model by re-running the GLS regression to obtain a revised expression for geoclimatic factor, and re-running the universal kriging analysis to produce a revised world digital map at quarter-degree resolution, similar to that provided as an integral part of the new *Rec. ITU-R P.530-18,* (2021).

6.4.2 Scope for future work

One limitation of the model is the lack of fading data from very short low-clearance fixed links. Care needs to be taken in collecting this data, as fade depths may be small, and may be obscured by effects such as equipment variations or rain attenuation, but this data would be useful to check, and if necessary correct, the model accuracy for very short links.

A long-term goal would be the development of numerical weather prediction models with sufficient accuracy in predicting vertical radio refractivity gradients in the surface layer of the atmosphere, to simulate propagation impairment of terrestrial radio systems.

In Chapter 2, we investigated parabolic equation techniques for modelling terrestrial radio propagation, and described a new convolutional technique for finite conductivity lower boundaries. This technique successfully satisfies the boundary condition, but we find that implementing a boundary with imperfect reflection, in this type of marching analysis, by image theory, results in a degree of error in the field strength prediction. A solution to this problem may provide a useful stable alternative to DMFT (Dockery and Kuttler 1996), with its occasional stability problems (Kuttler and Janaswamy 2002).

Appendix A

Spatial data interpolation

DATA collected from sources such as surface weather stations has a very irregular spatial distribution around the surface of the Earth. An estimate of a parameter measured at these stations may be required at other locations, and this is provided by a digital map, generally a regular grid of estimates covering the surface of the Earth. These estimates are provided by spatial interpolation, so we wish to find the most suitable interpolation method to produce such a map from several thousand weather stations wordwide.

A.1 Introduction

Propagation models typically use parameters that vary with location over the surface of the Earth, but may only have been measured at certain locations, such as surface weather stations, or radiosonde stations. These are likely to be distributed over the Earth's surface in a very irregular way. If the correlation of the parameter between two locations can be assumed to be high for closely spaced locations and reduces with distance, it may be reasonable to estimate the value of the parameter by interpolating between the values at nearby locations where measurements are available. It is often convenient to produce a digital map in the form of a grid, quasi rectangular in terms of equal steps of latitude and longitude, providing interpolated values at those grid points. The estimated value is then obtained at any location by bilinear interpolation from the four grid points surrounding the required location.

Accordingly, we describe bilinear interpolation first, and then some of the most important of the many methods available to estimate the value at those rectangular grid points from the irregularly located known data points.

A.1.1 Rectangular gridded data-bilinear interpolation

Bilinear interpolation over a two dimensional surface, notionally assumed to be a plane over the short interpolation distance involved, is based on linear interpolation along the straight line between two points. In the usual case of a rectangular grid in terms of latitude and longitude, suppose the two grid points to the north of the required point $\text{lat}_0, \text{long}_0$ are $\text{lat}_{\text{NW}}, \text{long}_{\text{NW}}$ and $\text{lat}_{\text{NE}}, \text{long}_{\text{NE}}$ with values v_{NW} and v_{NE} respectively, then they are interpolated to estimate a value v_N due north of $\text{lat}_0, \text{long}_0$, as

$$v_N = \frac{v_{\text{NW}}(\text{long}_{\text{NE}} - \text{long}_0) + v_{\text{NE}}(\text{long}_0 - \text{long}_{\text{NW}})}{\text{long}_{\text{NE}} - \text{long}_{\text{NW}}}. \tag{A.1}$$

Similarly, a value v_S due south of $\text{lat}_0, \text{long}_0$, is interpolated from values v_{SW} and v_{SE} at grid points $\text{lat}_{\text{SW}}, \text{long}_{\text{SW}}$ and $\text{lat}_{\text{SE}}, \text{long}_{\text{SE}}$ respectively, as

$$v_S = \frac{v_{\text{SW}}(\text{long}_{\text{SE}} - \text{long}_0) + v_{\text{SE}}(\text{long}_0 - \text{long}_{\text{SW}})}{\text{long}_{\text{SE}} - \text{long}_{\text{SW}}}. \tag{A.2}$$

Then the final linear interpolation

$$v_0 = \frac{v_N(\text{lat}_0 - \text{lat}_{\text{SW}}) + v_S(\text{lat}_{\text{NW}} - \text{lat}_0)}{\text{lat}_{\text{NW}} - \text{lat}_{\text{SW}}} \tag{A.3}$$

provides the estimated value v_0 at $\text{lat}_0, \text{long}_0$.

A.1.2 Irregularly located data

Data from sources such as weather stations has a very irregular spatial distribution over the surface of the Earth, as they are usually located in cities ar at airports, and very few are located in mid-ocean locations. The closest known values to any location may be not far away, or they might be hundreds or thousands of kilometres away. The world map of interpolated values should be continuous, and preferably have continuous derivatives, so that contour lines appear as smooth curves with out sudden direction changes.

There is an important distinction to be made, between interpolation and fitting: interpolation provides a value surface that exactly matches the known values at those locations. Fitting relaxes that requirement, allowing the surface to depart slightly from those known values, which may be useful if the measured values have random error. All the ad hoc methods described here are exact interpolation methods, while kriging may be chosen to be either an exact interpolation or a fitting method.

A.2 Ad hoc methods

The somewhat derogatory term *ad hoc* tends to be applied to spatial interpolation methods that are practically convenient, but not mathematically provable as optimum, in terms of prediction accuracy, for some set of assumptions about the data being interpolated. These assumptions may not be completely realistic, so it is worth investigating ad hoc methods, to see if any have performance close to the ideally optimum methods, while having useful practical advantages over them.

A.2.1 Inverse distance weighting, and Shepard interpolation

A popular spatial interpolation method in the past was Shepard interpolation (Shepard 1968). It is often rather incorrectly described as inverse distance weighting, but in fact the algorithm is far more involved than that. A good detailed description of the algorithm is given in Willmott *et al.* (1985). The interpolation uses a small number of closest local known points, typically 7, but always at least 4 in sparsely populated regions and no more than 10 in heavily populated regions.

A.2.2 Delaunay Triangulation

The Delaunay triangles are determined by finding triangles joining three known points, such that the circumcircle of each triangle does not contain any other known points, as demonstrated in Figure A.1. The solution to this problem becomes non-unique if four or more points lie on the same circumcircle.

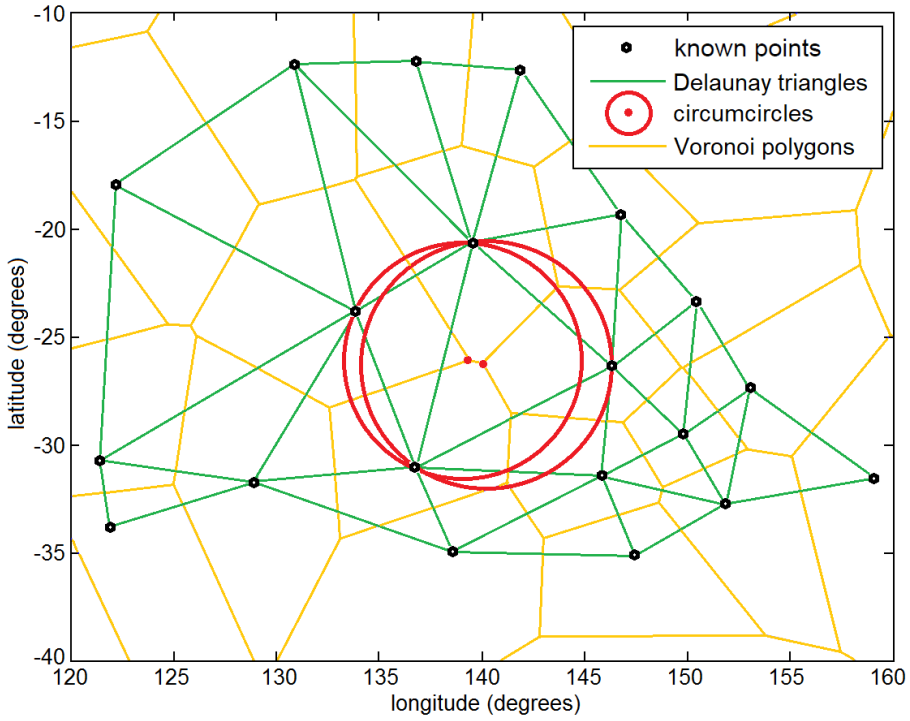

Figure A.1. Delaunay triangulation. showing the Delaunay triangles joining the known points. Two of the circumcircles are shown, with centres not far apart; the four points on these two circles are close to being on the same circumcircle. The vertices of Voronoi polygons may be found by Delaunay triangulation, as the circumcircle centres.

A.2.3 Natural neighbour interpolation

Natural neighbour interpolation (Sibson 1980) provides a unique exact interpolation that guarantees continuous first and second derivatives everywhere except at the known points (Sambridge *et al.* 1995), while only depending on local data, the natural neighbours of the interpolation point. Voronoi polygons contain all locations that are closer to a particular data point location than any other, and natural neighbours are data points with adjoining Voronoi polygons.

Conceptually, natural neighbour interpolation is very simple, as illustrated in Figure A.2. If the interpolation point is treated as a new data point, then the weights assigned to

its natural neighbours are proportional to the overlap areas of its Voronoi polygon (red dashed line) with the previously existing Voronoi polygons.

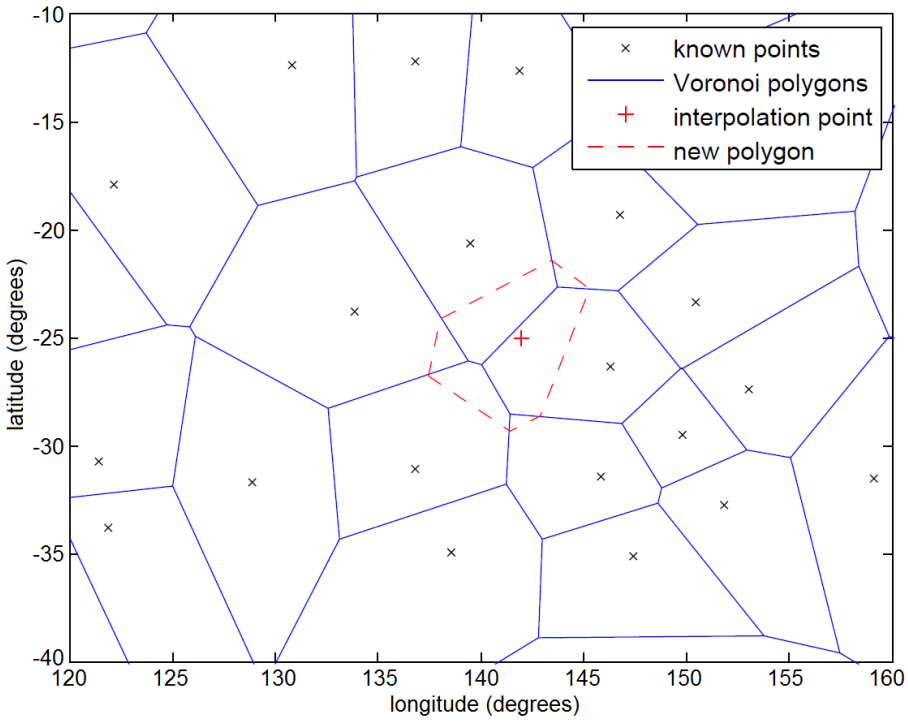

Figure A.2. Natural neighbour interpolation example. showing the Voronoi polygons corresponding to the known points, overlapped by a new polygon for a location to be interpolated. The interpolation weights are proportional to the six areas of overlap of the original polygons, after Salamon *et al.* (2020, Figure 2).

Natural neighbour interpolation is well suited to our problem of interpolating over the surface of the Earth, as this surface has no boundary, requiring special treatment. If we assume the Earth to be spherical, then spherical polygon areas are easily calculated from the sum of internal angles (Todhunter 1886). Natural neighbour interpolation is ideally suited to interpolation of parameters from highly irregular distributed locations (Sambridge *et al.* 1995), as is the case with our weather stations. This interpolation method appears to have the ability to generate an interpolated surface from only the neighbours of the interpolation point, to rival that achieved by kriging using all known points, in terms of smoothness and accuracy. We compare accuracies, by cross-validation, below. Using only local data is an advantage, as it obviates any stationarity requirement.

However, points far removed from the interpolation point may be given considerable weight if the data points are very irregularly spaced (Cressie 1993), as is the case with surface weather station data. This is likely to be the case for coastal weather stations

having large Voronoi polygons extending out into the ocean where there are few stations. Figure A.3 demonstrates this for the Australian region.

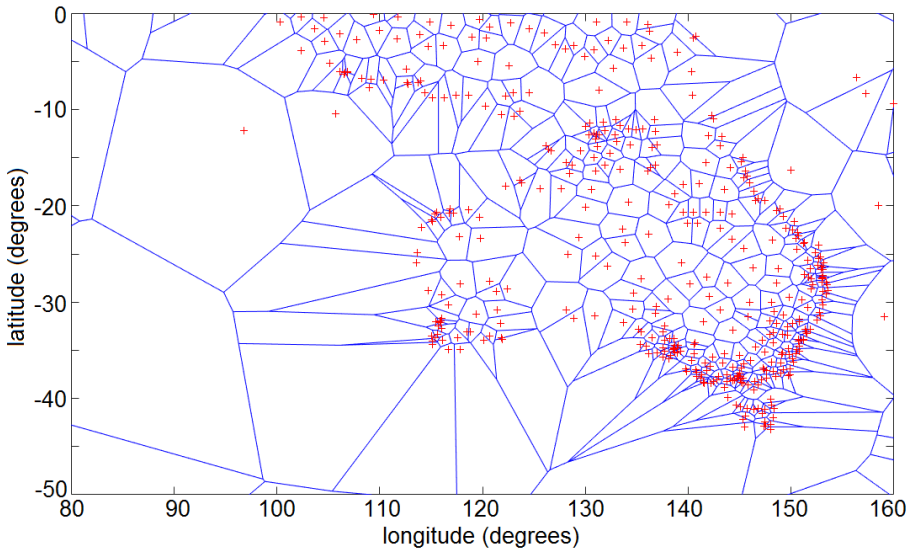

Figure A.3. Voronoi polygons for surface weather stations in the Australian region. The red crosses are station locations, and those on the west coast of Australia have polygons extending far into the Indian Ocean, where there are few stations. Coastal stations a little further to the west than their neighbours appear to have disproportionally large Voronoi polygons, after Salamon *et al.* (2020, Figure 3)

We introduce an amendment to combat the irregular polygons displayed in Figure A.3. Each vertex of a Voronoi polygon is the centre of a circumcircle of three or more data point locations. The radii of the circumcircles of the vertices of a polygon will vary greatly in the case of polygons with a centroid far removed from the corresponding data point.

A potential solution to the problem may be to identify the polygon with the largest ratio between maximum and minimum radius of its vertex circumcircles. If that ratio exceeds a pre-defined threshold, say 5:1, then the natural neighbour interpolated value at the maximum radius vertex of that polygon is calculated, and a new "quasi-known" point is created at that location. That process is repeated until no polygons have a maximum to minimum vertex circumcircle ratio exceeding the threshold value. The result of that process applied to the stations of Figure A.3 is shown in Figure A.4, for a radius ratio threshold of 5:1.

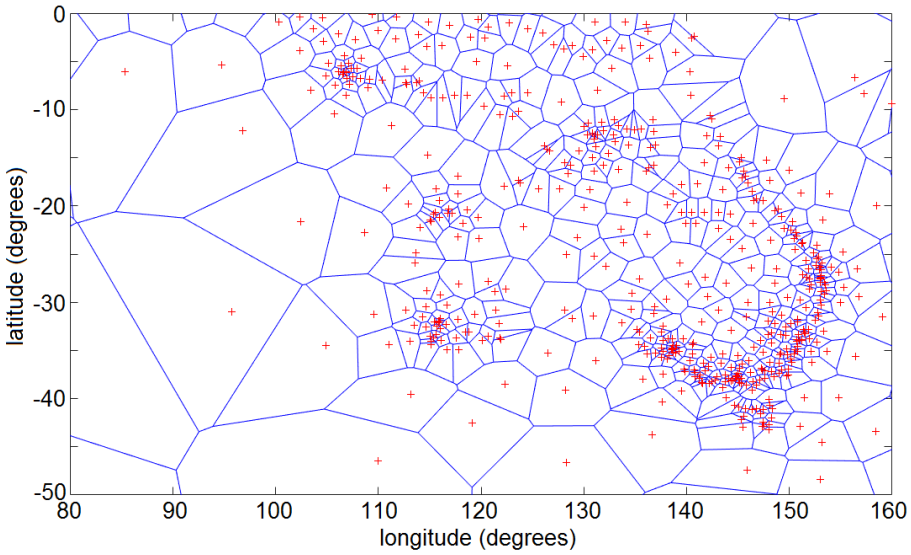

Figure A.4. Voronoi polygons for surface weather stations in the Australian region, with additional interpolated "quasi-stations" to eliminate very irregular polygons. These interpolated points are added at polygon vertices until no polygon has vertex circumcircle radii spanning a ratio exceeding 5:1, after Salamon *et al.* (2020, Figure 4).

A.3 Kriging

Kriging in its various forms (Cressie 1993) is a popular technique for linear spatial interpolation as it is the Best Linear Unbiased Predictor (BLUP) if the assumptions relevant to the particular form of kriging are met. We consider this as an option for interpolating parameters derived from weather station data.

Named after D. G. Krige, who applied the idea to the prediction of the spatial distribution of ore content, kriging was fully described later (Matheron 1963).

A.3.1 Simple kriging

Simple kriging assumes the data has a stationary and known mean as well as isotropic spatial variation, as a function of distance. The simple kriging system can be described as

$$\begin{bmatrix} w_1 \\ \vdots \\ w_n \end{bmatrix} = \begin{bmatrix} C_{1,1} & \cdots & C_{1,n} \\ \vdots & \ddots & \vdots \\ C_{n,1} & \cdots & C_{n,n} \end{bmatrix}^{-1} \begin{bmatrix} C_{1,P} \\ \vdots \\ C_{n,P} \end{bmatrix} \tag{A.4}$$

where $w_1..w_n$ are the weights applied to the n data points, the terms $C_{i,j}$ are the predicted covariance function $C(h)$ values for the distances between pairs of known points

i and j, and $C_{i,P}$ are the predicted $C(h)$ values for the distances $h(i, P)$ between known points and the interpolation point.

In general the sum of weights in the simple kriging system is less than 1, especially if the interpolation point is remote from known points; the weights are applied to the differences between the known values and the known mean, to give the difference between the interpolated value and the known mean. The ordinary kriging and universal kriging systems can be expressed in either semivariogram form or covariance form, both yielding the same weights which sum to unity, but in simple kriging the covariance form of (A.4) must be used, as the same expression in semivariogram form results in different weights, summing to greater than unity. Simple kriging is sometimes called optimal interpolation, or Optimal Statistical Objective Analysis (OSOA) (Lystad *et al.* 1998).

Ordinary kriging does not require the mean value to be known, and since the weights sum to unity, the weights may be applied directly to the known values, so generally ordinary kriging is used in preference to simple kriging.

A.3.2 Ordinary kriging

Ordinary kriging is the most popular form of this technique, and assumes the data has a stationary but unknown mean, and has stationary and known isotropic spatial variation, as a function of distance. The ordinary kriging system adds an extra row and column to the simple kriging system to ensure the sum of weights is unity, and can be described as

$$\begin{bmatrix} w_1 \\ \vdots \\ w_n \\ \mu \end{bmatrix} = \begin{bmatrix} \gamma_{1,1} & \cdots & \gamma_{1,n} & 1 \\ \vdots & \ddots & \vdots & \vdots \\ \gamma_{n,1} & \cdots & \gamma_{n,n} & 1 \\ 1 & \cdots & 1 & 0 \end{bmatrix}^{-1} \begin{bmatrix} \gamma_{1,P} \\ \vdots \\ \gamma_{n,P} \\ 1 \end{bmatrix} \tag{A.5}$$

where $w_1..w_n$ are the weights applied to the n data points, the terms $\gamma_{i,j}$ are the predicted semivariogram function $\gamma(h)$ values for the distances between pairs of known points i and j, and $\gamma_{i,P}$ are the predicted $\gamma(h)$ values for the distances $h(i, P)$ between known points and the interpolation point.

A number of different semivariogram functions $\gamma(h)$ may be used (Cressie 1993), and the *nugget effect* is often employed, where $\gamma(h)$ is discontinuous at the origin, with $\gamma(h = 0) = 0$ and $\gamma(h > 0) > 0$. This allows the fitted surface to not pass through the known points. However, we are considering exact interpolation, so the semivariogram functions described below are continuous, forcing the interpolated surface to

pass through the known points. We find this to be workable provided the semivariogram function has non-zero, and preferably maximum, slope at the origin.

Two useful functions for map interpolation are the exponential function

$$\gamma(h) = \sigma^2[1 - \exp(-h/h_0)], \tag{A.6}$$

and the power function

$$\gamma(h) = b|h|^\lambda, 0 \leq \lambda < 2. \tag{A.7}$$

In (A.6), σ^2 is the data variance, although the weights given by (A.5) are independent of the value of σ^2, or the value of constant b in (A.7). Therefore, we may fit the semivariogram function to the data by varying one constant, h_0 in (A.6), or λ in (A.7), to find the minimum RMS interpolation error, as indicated by cross-validation.

Alternatively, (A.5) may have covariance terms, for example $C_{i,j} = \sigma^2 \exp(-h(i,j)/h_0)]$ in the case of the exponential function, replacing the $\gamma_{i,j}$ terms. This is an equivalent formulation, except the Lagrange parameter μ then has the opposite sign. The $n+1$'th row and column in the semivariogram or covariance matrix provides unity sum of weights, ensuring a fit to the unknown mean of the data.

The stationary mean and covariance assumption of ordinary kriging is unlikely to be met with world-wide surface weather station data, with widely varying terrain and climate types, so kriging may not necessarily be the BLUP.

Another problem for our application is that (A.5) requires inversion of an $n+1$ by $n+1$ matrix, readily achieved if n is a few hundred or less, but we are interpolating data from several thousand weather stations world-wide. A solution to this problem may be expected to be to restrict the kriging to a smaller number of local points, but we find that that introduces discontinuities in the interpolated surface.

A.3.3 Universal kriging

Universal kriging (Cressie 1993) extends ordinary kriging of (A.5) to allow for non-stationary mean, estimated in terms of p functions of location s, $f_1(s)$ to $f_p(s)$. The semivariogram matrix $\mathbf{G}$ is similar to that in (A.5), but with additional rows and columns

for the functions $f_1(s)$ to $f_p(s)$:

$$\mathbf{G} = \begin{bmatrix} \gamma_{1,1} & . & \gamma_{1,n} & 1 & f_1(s_1) & . & f_p(s_1) \\ . & . & . & . & . & . & . \\ \gamma_{n,1} & . & \gamma_{n,n} & 1 & f_1(s_n) & . & f_p(s_n) \\ 1 & . & 1 & 0 & 0 & . & 0 \\ f_1(s_1) & . & f_1(s_n) & 0 & 0 & . & 0 \\ . & . & . & . & . & . & . \\ f_p(s_1) & . & f_p(s_n) & 0 & 0 & . & 0 \end{bmatrix} \tag{A.8}$$

and the value at location s_P is obtained as a weighted mean of the n known values at locations s_1 to s_n. The weights w_1 to w_n are given by

$$\begin{bmatrix} w_1 \\ \vdots \\ w_n \\ m_0 \\ m_1 \\ . \\ m_p \end{bmatrix} = \mathbf{G}^{-1} \begin{bmatrix} \gamma_{1,P} \\ \vdots \\ \gamma_{n,P} \\ 1 \\ f_1(s_P) \\ . \\ f_n(s_P) \end{bmatrix}. \tag{A.9}$$

If a semivariogram function without nugget effect is used, such as (A.6) or (A.7), the result of (A.9) is a smooth interpolation surface that passes through the known points, and close to them it is predominantly interpolated from them.

A.4 Comparative testing

The Harvey (1987) 75 m sub-refractive parameter dN_{75} in the Australian region is a sensitive test case for different interpolation methods, as it varies over a wide range over much of the Australian land mass. The results of interpolation testing for 354 weather stations in this region (latitudes 10 to 50 degrees south, longitudes 90 to 160 east), by leave-one-out cross-validation are shown in Table A.1.

We test ordinary kriging (OK) with the lowest RMS error exponential model and power model found in the testing, as well as conventional natural neighbour interpolation (NNI, no infill), and added interpolated points as described above (NNI, infill if ratio>5:1).

Table A.1. Leave-one-out interpolation cross-validation for parameter dN_{75} from 354 weather stations in the Australian region. Ordinary kriging with a power model has lowest RMS error, closely followed by the exponential model and natural neighbour interpolation (NNI) with added points.

Method	details	RMS error	correl. coeff. r
Ordinary kriging, 50 closest	exponential, $h_0 = 300$	7.5192	0.75253
Ordinary kriging, 50 closest	power, $\lambda = 0.3$	7.1765	0.77293
Natural neighbour interpolation	original algorithm, no infill	7.5518	0.75053
Natural neighbour interpolation	infill if vertex ratio>5:1	7.5113	0.75310
Shepard interpolation	complete algorithm	7.7105	0.74218

The Shepard interpolation results in Table A.1 are for the point selection method and complete interpolation algorithm as described in Willmott *et al.* (1985), for the method of Shepard (1968).

For each method, leave-one-out testing is used; for each station the observed value is compared with an interpolation that does not include that station. The RMS error (N-units), and Pearson's correlation coefficient, r, between the observed and interpolated values, are shown in Table A.1.

Although ordinary kriging with a power model, $\gamma(h) = b|h|^{0.3}$, has lowest RMS error and best correlation in Table A.1, this method, using the 50 closest points, is less local than natural neighbour interpolation, using typically 6 natural neighbours. As a result, the kriging interpolation appears to suffer more than NNI from leakage of the high coastal and inland values into the ocean where values are low but measurements very sparse. In addition, kriging with just the 50 closest stations suffers from discontinuities as outlier stations are switched in or out of the interpolation. These effects are demonstrated for kriging in Figure A.5.

Figure A.6 shows the same parameter, with natural neighbour interpolation, modified by adding interpolated points to eliminate vertex circumcircle radius ratios exceeding 5:1. While this seems to improve accuracy, judging by the results in Table A.1, conventional natural neighbour interpolation, shown in Figure A.7, has smoother contours and appears to have less leakage of land values into the ocean, particularly in the Great Australian Bight region, than the modified method of Figure A.6.

The added points in the modified method of Figure A.6 potentially add discontinuities in the derivatives of the interpolated surface. This may be the reason for the Indian ocean contours in Figure A.7 being smoother than those in Figure A.6. The added points do not always reduce the interpolation error; in a similar analysis with surface refractivity anomaly parameter $N_{sA99.9}$ from the same weather stations, added points at the same locations slightly increases RMS error, although correlation coefficient is slightly improved.

Accordingly, we choose conventional natural neighbour interpolation to produce digital maps of the weather station parameters, as cross-validation indicates it is close to the accuracy achieved by kriging, while producing a superior digital map.

In practice a digital map on a regular grid, at a spacing typically in the region of 0.5 degrees in latitude and longitude, have been used to obtain parameter values for radio link design. The path centre coordinates of the link are used to interpolate a value. Two methods of doing this are provided in *Rec. ITU-R P1144-9,* (2017). Bilinear interpolation from the four grid points surrounding the interpolation location has been generally used, but bicubic interpolation may be considered. We test these options by producing the world-wide digital map from the station data, on a 0.5 degree grid, using natural neighbour interpolation, and then re-interpolate back from the grid to the station coordinates, and observe the error.

The unexpected result is that bilinear interpolation appears to be generally more accurate than bicubic interpolation, when tested in this way, so in the following regression models, we use bilinear interpolation of values from a digital map with a 0.25 degree grid spacing. This replicates the procedure to be used by link designers in making a prediction, rather than interpolating directly from weather station locations to link locations.

A.5 Parameters from weather stations

As the number of weather stations providing useful data far exceeds the practical matrix inversion capability of a single worldwide kriging system, and considering the discontinuities in digital maps using kriging of only local data, seen in Figure A.5, natural neighbour interpolation is used in our research to produce worldwide digital maps of parameters derived from weather station data.

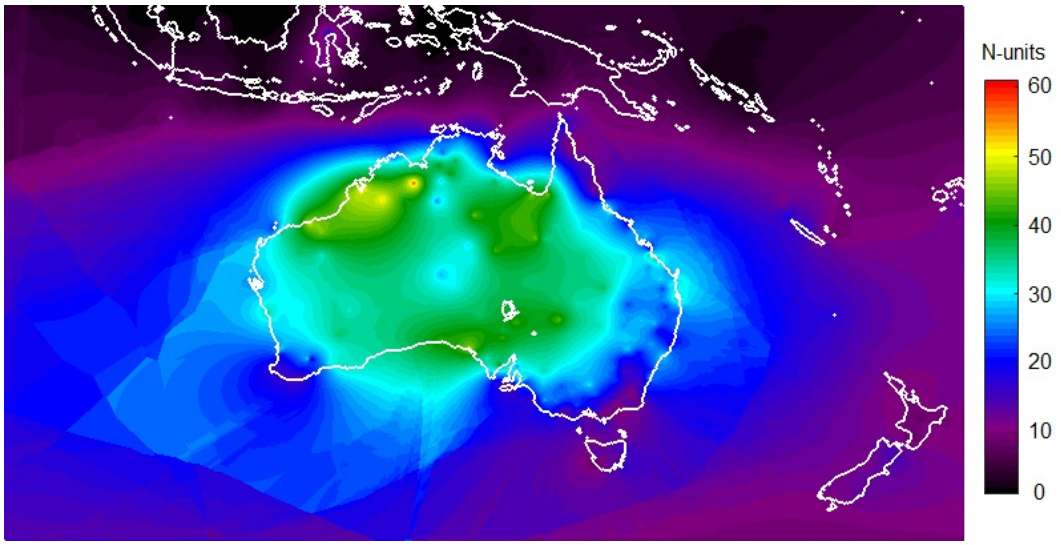

Figure A.5. Ordinary kriging of dN_{75} from the 50 closest stations, with a power model $\gamma(h) = b|h|^{0.3}$, for the Australian region. Leakage of overland values to the ocean in the Great Australian Bight region is seen, and discontinuity where high-value stations are included or excluded from the kriging system.

Sample code to produce natural neighbour maps is provided in Appendix C. The code is a version of that used to produce Figures A.5, A.6 and A.7, but simplified to only provide conventional natural neighbour interpolation of Figure A.7, and omitting a speed-up routine that prevents re-calculation of vertices, if those from the previous pixel are still valid.

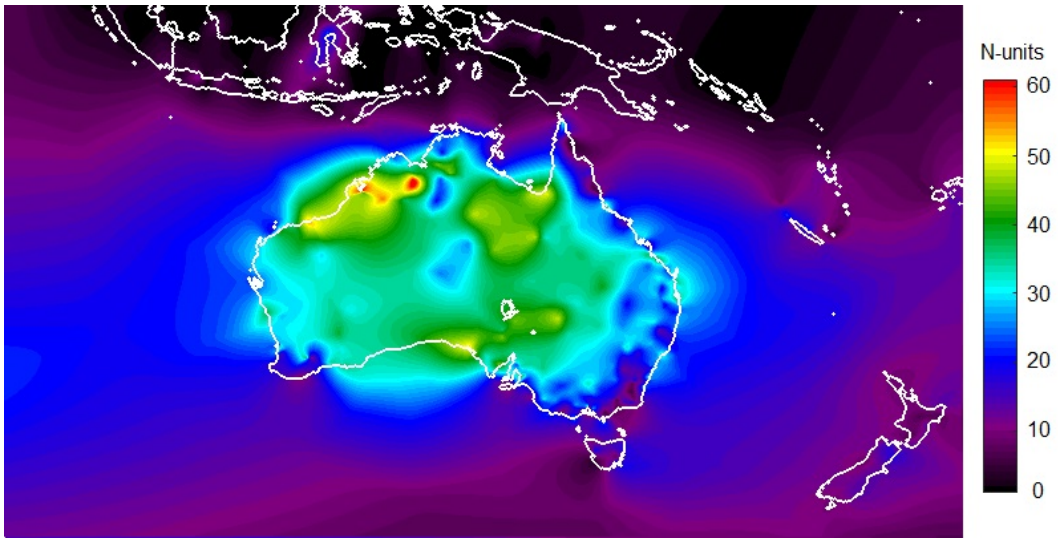

Figure A.6. Natural neighbour interpolation, with added points to eliminate vertex circumcircle radius ratios exceeding 5:1, of parameter dN_{75}. While leave-one-out testing suggests these added points improve accuracy, the contours in ocean areas appear to be less smooth than the conventional technique, and leakage of land values into ocean areas appears to be increased to the west and the south.

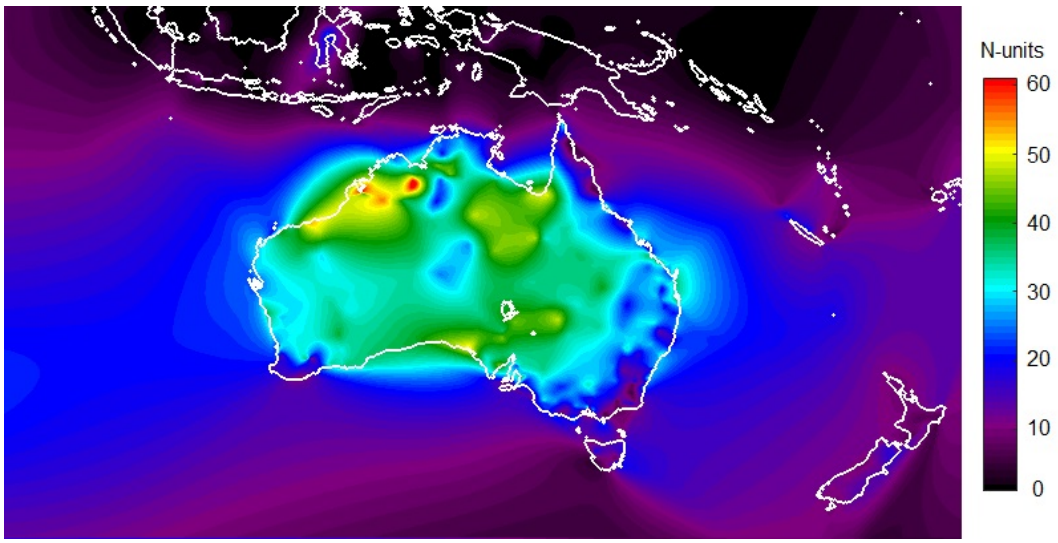

Figure A.7. Conventional natural neighbour interpolation of weather station parameter dN_{75}. A smooth interpolated surface is obtained even though only a small number of local points are used in each interpolation. Sample code to produce natural neighbour maps is provided in Appendix C.

Appendix B

Fading data from installed links

FADING data from medium to long path length links is now plentiful in much of Europe and Australia, but lacking in much of the rest of the world. Data from very short fixed links is lacking everywhere, so the procedure used in Australia to collect fading data from in-service radio links is described here, in case it may be usefully applied elsewhere.

B.1 Producing fading data from digital links

A brief description is provided here of the procedure used in Australia (*Australia: ITU-R doc. 3M/186,* 2011), (*Australia: ITU-R doc. 3M/45,* 2016), to produce average year worst-month fading distributions from installed radio links.

1. Identify line-of-sight links, with automatic transmit power control disabled, where minimum and maximum receive level data is continuously available for every 15 minutes, over a period of one or more years.

2. Process the data, estimating the receive level distributions for each 15 minute period, and accumlate these into monthly distributions. If only the 15 minute minimum and maximum levels are known, assume a uniform voltage distribution between those limits for each 15 minute period (*Australia: ITU-R doc. 3M/45,* 2016), but use any additional data; most Australian links also reported time below 4 levels.

3. Plot the receive level time series of fading months, to check that apparent fading is not equipment related. These plots include rain data from nearby weather stations, to ensure fading events are not rain related.

4. Each percentage point in the worst month distribution for the year is taken to be the worst case at that percentage point for the fading months. If more than one year of data is available, take the dB mean as the average year worst month distribution.

5. The Australian data is from 6 to 24 MHz bandwidth systems, but the fading distribution for a very narrow bandwidth system is required, having an approximate Rayleigh 10 dB per decade deep fading tail slope. Digital radio systems with finite bandwidths typically have an initial fading distribution tail slope around 10 dB per decade, but then reducing slope at the smallest percentages of time. This <10 dB per decade tail region is ignored, as not representative of narrow band fading.

Appendix C

Sample code for natural neighbour interpolation

ALTHOUGH a great deal of code was written for this research, much of it was relatively straightforward, but re-written many times in order to arrive at the solution to the various problems, as presented in this thesis, so new code suited to particular applications may be relatively easily produced, from the models we have described. Natural neighbour interpolation (Sibson 1980, Sambridge *et al.* 1995) is an exception to this; although its application to interpolation over the surface of a sphere, as described in Appendix A, is conceptually simple, producing reliable code for it is far from straightforward. We provide here the Matlab/Octave code for producing a digital map from geographically scattered data points, to provide a source of tested code for natural neighbour interpolation over the surface of the Earth, approximated as a sphere.

C.1 Circumcentres of spherical triangles

Our method for finding the circumcentre of a spherical triangle, as used in our natural neighbour interpolation code, is derived as follows:

An analytic expression for the coordinates, latitude ϕ_0 and longitude λ_0, of the circumcentre of a spherical triangle, may be found by solving for equal great-circle distance between (ϕ_0, λ_0), and each of the three vertices of the triangle, (ϕ_1, λ_1), (ϕ_2, λ_2), and (ϕ_3, λ_3), using (3) above.

Solution of this system for longitude λ_0 yields

$$\lambda_0 = \arctan(a/b) \tag{C.1}$$

where

$$\begin{aligned} a = &\sin(\phi_3)\cos(\phi_1)\cos(\lambda_1) - \sin(\phi_3)\cos(\phi_2)\cos(\lambda_2) \\ &+ \sin(\phi_1)\cos(\phi_2)\cos(\lambda_2) - \sin(\phi_2)\cos(\phi_1)\cos(\lambda_1) \\ &+ \sin(\phi_2)\cos(\phi_3)\cos(\lambda_3) - \sin(\phi_1)\cos(\phi_3)\cos(\lambda_3) \end{aligned} \tag{C.2}$$

and

$$\begin{aligned} b = &\sin(\phi_3)\cos(\phi_2)\sin(\lambda_2) - \sin(\phi_3)\cos(\phi_1)\sin(\lambda_1) \\ &+ \sin(\phi_2)\cos(\phi_1)\sin(\lambda_1) - \sin(\phi_1)\cos(\phi_2)\sin(\lambda_2) \\ &+ \sin(\phi_1)\cos(\phi_3)\sin(\lambda_3) - \sin(\phi_2)\cos(\phi_3)\sin(\lambda_3). \end{aligned} \tag{C.3}$$

Alternative expressions for latitude are either

$$\phi_0 = \arctan\left[\frac{\cos(\phi_2)\cos(\lambda_0 - \lambda_2) - \cos(\phi_1)\cos(\lambda_0 - \lambda_1)}{\sin(\phi_1) - \sin(\phi_2)}\right] \tag{C.4}$$

or if $|\sin(\phi_1) - \sin(\phi_2)| << |\sin(\phi_3) - \sin(\phi_2)|$, use

$$\phi_0 = \arctan\left[\frac{\cos(\phi_2)\cos(\lambda_0 - \lambda_2) - \cos(\phi_3)\cos(\lambda_0 - \lambda_3)}{\sin(\phi_3) - \sin(\phi_2)}\right]. \tag{C.5}$$

However, if $\phi_1 = \phi_2 = \phi_3$, the circumcircle is the line of that latitude, and the two circumcentres are the two poles.

There are two circumcentres for any spherical triangle. Coordinates of one are given by (C.1) and (C.4) or (C.5) above. The other is diametrically opposite (ϕ_0, λ_0) with coordinates $\phi_0' = -\phi_0$ and $\lambda_0' = \lambda_0 + \pi$ or $\lambda_0' = \lambda_0 - \pi$.

C.2 Code to generate a natural neighbour digital map

This code is a version of the software used to create natural neighbour interpolated maps from weather station data, in this thesis. The code has been simplified by omitting a speed-up routine that prevents re-calculation of vertices, if those from the previous pixel are still valid, and the digital file output code has been omitted.

This code is provided as a starting point for writing spherical surface natural neighbour interpolation software for other purposes.

Some long lines of code have been continued on the next line to fit on the page; append to the previous line before executing.

```
%%%%%%%%%%%%%%%%%%%%%%%%%%%%%%%%%%%%%%%%%%%%%%%%%%%%%%%%%%%%%%%%%%%%%%%%%%%%
% This version of the mapping program uses Sibson 1980 natural neighbour   %
% interpolation. Data output code is omitted, but may be readily added.     %
% Speedup by keeping same vertices if possible, is omitted for simplicity. %
% This code runs in either Matlab or Octave.                                %
%%%%%%%%%%%%%%%%%%%%%%%%%%%%%%%%%%%%%%%%%%%%%%%%%%%%%%%%%%%%%%%%%%%%%%%%%%%%
% Make variables for FindNewVertices.m and NNInterpolate.m global
global lat0 long0 latVert longVert distVert nVertices stationA stationB stationC
global dVertices DstationA DstationB DstationC DlatVert DlongVert DdistVert
global tVertices TstationA TstationB TstationC TlatVert TlongVert TdistVert
global interpValue interpWeight nStations station latitude longitude

showStations=false;
blackCoast=false;     % otherwise white coast

% Define the area to be mapped and read coastline data
% Australia 0.5 degree
vertPixels=100;   % 100*30/60 = 50 degrees (0 to -50)
horizPixels=180;  % 180*30/60 = 90 degrees (90 to 180)
resolMins=30;     % best GLOBE resolution is 1/2 minute
maxLat=0;
minLong=90;
disp('Reading coast-line data');
[coastline]=csvread('Coast100x180AUSnh.csv');
```

```
[coastPoints,~]=size(coastline);

% specify Earth physical radius (km)
earthRad=6371; % used in distance calcs

% read known points
% Australian region only, 8-year data, with revised dN75mH
x=csvread('WSparametersSE30N60E2010to17rev2.csv');
% columns are: Lat,Long,MedNs,NsA0.1,NsA90-10,dN75mH

% choose which map to produce: (digMap)
% 1 MedNs
% 2 NsA0.1
% 3 NsA99.9 (was NsA90-10)
% 4 Harvey dN75mH
digMap=4;

[n,~]=size(x);
disp('Reading weather station data');
m=0;
for k=1:n
    m=m+1;
    latitude(m)=x(k,1);
    longitude(m)=x(k,2);
    if digMap==1
        value(m)=x(k,3);
    elseif digMap==2
        value(m)=x(k,4);
    elseif digMap==3
        value(m)=x(k,6);
    elseif digMap==4
        value(m)=x(k,7); % Harvey dN 75m mean positive value
    end
    % number of measurements at this pixel location
    nMeas(m)=1;
```

```
end
n=m;

% merge any duplicate measurements
k=1;
while k<n
    k=k+1;
    % compare ny(k), nx(k) with preceding points
    j=0;
    while j<k-1
        j=j+1;
     if abs(latitude(j)-latitude(k))<0.01 && abs(longitude(j)-longitude(k))<0.01
            % duplicate found; merge k with j
            disp(['merging point ',num2str(k),' with ',num2str(j),
      ' (same lat/long = ',num2str(latitude(k)),'/',num2str(longitude(k)),')']);
            value(j)=(nMeas(j)*value(j)+nMeas(k)*value(k))/(nMeas(j)+nMeas(k));
            if k<n
                % shift all remaining points down 1 in the list
                for m=k:n-1
                    latitude(m)=latitude(m+1);
                    longitude(m)=longitude(m+1);
                    value(m)=value(m+1);
                end
            end
            n=n-1;
        end
    end
end

% Natural neighbour interpolation - first find the vertices
disp('Finding Voronoi polygon vertices');
nVertices=0;
% start with first 3 points
pointA=1;
pointB=2;
```

```
pointC=3;
% find the two circumcentres of the above 3 points
phi1=(pi/180)*latitude(pointA);
phi2=(pi/180)*latitude(pointB);
phi3=(pi/180)*latitude(pointC);
lambda1=(pi/180)*longitude(pointA);
lambda2=(pi/180)*longitude(pointB);
lambda3=(pi/180)*longitude(pointC);
if phi1==phi2 && phi2==phi3
    % 3 equal latitude points
    phi0=pi/2;
    lambda0=0;
else
    topLine=-sin(phi3)*cos(phi2)*cos(lambda2)+sin(phi3)*cos(phi1)*cos(lambda1)
              -sin(phi2)*cos(phi1)*cos(lambda1)+sin(phi1)*cos(phi2)*cos(lambda2)
             -sin(phi1)*cos(phi3)*cos(lambda3)+sin(phi2)*cos(phi3)*cos(lambda3);
    botLine=+sin(phi3)*cos(phi2)*sin(lambda2)-sin(phi3)*cos(phi1)*sin(lambda1)
              +sin(phi2)*cos(phi1)*sin(lambda1)-sin(phi1)*cos(phi2)*sin(lambda2)
             +sin(phi1)*cos(phi3)*sin(lambda3)-sin(phi2)*cos(phi3)*sin(lambda3);
    lambda0=atan(topLine/botLine);
    if abs(sin(phi3)-sin(phi2))<abs(sin(phi1)-sin(phi2))
        phi0=atan((cos(phi2)*cos(lambda0-lambda2)
                        -cos(phi1)*cos(lambda0-lambda1))/(sin(phi1)-sin(phi2)));
    else
        phi0=atan((cos(phi2)*cos(lambda0-lambda2)
                        -cos(phi3)*cos(lambda0-lambda3))/(sin(phi3)-sin(phi2)));
    end
end
latC=(180/pi)*phi0;
longC=(180/pi)*lambda0;

% calculate distance
[distThisVertex,~,~]=DistBearing(latC,longC,latitude(pointA),longitude(pointA));
% Add this to the list of vertices
nVertices=nVertices+1;
```

```
latVert(nVertices)=latC;
longVert(nVertices)=longC;
distVert(nVertices)=distThisVertex;
stationA(nVertices)=pointA;
stationB(nVertices)=pointB;
stationC(nVertices)=pointC;

% now do the other circumcentre
latC=-latC;
if longC<0
    longC=longC+180;
else
    longC=longC-180;
end
% calculate distance
[distThisVertex,~,~]=DistBearing(latC,longC,latitude(pointA),longitude(pointA));
% Add this to the list of vertices
nVertices=nVertices+1;
latVert(nVertices)=latC;
longVert(nVertices)=longC;
distVert(nVertices)=distThisVertex;
stationA(nVertices)=pointA;
stationB(nVertices)=pointB;
stationC(nVertices)=pointC;

% Now add the other known points one at a time, updating list of vertices
m=3;
while m<n
    m=m+1;
    % Find if point m is within any existing vertex circumcircles;
    % if it is, replace that vertex with a new one plus two others.
    extraVertices=0;
    deleteVertices=0;
    for k=1:nVertices
        % distance from new point to vertex k
```

```
[distance,~,~]=DistBearing(latitude(m),longitude(m),latVert(k),longVert(k));
    if distance<distVert(k)
        % Replace vertex k with 3 new ones;
        % stationA(k) + stationB(k) + point m
        % stationB(k) + stationC(k) + point m
        % stationC(k) + stationA(k) + point m
        % but only where stationA(k), stationB(k) or stationC(k)
        % does not duplicate m
        stationAk=stationA(k);
        stationBk=stationB(k);
        stationCk=stationC(k);
        deleteVertices=deleteVertices+1;

        %%%%%%%%%%%%%%%%%%%%%%%%%%%%%%%%%%%%%%
        % stationA(k) + stationB(k) + point m %
        %%%%%%%%%%%%%%%%%%%%%%%%%%%%%%%%%%%%%%
        % find the two circumcentres of these 3 points
        phi1=(pi/180)*latitude(stationAk);
        phi2=(pi/180)*latitude(stationBk);
        phi3=(pi/180)*latitude(m);
        lambda1=(pi/180)*longitude(stationAk);
        lambda2=(pi/180)*longitude(stationBk);
        lambda3=(pi/180)*longitude(m);
        if phi1==phi2 && phi2==phi3
            % 3 equal latitude points
            phi0=pi/2;
            lambda0=0;
        else
            topLine=-sin(phi3)*cos(phi2)*cos(lambda2)
          +sin(phi3)*cos(phi1)*cos(lambda1)-sin(phi2)*cos(phi1)*cos(lambda1)
          +sin(phi1)*cos(phi2)*cos(lambda2)-sin(phi1)*cos(phi3)*cos(lambda3)
                                          +sin(phi2)*cos(phi3)*cos(lambda3);
            botLine=+sin(phi3)*cos(phi2)*sin(lambda2)
          -sin(phi3)*cos(phi1)*sin(lambda1)+sin(phi2)*cos(phi1)*sin(lambda1)
          -sin(phi1)*cos(phi2)*sin(lambda2)+sin(phi1)*cos(phi3)*sin(lambda3)
```

```
                                        -sin(phi2)*cos(phi3)*sin(lambda3);
    lambda0=atan(topLine/botLine);
    if abs(sin(phi3)-sin(phi2))<abs(sin(phi1)-sin(phi2))
        phi0=atan((cos(phi2)*cos(lambda0-lambda2)
            -cos(phi1)*cos(lambda0-lambda1))/(sin(phi1)-sin(phi2)));
    else
        phi0=atan((cos(phi2)*cos(lambda0-lambda2)
            -cos(phi3)*cos(lambda0-lambda3))/(sin(phi3)-sin(phi2)));
    end
end
latC=(180/pi)*phi0;
longC=(180/pi)*lambda0;
latT=(180/pi)*phi1;
longT=(180/pi)*lambda1;
% calculate distance
[distance,~,~]=DistBearing(latC,longC,latT,longT);
X=distance/earthRad;
if X>pi/2
    % this is the wrong circumcentre, so swap to the other one
    latC=-latC;
    if longC<0
        longC=longC+180;
    else
        longC=longC-180;
    end
    X=pi-X;
end
distThisVertex=X*earthRad;
% check that this circumcircle doesn't contain any
% already added points
minDist=999999;
nMinD=0;
for i=1:m-1
    if i~=stationAk && i~=stationBk
    [distance,~,~]=DistBearing(latC,longC,latitude(i),longitude(i));
```

```
            if distance<minDist
                minDist=distance;
                nMinD=i;
            end
        end
    end
    if minDist<distThisVertex || m==stationAk || m==stationBk ||
                                                    stationAk==stationBk
        % try inverting this vertex
        latC=-latC;
        if longC<0
            longC=longC+180;
        else
            longC=longC-180;
        end
        distThisVertex=pi*earthRad-distThisVertex;
        % check that this circumcircle doesn't contain any
        % already added points
        minDist=999999;
        nMinD=0;
        for i=1:m-1
            if i~=stationAk && i~=stationBk
        [distance,~,~]=DistBearing(latC,longC,latitude(i),longitude(i));
                if distance<minDist
                    minDist=distance;
                    nMinD=i;
                end
            end
        end
        if minDist<distThisVertex || m==stationAk || m==stationBk ||
                                                    stationAk==stationBk
            skipFirst=true;
        else
            skipFirst=false;
            % Add this to the list of vertices
```

```
            latVert(k)=latC;
            longVert(k)=longC;
            distVert(k)=distThisVertex;
            stationA(k)=stationAk;
            stationB(k)=stationBk;
            stationC(k)=m;
        end
    else
        skipFirst=false;
        % Add this to the list of vertices to replace previous k
        latVert(k)=latC;
        longVert(k)=longC;
        distVert(k)=distThisVertex;
        stationA(k)=stationAk;
        stationB(k)=stationBk;
        stationC(k)=m;
    end

    %%%%%%%%%%%%%%%%%%%%%%%%%%%%%%%%%%%%%%%%
    % stationB(k) + stationC(k) + point m %
    %%%%%%%%%%%%%%%%%%%%%%%%%%%%%%%%%%%%%%%%
    % find the two circumcentres of these 3 points
    phi1=(pi/180)*latitude(stationBk);
    phi2=(pi/180)*latitude(stationCk);
    phi3=(pi/180)*latitude(m);
    lambda1=(pi/180)*longitude(stationBk);
    lambda2=(pi/180)*longitude(stationCk);
    lambda3=(pi/180)*longitude(m);
    if phi1==phi2 && phi2==phi3
        % 3 equal latitude points
        phi0=pi/2;
        lambda0=0;
    else
        topLine=-sin(phi3)*cos(phi2)*cos(lambda2)
      +sin(phi3)*cos(phi1)*cos(lambda1)-sin(phi2)*cos(phi1)*cos(lambda1)
```

```
  +sin(phi1)*cos(phi2)*cos(lambda2)-sin(phi1)*cos(phi3)*cos(lambda3)
                                   +sin(phi2)*cos(phi3)*cos(lambda3);
    botLine=+sin(phi3)*cos(phi2)*sin(lambda2)
  -sin(phi3)*cos(phi1)*sin(lambda1)+sin(phi2)*cos(phi1)*sin(lambda1)
  -sin(phi1)*cos(phi2)*sin(lambda2)+sin(phi1)*cos(phi3)*sin(lambda3)
                                   -sin(phi2)*cos(phi3)*sin(lambda3);
    lambda0=atan(topLine/botLine);
    if abs(sin(phi3)-sin(phi2))<abs(sin(phi1)-sin(phi2))
        phi0=atan((cos(phi2)*cos(lambda0-lambda2)
            -cos(phi1)*cos(lambda0-lambda1))/(sin(phi1)-sin(phi2)));
    else
        phi0=atan((cos(phi2)*cos(lambda0-lambda2)
            -cos(phi3)*cos(lambda0-lambda3))/(sin(phi3)-sin(phi2)));
    end
end
latC=(180/pi)*phi0;
longC=(180/pi)*lambda0;
latT=(180/pi)*phi1;
longT=(180/pi)*lambda1;
% calculate distance
[distance,~,~]=DistBearing(latC,longC,latT,longT);
X=distance/earthRad;
if X>pi/2
    % this is the wrong circumcentre, so swap to the other one
    latC=-latC;
    if longC<0
        longC=longC+180;
    else
        longC=longC-180;
    end
    X=pi-X;
end
distThisVertex=X*earthRad;
% check that this circumcircle doesn't contain
% any already added points
```

```
minDist=999999;
nMinD=0;
for i=1:m-1
    if i~=stationBk && i~=stationCk
    [distance,~,~]=DistBearing(latC,longC,latitude(i),longitude(i));
        if distance<minDist
            minDist=distance;
            nMinD=i;
        end
    end
end
if minDist<distThisVertex || m==stationBk || m==stationCk ||
                                                    stationBk==stationCk
    % try inverting this vertex
    latC=-latC;
    if longC<0
        longC=longC+180;
    else
        longC=longC-180;
    end
    distThisVertex=pi*earthRad-distThisVertex;
    % check that this circumcircle doesn't contain any
    % already added points
    minDist=999999;
    nMinD=0;
    for i=1:m-1
        if i~=stationBk && i~=stationCk
    [distance,~,~]=DistBearing(latC,longC,latitude(i),longitude(i));
            if distance<minDist
                minDist=distance;
                nMinD=i;
            end
        end
    end
    if minDist<distThisVertex || m==stationBk || m==stationCk ||
```

```
                                                    stationBk==stationCk
            skipSecond=true;
        else
            skipSecond=false;
            % Add this to the list of vertices
            if skipFirst
                latVert(k)=latC;
                longVert(k)=longC;
                distVert(k)=distThisVertex;
                stationA(k)=stationBk;
                stationB(k)=stationCk;
                stationC(k)=m;
            else
                extraVertices=extraVertices+1;
                latVert(nVertices+extraVertices)=latC;
                longVert(nVertices+extraVertices)=longC;
                distVert(nVertices+extraVertices)=distThisVertex;
                stationA(nVertices+extraVertices)=stationBk;
                stationB(nVertices+extraVertices)=stationCk;
                stationC(nVertices+extraVertices)=m;
            end
        end
    else
        skipSecond=false;
        % Add this to the list of vertices
        if skipFirst
            latVert(k)=latC;
            longVert(k)=longC;
            distVert(k)=distThisVertex;
            stationA(k)=stationBk;
            stationB(k)=stationCk;
            stationC(k)=m;
        else
            extraVertices=extraVertices+1;
            latVert(nVertices+extraVertices)=latC;
```

```
            longVert(nVertices+extraVertices)=longC;
            distVert(nVertices+extraVertices)=distThisVertex;
            stationA(nVertices+extraVertices)=stationBk;
            stationB(nVertices+extraVertices)=stationCk;
            stationC(nVertices+extraVertices)=m;
        end
    end

    %%%%%%%%%%%%%%%%%%%%%%%%%%%%%%%%%%%%%%%%
    % stationC(k) + stationA(k) + point m %
    %%%%%%%%%%%%%%%%%%%%%%%%%%%%%%%%%%%%%%%%
    % find the two circumcentres of these 3 points
    phi1=(pi/180)*latitude(stationCk);
    phi2=(pi/180)*latitude(stationAk);
    phi3=(pi/180)*latitude(m);
    lambda1=(pi/180)*longitude(stationCk);
    lambda2=(pi/180)*longitude(stationAk);
    lambda3=(pi/180)*longitude(m);
    if phi1==phi2 && phi2==phi3
        % 3 equal latitude points
        phi0=pi/2;
        lambda0=0;
    else
        topLine=-sin(phi3)*cos(phi2)*cos(lambda2)
      +sin(phi3)*cos(phi1)*cos(lambda1)-sin(phi2)*cos(phi1)*cos(lambda1)
      +sin(phi1)*cos(phi2)*cos(lambda2)-sin(phi1)*cos(phi3)*cos(lambda3)
                                       +sin(phi2)*cos(phi3)*cos(lambda3);
        botLine=+sin(phi3)*cos(phi2)*sin(lambda2)
      -sin(phi3)*cos(phi1)*sin(lambda1)+sin(phi2)*cos(phi1)*sin(lambda1)
      -sin(phi1)*cos(phi2)*sin(lambda2)+sin(phi1)*cos(phi3)*sin(lambda3)
                                       -sin(phi2)*cos(phi3)*sin(lambda3);
        lambda0=atan(topLine/botLine);
        if abs(sin(phi3)-sin(phi2))<abs(sin(phi1)-sin(phi2))
            phi0=atan((cos(phi2)*cos(lambda0-lambda2)
                -cos(phi1)*cos(lambda0-lambda1))/(sin(phi1)-sin(phi2)));
```

```
    else
        phi0=atan((cos(phi2)*cos(lambda0-lambda2)
            -cos(phi3)*cos(lambda0-lambda3))/(sin(phi3)-sin(phi2)));
    end
end
latC=(180/pi)*phi0;
longC=(180/pi)*lambda0;
latT=(180/pi)*phi1;
longT=(180/pi)*lambda1;
% calculate distance
[distance,~,~]=DistBearing(latC,longC,latT,longT);
X=distance/earthRad;
if X>pi/2
    % this is the wrong circumcentre, so swap to the other one
    latC=-latC;
    if longC<0
        longC=longC+180;
    else
        longC=longC-180;
    end
    X=pi-X;
end
distThisVertex=X*earthRad;
% check that this circumcircle doesn't contain any
% already added points
minDist=999999;
nMinD=0;
for i=1:m-1
    if i~=stationCk && i~=stationAk
    [distance,~,~]=DistBearing(latC,longC,latitude(i),longitude(i));
        if distance<minDist
            minDist=distance;
            nMinD=i;
        end
    end
```

```
end
if minDist<distThisVertex || m==stationCk || m==stationAk ||
                                                    stationCk==stationAk
    % try inverting this vertex
    latC=-latC;
    if longC<0
        longC=longC+180;
    else
        longC=longC-180;
    end
    distThisVertex=pi*earthRad-distThisVertex;
    % check that this circumcircle doesn't contain any
    % already added points
    minDist=999999;
    nMinD=0;
    for i=1:m-1
        if i~=stationCk && i~=stationAk
    [distance,~,~]=DistBearing(latC,longC,latitude(i),longitude(i));
            if distance<minDist
                minDist=distance;
                nMinD=i;
            end
        end
    end
    if minDist<distThisVertex || m==stationCk || m==stationAk ||
                                                    stationCk==stationAk
        skipThird=true;
    else
        skipThird=false;
        % Add this to the list of vertices
        if skipFirst && skipSecond
            latVert(k)=latC;
            longVert(k)=longC;
            distVert(k)=distThisVertex;
            stationA(k)=stationCk;
```

```
                stationB(k)=stationAk;
                stationC(k)=m;
            else
                extraVertices=extraVertices+1;
                latVert(nVertices+extraVertices)=latC;
                longVert(nVertices+extraVertices)=longC;
                distVert(nVertices+extraVertices)=distThisVertex;
                stationA(nVertices+extraVertices)=stationCk;
                stationB(nVertices+extraVertices)=stationAk;
                stationC(nVertices+extraVertices)=m;
            end
        end
    else
        skipThird=false;
        % Add this to the list of vertices
        if skipFirst && skipSecond
            latVert(k)=latC;
            longVert(k)=longC;
            distVert(k)=distThisVertex;
            stationA(k)=stationCk;
            stationB(k)=stationAk;
            stationC(k)=m;
        else
            extraVertices=extraVertices+1;
            latVert(nVertices+extraVertices)=latC;
            longVert(nVertices+extraVertices)=longC;
            distVert(nVertices+extraVertices)=distThisVertex;
            stationA(nVertices+extraVertices)=stationCk;
            stationB(nVertices+extraVertices)=stationAk;
            stationC(nVertices+extraVertices)=m;
        end
    end

    if skipFirst && skipSecond && skipThird
        % mark this vertex for deletion
```

```
                distVert(k)=999999999;
            end

        end % if distance<distVert(k)

    end % for k=1:nVertices finding existing vertices affected by point m

    nVertices=nVertices+extraVertices;

    % remove any vertices marked for deletion
    nn=0;
    for k=1:nVertices
        if distVert(k)<999999
            nn=nn+1;
            latVert(nn)=latVert(k);
            longVert(nn)=longVert(k);
            distVert(nn)=distVert(k);
            stationA(nn)=stationA(k);
            stationB(nn)=stationB(k);
            stationC(nn)=stationC(k);
        end
    end
    nVertices=nn;

    disp([num2str(m),' stations  ',num2str(nVertices),' vertices']);

end % for m=4:n (now while m<n) adding new points one at a time


%%%%%%%%%%%%%%%%%%%%%%%%%%%%%%%%%%%%%%%%%%%%%%%%%%%%%%%%%%%%
% produce map by natural neighbour interpolation %
%%%%%%%%%%%%%%%%%%%%%%%%%%%%%%%%%%%%%%%%%%%%%%%%%%%%%%%%%%%%
% Initialise display matrix
displayMat=ones(vertPixels+1,horizPixels+1);
disp(['Producing Natural Neighbour Interpolated image']);
```

```
% Horizontal scan
for y=1:vertPixels+1
    lat0=maxLat-y*resolMins/60+resolMins/60; % no half pixel offset
    disp(num2str(lat0));
    % reset speedup flag for each horizontal scan
    verticesFound=false;
    for x=1:horizPixels+1
        long0=minLong+x*resolMins/60-resolMins/60; % no half pixel offset

        % Find new vertices for added point lat0, long0 (all in/out global)
        dVertices=0; % count of existing vertices within the new polygon
        DlatVert=0;
        DlongVert=0;
        DdistVert=0;
        DstationA=0;
        DstationB=0;
        DstationC=0;
        tVertices=0; % count of new vertices around the new polygon
        TlatVert=0;
        TlongVert=0;
        TdistVert=0;
        TstationA=0;
        TstationB=0;
        TstationC=0;
        FindNewVertices;

        % check if lat0, long0 is one of the known points
        unknownPoint=true;
        for k=1:nStations
            if station(k)>0
                if abs(latitude(station(k))-lat0)
                                        +abs(longitude(station(k))-long0)==0
                    unknownPoint=false;
                    interpValue=value(station(k));
```

```
                    interpWeight=1;
                end
            end
        end

        if unknownPoint
            % Natural Neighbour Interpolation (all input/output global)
            NNInterpolate;
            interpValue=interpValue/interpWeight;
            interpWeight=1;
        end % if unknownPoint

        if interpWeight>0
            interpValue=interpValue/interpWeight;
            % divider to give range to 60
            if digMap==1
                divider=10;  % Ns
            elseif digMap==2
                divider=-2;  % NsA0.1
            elseif digMap==3
                divider=2;  % NsA99.9    (was divider=1;   % NsA90-10)
            elseif digMap==4
                divider=1;   % dN75mH
            end
            % spectral colour for plotted value
            colour=min(round(max(interpValue/divider,1)),60);
        else
            % grey to indicate no known value
            colour=62;
            % reset speedup flag if intepolation failed
            verticesFound=false;
        end
        displayMat(y,x)=colour;
    end
end
```

```
% Add coastline generated from Globe v1 30 sec DEM
disp('Adding coast-line');

% white/black to indicate coast
if blackCoast
    colour=1;
else
    colour=63;
end
for m=1:coastPoints
    x=coastline(m,2);
    y=coastline(m,1);
    displayMat(y,x)=colour;
end

% put small black/white dots or crosses at known locations:
if showStations
    if blackCoast
        colour=63;
    else
        colour=1;
    end
    for k=1:n
        lat0=latitude(k);
        long0=longitude(k);
        y=round((maxLat-lat0+resolMins/120)/(resolMins/60));
        x=round((long0-minLong+resolMins/120)/(resolMins/60));
        if x>1 && x<horizPixels && y>1 && y<vertPixels
            displayMat(y,x)=colour;
        %    displayMat(y,x-1)=colour;
        %    displayMat(y,x+1)=colour;
        %    displayMat(y-1,x)=colour;
        %    displayMat(y+1,x)=colour;
        end
```

```
    end
end

% Matlab plotting [the following two long lines have been wrapped six times]
%     1     2     3         4     5         6     7         8     9
cMap=[0,0,0;1,0,1;1.5,0,1.5;2,0,2;2.5,0,2.5;3,0,3;3.5,0,3.5;4,0,4;4.5,0,4.5;
      10    11        12    13        14    15        16    17
      5,0,5;4.5,0,5.5;4,0,6;3.5,0,6.5;3,0,7;2.5,0,7.5;2,0,8;1.5,0,8.5;
      18    19        20     21     22     23     24     25     26
      1,0,9;0.5,0,9.5;0,0,10;0,1,10;0,2,10;0,3,10;0,4,10;0,5,10;0,6,10;
      27     28     29     30      31      32      33      34      35
      0,7,10;0,8,10;0,9,10;0,10,10;0,9.6,9;0,9.2,8;0,8.8,7;0,8.4,6;0,8,5;
      36      37      38      39      40    41      42      43      44
      0,7.6,4;0,7.2,3;0,6.8,2;0,6.4,1;0,6,0;1,6.4,0;2,6.8,0;3,7.2,0;4,7.6,0;
      45    46      47      48      49      50=+0dB 51     52     53
      5,8,0;6,8.4,0;7,8.8,0;8,9.2,0;9,9.6,0;10,10,0;10,9,0;10,8,0;10,7,0;
      54     55     56     57     58     59     60     ground grey white
      10,6,0;10,5,0;10,4,0;10,3,0;10,2,0;10,1,0;10,0,0;5,2,0;5,5,5;10,10,10];
cMap=cMap/10;
imshow(displayMat,cMap);
```

C.3 Natural neighbour interpolation: NNInterpolate.m

[Some long lines of code have been continued on the next line to fit on the page; append to the previous line before executing.]

```
%%%%%%%%%%%%%%%%%%%%%%%%%%%%%%%%%%%%%%%%%%%%%%%%%%%%%%%%%%%%%%%%%%%%%%%%
%  Make an ordered list of each polygon, calculate its area,  %
%  and estimate value as an area weighted mean.               %
%%%%%%%%%%%%%%%%%%%%%%%%%%%%%%%%%%%%%%%%%%%%%%%%%%%%%%%%%%%%%%%%%%%%%%%%
interpValue=0;
interpWeight=0;
for k=1:nStations
    if station(k)>0
        nStnList=0;
        stnListLink1=0;
        stnListLink2=0;
        for j=1:dVertices
            if station(k)==DstationA(j) || station(k)==DstationB(j) ||
                                                        station(k)==DstationC(j)
                nStnList=nStnList+1;
                stnListLat(nStnList)=DlatVert(j);
                stnListLong(nStnList)=DlongVert(j);
                if station(k)==DstationA(j)
                    stnListLink1(nStnList)=DstationB(j);
                    stnListLink2(nStnList)=DstationC(j);
                elseif station(k)==DstationB(j)
                    stnListLink1(nStnList)=DstationA(j);
                    stnListLink2(nStnList)=DstationC(j);
                else
                    stnListLink1(nStnList)=DstationA(j);
                    stnListLink2(nStnList)=DstationB(j);
                end
            end
        end
        for j=1:tVertices
            if station(k)==TstationA(j) || station(k)==TstationB(j) ||
```

```
                                                    station(k)==TstationC(j)
            nStnList=nStnList+1;
            stnListLat(nStnList)=TlatVert(j);
            stnListLong(nStnList)=TlongVert(j);
            if station(k)==TstationA(j)
                stnListLink1(nStnList)=TstationB(j);
                stnListLink2(nStnList)=TstationC(j);
            elseif station(k)==TstationB(j)
                stnListLink1(nStnList)=TstationA(j);
                stnListLink2(nStnList)=TstationC(j);
            else
                stnListLink1(nStnList)=TstationA(j);
                stnListLink2(nStnList)=TstationB(j);
            end
        end
    end

    j=1;
    nLinkedList=1;
    linkedListLat(nLinkedList)=stnListLat(j);
    linkedListLong(nLinkedList)=stnListLong(j);
    linkingNumber=stnListLink1(j);
    loopNotComplete=true;
    while loopNotComplete
        % find another vertex containing linkingNumber
        linkNotFound=true;
        while linkNotFound
            j=j+1;
            if j>nStnList
                j=1;
            end
            if stnListLink1(j)==linkingNumber
                linkNotFound=false;
                linkingNumber=stnListLink2(j);
            elseif stnListLink2(j)==linkingNumber
```

```
                linkNotFound=false;
                linkingNumber=stnListLink1(j);
            end
        end
        nLinkedList=nLinkedList+1;
        linkedListLat(nLinkedList)=stnListLat(j);
        linkedListLong(nLinkedList)=stnListLong(j);
        if j==1
            loopNotComplete=false;
        end
    end

    % We now have an ordered loop of coordinates in
    % linkedListLat(1:nLinkedList), linkedListLong(1:nLinkedList)
    % forming a convex spherical polygon.
    % Go around the polygon calculating the side bearings.
    for j=1:nLinkedList-1
        [distance, Zs, Zt]=DistBearing(linkedListLat(j),linkedListLong(j),
                                    linkedListLat(j+1),linkedListLong(j+1));
        listBearingNext(j)=Zs;
        if j+1==nLinkedList
            listBearingLast(1)=Zt;
        else
            listBearingLast(j+1)=Zt;
        end
    end % calculating side bearings for station k sub-polygon
    % calculate sub-polygon area from sum of internal angles, theta
    theta=0;
    for j=1:nLinkedList-1
        intAngle=listBearingNext(j)-listBearingLast(j);
        if intAngle>pi
            intAngle=intAngle-2*pi;
        elseif intAngle<-pi
            intAngle=intAngle+2*pi;
        end
```

```
            theta=theta+intAngle;
        end
        % Sign of theta depends on if the loop is clockwise or anti-clockwise.
        % Area of spherical polygon by spherical excess (Todhunter 1886)
        area=(abs(theta)-((nLinkedList-1)-2)*pi())*(earthRad^2);

        % Robin Sibson 1980 Natural Neighbour Interpolation
        interpValue=interpValue+area*value(station(k));
        interpWeight=interpWeight+area;

    end % if station(k)>0
end % for k=1:nStations
```

C.4 Find Voronoi polygon vertices: FindNewVertices.m

[Some long lines of code have been continued on the next line to fit on the page; append to the previous line before executing.]

```
%%%%%%%%%%%%%%%%%%%%%%%%%%%%%%%%%%%%%%%%%%%%%%%%%%%%%%%%%%%%%%%%%%%%%%%%%%%%
% Find if lat0,long0 is within any existing vertex circumcircles; %
% if it is, replace that vertex with a new one plus two others.   %
%%%%%%%%%%%%%%%%%%%%%%%%%%%%%%%%%%%%%%%%%%%%%%%%%%%%%%%%%%%%%%%%%%%%%%%%%%%%
% All inputs and outputs are global variables
tVertices=0; % count of new vertices around the new polygon
dVertices=0; % count existing vertices would be absorbed within the new polygon
for k=1:nVertices
    % distance from new point to vertex k
    [distance, Zs, Zt]=DistBearing(lat0,long0,latVert(k),longVert(k));
    if distance<distVert(k)
        % Replace vertex k with 3 new ones;
        % stationA(k) + stationB(k) + point 0 [lat0,long0]
        % stationB(k) + stationC(k) + point 0
        % stationC(k) + stationA(k) + point 0
        stationAk=stationA(k);
        stationBk=stationB(k);
        stationCk=stationC(k);
        % add this vertex to the list of deleted ones
        dVertices=dVertices+1;
        DlatVert(dVertices)=latVert(k);
        DlongVert(dVertices)=longVert(k);
        DdistVert(dVertices)=distVert(k);
        DstationA(dVertices)=stationA(k);
        DstationB(dVertices)=stationB(k);
        DstationC(dVertices)=stationC(k);
```

```
%%%%%%%%%%%%%%%%%%%%%%%%%%%%%%%%%%%%%%%%%%%%
% stationA(k) + stationB(k) + point 0 %
%%%%%%%%%%%%%%%%%%%%%%%%%%%%%%%%%%%%%%%%%%%%
% find the two circumcentres of these 3 points
phi1=(pi/180)*latitude(stationAk);
phi2=(pi/180)*latitude(stationBk);
phi3=(pi/180)*lat0;
lambda1=(pi/180)*longitude(stationAk);
lambda2=(pi/180)*longitude(stationBk);
lambda3=(pi/180)*long0;
if phi1==phi2 && phi2==phi3
    % 3 equal latitude points
    phi0=pi/2;
    lambda0=0;
else
    topLine=-sin(phi3)*cos(phi2)*cos(lambda2)
     +sin(phi3)*cos(phi1)*cos(lambda1)-sin(phi2)*cos(phi1)*cos(lambda1)
     +sin(phi1)*cos(phi2)*cos(lambda2)-sin(phi1)*cos(phi3)*cos(lambda3)
                                      +sin(phi2)*cos(phi3)*cos(lambda3);
    botLine=+sin(phi3)*cos(phi2)*sin(lambda2)
     -sin(phi3)*cos(phi1)*sin(lambda1)+sin(phi2)*cos(phi1)*sin(lambda1)
     -sin(phi1)*cos(phi2)*sin(lambda2)+sin(phi1)*cos(phi3)*sin(lambda3)
                                      -sin(phi2)*cos(phi3)*sin(lambda3);
    lambda0=atan(topLine/botLine);
    if abs(sin(phi3)-sin(phi2))<abs(sin(phi1)-sin(phi2))
        phi0=atan((cos(phi2)*cos(lambda0-lambda2)
               -cos(phi1)*cos(lambda0-lambda1))/(sin(phi1)-sin(phi2)));
    else
        phi0=atan((cos(phi2)*cos(lambda0-lambda2)
               -cos(phi3)*cos(lambda0-lambda3))/(sin(phi3)-sin(phi2)));
    end
end
latC=(180/pi)*phi0;
longC=(180/pi)*lambda0;
latT=(180/pi)*phi1;
```

```
longT=(180/pi)*lambda1;
% calculate distance
[distance,~,~]=DistBearing(latC,longC,latT,longT);
X=distance/earthRad;
if X>pi/2
    % this is the wrong circumcentre, so swap to the other one
    latC=-latC;
    if longC<0
        longC=longC+180;
    else
        longC=longC-180;
    end
    X=pi-X;
end
distThisVertex=X*earthRad;
% check that this circumcircle doesn't contain any already added points
minDist=999999;
nMinD=0;
for i=1:n % was 1:m-1
    if i~=stationAk && i~=stationBk
       [distance,~,~]=DistBearing(latC,longC,latitude(i),longitude(i));
        if distance<minDist
            minDist=distance;
            nMinD=i;
        end
    end
end
if minDist<distThisVertex || stationAk==stationBk
    % try inverting this vertex
    latC=-latC;
    if longC<0
        longC=longC+180;
    else
        longC=longC-180;
    end
```

```
        distThisVertex=pi*earthRad-distThisVertex;
        % check this circumcircle doesn't contain any already added points
        minDist=999999;
        nMinD=0;
        for i=1:n % was 1:m-1
            if i~=stationAk && i~=stationBk
           [distance,~,~]=DistBearing(latC,longC,latitude(i),longitude(i));
                if distance<minDist
                    minDist=distance;
                    nMinD=i;
                end
            end
        end
        if minDist<distThisVertex || stationAk==stationBk
            % point nMinD is inside circumcircle stationAk,Bk,
            % radius distThisVertex centre latC longC
        else
            % Add this to the list of new vertices
            tVertices=tVertices+1;
            TlatVert(tVertices)=latC;
            TlongVert(tVertices)=longC;
            TdistVert(tVertices)=distThisVertex;
            TstationA(tVertices)=stationAk;
            TstationB(tVertices)=stationBk;
            TstationC(tVertices)=0;
        end
    else
        tVertices=tVertices+1;
        TlatVert(tVertices)=latC;
        TlongVert(tVertices)=longC;
        TdistVert(tVertices)=distThisVertex;
        TstationA(tVertices)=stationAk;
        TstationB(tVertices)=stationBk;
        TstationC(tVertices)=0;
    end
```

```
%%%%%%%%%%%%%%%%%%%%%%%%%%%%%%%%%%%%%%%
% stationB(k) + stationC(k) + point 0 %
%%%%%%%%%%%%%%%%%%%%%%%%%%%%%%%%%%%%%%%
% find the two circumcentres of these 3 points
phi1=(pi/180)*latitude(stationBk);
phi2=(pi/180)*latitude(stationCk);
phi3=(pi/180)*lat0;
lambda1=(pi/180)*longitude(stationBk);
lambda2=(pi/180)*longitude(stationCk);
lambda3=(pi/180)*long0;
if phi1==phi2 && phi2==phi3
    % 3 equal latitude points
    phi0=pi/2;
    lambda0=0;
else
    topLine=-sin(phi3)*cos(phi2)*cos(lambda2)
     +sin(phi3)*cos(phi1)*cos(lambda1)-sin(phi2)*cos(phi1)*cos(lambda1)
     +sin(phi1)*cos(phi2)*cos(lambda2)-sin(phi1)*cos(phi3)*cos(lambda3)
                                     +sin(phi2)*cos(phi3)*cos(lambda3);
    botLine=+sin(phi3)*cos(phi2)*sin(lambda2)
     -sin(phi3)*cos(phi1)*sin(lambda1)+sin(phi2)*cos(phi1)*sin(lambda1)
     -sin(phi1)*cos(phi2)*sin(lambda2)+sin(phi1)*cos(phi3)*sin(lambda3)
                                     -sin(phi2)*cos(phi3)*sin(lambda3);
    lambda0=atan(topLine/botLine);
    if abs(sin(phi3)-sin(phi2))<abs(sin(phi1)-sin(phi2))
        phi0=atan((cos(phi2)*cos(lambda0-lambda2)
               -cos(phi1)*cos(lambda0-lambda1))/(sin(phi1)-sin(phi2)));
    else
        phi0=atan((cos(phi2)*cos(lambda0-lambda2)
               -cos(phi3)*cos(lambda0-lambda3))/(sin(phi3)-sin(phi2)));
    end
end
latC=(180/pi)*phi0;
longC=(180/pi)*lambda0;
latT=(180/pi)*phi1;
```

```
longT=(180/pi)*lambda1;
% calculate distance
[distance,~,~]=DistBearing(latC,longC,latT,longT);
X=distance/earthRad;
if X>pi/2
    % this is the wrong circumcentre, so swap to the other one
    latC=-latC;
    if longC<0
        longC=longC+180;
    else
        longC=longC-180;
    end
    X=pi-X;
end
distThisVertex=X*earthRad;
% check that this circumcircle doesn't contain any already added points
minDist=999999;
nMinD=0;
for i=1:n % was 1:m-1
    if i~=stationBk && i~=stationCk
   [distance, Zs, Zt]=DistBearing(latC,longC,latitude(i),longitude(i));
        if distance<minDist
            minDist=distance;
            nMinD=i;
        end
    end
end
if minDist<distThisVertex || stationBk==stationCk
    % try inverting this vertex
    latC=-latC;
    if longC<0
        longC=longC+180;
    else
        longC=longC-180;
    end
```

```
        distThisVertex=pi*earthRad-distThisVertex;
        % check this circumcircle doesn't contain any already added points
        minDist=999999;
        nMinD=0;
        for i=1:n % was 1:m-1
            if i~=stationBk && i~=stationCk
       [distance, Zs, Zt]=DistBearing(latC,longC,latitude(i),longitude(i));
                if distance<minDist
                    minDist=distance;
                    nMinD=i;
                end
            end
        end
        if minDist<distThisVertex || stationBk==stationCk
            % point nMinD is inside circumcircle stationBk, Ck,
            % radius distThisVertex,'  centre latC, longC
        else
            % Add this to the list of new vertices
            tVertices=tVertices+1;
            TlatVert(tVertices)=latC;
            TlongVert(tVertices)=longC;
            TdistVert(tVertices)=distThisVertex;
            TstationA(tVertices)=stationBk;
            TstationB(tVertices)=stationCk;
            TstationC(tVertices)=0;
        end
    else
        tVertices=tVertices+1;
        TlatVert(tVertices)=latC;
        TlongVert(tVertices)=longC;
        TdistVert(tVertices)=distThisVertex;
        TstationA(tVertices)=stationBk;
        TstationB(tVertices)=stationCk;
        TstationC(tVertices)=0;
    end
```

```
%%%%%%%%%%%%%%%%%%%%%%%%%%%%%%%%%%%%%%%%%%%%
% stationC(k) + stationA(k) + point 0 %
%%%%%%%%%%%%%%%%%%%%%%%%%%%%%%%%%%%%%%%%%%%%
% find the two circumcentres of these 3 points
phi1=(pi/180)*latitude(stationCk);
phi2=(pi/180)*latitude(stationAk);
phi3=(pi/180)*lat0;
lambda1=(pi/180)*longitude(stationCk);
lambda2=(pi/180)*longitude(stationAk);
lambda3=(pi/180)*long0;
if phi1==phi2 && phi2==phi3
    % 3 equal latitude points
    phi0=pi/2;
    lambda0=0;
else
    topLine=-sin(phi3)*cos(phi2)*cos(lambda2)
     +sin(phi3)*cos(phi1)*cos(lambda1)-sin(phi2)*cos(phi1)*cos(lambda1)
     +sin(phi1)*cos(phi2)*cos(lambda2)-sin(phi1)*cos(phi3)*cos(lambda3)
                                      +sin(phi2)*cos(phi3)*cos(lambda3);
    botLine=+sin(phi3)*cos(phi2)*sin(lambda2)
     -sin(phi3)*cos(phi1)*sin(lambda1)+sin(phi2)*cos(phi1)*sin(lambda1)
     -sin(phi1)*cos(phi2)*sin(lambda2)+sin(phi1)*cos(phi3)*sin(lambda3)
                                      -sin(phi2)*cos(phi3)*sin(lambda3);
    lambda0=atan(topLine/botLine);
    if abs(sin(phi3)-sin(phi2))<abs(sin(phi1)-sin(phi2))
        phi0=atan((cos(phi2)*cos(lambda0-lambda2)
               -cos(phi1)*cos(lambda0-lambda1))/(sin(phi1)-sin(phi2)));
    else
        phi0=atan((cos(phi2)*cos(lambda0-lambda2)
               -cos(phi3)*cos(lambda0-lambda3))/(sin(phi3)-sin(phi2)));
    end
end
latC=(180/pi)*phi0;
longC=(180/pi)*lambda0;
```

```
latT=(180/pi)*phi1;
longT=(180/pi)*lambda1;
% calculate distance
[distance,~,~]=DistBearing(latC,longC,latT,longT);
X=distance/earthRad;
if X>pi/2
    % this is the wrong circumcentre, so swap to the other one
    latC=-latC;
    if longC<0
        longC=longC+180;
    else
        longC=longC-180;
    end
    X=pi-X;
end
distThisVertex=X*earthRad;
% check that this circumcircle doesn't contain any already added points
minDist=999999;
nMinD=0;
for i=1:n % was 1:m-1
    if i~=stationCk && i~=stationAk
       [distance,~,~]=DistBearing(latC,longC,latitude(i),longitude(i));
        if distance<minDist
            minDist=distance;
            nMinD=i;
        end
    end
end
if minDist<distThisVertex || stationCk==stationAk
    % try inverting this vertex
    latC=-latC;
    if longC<0
        longC=longC+180;
    else
        longC=longC-180;
```

```
        end
        distThisVertex=pi*earthRad-distThisVertex;
        % check this circumcircle doesn't contain any already added points
        minDist=999999;
        nMinD=0;
        for i=1:n % was 1:m-1
            if i~=stationCk && i~=stationAk
           [distance,~,~]=DistBearing(latC,longC,latitude(i),longitude(i));
                if distance<minDist
                    minDist=distance;
                    nMinD=i;
                end
            end
        end
        if minDist<distThisVertex || stationCk==stationAk
            % point nMinD is inside circumcircle stationCk, Ak
            % radius distThisVertex centre latC, longC
        else
            % Add this to the list of new vertices
            tVertices=tVertices+1;
            TlatVert(tVertices)=latC;
            TlongVert(tVertices)=longC;
            TdistVert(tVertices)=distThisVertex;
            TstationA(tVertices)=stationCk;
            TstationB(tVertices)=stationAk;
            TstationC(tVertices)=0;
        end
    else
        tVertices=tVertices+1;
        TlatVert(tVertices)=latC;
        TlongVert(tVertices)=longC;
        TdistVert(tVertices)=distThisVertex;
        TstationA(tVertices)=stationCk;
        TstationB(tVertices)=stationAk;
        TstationC(tVertices)=0;
```

```
        end

    end % if distance<distVert(k)

end % for k=1:nVertices finding existing vertices affected by point 0

% make list of stations in the interpolation
nStations=0;
station=0;
% Internal vertices
for k=1:dVertices
    % add the three station numbers to the list if not there
    if DstationA(k)>0 && ~max(station==DstationA(k))
        nStations=nStations+1;
        station(nStations)=DstationA(k);
    end
    if DstationB(k)>0 && ~max(station==DstationB(k))
        nStations=nStations+1;
        station(nStations)=DstationB(k);
    end
    if DstationC(k)>0 && ~max(station==DstationC(k))
        nStations=nStations+1;
        station(nStations)=DstationC(k);
    end
end

% External vertices
for k=1:tVertices
    % add the three station numbers to the list if not there
    if TstationA(k)>0 && ~max(station==TstationA(k))
        nStations=nStations+1;
        station(nStations)=TstationA(k);
    end
    if TstationB(k)>0 && ~max(station==TstationB(k))
        nStations=nStations+1;
```

```
        station(nStations)=TstationB(k);
    end
    if TstationC(k)>0 && ~max(station==TstationC(k))
        nStations=nStations+1;
        station(nStations)=TstationC(k);
    end
end
```

C.5 Calculate distance and bearings: DistBearing.m

```
function [distance,Zs,Zt]=DistBearing(latitude1,longitude1,latitude2,longitude2)

% Approximate Earth physical radius (km)
earthRad=6371; % used in distance calcs

phiS=(pi/180)*latitude1;
phiT=(pi/180)*latitude2;
lambdaD=(pi/180)*(longitude1-longitude2);
 % distance from law of cosines
X=real(acos(sin(phiT)*sin(phiS)+cos(phiT)*cos(phiS)*cos(lambdaD)));
if abs(lambdaD)+abs(phiS-phiT)>0 && X<1.0e-06
    % the above expression has failed or suffers numeric inaccuaracy,
    % so use the following approximation
    X=sqrt(lambdaD*cos(phiS)*lambdaD*cos(phiT)+(phiS-phiT)^2);
end
if lambdaD==0
    if phiS<phiT
        Zs=0;
        Zt=pi;
    else
        Zs=pi;
        Zt=0;
    end
else
    Zt=real(acos((sin(phiS)-sin(phiT)*cos(X))/(cos(phiT)*sin(X))));
    Zs=real(acos((sin(phiT)-sin(phiS)*cos(X))/(cos(phiS)*sin(X))));
    if sin(lambdaD)<0
        Zt=2*pi-Zt;
    else
        Zs=2*pi-Zs;
    end
end
% fix bearings at poles
if phiS==pi/2
```

```
    Zs=pi-lambdaD;
    if Zs>2*pi
        Zs=Zs-2*pi;
    elseif Zs<0
        Zs=Zs+2*pi;
    end
elseif phiS==-pi/2
    Zs=-lambdaD;
    if Zs<0
        Zs=Zs+2*pi;
    end
end
if phiT==pi/2
    Zt=pi+lambdaD;
    if Zt>2*pi
        Zt=Zt-2*pi;
    elseif Zt<0
        Zt=Zt+2*pi;
    end
elseif phiT==-pi/2
    Zt=lambdaD;
    if Zt<0
        Zt=Zt+2*pi;
    end
end
distance=X*earthRad;
```

Bibliography

Australia: ITU-R doc. 3J/112, (2010). *Terrain General Diffraction Model Testing, the Delta-Bullington Method – Proposal for Effective Heights.* Erice, Italy.

Australia: ITU-R doc. 3J/169, (2018). *Proposed Amendment to Recommendation ITU-R P.453-13 Section 3.2.* Geneva, Switzerland.

Australia: ITU-R doc. 3M/186, (2011). *New Source of Measured Data for ITU-R Study Group 3 Databank Table I-2, Line-of-sight Average Worst-month Multipath Fading and Enhancement in Narrow Bandwidths.* Geneva, Switzerland.

Australia: ITU-R doc. 3M/235, (2021). *DBSG3 Table I-2 Line-of-sight Average Year Worst-month Multipath Fading and Enhancement – Proposed Updates to Existing Records.* Geneva, Switzerland.

Australia: ITU-R doc. 3M/236, (2021). *Revised Proposed Revision to the Multipath Model in Recommendation ITU-R P.530-17.* Geneva, Switzerland.

Australia: ITU-R doc. 3M/45, (2016). *New Australian Data for DBSG3 Table I-2 Line-of-sight Average Worst-month Multipath Fading and Enhancement in Narrow Bandwidths.* Geneva, Switzerland.

Barclay-L. (2008). New challenges in the understanding of surface wave propagation, *Proc. ISART 2008, ISART papers*, Boulder Colorado, USA, pp. 112–117.

Barnett-W. T. (1972). Multipath propagation at 4, 6, and 11 GHz, *Bell Syst. Tech. J*, **51**(2), pp. 321–361. doi: 10.1002/j.1538-7305.1972.tb01923.x.

Barrios-A. E. (1994). A terrain parabolic equation model for propagation in the troposphere, *IEEE Trans. Antennas Propagat.*, **42**, pp. 90–98.

Battesti-J., and Boithias-L. (1964). Étude des sections longues dans les faisceaux hertziens en visibilité (Study of long line-of-sight radio paths), *Annales des Télécommunications*, **19**(7-8), pp. 173–187. doi: 10.1007/bf03021656.

Bean-B. R. (1962). The radio refractive index of air, *Proc. IRE*, **50**(3), pp. 260–273.

Boithias-L., and Battesti-J. (1967). Protection contre les évanouissements sur les faisceaux hertziens en visibilité (Protection against fading on line-of-sight radio paths), *Annales des Télécommunications*, **22**(9-10), pp. 230–242. doi: 10.1007/bf03000121.

Bérenger-J.-P. (1994). A perfectly matched layer for the absorption of electromagnetic waves, *J. Comp. Phys.*, **114**, p. 185–200.

Bullington-K. (1947). Radio propagation at frequencies above 30 megacycles, *Proc. IRE*, Vol. 35, (10), pp. 1122–1136. doi: 10.1109/JRPROC.1947.232600.

Claverie-J. (2019). Vertical refractivity profiles within the marine surface boundary layer, *Proc. EuCAP 2019*, Krakow, Poland.

Coleman-C. J. (2005). A Kirchhoff integral approach to estimating propagation in an environment with nonhomogeneous atmosphere and complex boundaries, *IEEE Trans. Ant. Prop*, **53**(10), pp. 3174–3179. doi: 10.1109/TAP.2005.856359.

Coleman-C. J. (2010). An FFT-based Kirchhoff integral technique for the simulation of radio waves in complex environments, *Radio Sci.*, **RS-2002**, pp. 1–14. doi: 10.1029/2009RS004197.

Collin-R.-E. (2004). Hertzian dipole radiating over a lossy earth or sea: some early and late 20th-century controversies, *IEEE Antennas and Propagation Magazine*, **46**, p. 64–79.

Craig-K. H., and Levy-M. F. (1991). Parabolic equation modelling of the effects of multipath and ducting on radar systems, *Proc. IEE - Part F: Radar and signal processing*, **138**(2), pp. 153–162. doi: 10.1049/ip-f-2.1991.0021.

Cressie-N. A. C. (1993). *Statistics for spatial data*, rev. edn, Wiley, New York, USA.

da Silva-M. A. N., Costa-E., and Liniger-M. (2005). Application of computationally-intensive propagation models to the prediction of path losses due to mountainous terrain in the VHF frequency band, *Proc. URSI ClimDiff 2005*, Cleveland Ohio, USA, art. no. Diff 23.

Dee-D., Uppala-S., Simmons-A., Berrisford-P., Poli-P., Kobayashi-S., Andrae-U., Balmaseda-M., Balsamo-G., Bauer-P., Bechtold-P., Beljaars-A., van de Berg-L., Bidlot-J., Bormann-N., Delsol-C., Dragani-R., Fuentes-M., Geer-A., Haimberger-L., Healy-S., Hersbach-H., Hólm-E., Isaksen-L., Kållberg-P., Köhler-M., Matricardi-M., McNally-A., Monge-Sanz-B., Morcrette-J.-J., Park-B.-K., Peubey-C., de Rosnay-P., Tavolato-C., Thépaut-J.-N., and Vitart-F. (2011). The ERA-Interim reanalysis: configuration and performance of the data assimilation system, *Q. J. R. Meteorol. Soc.*, **137**, pp. 553–597. doi: 10.1002/qj.828.

Delbridge-A. (2001). *The Macquarie Dictionary*, 3rd edn, The Macquarie Library, North Ryde, NSW, Australia.

Deygout-J. (1966). Multiple knife-edge diffraction of microwaves, *IEEE Trans. Ant. Prop*, **14**(4), pp. 480–489. doi: 10.1109/tap.1966.1138719.

Dockery-G. D., and Kuttler-J. R. (1996). An improved impedance boundary algorithm for Fourier split-step solutions of the parabolic wave equation, *IEEE Trans. Antennas Propagat.*, **44**(12), pp. 1592–1599. doi: 10.1109/8.546245.

Donohue-D. J., and Kuttler-J. R. (2000). Propagation modeling over terrain using the parabolic wave equation, *IEEE Trans. Antennas Propagat.*, **48**(2), pp. 260–277. doi: 10.1109/8.833076.

Durbin-J., and Watson-G. S. (1951). Testing for serial correlation in least squares regression II, *Biometrika*, **38**(1), pp. 159–177.

Durbin-J., and Watson-G. S. (1971). Testing for serial correlation in least squares regression III, *Biometrika*, **58**(1), pp. 1–19. doi: 10.2307/2334313.

Epstein-J., and Peterson-D. W. (1953). An experimental study of wave propagation at 850 mc/s, *Proc. IRE*, Vol. 41, (5), pp. 595–611.

Ewenz-C. M., Kulessa-A. S., and Salamon-S. J. (2001). Using mesoscale models together with PEM propagation models to determine microwave link output, *Proc. URSI Climpara 2001*, pp. 89–92.

Feit-M. D., and Fleck-J. A. (1978). Light propagation in graded-index fibers, *Applied Optics*, **17**(24), pp. 3990–3998. doi: 10.1364/ao.17.003990.

Giovaneli-C. L. (1984). An analysis of simplified solutions for multiple knife-edge diffraction, *IEEE Trans. Antennas Propagat.*, **32**(3), pp. 297–301. doi: 10.1109/tap.1984.1143299.

Grabner-M., and Kvicera-V. (2005). Statistics of lower atmosphere refractivity in Czechia, *Proc. Asia-Pacific Microwave Conf.* doi: 10.1109/APMC.2005.1606923.

Grabner-M., Kvicera-V., Pechac-P., Kvicera-M., Valtr-P., and Martellucci-A. (2014). World maps of atmospheric refractivity statistics, *IEEE Trans. Antennas Propagat.*, **62**(7), pp. 3714–3722. doi: 10.1109/TAP.2014.2317474.

Green-H.-E. (2007). Derivation of the Norton surface wave using the compensation theorem, *IEEE Antennas and Propagation Magazine*, **49**, p. 47–57.

Harvey-R. A. (1987). A subrefractive fading model for microwave paths using surface synoptic meteorological data, *IEEE Trans. Ant. and Prop.*, **AP-35**(7), pp. 832–844. doi: 10.1109/tap.1987.1144173.

Hersbach-H., Bell-B., Berrisford-P., Hirahara-S., Horányi-A., Muñoz-Sabater-J., Nicolas-J., Peubey-C., Radu-R., Schepers-D., Simmons-A., Soci-C., Abdalla-S., Abellan-X., Balsamo-G., Bechtold-P., Biavati-G., Bidlot-J., Bonavita-M., Chiara-G. D., Dahlgren-P., Dee-D., Diamantakis-M., Dragani-R., Flemming-J., Forbes-R., Fuentes-M., Geer-A., Haimberger-L., Healy-S., Hogan-R. J., Hólm-E., Janisková-M., Keeley-S., Laloyaux-P., Lopez-P., Lupu-C., Radnoti-G., de Rosnay-P., Rozum-I., Vamborg-F., Villaume-S., and Thépaut-J.-N. (2020). The ERA5 global reanalysis, *Q. J. R. Meteorol. Soc.*, **146**, pp. 1999–2049. doi: 10.1002/qj.3803.

Hewitt-T. (2003). Propagation data requirements for radiocommunications system planning, in L. Barclay (ed), *Propagation of Radiowaves*, 2nd edn, The Institution of Engineering and Technology, London, United Kingdom.

Holm-P. D. (2007). Wide-angle shift-map PE for a piecewise linear terrain—a finite-difference approach, *IEEE Trans. Ant. Prop*, **55**(10), pp. 2773–2789. doi: 10.1109/TAP.2007.905865.

Kizer-G. (2008). Improvements in fixed point-to-point microwave radio path design, *Wireless telecomm. symp.* Pomona, CA, USA, doi: 10.1109/WTS.2008.4547588.

Kulessa-A. S., Ewenz-C. M., and Lieff-W. (2001). Determining refractivity structure from non-hydrostatic mesoscale models, *Proc. URSI Climpara 2001*, pp. 83–87.

Kuttler-J. R., and Dockery-G. D. (1991). Theoretical description of the parabolic approximation Fourier split-step method of representing electromagnetic propagation in the troposphere, *Radio Sci.*, **26**(2), pp. 381–393. doi: 10.1029/91rs00109.

Kuttler-J. R., and Janaswamy-R. (2002). Improved Fourier transform methods for solving the parabolic wave equation, *Radio Sci.* doi: 10.1029/2001RS002488.

Levy-M. (2000). *Parabolic Equation Methods for Electromagnetic Wave Propagation*, 1st edn, The Institution of Engineering and Technology, London, United Kingdom.

Levy-M. F. (1990). Parabolic equation modelling of propagation over irregular terrain, *Electronics Letters*, **26**(15), pp. 1153–1155.

Liniger-M., Baumberger-A., Rohner-M., and Cocco-T. (2003). Application of different diffraction models in mountainous terrain, *Proc. URSI ClimDiff 2003*, Fortalesa, Brazil, art. no. Diff.32.

Lystad-S., Hayton-T., Marsh-A., and Tjelta-T. (1998). Interpolation of clear air parameters observed at non-regular observation locations, *Proc. URSI Climpara '98*, Ottawa, Canada, pp. 15–26.

Matheron-G. (1963). Principles of geostatistics, *Economic Geology*, **58**, pp. 1246–1266.

Millington-G., Hewitt-R., and Immirzi-F. S. (1962). Double knife-edge diffraction in field-strength predictions, *Proc. IEE - Part C: Monographs*, **109**(16), pp. 419–429. doi: 10.1049/pi-c.1962.0059.

Milsom-J. (2003). Surface waves, and sky waves below 2 MHz, in L Barclay (ed), *Propagation of radiowaves*, 2nd edn, The Institution of Engineering and Technology, London, United Kingdom.

Morita-K. (1970). Prediction of Rayleigh fading probability of line-of sight microwave links, *Review of the Elec. Comm. Labs, NTT Corp.*, **18**, pp. 810–821.

NOAA / ESRL Radiosonde Database, (2018). *US National Oceanic and Atmospheric Administration, Earth System Research Laboratory.* Web. http://www.esrl.noaa/raobs/Welcome.cgi.

NOAA Global Hourly Data, (2022). *US National Oceanic and Atmospheric Administration, Surface Weather Station Data.* Web. https://www1.ncdc.noaa.gov/pub/data/noaa/.

NOAA IGRA Radiosonde Database, (2022). *US National Oceanic and Atmospheric Administration, Integrated Global Radiosonce Archive.* Web. https://www.ncei.noaa.gov/products/weather-balloon/integrated-global-radiosonde-archive.

Norton-K. A. (1937). The physical reality of space and surface waves in the radiation field of radio antennas, *Proc. IRE*, Vol. 25, pp. 1192–1202. doi: 10.1109/jrproc.1937.228543.

Norton-K. A. (1941). The calculation of ground-wave field intensity over a finitely conducting spherical earth, *Proc. IRE*, Vol. 29, pp. 623–639. doi: 10.1109/JRPROC.1941.233636.

Obukhov-A. (1971). Turbulence in an atmosphere with a non-uniform temperature, *Bound.-Layer Meteorol.*, **2**(1), pp. 7–29. doi: 10.1007/bf00718085.

Olsen-R. L., and Tjelta-T. (1999). Worldwide techniques for predicting the multipath fading distribution on terrestrial LOS links: background and results of tests, *IEEE Trans. Ant. Prop*, **47**(1), pp. 157–170. doi: 10.1109/8.753006.

Olsen-R. L., Tjelta-T., Martin-L., and Segal-B. (2003). Worldwide techniques for predicting the multipath fading distribution on terrestrial LOS links: comparison with regional techniques, *IEEE Trans. Ant. Prop*, **51**(1), pp. 23–30. doi: 10.1109/tap.2003.808538.

Ozgun-O., Apaydin-G., Kuzuogluc-M., and Sevgi-L. (2011). PETOOL: MATLAB-based one-way and two-way split-step parabolic equation tool for radiowave propagation over variable terrain, *Computer Physics Communications*, **182**, p. 2638–2654. doi: 10.1016/j.cpc.2011.07.017.

Paulus-R. A. (1990). Evaporation duct effects on sea clutter, *IEEE Trans. Antennas Propagat.*, **AP-38**(11), pp. 1765–1771.

Pearson-K. W. (1965). Method for the prediction of the fading performance of a multisection microwave link, *Proc. IEE*, Vol. 112, pp. 1291–1300. doi: 10.1049/piee.1965.0216.

Rec. ITU-R P.1057-6, (2019). *Probability Distributions Relevant to Radiowave Propagation Modelling.* Web. https://www.itu.int/rec/R-REC-P.1057-6-201908-I/en.

Rec. ITU-R P1144-9, (2017). *Guide to the Application of the Propagation Methods of Radiocommunication Study Group 3.* Web. https://www.itu.int/rec/R-REC-P.1144-9-201712-I/en.

Rec. ITU-R P.311-17, (2017). *Acquisition, Presentation and Analysis of Data in Studies of Radiowave Propagation.* Web. https://www.itu.int/rec/R-REC-P.311-17-201712-I/en.

Rec. ITU-R P453-14, (2019). *Propagation by Diffraction.*
Web. https://www.itu.int/rec/R-REC-P.453-14-201908-I/en.

Rec. ITU-R P526-12, (2012). *Propagation by Diffraction.*
Web. https://www.itu.int/rec/R-REC-P.526-12-201202-I/en.

Rec. ITU-R P526-15, (2019). *Propagation by Diffraction.*
Web. https://www.itu.int/rec/R-REC-P.526-15-201910-I/en.

Rec. ITU-R P.530-13, (2009). *Propagation Data and Prediction Methods Required for the Design of Terrestrial Line-of-sight Systems.* Web. https://www.itu.int/rec/R-REC-P.530-13-200910-S/en.

Rec. ITU-R P.530-17, (2017). *Propagation Data and Prediction Methods Required for the Design of Terrestrial Line-of-sight Systems.* Web. https://www.itu.int/rec/R-REC-P.530-17-201712-I/en.

Rec. ITU-R P.530-18, (2021). *Propagation Data and Prediction Methods Required for the Design of Terrestrial Line-of-sight Systems.* Web. https://www.itu.int/rec/R-REC-P.530-18-202109-I/en.

Rec. ITU-R P.530-8, (1999). *Propagation Data and Prediction Methods Required for the Design of Terrestrial Line-of-sight Systems.* Web. https://www.itu.int/rec/R-REC-P.530-8-199910-S/en.

Rec. ITU-R P.530-9, (2001). *Propagation Data and Prediction Methods Required for the Design of Terrestrial Line-of-sight Systems.* Web. https://www.itu.int/rec/R-REC-P.530-9-200102-S/en.

Rec. ITU-R P.581-2, (1990). *The Concept of "Worst Month"*
Web. https://www.itu.int/rec/R-REC-P.581-2-199006-I/en.

Rec. ITU-R P.841-6, (2019). *Conversion of Annual Statistics to Worst-month Statistics.*
Web. https://www.itu.int/rec/R-REC-P.841-6-201908-I/en.

Report CCIR 338, (1966). *Propagation Data and Prediction Methods Required for Line-of-sight Radio-relay Systems, Oslo.*

Report CCIR 338-6, (*1990*). *Propagation Data and Prediction Methods Required for Line-of-sight Radio-relay Systems, Geneva.*

Rueger-J. M. (*2002*). Refractive index formulae for radio waves, *Proc. Int. Fed. Surveyors* (*FIG*) *XXII Internat. Congress*, pp. 19–26.

Ryan-F. J. (1991). Analysis of electromagnetic propagation over variable terrain using the parabolic wave equation, *Technical Report 1453*, Naval Ocean Systems Center, San Diego, California.

Salamon-S. J., and Kulessa-A. S. (2004). Predicting the impact of trans-horizon terrestrial interference on digital fixed links, *Proc. URSI-F 2004*, Cairns, Australia, pp. 156–162.

Salamon-S. J., and Wilson-C. D. (2008). Reducing discontinuity in practical prediction of diffraction loss in irregular terrain, *Proc. ISART 2008, ClimDiff papers*, Boulder Colorado, USA, pp. 259–266.

Salamon-S. J., Hansen-H. J., and Abbott-D. (2013). A transform space filtered, wide frequency-range implementation of the parabolic equation method, *Proc. RADAR 2013*, Adelaide, Australia. doi: 10.1109/radar.2013.6652010.

Salamon-S. J., Hansen-H. J., and Abbott-D. (2014a). Prediction of surface refractivity gradient distributions, from weather station surface data, *Proc. EuCAP 2014*, The Hague, Netherlands, pp. 507–511. doi: 10.1109/eucap.2014.6901750.

Salamon-S. J., Hansen-H. J., and Abbott-D. (2014b). Surface refractivity gradient data for radio system design, *Proc. URSI GASS 2014*, Beijing, China. doi: 10.1109/ACCESS.2020.2987618.

Salamon-S. J., Hansen-H. J., and Abbott-D. (2015). Modelling radio refractive index in the atmospheric surface layer, *Electronics Letters*, **51**(14), pp. 1119–1121. doi: 10.1049/el.2015.0195.

Salamon-S. J., Hansen-H. J., and Abbott-D. (2016). Radio link clear-air fading prediction from surface weather station data, *Proc. ISAP 2016*, Okinawa, Japan, pp. 72–73.

Salamon-S. J., Hansen-H. J., and Abbott-D. (2019). How real are observed trends in small correlated datasets?, *Royal Society open science*. doi: 10.1098/rsos.181089.

Salamon-S. J., Hansen-H. J., and Abbott-D. (2020). Universal kriging prediction of line-of-sight microwave fading, *IEEE Access*, **8**, pp. 74743–74758. doi: 10.1109/ACCESS.2020.2987618.

Sambridge-M., Braun-J., and McQueen-H. (1995). Geophysical parametrization and interpolation of irregular data using natural neighbours, *Geophys. J. Int.*, **122**, pp. 837–857.

Schiavone-J. A. (1981). Prediction of positive refractivity gradients for line-of-sight microwave radio paths, *Bell Syst. Tech. J*, **60**(6), pp. 803–822. doi: 10.1002/j.1538-7305.1981.tb03382.x.

Shepard-D. (1968). A two-dimensional interpolation for irregularly-spaced data, *Proc. 1968 ACM Nat. Conf.*, pp. 517–524.

Shepherd-G. (1979). East-west 6.7 GHz propagation study, *Technical Report 9/79*, Telecom Australia Radiocom Branch, Melbourne, Australia.

Sibson-R. (1980). The Dirichiet tessellation as an aid in data analysis, *Scand. J. Statistics*, **7**, p. 14–20.

Sommerfeld-A. N. (1909). The propagation of waves in wireless telegraphy, *Ann. Phys. (Leipzig)*, **28**, pp. 665–737.

Tang-H., Wang-H., Huang-X., and Wu-S. (2012). A case study of subrefraction and its influence on electromagnetic waves propagation, *Proc. CEEM 2012*, pp. 58–62.

Telenor ASA: ITU-R doc. 3M/175, (2006). *Test of Methods for Predicting the Tail of the Multipath Fading Distribution.* Geneva, Switzerland.

Thomson-D. J., and Chapman-N. R. (1983). A wide-angle split-step algorithm for the parabolic equation, *J. Acoust. Soc. Am.*, **74**, p. 1848–1854. doi: 10.1121/1.390272.

Tjelta-T., Hayton-T. G., Segal-B., and Salonen-E. L. (1998). Correlation of observed multipath occurrence with climatic parameters derived from radiosondes, surface stations, and numerical atmosphere models, *Proc. URSI Climpara '98*, Ottawa, Canada, pp. 85–97.

Tjelta-T., Olsen-R. L., and Martin-L. (1990). Systematic development of new multivariable techniques for predicting the distribution of multipath fading on terrestrial microwave links, *IEEE Trans. Antennas Propagat.*, **38**(10), pp. 1650–1665.

Todhunter-I. (1886). *Spherical Trigonometry*, 5th edn, Macmillan, London, England.

United Kingdom: ITU-R doc. 3J/64, (2009). *A New Approach to Diffraction Modelling for a General Path, the "Delta" Method.* Geneva, Switzerland.

Vigants-A. (1975). Space-diversity engineering, *Bell Syst. Tech. J*, **54**(1), pp. 103–142.

Vigants-A. (1981). Microwave radio obstruction fading, *Bell Syst. Tech. J*, **60**(6), pp. 785–801.

Wait-J.-A. (1998). The ancient and modern history of EM ground-wave propagation, *IEEE Antennas and Propagation Magazine*, **40**, p. 7–24.

Willmott-C. J., Rowe-M., and Philpot-W. D. (1985). Small-scale climate maps: a sensitivity analysis of some common assumptions associated with grid-point interpolation and contouring, *Amer. Cartographer*, **12**(1), pp. 5–16.

Zhamsuyeva-G. (1998). Variation of radiometeorological parameters in the lower atmosphere near Lake Baikal, *Proc. URSI Climpara '98*, Ottawa, Canada, pp. 116–117.

Appendix D

Biography

Stephen J. Salamon graduated from the University of Adelaide, initially with B.Sc. (Physics, Comp. Sci.) in 1976, followed by B.E. (Elec.) in 1981 and then, after initially being a broadcast station engineer, in late 1981 he joined Telecom Australia as a radio link design engineer. Between 1985 and 1992 he designed radio systems in remote regions of Australia for the Rural and Remote Areas Program. In 1995 he joined Telstra Corporation Operations as a Principal Engineer in the point-to-point radio national leadhouse group. While there, he was in 2000 author of the Telstra Corporation technical manual on line-of-sight radio link design and performance prediction, based as far as possible on *ITU-R Recommendations*, but taking into account his own analysis of long-term performance data from hundreds of radio links around Australia. His first conference paper as prime author, for URSI in 2004, was instrumental in successfully coordinating Australia's 2006 rollout of the 3G network with fixed radio links that then still occupied the same 850 MHz band.

Since 1998 he has been an active member of Australian Radio Study Group 3, drafting many Australian inputs to the Working Parties of ITU-R Study Group 3 (radiowave propagation). He has been an Australian Delegate to these meetings since 2008, contributing to the development of prediction models for terrain diffraction, interference propagation, and terrestrial link design. In 2009 he contributed to amending the scope of *Recommendation ITU-R P.452* on terrestrial interference, extending the frequency range down from 700 MHz to 100 MHz. In 2011 he was chosen to chair the Drafting Group in Working Party 3J (propagation fundamentals), that successfully resolved the long-standing international impasse on the final form of the general terrain diffraction model, for *Recommendation ITU-R P.526*, and all other P-series *ITU-R Recommendations* requiring such a model. In 2017, he drafted and presented an Australian input document,

which was adopted in full, achieving consistency between the various diversity improvement models in *Recommendation ITU-R P.530*, and making frequency diversity predictions consistent with observations in severe fading environments, such as parts of Australia. In that year he also contributed to the development of the urban microwave slant-path clutter loss model, required for ITU-R sharing studies for 5G. His latest significant contribution has been presenting the multipath fading model proposed in this thesis, which was adopted in full by ITU-R Study Group 3 in July 2021, and internationally approved and published in September 2021.

Since 2013 he has been a part-time PhD candidate in the School of Electrical and Electronic Engineering at the University of Adelaide, researching clear-air terrestrial radio fading, under Derek Abbott and Hedley Hansen. He is currently chairman of Australian Radio Study Group 3 (radiowave propagation). In international meetings he frequently leads the Australian Delegation to ITU-R Study Group 3, and is currently chairman of ITU-R SWG 3J-4 (vegetation attenuation and obstacle diffraction). He is a regular reviewer for *IEEE Transactions on Antennas and Propagation*.

D.1 Academic genealogy

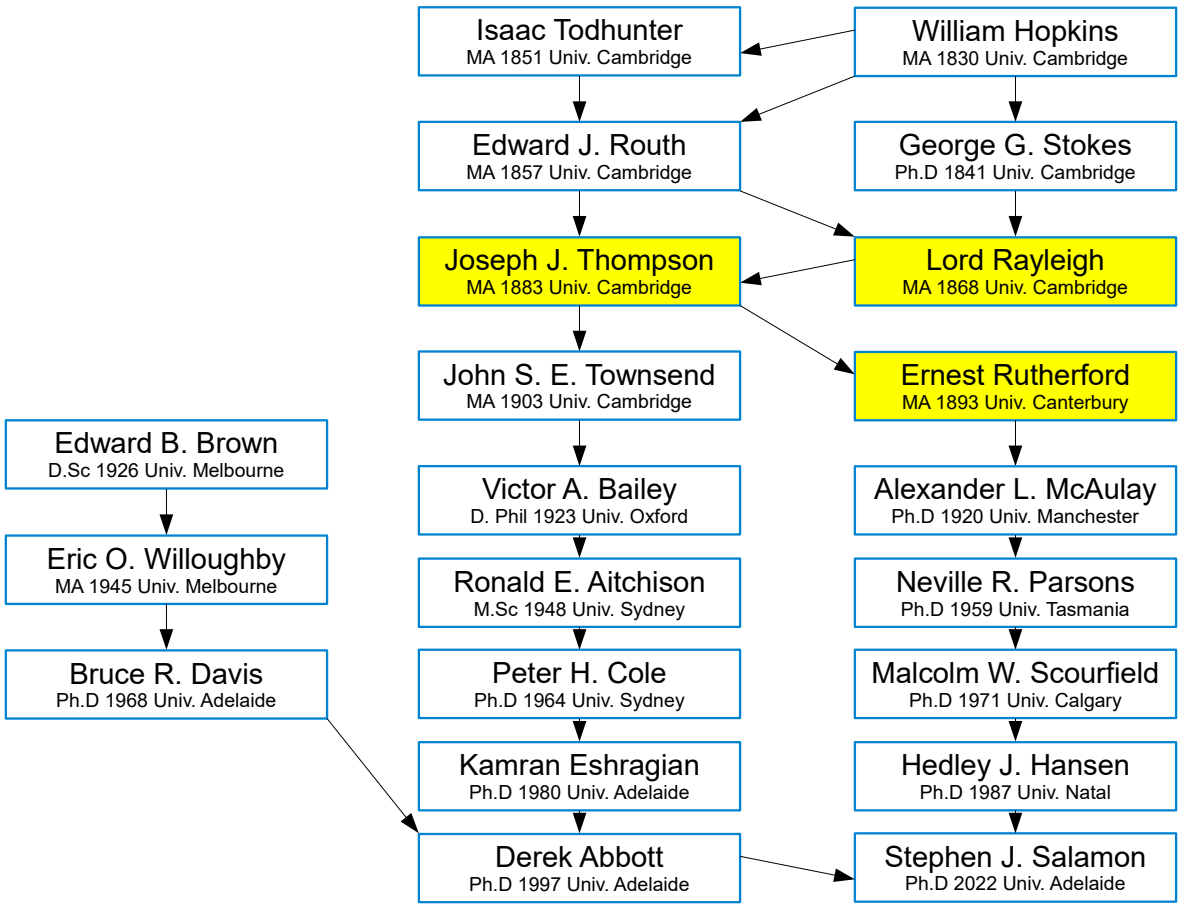

Supervisor-student relationships are shown back in time to William Hopkins, whose students included James Clerk Maxwell and Lord Kelvin, as well as Isaac Todhunter and George Stokes shown here. Additional mentor-protegé relationships, particularly at Cambridge University, are not shown here for clarity. Nobel laureates are shown with gold background.

Professor Eric Willoughby was the first chair of the Electrical Engineering Department at the University of Adelaide, and Associate Professor Edward (Eddy) Brown was a founding academic in the Department of Electrical Engineering at the University of Melbourne.